

POLITECNICO DI TORINO

Master's Degree in Mechanical Engineering

Department of Mechanical and Aerospace Engineering

Enhancement of PCM materials using metal fins in a battery thermal management system



Supervisor:

Prof. Davide Papurello

Co-Supervisor:

Prof. Marco Carlo Masoero

Candidate

Pierluca Paciolla

March/April graduation session

Academic Year 2021/2022

Abstract

It is clear that the world of transport is dominated by oil: today 55% of global demand for oil comes from the transport sector as a whole, the trend will increase over the years (60% in 2040). The increasingly critical scenario of pollutant emissions calls for the use of alternative propulsion sources. These include the use of hybrid propulsion vehicles (HEVs) whose operating principle is based on batteries of various types, including lithium-ion batteries. The optimal operation of the batteries is obtained when they work in a temperature range ranging from 15 °C to 35 °C. Working with temperature values in the range of 0 °C, the main effect is the loss of energy and power. On the other hand, excessively high temperatures can lead to catastrophic phenomena such as the Thermal Runaway. The need to limit the temperature gradient of the battery to less than 5 °C should not be overlooked. Because of this, it is useful to implement an effective battery body cooling system (BTMS). In this case study a lithium-ion battery with "Pouch" structure and chemical composition of the NMC cathode is analysed. For temperature control, a passive system is used, which uses the latent heat of material phase change to obtain battery cooling (LHTES) as a useful effect. The first step of the study consists in the simulation, through the software ANSYS FLUENT, of the thermal behaviour of the cell in order to obtain a temperature trend of the numerical model similar to that obtained by experimentation. The cooling system of the cell consists in the coating of the latter with phase change material (PCM), in particular n-Octadecane (paraffin) was chosen because of its thermophysical properties and the convenient market price. Octadecane has high latent heat values (about 225 kJ/kg) at the expense of thermal conductivity values of the order of 0.385 W/mk. To overcome this problem, a system of increasing the performance of the PCM is adopted: PCM-Fin Structure. The second step, therefore, concerns the study of the thermal behaviour of the battery subject first to a layer of pure PCM and, later, to a layer of PCM-Fin Structure. Having analysed the effects of cooling on the single cell, the analysis involves the study of the thermal behaviour of a battery pack with 1P3S configuration. The last part of the work consists in the variation of geometric parameters such as thickness of the PCM, thickness and spacing of the fins in the battery pack in order to verify how the variation of these leads to a consequent variation of the thermal behaviour of the entire package.

*“Simulating in CFD is like putting clothes in a washing machine
and expecting them to stay in the same position”*
Authors

Table of Contents

Abstract	i
List of Tables	vi
List of Figures	vii
Chapter 1 Introduction	1
1.1 Energy Aspects	1
1.2 Motivations	9
1.3 Scope of research	10
1.4 Outline of the thesis	12
Chapter 2 Overview	13
2.1 Battery overview.....	13
2.2 LIB Chemistry	14
2.3 Battery working principles	15
2.4 Cylindrical Cells	16
2.5 Prismatic Cells	17
2.6 Pouch Cells	18
2.7 Adverse effects of temperature	20
2.7.1 Performance degradation.....	20
2.7.2 Temperature maldistribution.....	21
2.7.3 Low temperature performance	21
2.7.4 Thermal Runaway	23
2.8 Battery Thermal management systems	24
2.8.1 Air cooling.....	24
2.8.2 Liquid cooling	29
2.8.3 PCM	32
2.8.3.1 Classification	33
2.8.3.2 Solid-liquid phase change system	35
2.8.3.3 Thermal Conductivity Enhancement (TCE) methods.....	38
2.8.3.3.1 Fins	39
Chapter 3 Physics of the problem.....	40

3.1 Thermal Model	40
3.2 MSMD Approach	43
3.2.1 Chen’s Model	45
3.2.1.1 Model Extraction	49
3.2.2 ECM in Ansys Fluent	51
3.3 PCM Problem	53
3.3.1 PCM in Ansys Fluent	55
3.4 Boundary Conditions	56
Chapter 4 Model development	58
4.1 Li-ion cell properties	59
4.2 Li-ion cell geometry	59
4.3 Meshing	63
4.4 Model Set Up	66
4.4.1 ECM Parameters	68
4.5 Cooling Systems	75
4.5.1 Heat Sinks geometry	75
4.5.1.1 Heat sinks meshing	78
4.5.2 PCM	80
4.5.2.1 PCM Meshing	83
4.5.3 PCM with Heat Sinks	84
4.5.3.1 PCM with Heat Sinks meshing	86
4.6 Materials	88
4.6.1 Thermophysical Properties of the cell	88
4.6.2 Passive components materials	93
4.6.3 PCM selection for the application	94
4.6.3.1 PCM parameters	96
4.7 Boundary Conditions	99
4.8 Solution	100
4.9 Contact resistance	101
4.10 Battery Pack	104
4.10.1 Battery Pack Geometry	105
4.10.2 Battery pack Meshing	108

Chapter 5 Results and Discussion	110
5.1 Model Validation	110
5.2 Ambient temperature and C-rates effects	119
5.3 Hot spots identification	126
5.4 Cooling systems performance	130
5.4.1 Heat Sinks performance	130
5.4.2 Pure PCM performance	135
5.4.3 PCM-Fin structure performance	142
5.5 Battery Pack performance	150
5.5.1 Battery Pack with pure PCM performance	154
5.5.2 Effect of PCM thickness	160
5.5.3 Battery Pack with PCM-Fin structure performance	164
5.5.4 Effect of fin thickness and spacing	172
5.5.5 Effect of the number of plates	181
Chapter 6 Conclusions	191
References	193

List of Tables

Table 1 Cell capacity at different operating temperatures and C-rates [Ah]. [79].....	59
Table 2 Cell geometric characteristics. [79]	60
Table 3 “Named Selection” of the elements.	64
Table 4 Parameters in Model Option.	66
Table 5 Dimensions of heat sinks and heat sinks plate.	76
Table 6 “Named Selection” of the elements.	79
Table 7 PCM geometric characteristics.	81
Table 8 “Named Selection” of the elements.	87
Table 9 Specification of the pouch cell used for the experiments. [87]	91
Table 10 Specification of the pouch cell used for the simulation. [87].....	91
Table 11 Specification of the Al used for the simulation. [84].....	93
Table 12 Specification of the Al used for the simulation. [84].....	93
Table 13 PCM Thermophysical properties.	98
Table 14 Meters related to the heating of current collecting tabs.	102
Table 15 Parameters related to the heating of current collecting tabs.	102
Table 16 ECM Parameters in ANSYS FLUENT.....	113
Table 17 parameters for the calculation of Center temperature MSE.....	116
Table 18 Parameters for the calculation of voltage MSE.....	117
Table 19 ECM Parameters in ANSYS FLUENT @0 °C.	120
Table 20 ECM Parameters in ANSYS FLUENT @45°C.	122
Table 21 ECM Parameters in ANSYS FLUENT @25°C and 2-C Rate.....	124
Table 22 Summary of the performance of the various cooling systems with 1C discharge current.	149
Table 23 Summary of the performance of the various cooling systems with 2C discharge current.	149
Table 24 Summary of the performance of the various Battery Pack cooling systems with 1C discharge current.	171
Table 25 Summary of the performance of the various Battery Pack cooling systems with 2C discharge current.	171
Table 26 Fin thickness.....	172
Table 27 Fin number and spacing.	176

List of Figures

Figure 1 Oil demand (Mb/d): transport and other energy sectors [1].	1
Figure 2 Gt = Giga tons of CO ₂ equivalent emitted by the transport sector [1].	2
Figure 3 Energy pathways for fuels [1].	3
Figure 4 Comparison of vehicle efficiencies [1].	5
Figure 5 Comparison of energy density per unit volume and per unit weight [1].	5
Figure 6 PWT+energy source [kg] in terms of Range on NEDC (km) [1].	6
Figure 7 Schematic representation of series HEV [1].	6
Figure 8 Schematic representation of parallel HEV [1].	7
Figure 9 State of charge (SOC) in terms of time [1].	8
Figure 10 Typical components of lithium-ion batteries (LIBs) and their compositions.	14
Figure 11 Schematic illustration of lithium-ion battery [7].	15
Figure 12 Schematic to show the structure of a cylindrical Li-Ion cell.	16
Figure 13 Schematic to show the structure of a prismatic Li-Ion cell.	17
Figure 14 Schematic to show the structure of a Li-Ion pouch cell.	19
Figure 15 Thermal runaway characteristic of Li-ion battery.	23
Fig. 16 Passive and active air-cooling [30].	25
Figure 17 Schematic of the air cool BTMSs [38].	27
Figure 18 System used in [39].	27
Figure 19 3D model of the battery module and its variation during the discharge process with different widths of cooling plate and a fixed flow rate of 0.17kg/s.	30
Figure 20 The schematic of the novel channels design procedure (a) the empty plate (b) extracted streamline (c) build the channels in 2D (d) 3-Dimensional channels.	31
Figure 21 PCM classification considering material composition.	33
Figure 22 a) Illustrations of the internal structure of a disassembled 18650 cylindrical battery and the design of a PCM-embedded battery; b) Schematic of a passively cooled 40-cell battery pack; c) Schematic of a hybrid cooling design for the battery pack. [60]	36
Figure 23 Optimization of Y shaped fins as TCE. Liquid fraction (half left) and Temperature (half right) profiles: initial (left) and optimal design (right).	39
Figure 24 State of the art. (a) Thevenin, (b) impedance, and (c) runtime-based electrical battery models.	44
Figure 25 Proposed electrical battery model.	45
Figure 26 Typical battery characteristic curves of usable capacity versus (a) cycle number, (b) temperature, (c) current, and (d) storage time, as well as (e) open circuit voltage versus SOC and (f) transient response to a step load-current event.	48
Figure 27 R _(Transient_S) . [73].	50
Figure 28 Open Circuit Voltage. [73]	50
Figure 29 Electric Circuits Used in the ECM Model. [72]	51
Figure 30 Solid–liquid interface for a multidimensional situation [76].	54

Figure 31 The temperature distributions of the center section under different rates. (a) 1C; (b) 3C; (c) 5C; (d) 10C. [80]	61
Figure 32 The temperature distribution of battery center section at different rates. (a) 1C; (b) 3C; (c) 5C; (d) 10C. [80]	62
Figure 33 geometry of the cell.	62
Figure 34 Mesh of the cell.	64
Figure 35 “Element Quality” of the cell.	65
Figure 36 “Grid Space Independency Test” of the cell.	65
Figure 37 Model Option for MSMD Battery Model.	67
Figure 38 Chen’s model parameters for MSMD Battery Model.	68
Figure 39 Battery Center Temperature @ 25 °C and 1 C-rate.	69
Figure 40 Temperature comparison @ 25 °C and 1 C-rate. [81]	69
Figure 41 Voltage comparison @25°C and 1 C-rate. [81]	70
Figure 42 Extracted parameter of the polymer Li-ion battery at room temperature. [73]	71
Figure 43 Average values of R0. [79]	71
Figure 44 Average values of R1. [79]	72
Figure 45 Average values of Uoc [V]. [79]	72
Figure 46 Average values of C1 [F]. [79]	73
Figure 47 Battery with Heat Sinks geometry.	75
Figure 48 Sketch of the experimental system and thermocouples locations in single battery. [82]	77
Figure 49 Comparisons of the inhomogeneous temperature contours and evolution history obtained from prediction and measure during 3C discharge under different thermal management modes: (a) natural convection, (b) heat sink without PCM. [82].	77
Figure 50 “Element Quality” of the Heat Sinks.	78
Figure 51 “Mesh Metric” of the Heat Sinks.	78
Figure 52 Battery with pure PCM geometry.	80
Figure 53 Comparisons of the inhomogeneous temperature contours and evolution history obtained from prediction and measure during 3C discharge under thermal management mode: pure PCM. [82].	82
Figure 54 "Element Quality" of the Battery with Pure PCM	83
Figure 55 “Element Quality” of the Battery and Pure PCM.	83
Figure 56 Battery with PCM and Heat Sinks geometry.	84
Figure 57 Evolution of Tmax and PCM liquid fraction. [82].	85
Figure 58 “Element Quality” of the Battery with PCM and Heat Sinks.	86
Figure 59 A sample 3.2 V/10 Ah LFP aluminum-laminated battery. [80]	88
Figure 60 Schematic representation of the effective thermal conductivity at the interface. The elements are connected in (A) parallel; (B) series. [83].	89
Figure 61 Orthotropic Conductivity.	92
Figure 62 Thermophysical properties of PCMs investigated for different applications. [86].	95

Figure 63 Paraffins properties. [29]	95
Figure 64 Piecewise-Linear Profile of Specific Heat.....	97
Figure 65 “Active_wall_convection” ANSYS.	99
Figure 66 Positions of the temperature sensors on the cell (frontside and backside, up and down respectively). [81].....	100
Figure 67 Equations solved in ANSYS.....	100
Figure 68 “Coupled wall” in Mesh Interfaces.	101
Figure 69 Electric contacts resistance.	103
Figure 70 Comparison the temperature field (real measured and simulated).....	103
Figure 71 Battery Pack geometry.	105
Figure 72 Battery Pack with PCM geometry.....	106
Figure 73 Battery Pack with PCM and Heat sinks geometry.	107
Figure 74 Battery Pack with PCM and Heat sinks Mesh.	108
Figure 75 Battery Pack with PCM and Heat sinks “Element Quality”.....	109
Figure 76 Identification of measuring points.	111
Figure 77 Voltage comparison @25°C and 1 C-rate.	112
Figure 78 Temperature comparison @25°C and 1 C-rate.....	112
Figure 79 Voltage Comparison @25°C and 1C Rate.	113
Figure 80 Corner Temperature Comparison @25°C and 1C Rate.	114
Figure 81 Center Temperature Comparison @25°C and 1C Rate.....	114
Figure 82 Battery contour of Temperature @25°C and 1C Rate (3600 s).....	118
Figure 83 Battery contour of Temperature @0°C and 1C Rate (3600 s).....	120
Figure 84 Battery contour of Temperature @45°C and 1C Rate (3600 s).....	122
Figure 85 Simulated Max Temperature @25°C and 2C Rate.	125
Figure 86 Simulated Corner and Center Temperature @25°C and 2C Rate.....	126
Figure 87 Simulated Temperature Contour at different time steps @25°C and 2C Rate.	127
Figure 88 Simulated Temperature Contour at 1800 s @25°C and 2C Rate.....	128
Figure 89 Delta active Temperature @25°C and 2C Rate.	129
Figure 90 Simulated Temperature with Heat Sinks @25°C and 1C Rate.....	130
Figure 91 Simulated Temperature Contour at 3600 s @25°C and 1C Rate.....	131
Figure 92 Simulated average Heat Sinks Temperature @25°C and 1C Rate.	132
Figure 93 Simulated Temperature with Heat Sinks @25°C and 2C Rate.....	132
Figure 94 Simulated Temperature Contour at different time steps @25°C and 2C Rate.	133
Figure 95 Simulated Temperature Contour without Heat Sinks at 1800 s @25°C and 2C Rate.	134
Figure 96 Simulated Temperature Contour at 1800 s @25°C and 2C Rate.....	134
Figure 97 Simulated Temperature with PCM @25°C and 1C Rate.	135
Figure 98 Simulated Temperature Contour without PCM at 3600 s @25°C and 1C Rate.	136

Figure 99 Simulated Temperature Contour with PCM at 3600 s @25°C and 1C Rate.	136
Figure 100 Simulated Liquid Fraction Contour at 3600 s @25°C and 1C Rate.	137
Figure 101 Simulated Max PCM Temperature @25°C and 1C Rate.	137
Figure 102 Simulated Max PCM liquid fraction @25°C and 1C Rate.	138
Figure 103 Simulated Temperature with PCM @25°C and 2C Rate.	139
Figure 104 Simulated PCM liquid fraction Contour at 1800 s and 2C Rate.	140
Figure 105 Simulated Max PCM liquid fraction @25°C and 2C Rate.	140
Figure 106 Simulated Temperature Contour with PCM at 1800 s @25°C and 2C Rate.	141
Figure 107 Simulated Max PCM Temperature @25°C and 2C Rate.	141
Figure 108 Simulated Temperature with PCM-Fin structure @25°C and 1C Rate.	142
Figure 109 Simulated PCM-Fin structure liquid fraction Contour at 3600 s and 1C Rate.	143
Figure 110 Simulated Temperature Contour with PCM-Fin structure at 3600 s @25°C and 1C Rate.	143
Figure 111 Simulated Max PCM-Fin structure liquid fraction @25°C and 1C Rate.	144
Figure 112 Simulated Temperature with PCM-Fin structure @25°C and 2C Rate.	145
Figure 113 Simulated Temperature Contour with PCM-Fin structure at 1800 s @25°C and 2C Rate.	146
Figure 114 Simulated Temperature Contour with PCM-Fin structure at different time steps @25°C and 2C Rate.	146
Figure 115 Comparison of Center Temperature for pure PCM and PCM-Fin structure @25°C and 2C Rate.	147
Figure 116 Simulated PCM-Fin structure liquid fraction Contour at 1800 s and 2C Rate.	147
Figure 117 Comparison of Max liquid fraction for pure PCM and PCM-Fin structure @25°C and 2C Rate.	148
Figure 118 Simulated Max Temperature @25°C and 1C Rate.	150
Figure 119 Simulated Battery Pack Temperature Contour at 3600 s @25°C and 1C Rate.	151
Figure 120 Simulated Max Temperature @25°C and 2C Rate.	152
Figure 121 Simulated Battery Pack Temperature Contour at different time steps @25°C and 2C Rate.	153
Figure 122 Simulated Battery Pack Temperature Contour at 1800 s @25°C and 2C Rate.	153
Figure 123 Simulated Battery Pack Max Temperature with PCM @25°C and 1C Rate.	154
Figure 124 Simulated Battery Pack Temperature Contour with PCM at 3600 s @25°C and 1C Rate.	155
Figure 125 Simulated Battery Pack Average PCM liquid fraction @25°C and 1C Rate.	156

Figure 126 Simulated Battery Pack Liquid Fraction Contour at 3600 s @25°C and 1C Rate.	156
Figure 127 Simulated Battery Pack Max Temperature with PCM @25°C and 2C Rate	157
Figure 128 Simulated Battery Pack Temperature Contour with PCM at 1800 s @25°C and 2C Rate.	157
Figure 129 Simulated Battery Pack Max PCM Temperature @25°C and 2C Rate. ...	158
Figure 130 Simulated Battery Pack Liquid Fraction Contour at 1800 s @25°C and 2C Rate.	158
Figure 131 Simulated Battery Pack Max PCM liquid fraction @25°C and 2C Rate. .	159
Figure 132 Simulated Battery Pack Average PCM liquid fraction @25°C and 2C Rate.	159
Figure 133 Simulated Battery Pack Temperature Contour with 5 mm PCM at 1800 s @25°C and 2C Rate.	160
Figure 134 Simulated Battery Pack Temperature Contour with 11 mm PCM at 1800 s @25°C and 2C Rate.	160
Figure 135 Simulated Battery Pack Max Temperature with different PCM thickness @25°C and 2C Rate.	161
Figure 136 Simulated Battery Pack Max Temperature difference (ΔT_{max}) with PCM Thickness @25°C and 2C Rate.	162
Figure 137 Simulated Battery Pack Liquid Fraction Contour with 5 mm PCM at 1800 s @25°C and 2C Rate.	162
Figure 138 Simulated Battery Pack Average liquid fraction comparison with PCM Thickness @25°C and 2C Rate.	163
Figure 139 Simulated Battery Pack Liquid Fraction Contour with 11 mm PCM at 1800 s @25°C and 2C Rate.	163
Figure 140 Simulated Battery Pack Max Temperature with PCM-Fin Structure @25°C and 1C Rate.	164
Figure 141 Simulated Battery Pack Temperature Contour with PCM-Fin structure at 3600 s @25°C and 1C Rate.	165
Figure 142 Simulated Battery Pack with PCM-Fin structure Average PCM liquid fraction @25°C and 1C Rate.	166
Figure 143 Simulated Battery Pack Liquid Fraction Contour with PCM-Fin structure at 3600 s @25°C and 1C Rate.	166
Figure 144 Simulated Battery Pack Max Temperature with PCM-Fin Structure @25°C and 2C Rate.	167
Figure 145 Simulated Battery Pack with PCM-Fin structure Temperature Contour at different time steps @25°C and 2C Rate.	168
Figure 146 Simulated Battery Pack Temperature Contour with PCM-Fin structure at 1800 s @25°C and 2C Rate.	169
Figure 147 Simulated Battery Pack Liquid Fraction Contour with PCM-Fin structure at 1800 s @25°C and 2C Rate.	169

Figure 148 Simulated Battery Pack with PCM-Fin structure Average PCM liquid fraction @25°C and 2C Rate.....	170
Figure 149 Simulated Battery Pack Temperature Contour with 2mm Fin thickness at 1800 s @25°C and 2C Rate.....	172
Figure 150 Simulated Battery Pack Temperature Contour with 2.5mm Fin thickness at 1800 s @25°C and 2C Rate.....	173
Figure 151 Simulated Battery Pack Max Temperature (T_{max}) with Fin thickness @25°C and 2C Rate.....	173
Figure 152 Simulated Battery Pack Max Temperature difference (ΔT_{max}) with Fin thickness @25°C and 2C Rate.....	174
Figure 153 Simulated Battery Pack Liquid Fraction Contour with 2 mm Fin thickness at 1800 s @25°C and 2C Rate.....	175
Figure 154 Simulated Battery Pack Liquid Fraction Contour with 2.5 mm Fin thickness at 1800 s @25°C and 2C Rate.....	175
Figure 155 Simulated Battery Pack Average liquid fraction comparison with Fin thickness @25°C and 2C Rate.....	176
Figure 156 Simulated Battery Pack Temperature Contour with 20 Fins at 1800 s @25°C and 2C Rate.....	177
Figure 157 Simulated Battery Pack Temperature Contour with 15 Fins at 1800 s @25°C and 2C Rate.....	177
Figure 158 Simulated Battery Pack Max Temperature (T_{max}) with Fin Spacing @25°C and 2C Rate.....	178
Figure 159 Simulated Battery Pack Max Temperature difference (ΔT_{max}) with Fin Spacing @25°C and 2C Rate.....	179
Figure 160 Simulated Battery Pack Liquid Fraction Contour with 6.3 mm Fin Spacing at 1800 s @25°C and 2C Rate.....	179
Figure 161 Simulated Battery Pack Liquid Fraction Contour with 4,75 mm Fin Spacing at 1800 s @25°C and 2C Rate.....	180
Figure 162 Simulated Battery Pack Max Temperatures with 4 Plates PCM-Fin Structure @25°C and 1C Rate.....	181
Figure 163 Simulated Battery Pack Max Temperature Comparison with 2 and 4 Plates @25°C and 1C Rate.....	182
Figure 164 Simulated Max Liquid Fraction of PCM 1 and PCM 2 @25°C and 1C Rate.....	183
Figure 165 Simulated Max Liquid Fraction Comparison with 2 and 4 Plates @25°C and 1C Rate.....	184
Figure 166 Simulated Battery Pack Temperature Contour with 4 PCM-Fin structure at 3600 s @25°C and 1C Rate.....	185
Figure 167 Simulated Battery Pack Liquid Fraction Contour with 4 PCM-Fin structure at 3600 s @25°C and 1C Rate.....	185
Figure 168 Simulated Battery Pack Max Temperatures with 4 Plates PCM-Fin Structure @25°C and 2C Rate.....	186

Figure 169 Simulated Battery Pack Max Temperature Comparison with 2 and 4 Plates @25°C and 2C Rate.....	187
Figure 170 Simulated Max Liquid Fraction of PCM 1 and PCM 2 @25°C and 2C Rate.....	187
Figure 171 Simulated Max Liquid Fraction Comparison with 2 and 4 Plates @25°C and 2C Rate.....	188
Figure 172 Simulated Battery Pack Liquid Fraction Contour with 4 PCM-Fin structure at 1800 s @25°C and 2C Rate.....	189
Figure 173 Simulated Battery Pack Temperature Contour with 4 PCM-Fin structure at 1800 s @25°C and 2C Rate.....	189

Chapter 1 Introduction

In this first chapter there will be introduced energy aspects that have pushed the automotive world to focus on the production of hybrid vehicles (HEVs). The discussion will also explain the reasons for the study and the consequent expected objectives. Finally, a brief outline of the thesis will be presented so that the reader can orient themselves in the study of the latter.

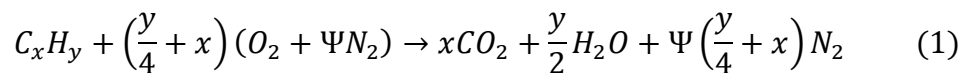
1.1 Energy Aspects

It is clear that the world of transport is dominated by oil: today 42% of global demand for oil comes from the transport sector as a whole (road, iron, water, air, etc.), the trend will increase over the years (54% in 2040). In the **Figure 1** it can be seen the data shown in [Mb/day] = millions of barrels per day. The first line provides information on the total demand for oil in all sectors, not just transport, which is growing over time, as shown in the box. It is noticeable that the transport sector is the one which is growing the most. The global scenario says that the demand for oil will continue to increase by 2040, while this increase is mainly due to the transport sector.

			Stated Policies		Sustainable Development		Current Policies	
	2000	2018	2030	2040	2030	2040	2030	2040
Road transport	30.1	42.2	45.5	44.5	36.7	22.8	48.9	53.4
Aviation and shipping	8.3	12.0	14.5	16.8	11.2	9.4	15.7	19.2
Industry and petrochemicals	14.4	18.3	21.5	22.9	18.9	18.5	21.5	23.0
Buildings and power	14.3	12.3	10.5	9.2	8.4	5.8	11.5	11.1
Other sectors	10.2	12.0	13.3	13.1	12.0	10.4	13.8	14.2

Figure 1 Oil demand (Mb/d): transport and other energy sectors [1].

Oil is generally used to produce fuels such as gasoline (gasoline) or diesel (diesel oil). The chemical form of these fuels is C_xH_y (x about 7 and y about 13). Gasoline, like diesel, is a mix of hundreds of hydrocarbons; therefore, this formula is indicative of the average value. When the fuel is oxidized, the following reaction occurs:



Ψ represents the number of moles of N_2 that are in the air compared to oxygen (typically it is about 3.77). The oil that is oxidized then produces CO_2 first. This is considered a stoichiometric and complete combustion, but the actual combustion is incomplete: presence of CO or HC , unburned hydrocarbons, formation of PM particulates, carbonaceous particles. In addition, it must be considered that, at room temperature, O and N do not bind, while in a combustion system at high temperatures (in engines it is possible to reach 3000 K) N and O react by forming compounds of nitrogen oxides NO_x . These represent the so-called primary pollutant emissions (because they are emitted by the engine). These species give air quality problems (air quality) because they have a direct negative effect on human health. CO_2 , on the other hand, is not in itself a pollutant, it has no effect on health, but it is a greenhouse gas (greenhouse gas) that causes global warming: the local emission of CO_2 has the same effect on a global scale. A virtuous objective that should be set is to limit heating to 2 °C, compared to the condition in 1990, that is to limit the concentration of CO_2 in the atmosphere to 450 ppm, a threshold value beyond which there is a risk that the increase of 2 °C.

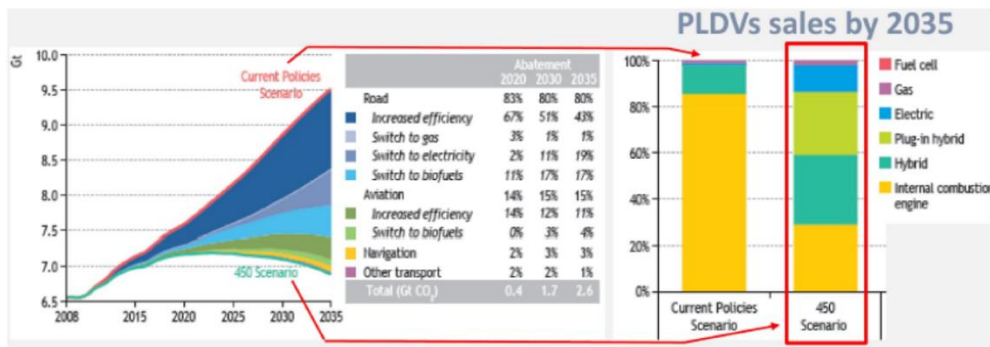


Figure 2 Gt = Giga tons of CO_2 equivalent emitted by the transport sector [1].

So, the transport system is linked to the two problems of global warming and the production of pollutants, predominant because it depends on oil, difficult to replace with another cleaner energy source, not carbon based. The **Figure 2** above shows the ordered Gt = Giga tons of CO_2 equivalent, emitted by the transport sector. This concerns forecasts: the red line identifies the current policy scenario while the green line identifies the 450 scenario. The first is the most pessimistic scenario from the environmental point of view, it is the less stringent scenario. Scenario 450 is the one that limits the 450 ppm of CO_2 in the atmosphere. The reality will probably be in the middle. The blue-coloured area is road transport, the green area is aviation, the yellow area is sea transport. The bulk of the CO_2

reduction is expected by road transport, which is responsible for the increased production of CO_2 . Most of the CO_2 reduction concerns increased efficiency, that is, improving the overall efficiency of the vehicle: lightening, aerodynamics, engine, etc. Another important slice in the reduction is identified by the switch to alternative fuels (switch to gas/switch to Biofuels) natural gas or biofuels. The advantage of biofuels is that they are derived from biomass (plant or organic waste), it derives from something that in its life has absorbed CO_2 ; therefore, burning releases into the atmosphere the CO_2 that first absorbed, the total balance is 0, theoretically. In fact, for the transformation into biomass there will still be an energy expenditure that will lead to the production of CO_2 , making no such budget. Electrification (switch to Electricity) allows both to improve the efficiency of the powertrain, and to replace the oil fuel with electricity. Again, it depends on how this electricity is produced. This means that the impact on CO_2 of the transport sector would be equal to that of any other sector, reducing the problem to the production of electricity using sources that are not fuel based.

The focus now shifts to the use of alternative fuel, which is alternative to oil, such as methane, natural gas or biological fuels, biofuels. About alternative fuels, it is useful to change the approach, it must be considered that different fuels are not obtainable from oil, but from other primary energy sources, as can be seen from the **Figure 3**. Distinctions must be made between powertrain (combustion or electric), the energy carrier (Energy carrier) and the primary energy source (Primary energy) used to produce the energy carrier. Fuels can be produced in several ways, as the **Figure 3** shows. It can be distinguished the transition from energy carrier to powertrain in TTW (Tank to wheel), from the tank to the vehicle, which consists in the efficiency of the vehicle, the consumption or emissions are due to how much the vehicle consumes. The WTT (Well to tank) identifies what is spent in energy terms to produce the energy carrier: it is true

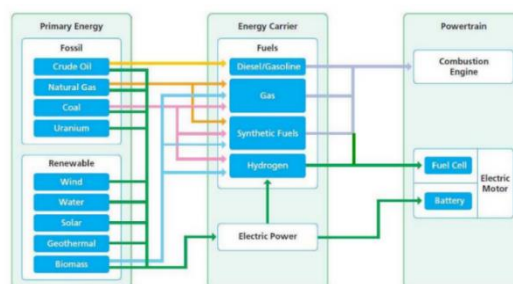


Figure 3 Energy pathways for fuels [1].

that for electricity the TTW is 0, but it will not be the WTT. The overall impact is what is called WTW (Well to Wheel) = TTW + WTT.

In terms of electrification, the increasing use of electric energy on the conventional propulsion system is considered. This leads to the production of hybrid vehicles, which have on board electric machines and thermal machines, plug-in hybrids, which add the possibility of recharging the batteries onboard from the network, or finally pure electric vehicles, today not much present on the market (in 99% of cases they are battery vehicles, for this reason pure electric vehicles are also indicated with BEV (Battery Electric Vehicles)). There are several ways of classification, such as FEV (Full Electric Vehicles) or FCEV (Fuel Cell Electric Vehicles)). Even in the most optimistic 450 scenario, there is a diffusion of the pure electric vehicle below 20%.

Next, the vehicle is compared in electrical terms and in terms of the traditional engine by verifying the available power and emissions imposed by legislation. Assuming that the vehicle does the regulatory driving cycle, the traction energy required by the vehicle depends on factors such as inertia, gravity in case of slope, aerodynamic resistance, internal friction losses in the transmission and wheel friction. Fixing the mission in terms of power, considering that the driving cycle is fixed and that, therefore, speed and acceleration are known, it can be said that in terms of inertia it will depend only on the mass of the vehicle. In terms of aerodynamic drag, being the same vehicle, there will be no differences. For rolling resistance, supposing to use the same tires, it will still depend only on the mass. Then, considering the same vehicle, the driving cycle and the mass of the latter are compared. The total primary energy (total primary energy) is evaluated not only with what is needed on board to move the vehicle, but with a WTW view, that is, from the source of production of the energy carrier. The WTW efficiency of a conventional motor is extremely low, because in the driving cycle, the motor works on points even far from the maximum efficiency, however around 50%. For an electric vehicle, the energy is produced by the grid, perhaps in various ways, but still at high efficiency. The range on the final energy consumption values is much wider for the conventional vehicle because it depends on the type of car considered, whether gasoline or diesel. From the data it can be said that the most efficient thermal vehicle can almost

be as efficient as an electric vehicle. If electricity produced only from renewable sources is considered, then the efficiency of the first case would go to 1, getting lower total values.

Figure 4 Comparison of vehicle efficiencies [1].

Type	Power plant efficiency	Grid efficiency	Vehicle efficiency	Total primary energy [Wh/km]
BEV (Range 150 km)	45%	93%	60-65%	510-570
BEV (Range 150 km)	RE only	93%	60-65%	230-260
Conventional vehicle	WTW Powertrain efficiency 16-23%			600-900

Moreover, even in terms of CO_2 production (obviously it would not make sense to compare TTW because it would get banally 0 for the electric motor) in WTW optics, and in the worst case, the emissions are significantly lower than those produced by the conventional vehicle. The problem in electric vehicles is the weight of batteries. A liquid fuel has a high energy density per unit volume and per unit weight. A battery today, for example, lithium-ion, which has the best ratio of energy/volume to energy/weight, has two orders of magnitude of weight more than liquid fuel. This means that to obtain the same autonomy of the thermal vehicle, it would be necessary a battery weight that exceeds that of the vehicle. This means that the comparison at equal mass cannot be made. Therefore, the comparison must be made in terms of the weight of the powertrain.

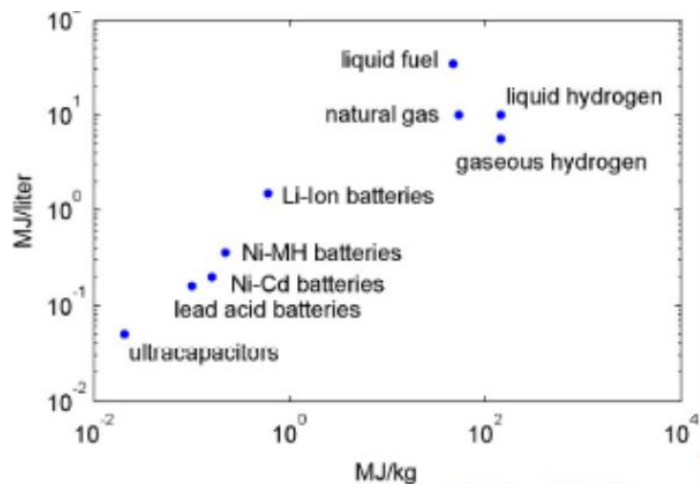


Figure 5 Comparison of energy density per unit volume and per unit weight [1].

The intersection between the curves with diesel or petrol powertrain and those with an electric powertrain indicates those points where the previous comparison makes sense: that is, the two powertrains weigh in the same way. Purely electric vehicles present a variety of problems, including reduced driving range in terms of km and the lack of fast charging systems.

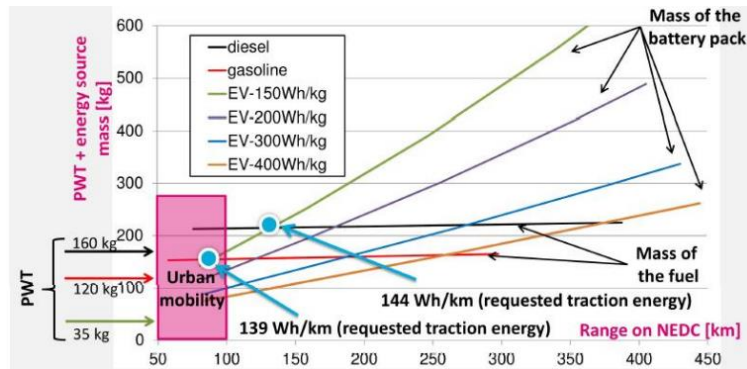


Figure 6 PWT+energy source [kg] in terms of Range on NEDC (km) [1].

Generally, the hybrid is a preferable solution over pure electric. The hybrid involves the combination of two or more power sources that can provide the handling directly or indirectly. A series hybrid, like the one schematized in **Figure 7**, includes the thermal engine that feeds the batteries when they are empty. Only the electric machine provides energy to the wheels in a direct way, the thermal motor can provide it but indirectly, charging the batteries.

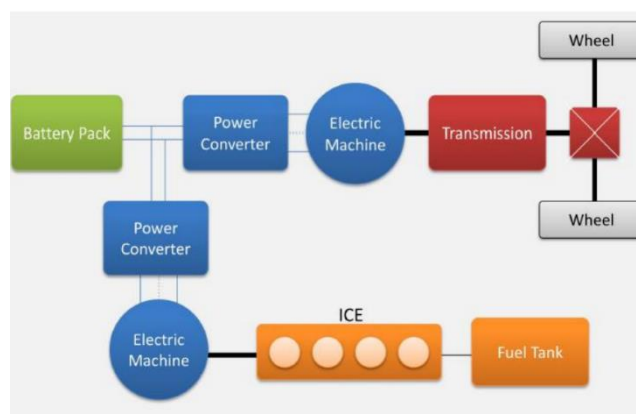


Figure 7 Schematic representation of series HEV [1].

A parallel hybrid has a mechanical connection between the thermal machine and the electric machine. The two machines can add up their power and provide it to the wheels, thus being able to work in parallel. This is the solution most commonly applied today. Talking about series or parallel solution, the presence of an electric machine on the hybrid has the function of making a smaller thermal engine, because, with the same overall power of the powertrain, on the solution in parallel both can work, managing to get a more efficient downsized thermal engine.

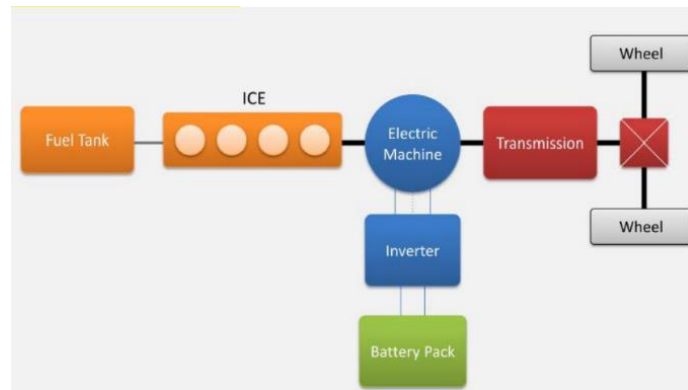


Figure 8 Schematic representation of parallel HEV [1].

A plug-in hybrid has the ability to be connected to the mains to recharge the electric part, unlike the traditional hybrid where the battery is regenerated either by the heat engine or by regenerative braking. This type of hybrid has the battery sized to have a certain autonomy in purely electric operation, called all electric range while allowing, for longer distances, to operate as a conventional hybrid.

In hybrids, one parameter must also be taken into account: SOC (State Of Charge), that is, the state of charge of the battery. This parameter represents the percentage of the total capacity of the accumulator considered in that point, at that time: therefore SOC 100% indicates fully charged battery, SOC 0% means completely discharged battery. It will take a minimum charge state to ensure the battery is running properly; hence, the SOC may vary between a maximum and a minimum. In conventional hybrids, the battery retains a state of charge around an average value, mode defined charge sustaining. This provides that at regular intervals the thermal engine will recharge the battery to maintain its state of charge around that value, managing to generally ensure the best performance by the vehicle. In the case of plug-in hybrid, the operation is charge depleting: during the all-electric range, the battery starts from the state of maximum charge and reaches the

minimum. At the minimum, the hybrid system will provide a new step in the field of charging. Obviously, having a longer range, for the weight problem, plug-in hybrids will have more technologically developed batteries to try to contain the weight (high-density batteries i.e. energy per unit of weight, e.g. Lithium-ion batteries).

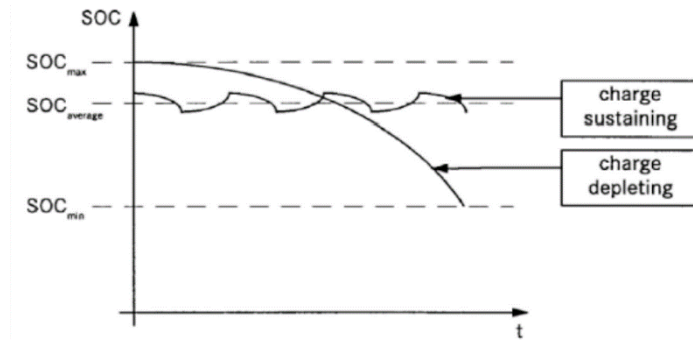


Figure 9 State of charge (SOC) in terms of time [1].

1.2 Motivations

As explained in the previous section, nowadays the production of vehicles is regulated by criteria that disregard, in part, the performance (speed and power of the car). Both those who buy, but especially those who produce, take into account the limits that a traditional vehicle presents: high fuel consumption with an overall efficiency limited to a maximum of 40% (in the case of new generation cars). Because of this, in recent decades, manufacturers have shown greater interest in the study and design of hybrid vehicles (HEVs).

Despite the many advances of recent years, hybrid vehicles still present problems such as long charging times, limited autonomy (in the case of pure electric driving), poor performance of batteries due to operating temperatures. All these reasons limit the spread of this type of vehicles on a large scale. Among those mentioned, the most important reason is the poor efficiency of batteries which, when operating at high temperatures or close to a threshold, do not guarantee safety and driving comfort to the user. Li-ion batteries with higher energy and power density as electric energy storage systems are expected to be the power source of the next generation of HEVs.

As will be explained in the next Chapter, one of the main problems of the Battery Pack is the high and uneven Temperature Distribution within the Pack itself. Of all the possible complications, high temperature has the most destructive effect on the performance of battery cells and modules, as it can lead to thermal leakage, fade capacity, limited driving range and other safety issues. Thermal runoff in stressful conditions can reduce battery life and create the risk of fire and explosion.

The main parameters should be considered in the thermal management systems of electric vehicles: maximum battery temperature, temperature gradients within the cells and modules for uniform temperature distribution, battery life, battery weight, compactness, safety, driving range and cost. In addition, thermal management systems (TMS) are also responsible for the prevention of thermal outflow, which can have catastrophic outcomes. Several thermal management systems have been developed based on battery characteristics, vehicle applications, drive cycle, size and weight limitations, cost and environmental impact. These thermal management systems vary in their objectives

(cooling vs. cooling and heating), method, (passive vs. active), heat transfer medium (air vs. liquid) and application (parallel vs. series or direct vs. indirect). Most of the time, the goal of a thermal management system is to improve the efficiency of the system, reduce the investment in the production of vehicles and reduce operating costs and the corresponding environmental impacts. To achieve these objectives, a systematic way of analysing these systems is necessary.

1.3 Scope of research

As explained in the previous section, one of the main limitations of hybrid vehicles is the insufficient efficiency of batteries. Because of this, any improvement that can be achieved on batteries is directly reflected in the performance of the HEV, allowing for an increase in large-scale sales. It is useful to remember that higher performances of the vehicle (in terms of speed and power) represent the need to "extract" more heat from the body of the batteries (in accordance with the law of Ohm). In addition to the excessive increase in temperature, as already mentioned, the main problem in the battery pack is the unevenness of the temperature distribution inside it. This is why different TMSs have been created to tackle this problem. Without an effective TMS, the temperature in the interior parts of the battery pack will increase in a nonlinear fashion. This can lead to local hot spots and the onset of thermal runaway, which is a destructive process in the battery pack.

The various types of BTMSs, with all their limitations and advantages, will be discussed in the **Chapter 2**. In the current study, the effect of different parameters on cooling effectiveness in the passive thermal management of "pouch" lithium-ion cell and pack with PCMs are investigated. The goal is to integrate the passive PCM thermal energy storage system with electric energy storage systems in HEVs in order to remove the accumulated heat in the system and improve the overall efficiency of the vehicle, which directly affects the performance of the HEVs.

Initially the study involved the analysis of a single cell subject to different cooling systems, then the cooling system for the battery pack (consisting of three cells placed in series) was developed. The phase change material was placed in direct contact with the walls from the active part of the battery. Only later an aluminium layer (the metal fins)

was inserted in order to increase the heat exchange surface between the cell and PCM. Using this configuration, sensitivity analysis was conducted by varying geometric parameters such as the thickness of the PCM layer, rather than the thickness and spacing of the cooling fins. All the above studies were carried out with transient analysis using the ANSYS FLUENT 2021 R2 software.

The main objectives which have been pursued in this paper are listed below:

- Conduct a transient analysis to evaluate the thermal behaviour of the battery and battery pack;
- Develop a model for the single cell through CFD simulation with subsequent experimental validation of the data obtained through numerical analysis;
- Choose the best configuration of PCM to be used in function of melting Temperature, latent heat and cost;
- Check the effect of various types of cooling systems on the thermal behaviour of the cell;
- Implement and solve in transient the case a battery pack to study the thermal behaviour and temperature distribution inside it;
- Carry out sensitivity analysis on the battery pack in order to verify the effect of these variations on the temperature distribution and the maximum temperature reached.

1.4 Outline of the thesis

The thesis consists of 6 chapters. Chapter 2 deals with an overview of lithium-ion batteries: composition, chemical composition of the cathode, anode, electrolyte and collectors, principle of operation and thermal issues. In the second part of the chapter the main cooling systems (BTMSs) are summarized and particular attention is paid to the type of passive cooling (central focus of this work). In the final analysis, the system of increasing the performance of PCM is presented through the insertion of an aluminium fin.

Chapter 3 presents the physics of the problem with the introduction of characteristic equations such as the energy balance equation. The second part describes the equivalent circuit model (ECM) with which the analysis of the thermal behaviour of the battery was conducted. Then the implementation of the model parameters within the ANSYS software was introduced and finally the characteristic equations for the boundary conditions of the problem were reported.

In Chapter 4 it is introduced the development of the model through ANSYS FLUENT; the geometries, the meshes and the thermophysical parameters of all the members of the model beyond that the motivations have carried to the choice of a particular species of PCM are brought back.

The results obtained are presented in Chapter 5. The first part explains the validation of the numerical model with respect to the experimental data. The analysis of the variation of parameters such as ambient temperature and discharge current is then presented. The second part shows the results obtained for the models of the single cell and the battery pack subject to cooling systems. Finally, the results of the sensitivity analysis on the battery pack are reported with the discussion on the efficiency in terms of maximum temperature and temperature distribution.

Chapter 6 sets out the conclusions and prospects for future work.

Chapter 2 Overview

After explaining the environmental issues related to pollutant emissions, it is useful to summarize the fundamental characteristics of the main components of hybrid vehicles: lithium-ion batteries.

2.1 Battery overview

The lithium-ion cell is typically comprised of a positive electrode, a negative electrode, electrolyte, separator, current collector and a case. Electrodes are the key components inside Li-ion batteries which determine the capacity and energy density of the battery. There are few types of Li-Ion batteries: cylindrical, coins, prismatic and pouch [2]. Typically, prismatic and pouch geometries are used for high-capacity applications, such as EV, HEV and HEV. Similarly to other chemistries, Li-Ion batteries are composed of six components: positive current collector, cathode, negative current collector, anode, electrolyte and separator [2]. The cathode (positive electrode) is typically a lithium oxide while the anode (negative electrode) is a compound made with carbon (e.g. graphite) and/or silicon. The electrolyte is a lithium salt dissolved in organic solvents (e.g. ethylene carbonate, diethyl carbonate, dimethyl carbonate) [2]. In terms of costs, there are different values (mainly derived from EV market) available in literature, even if the most widely accepted range is 200–384 \$/kWh [24] with an average in 2016 of 227 \$/kWh (-77% compared to 2010) [3]. Moreover, Cairn Energy Research Advisors and Tesla claim values of respectively 139 \$/kWh and lower than 190 \$/kWh [3,4].

2.2 LIB Chemistry

Li-ions flow from the cathode (positive electrode) to the anode (negative electrode) when charging; during discharge, Li-ions flow from the anode to the cathode. The electrodes are separated by a thin, porous membrane (separator), generally polyolefin (PO); electrolyte (typically a combination of lithium salts in an organic solvent) soaks these components and provides the medium for the Li-ions and other molecules to flow [5]. Typically, five components comprise a LIB and are shown in **Figure 10**.

Component	Common Composition
Anode	Graphitic carbons, hard carbons, synthetic graphite, LTO, tin-based alloys, silicon-based alloys
Cathode	LMO, LCO, NCA, NMC, LFP, ECPs
Electrolyte	Lithium salts (mostly LiPF ₆) in organic solvents such as EC, DEC, DMC, PC, GBL, RTILs
Separator	Polypropylene, polyethylene, cellulosic paper, nonwoven fabrics, ceramic
Current Collector	Copper for anode Aluminum for cathode

LTO: lithium titanate, LMO: lithium manganese oxide, LCO: lithium cobalt oxide, NCA: lithium nickel cobalt aluminum oxide, NMC: lithium nickel manganese cobalt oxide, LFP: lithium iron phosphate, ECPs: electronic conducting polymers, EC: ethylene carbonate, DEC: diethyl carbonate, DMC: dimethyl carbonate, PC: propylene carbonate, GBL: gamma butyrolactone, RTILs: room temperature ionic liquids.

Figure 10 Typical components of lithium-ion batteries (LIBs) and their compositions.

EV's are now moving towards the use of NMC and NCA as they have superior energy and power densities to LFP. NCA batteries have a $LiNiCoAlO_2$ cathode and graphite anodes while NMC batteries have a $LiNiMnCoO_2$ cathode and a graphite anode. For instance, Tesla uses NCA chemistry in the EV models S and X and NMC in their Power Wall battery banks [6]. The higher voltages of NMC and NCA compared to LFP allows battery packs to be smaller, as they require less cells to achieve the specific voltage for a given application, resulting in more compact EVs [6]. LFP is still used in automotive applications but mostly in larger vehicle (e.g. buses) where battery volume is less of a concern [6].

2.3 Battery working principles

The schematic representation of the mechanisms of a $LiCoO_2$ /graphite Li-ion battery is shown in **Figure 11**. As can be seen, the charge/discharge process is characterized by the transport of lithium ions and electrons. During charge, lithium ions are extracted from the positive electrode particles and flow through the electrolyte and the separator to the negative side. To keep the electrical equilibrium, the same amount of electrons is released simultaneously at the surface of positive electrode particles. These electrons are then collected by the positive current collector and travel via the external circuit to the negative electrode to form the charge current. The lithium ions react with the electrons and are intercalated into the positive electrode materials ultimately. During discharge, the electrochemical process is inverse to what happens during charge. An equal amount of lithium ions and electrons escape from the negative electrode at the same time and migrate back to the positive electrode through the internal and the external passage respectively. By using the $LiFePO_4$ /graphite as the positive/negative electrode materials, the electrochemical reactions occurring inside the Li-ion battery during charge and discharge processes can be expressed as follows.

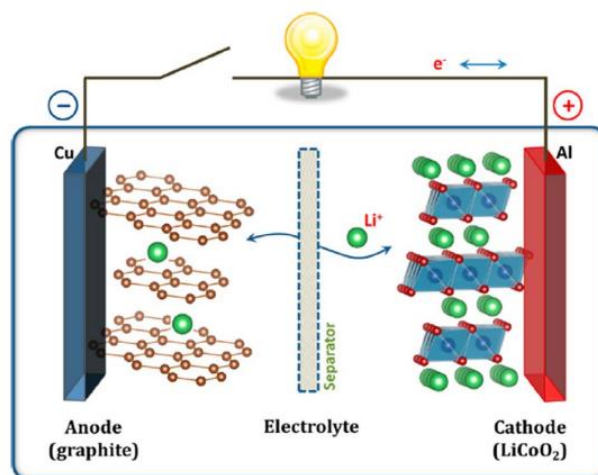
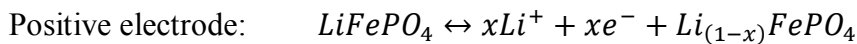


Figure 11 Schematic illustration of lithium-ion battery [7].

2.4 Cylindrical Cells

The cylindrical cell is one of the most widely used packaging types for Li-Ion cells, mainly due to their good mechanical stability and ease of manufacture [8]. Cylindrical cells possess high energy densities; however, they have a low packing efficiency due to the unavoidable space left between the cells when they are stacked together, resulting in a lower energy density at a pack level. **Figure 12** shows the structure of a typical cylindrical Li-Ion cell, where the electrodes are layered and spirally wound into a “jelly roll” which is then inserted into a steel can. Most cylindrical cells benefit from having built in safety devices such as positive thermal coefficient (PTC) switches that, when exposed to excessive current, heat up and become resistive, stopping the flow of current in the cell. As well as this, cylindrical cells also feature pressure relief mechanisms which are designed to release excessive pressure build up from the formation of gases inside the cell. Gasses inside the cell are usually generated due to abusive use of the cell, i.e. overcharging, physical damage or excessive temperature rises [9]. One great advantage of the cylindrical is also its mechanical stability; unlike prismatic and pouch cells, cylindrical cells exhibit minimal or no “swelling” due to build ups of internal gases and do not require any externally applied compression. The cylindrical is also available in a wide variety of standard formats; for Li-Ion cells, the most common formats are 14500, 18650 and 26650. The first two digits identify the diameter of the cell in millimetres, and the last three digits are the length of the cell in tenths of millimetres; therefore, an 18650 cell measures 18mm in diameter and 65mm in length.

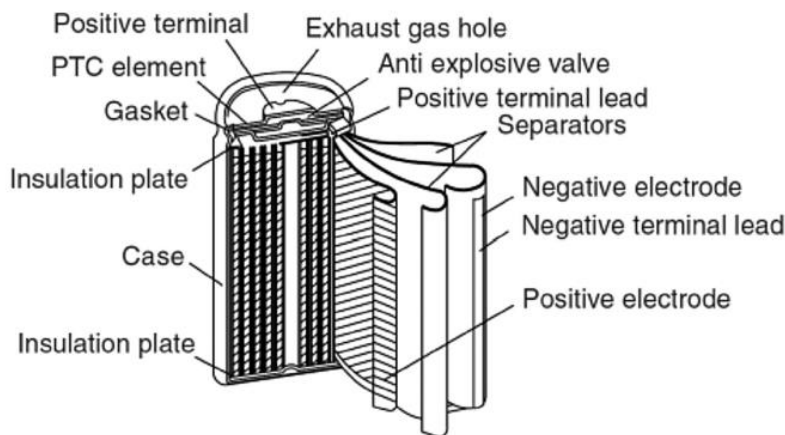


Figure 12 Schematic to show the structure of a cylindrical Li-Ion cell.

2.5 Prismatic Cells

The internal assembly of a prism is much the same as a cylindrical cell, however, in this case, the cells “jelly roll” are inserted into a prismatic can as shown by **Figure 13**. In some prismatic cells, the jelly roll is replaced with a laminated stack of anode-separator-cathode assemblies. Prismatic cells are slightly less energy dense than cylindrical cells due to a thicker can wall; however, they make up for the lost energy density by having a much better packing efficiency due to their cuboid format. Like cylindrical cells, prismatic cells also have in-built safety features such as thermal fuses and gas vent ports. There is currently a lack in standard formats of prismatic cells, as usually they are redesigned to make best use of the available space in each application. It can be seen that prismatic cells range of surface area to volume ratios are lower than that of cylindrical cells. From a thermal management perspective, this means that any proposed thermal management system would have to remove heat at a faster rate than for the equivalent cylindrical cell. Unlike cylindrical cells, prismatic cells are prone to “swelling” due to a build of gasses within the cell and are required to be assembled into rigid enclosures that applies compression to the two broad faces of the cell [10], further complicating the battery pack mechanical design. The cells expansion can be seen as a disadvantage from a thermal management perspective as the cells swelling can result in de-lamination of layers within the cell, which in turn would decrease its through-plane thermal conductivity and thus the rate at which heat can be dissipated from the cell [11].

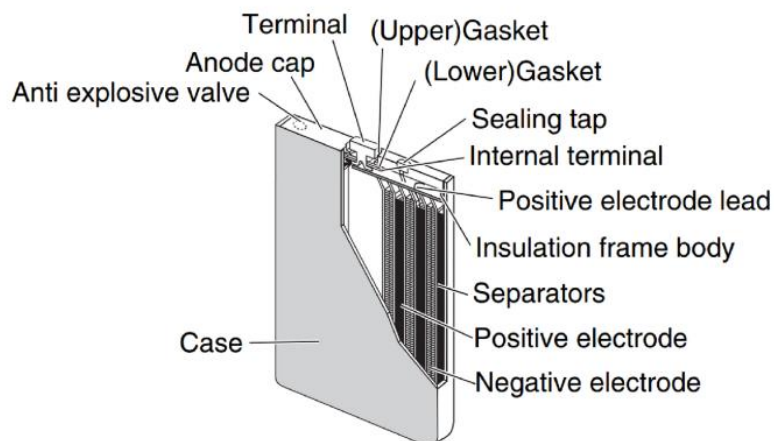


Figure 13 Schematic to show the structure of a prismatic Li-Ion cell.

2.6 Pouch Cells

Pouch cells are constructed by stacking multiple layered sheets of anode-separator-cathode assemblies which are then inserted into a pouch, the pouch is then filled with electrolyte and sealed, leaving the positive and negative terminals outside of the pouch, as shown by **Figure 14**. The material used for the pouch is a laminated aluminium film with a layer of polyamide on the outside and polyethylene on the inside to electrically insulate the casing material and prevent corrosion from the electrolyte. The elimination of the rigid metal enclosure saves weight and means the pouch is also capable of high energy densities and packing efficiencies. A disadvantage of having no rigid case however is that the cells are extremely vulnerable to external mechanical damage and swelling from internal gasses. Because of this, battery packs utilising pouch cells must extensively protect the cells from external damage and provide compression whilst still allowing for small expansions in the cells thickness, the pressure applied to the cell directly effects the cells' life [12].

It is also important to note that pouch cells lack in built safety features such as PTC switches and mechanical gas vents; instead, when gases are formed and pressure within the cell increases above a certain threshold, the gases will vent through an intentional weak spot in the cells pouch which is usually located in one corner of the cell. Currently there are no standards sizes of pouch cells as they are still a relatively immature technology in comparison to cylindrical cells and are easily manufactured to bespoke sizes. However, like prismatic cells, efforts have been made to standardise the dimensions of pouch cells by organisations such as the Association of German Automobile Manufacturers (VDA). Pouch cells are capable of high surface area to volume ratios when the cell width is small, this is beneficial for thermal management as heat can be dissipated via the two large faces of the cell.

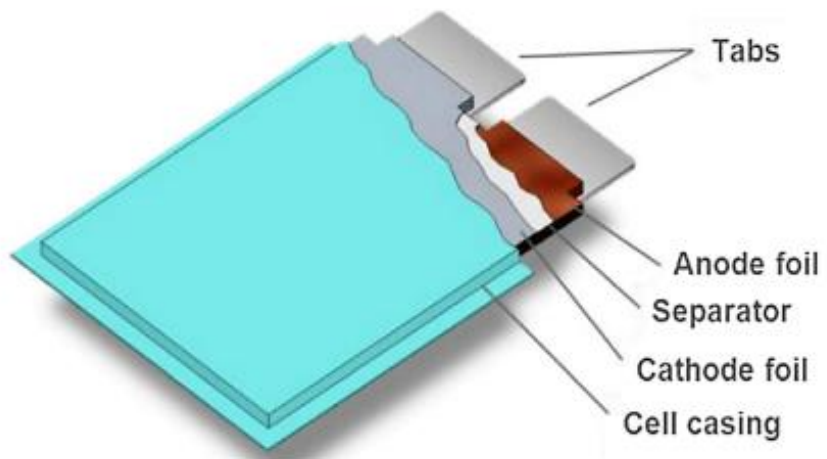


Figure 14 Schematic to show the structure of a Li-Ion pouch cell.

2.7 Adverse effects of temperature

There are two main temperature concerns about Li-ion batteries: (1) the operating temperature goes beyond the acceptable scope; (2) the low temperature uniformity leads to a localized degradation which shortens the battery duration life. To obtain the optimum performance the operating temperature of Li-ion battery needs to be kept within a narrow range (15–35 °C). Working in temperatures out of this scale, Li-ion batteries' performance, lifespan and safety will all be deteriorated. However, dreadful ambient environments (i.e. elevated or extremely cold temperatures) are unavoidable in practical applications. Under these adverse conditions, the battery will see its performance worsen significantly due to the improper operating or storage temperature. Thermal runaway of the battery may even be triggered under some extreme conditions. In this section, the adverse impacts of improper temperatures on Li-ion batteries are outlined briefly to elucidate the significance of the BTMSs. [13]

2.7.1 Performance degradation

The performance degradation of Li-ion batteries herein refers to the capacity fade and power loss under high temperatures. The battery performance degrades rapidly with the increase of temperature and thus few EVs can meet the expectation. Considering the massive combinations of diverse electrode materials and electrolyte composites, it's impractical to cover the performance degradation mechanisms of all these electrochemical batteries. Generally speaking, however, the capacity fade is attributed to the lithium loss and active material reduction [14] inside the battery while the origin of power abatement is the increasing cell internal resistance [15] due to the elevated temperature.

2.7.2 Temperature maldistribution

The expectations of adequate driving mileage and fast acceleration of the battery-based vehicles requires the development of large-scale battery packs. However, during the charge/discharge process, heat is produced as a result of the electrochemical reactions and internal resistances. The enlargement of battery systems inevitably brings about much more heat generation inside the pack, especially during the fast charging/discharging scenario. The heat will accumulate inside the pack if not dissipated effectively. Besides, the convection coefficient is higher at the surfaces of the outer batteries, thus provides better dissipation conditions than inner cells in the pack. Therefore, there is a great temperature discrepancy between the batteries at the center and those near the edges. The performance of an individual cell is a strong function of its temperature, which means that there will be a huge capacity variation from cell to cell. Apart from the uneven temperature distribution among cells, the temperature imbalance within a cell is an important concern as well. The heat generation rate is not the identical at different locations inside a Li-ion cell as the majority of electrochemical reactions occur at the electrodes. In summary, the temperature non-uniformity both from cell to cell and within cells will pose negative effects on the overall performance of the battery pack. Therefore, severe temperature maldistribution should be avoided and the maximum temperature deviation inside the battery pack is usually expected to be below 5 °C [16]. The electrode modification can improve the intra-cell temperature uniformity [17] while a well-designed BTMS can alleviate the inter-cell temperature inhomogeneity more effectively [18].

2.7.3 Low temperature performance

Many studies have implied that the cell performance is also poor under a low temperature. When the temperature is low, especially below $-20\text{ }^{\circ}\text{C}$, both the energy and power of the battery are markedly reduced [19,20]. The exact mechanisms related to the poor performance under the low temperature are still under debate and need to be studied thoroughly. The slower ionic conductivity of the electrolyte at low temperatures was ever thought to be the main cause that worsens the performance of Li-ion cells [21]. The thermal runaway due to successive exothermal reactions caused by elevated temperature is not likely to occur at a low temperature. However, the formation of the lithium plating

may arise [22]. The lithium dendrites grow on the negative electrode surface and decrease the charge capacity of the cell as some of the cyclable lithium intercalated in the graphite is lost. Furthermore, it may penetrate the separator thus results in internal short-circuits. It is obviously impractical to avoid the adoption of Li-ion batteries under the lower temperature in light of the demands of consumers living in the cold environments (e.g. high latitude regions). To alleviate the impacts of low temperature, batteries could be preheated to achieve an acceptable performance [23]. Nevertheless, it consumes the additional energy which declines the overall efficiency of the battery pack.

2.7.4 Thermal Runaway

Thermal runaway is attained mainly due to the short circuit or exothermic reactions during the improper charging and discharging, which may cause several chemical reactions and generate a significant amount of heat along with the gases, as depicted in **Figure 15**. It may also create a separate shrink which further augments the heat released and increases the temperature about 500 °C [24, 25]. Solid electrolytes which contain metastable components may exothermically decompose, once the temperature reaches about 90 °C. When the electrode of graphite is directly exposed through a partial solid electrolyte interface, then graphite may reach a temperature of 200 °C by reacting with the solvent at 100 °C exothermically, but the reaction always does not occur due to the presence of $LiPF_6$ salt, which slows down the reaction rate. When the battery temperature reaches 85 °C, an exothermic reaction may cause the decomposition of the solid electrolyte interface on the graphite electrodes. With further increase in the temperature, a secondary film is also decomposed at 110 °C. This phenomenon may result in evaporation of electrolyte which typically occurs around 140 °C and the vapor may trigger the combustion. Also, the separator can be melted between 130 °C and 190 °C that may cause a short circuit. It was also seen that thermal runaway temperature varies in accordance with the state of charge [26].

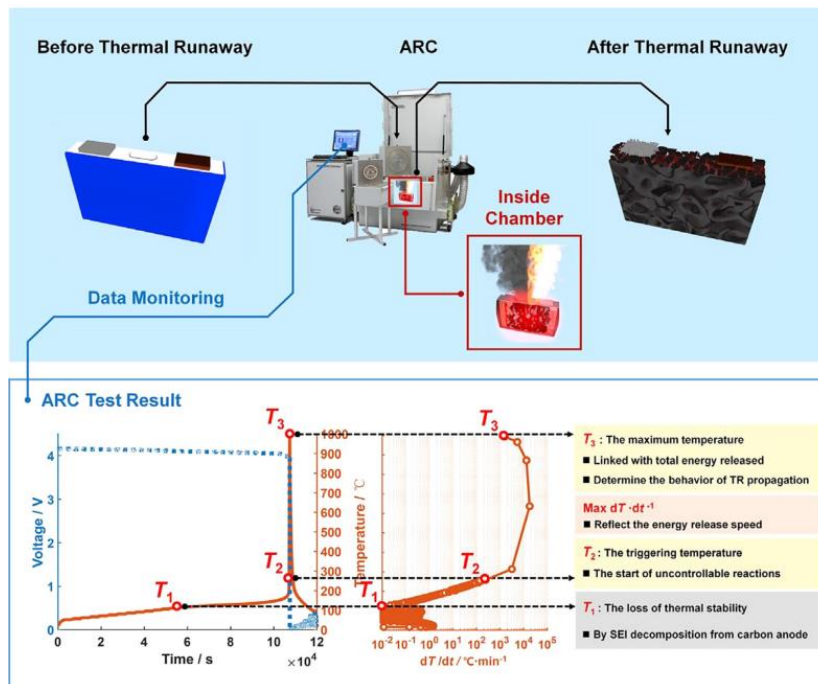


Figure 15 Thermal runaway characteristic of Li-ion battery.

2.8 Battery Thermal management systems

As it has been discussed in **Section 2.7**, improper temperature would bring about the unexpected performance degradation and may even lead to the thermal runaway of Li-ion batteries. Therefore, a BTMS is required when the battery pack is assembled. The primary aim of a BTMS is to maintain the batteries at the optimum operating temperature range with even temperature distribution inside the cell and the pack. A BTMS for cooling could be either passive (only the ambient environment is used) or active (the cooling media is forced by built-in devices). According to the heat removal position, BTMSs are categorized into internal or external systems. Currently, most thermal management strategies are external which means that heat is taken away at the battery surface. However, in almost all cases, the maximum temperature locates at the internal portion of the cell because of the thermal resistance between the battery core and the cooling medium. Raising the convection velocity may further increase the temperature difference within the cell [27]. The internal cooling technique which directly removes heat from inside is a promising option to improve the temperature uniformity [28]. However, the internal cooling is rarely studied and one of the causes attributes to the closure of batteries making the method difficult to implement. In terms of cooling medium, thermal management methods can be classified into:

- the air cooling;
- liquid cooling;
- phase change (liquid to gas) cooling, phase change (solid to liquid) cooling;
- combination of them.

All these types of BTMSs are introduced elaborately in this section. However, it is unrealistic to review all the relevant BTMS techniques considering the numerous works in this field.

2.8.1 Air cooling

Air-cooling is the most wide-spread TMS technique and is characterised by low costs, simple design but also low thermal performances due to air thermo-physical properties at operating conditions and high cell temperature dis-uniformity [29]. Considering the layout of the battery pack, in which the pack is usually configured with batteries arranged

in multiple rows, air-cooling method is commonly employed in EVs because the function can be colloquially designed by heating the pack with a flow of cold air [30]. Generally, air-cooling can be a passive air system or an active air system. **Fig. 16** shows a schematic of both systems. A passive system takes the air directly from the atmosphere or the cabin, whereas an active system takes pre-conditioned air from a heater or an air conditioner. Generally, passive systems' power can deliver some hundreds of watts cooling or heating power and for active systems, the power is restricted to 1 kW. Both systems require few elements to perform cooling such a fan, external power and heater in case of the active system. Because of cost and limitations, and also, its easiest approach, air cooling systems are used in BEVs.

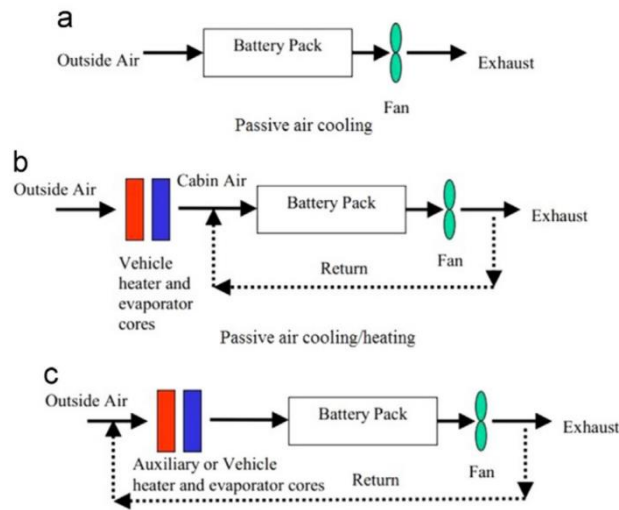


Fig. 16 Passive and active air-cooling [30].

In the literature, air-cooling system has been well documented over the years [31–32]. Despite its low-conductivity characteristic, air-cooling medium is still used in recent studies. Starting in the late '90s and early 2000s, Pesaran [33] presented an air-cooling study case and exposed the early problems of air media in an EVs and series HEVs configuration. Moreover, they asserted that low energy-density batteries can be cooled with active air-cooling, however, for LiBs and in particular, high-energy-density batteries, a redesign of the cooling system is required. If no active air cooling is integrated, a large thermal gradient in the battery pack can occur which can lead to uneven thermal distribution and further, thermal runaways can result. Therefore, there are several ways to improve it proposed in literature:

- Increase air flow rates: higher Reynolds number, higher heat transfer coefficients, but uneven temperature distribution, higher parasitic consumption. Chen et al. [34] report that air cooling has from two to three times the energy consumption compared to liquid cooling;
- Battery layout optimisation: use of wide spaces between cells and staggered configuration can improve the air flow turbulence and therefore Nusselt number values, but this leads to lower energy/ power EESS densities;
- Air flow path: possible better temperature uniformity with so called reciprocating air flow (i.e. alternate air-flow inlet-outlet), leading to 72% drop in temperature gradients, or Z-type configuration, but this requests higher complexity and control systems;
- TCE: Integration of metal/high conductive foam/matrices/honey-comb/fins/pins structures to improve the equivalent heat conductivity of air-flow [35,36];
- Mist cooling: mixture of air and water droplets to improve the equivalent heat transfer coefficient [37].

Chen et al. [38] have led various investigations on improving the cooling efficiency of an air-based module. They used numerical solutions involving computation fluid dynamic (CFD) approach along with an optimization algorithm to improve an air-cooled battery pack composed of prismatic cells **Figure 17**. Cell-spacing distribution, airflow rates, inlet and outlet widths, plenum length and positions (**Figure 17**) are objectives to be optimized in the numerical function. The battery system consisted of 8 prismatic cells and the testing was one discharge rate at 5C. Results supported by experimental work showed that high cooling efficiency is achieved when the inlet and outlet are located in the middle of the plenum (BTMS IX in **Figure 17**). Compared to the Z-type BTMS (BTMS I), the

maximum temperature and the maximum temperature difference among cells decrease by 4.3 °C and 6.0 °C respectively.

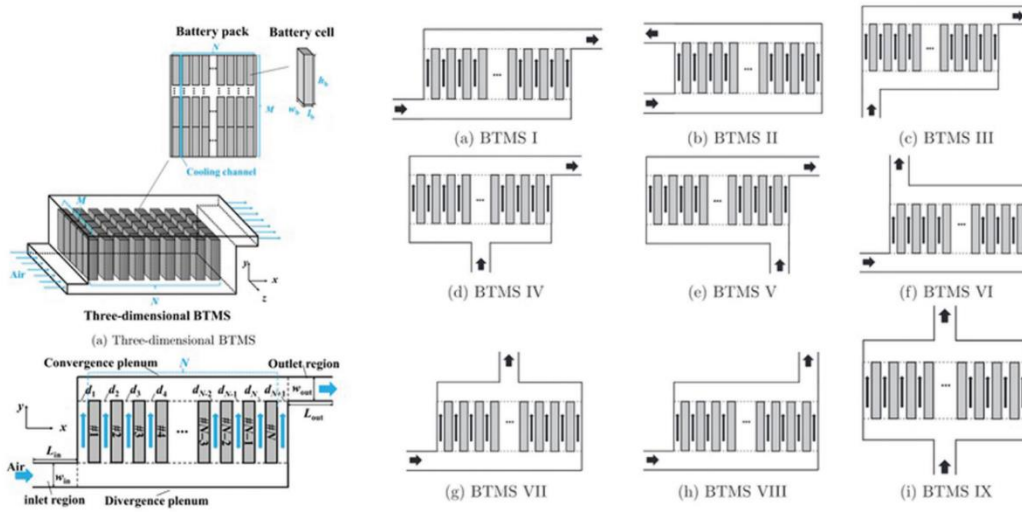


Figure 17 Schematic of the air cool BTMSs [38].

Jiaqiang et al.[39], proposed in their study to optimize the air-cooling performance of a battery module. Different air-cool BTMS are explored by changing the related air-flow position inlet and outlet as shown in **Figure 18**. The battery system consisted of 60 cylindrical cells and the testing was two discharge rates: 2.6 A and 1.3 A. Results showed that the airflow on different sides is better than on the same side. Moreover, the authors achieved the best performances with an additional baffle **Figure 18**. In the above studies,

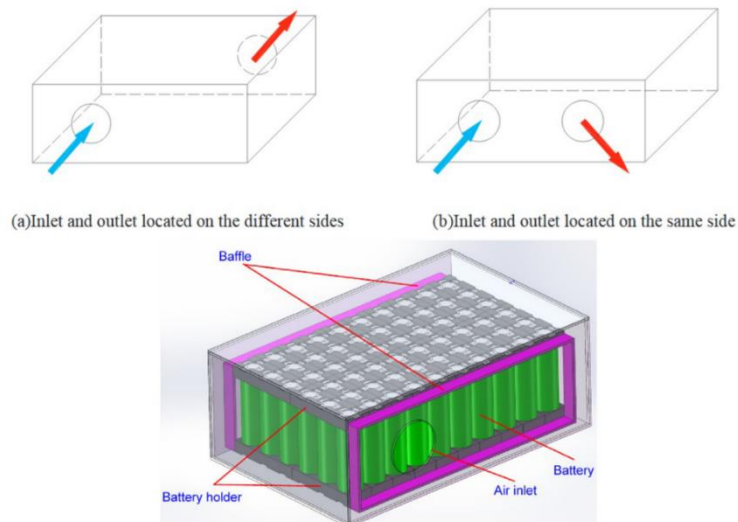


Figure 18 System used in [39].

the optimization of air-based TMS is mainly concentrated on large battery system composed of several.

Most of the above studies have investigated the cooling capability and efficiency of different air-cooling designs for Li-ion cells or module through both numerical and analytical methods. However, as described above with the various studies, in nearly a decade, the methodology has not slightly changed for the authors mainly concentrated their investigation on the same issues that needed to be improved 10 years ago (cell spacing, inlet/outlet position and size, etc.). Moreover, since the specific capacity and the heat transfer coefficient of air is much lower than many other mediums, it will be very difficult to meet the demands of heat dissipation for future extreme fast-charging applications. Therefore, an improvement of the cooling medium could be required. [40]

2.8.2 Liquid cooling

Compared to air-cooling, the liquid-based strategy is more efficient and can reduce significantly the battery temperature resulting from high-end heat transfer coefficient of water or other typically used fluids [41]. Generally, liquid-cooling management can be divided into three categories [41]:

- Immersing cooling: modules directly immerse with a dielectric fluid;
- Direct cooling: battery surface is in direct contact with the heat transfer fluid (HTF);
- Indirect cooling: distinct piping, cooling plate or a jacket is placed next to each battery cell.

Direct cooling and immersing cooling are not very common in battery vehicle applications, resulting from the practical aspect of the systems [42]. Nonetheless, they have been documented in the literature in recent years [43,44]. The last category, the indirect liquid-based system is much simpler to implement and the lower viscosity of the HTF (water, glycol, etc) than the dielectric fluids used in the direct or immersing cooling contributes to a much higher flow rate. To perform the indirect cooling, a metal plate with a tube or integrated channels is designed. The cold plate offers contact with the battery system on one surface. Many studies have proposed this indirect cooling method for batteries. In year 2000s, Pesaran et al. [45], first presented a study-case for which indirect liquid cooling performance is confronted with basic air medium. Although air-based cooling was found easy to design, it could not match the better performances of a liquid cooling system. Nowadays, the same comparison is still made. In [46], Han et al. presented the fundamental difference between air-cooling and liquid-cooling systems in terms of heat transfer performance symbolized with QITD (inlet temperature difference). A typical QITD for a liquid-cooling system is rated at 500 W/K, while for based air-cooling is about 70 W/ K. The maximum QITD for the air-cooling system proposed in the study was close to 150-200 W/K. This means that the same conclusions as in (Pesaran) are found, for which air-based system requires serious improvement while liquid-cooling could dissipate significantly heat. Today, most of the studies focus on the optimization of the cooling plate either by pure empirical investigation, by simulation or both. Thanks to the computational performances of today's software, researcher are now able to simulate

cooling plates for battery pack systems with detailed meshing. The simulation results of the cooling system give feedback to an optimal design. For example, Shang et al. [47], designed a liquid cooling system for a lithium-ion battery pack in a computational fluid dynamics software and as represented in **Figure 19**. They simulated various parameters such as the inlet mass flow, the inlet temperature, and the width of the cooling plate for a given flow rate of 0,17kg/s as shown in **Figure 19**. Results showed that the best cooling performance can be obtained when the inlet temperature is 18 °C, the width of the cooling plate is 70 mm.

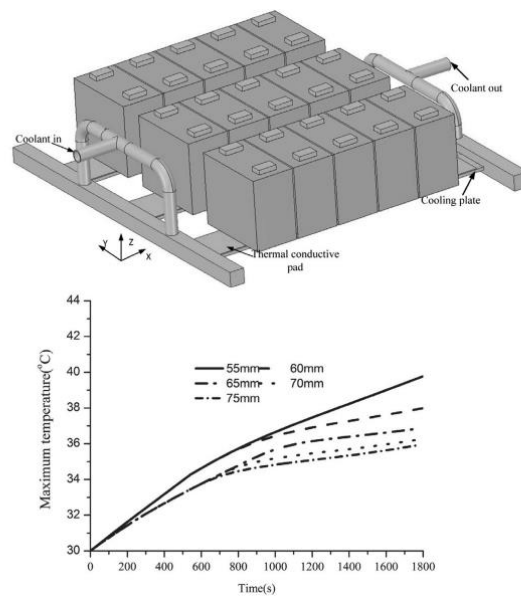


Figure 19 3D model of the battery module and its variation during the discharge process with different widths of cooling plate and a fixed flow rate of 0.17kg/s.

The same designing approach was done in [48] where Siqu Chen, et al. proposed to optimize a liquid cooling plate with objectives of lower temperature and energy consumption. The authors strategically simulated the cooling plate in CFD and used the Latin Hypercubes method for parameter combination. After finding the optimal design with a multi-objective optimization, the cooling plate was validated with an experimental test bench. Results showed good agreement for which a higher temperature reduction and lower temperature deviation were observed with the optimized experimental cooling plate.

Furthermore, as modelling methodologies are also employed for pure simulation purposes, researchers are trying to push the limit of liquid-based cooling design by proposing pure modelling studies such as sensitivity analysis, cold plate arrangement or microchannels optimization which requires the impressive computational effort of existing CFD tools.

Huang et al. [49], also optimized a cooling plate with streamline by adapting different parameters (mass flow rate, pressure, temperature, streamline channels). The schematic of the optimization procedure is shown in **Figure 20**. Results showed that the streamline shape improved the heat exchanger efficiency by 44.52% as well as the temperature uniformity.

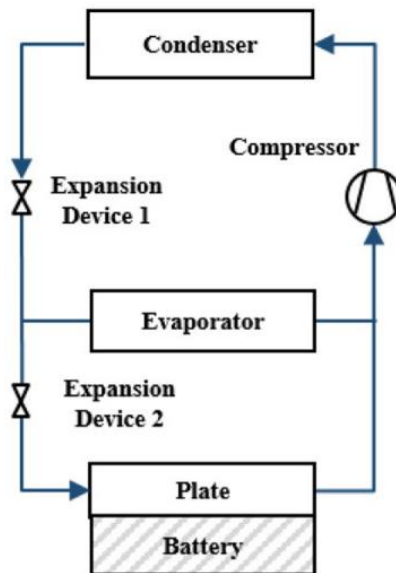


Figure 20 The schematic of the novel channels design procedure (a) the empty plate (b) extracted streamline (c) build the channels in 2D (d) 3-Dimensional channels

In conclusion, the liquid cooling system is promising, the existing CFD tool allows to push the limit of the cooling plate design. However, due to their complexity, cost, and potential leakage, manufacturers hesitate to use liquid-based cooling systems. Novel solutions are researched to ease its integration with existing cooling systems such as refrigerant.

2.8.3 PCM

The characteristic of the PCM based BTMS is that the PCM absorbs/ releases latent heat during the phase change. The PCM-based BTMS can lower the peak temperature rise during charge and discharge cycle [50]. The PCM has a strong ability of battery temperature management under transient conditions, even under significant temperature fluctuations [51]. Additionally, the PCM also has a high thermal capacity of PCM to keep the battery warm in a cold environment. According to the phase change type, the PCM can be classified as solid-liquid PCM, liquid-gas PCM and so on. The process of liquid-gas phase change includes evaporating stage [52,53] and boiling stage [54,55]. Solid-liquid phase change is mostly used by previous studies because the volume change during solid-liquid phase change is little and the phase change process is easy to control. Therefore, the solid-liquid phase change is a phase change way that was mainly introduced in this study. How to find a suitable PCM is the most important issue of the PCM based BTMS, and the selection of materials usually follows the following requirements:

- Large thermal capacity, including latent heat and specific heat. It determines the heat absorption capacity;
- High thermal conductivity. It determines the rate of heat dissipation and the continuous heat absorption capacity of the PCM. On the other hand, high thermal conductivity can reduce the capacity of heat preservation at the low-temperature environment;
- An appropriate phase-change temperature range;
- Low volume change ratio, no phase separation, low super-cooling degree and high chemical stability, including non-poisonous, non-flammable and no pollution;
- Easy availability, low cost and good durability.

2.8.3.1 Classification

PCMs are divided into 3 main groups (**Figure 21**): organic (paraffin, non-paraffin compounds such as fatty acids), inorganic (salt hydrates, metallics) and their eutectic mixtures. Historically, common PCMs used in the literature were paraffins.

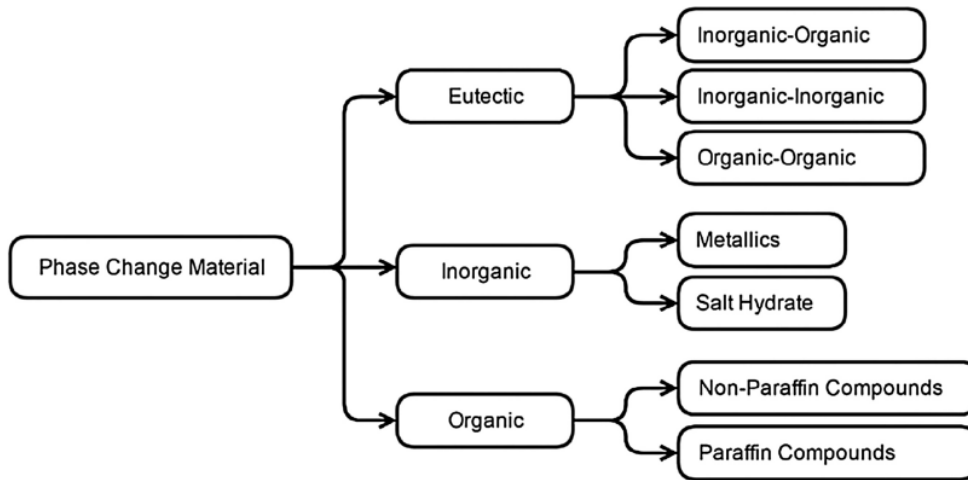


Figure 21 PCM classification considering material composition.

The organic and salt hydrates PCMs are promising for applications with temperatures lower than 100 °C (e.g. TMS of Li-Ion batteries) while eutectic mixtures can be employed for temperatures up to 250 °C. Organic materials have typically latent heat in the range 128–200 kJ/ kg while inorganic compounds (e.g. salt hydrates) reach values of 250–400 kJ/kg. Organic PCMs are typically divided into two main subcategories: paraffin and non-paraffin.

Paraffins are considered to be safe, reliable, chemically stable, predictable and cheap. Moreover, they have low volumetric expansion during phase transition and have low transition pressure. They are composed of chains of alkanes whose chemical structure and formula are $CH_3(CH_2)_m$ and C_nH_{2n+2} . Typically, their melting temperature and their latent heat grow logarithmically with their chain length (i.e. number of C atoms) [56]. Their main drawback is a low thermal conductivity in the range 0.15–0.21 W/m K.

Non-paraffins can be classified as esters, fatty acids, alcohols and glycols. Generally, non-paraffin organic PCMs are characterised by high heat of fusion, non-flammability, low thermal conductivity, mild toxicity and instability at high temperatures. Moreover, fatty

acids are the most important subgroup of this kind of PCM. They have high heat of fusion compared to paraffins and have no problems of thermal hysteresis and sub cooling during freezing processes (unlike salt-hydrates). Their general chemical structure and formula are $CH_3(CH_2)_mCOOH$ and $C_nH_{2n}O_2$. Latent heat and energy density of fatty acids increase with their melting temperature, and are typically in the range 150–200 kJ/kg and 35–51 kWh/m³. Their thermal conductivity is quite low, in the range 0.14–0.17 W/m K, leading to thermal diffusivities in the range $7.5\text{--}10 \times 10^{-8} m^2/s$. The good properties of fatty acids are: melting point congruency, good chemical stability, non-toxic, small volumetric expansion, compatibility with storage container materials (i.e. no corrosion), high latent heat, high energy density, derivation from common oils, no effect of sub cooling, no phase segregation. The only issue is that they are more expensive than other materials such as salt hydrates and paraffins; for instance, their specific cost is roughly 2–2.5 times that of paraffin and even more compared to salt-hydrates.

Inorganic PCMs are divided in salt hydrates and metallics. Salt hydrates are basically alloys or mixture of inorganic salts (AB) and water (nH_2O), to form a compound with equivalent chemical formula $AB \cdot (H_2O)_n$. The process of melting/solidification is basically a dehydration/hydration of the salt. This leads to the first issue of salt hydrates, i.e. non-congruent or sedimentation processes during melting (dehydration). This is due to the fact that dehydrated salts are heavier than water and tend to sediment at the container base. When solidification (hydration) need to be triggered, the system is characterised by areas of different salt concentration and consequently the complete solidification (hydration) is impossible, i.e. the material can't regenerate properly for the following charging phase. However, solutions to this problem have already been found, such as mechanical stirring, encapsulating the PCM to avoid the separation of dehydrated salt from its released water and adding special thickening materials. The other issue of salt hydrates is supercooling, due to poor nucleation properties of the material. This means that generally the nucleation rate of salt hydrates is quite low at transition temperatures and the material needs to be sub-cooled (or supercooled) before nucleation is naturally triggered. This means that the stored thermal energy is released at much lower temperatures, decreasing the exergy efficiency of the heat storage system. Overall, the good properties of salt hydrates are high latent heat, high thermal conductivity (2 times compared to paraffin and comparable to water), low volumetric expansion during

melting, low level of toxicity, low level of corrosivity (compatibility with plastics) and low cost (when pure).

The last category of inorganic PCMs is metallics (low temperature melting metals). They have high volumetric energy density but, due to high density, have low specific energy density. Moreover, they have high thermal conductivity, so TCE (Thermal Conductivity Enhancement) methods are not necessary in this case. In addition, eutectic mixtures (from the Greek eu = easy, teksis = melting) are mixtures of 2 or more PCMs which, at specific compositions, melt at a singular temperature. [56]

2.8.3.2 Solid-liquid phase change system

Compared with liquid-gas PCMs, the solid-liquid PCMs are more popular because the ratio of volume change is low and it is easy to be controlled. The paraffin is a typical kind of solid-liquid PCMs, and it can be used as a representative to illustrate the process of solid-liquid phase process. The phase change process of paraffin could be divided into four stages. The first stage is the initial stage before the paraffin melting. At the first stage, the temperature of the battery rises quickly. At the second stage, heat conduction becomes the main way to dissipate heat, and the rate of temperature rise is decreased by PCMs. At the third stage, a thermal balance is reached between heat generation and heat absorption by PCM. At the last stage, heat dissipation is through natural convection when the PCM melted completely. In different environments, the PCMs had the similar temperature plateau but the duration time was different when the heating power was the same.

A suitable material for the solid-liquid PCM based BTMS is beneficial to improve the thermal performance of the system. The latent heat, melting point and thermal conductivity are important parameters of solid-liquid PCM. The PCM with high latent heat can significantly reduce the temperature and the temperature difference [57,58].

In order to solve the safety problem of lithium-ion batteries, the BTMS using the solid-liquid PCMs were identified promising. The physicochemical characteristics of PCMs, such as the thermal conductivity, latent heat of PCM, melting temperature of PCMs, have the important effect on the performance of BTMS. For the solid-liquid PCM-BTMS, the

geometric parameters of the PCM, such as thickness, contact area, number of layers, structure, etc., are also important.

Malik et al. [59] investigated the effect of PCM plates with different thickness under the conditions of constant current discharge rates of 1C, 2C, 3C and 4C and different ambient temperature. The results showed that the voltage of the battery pack was improved by using the PCM plates compared with liquid cooling system. The temperature of the battery pack decreased dramatically and the maximum temperature remained below 40 °C with the use of PCM cooling strategy. The temperature difference in the x- and y-directions decreases by 64% and 72%, respectively.

The PCMs, including n-octadecane, n-eicosane, and n-docosane, based battery internal cooling system was proposed by Zhao et al. [60] (as shown in **Figure 22**). The hollow mandrel in the cooling system of cylindrical battery was replaced with a PCM-filled mandrel to absorb the heat in the battery. The result indicated that absorbing heat from the inside of the battery was more efficient than from absorbing heat from the outside. By adjusting the PCM core size distribution, the maximum temperature difference between the batteries was kept within 2 °C under natural convection condition.

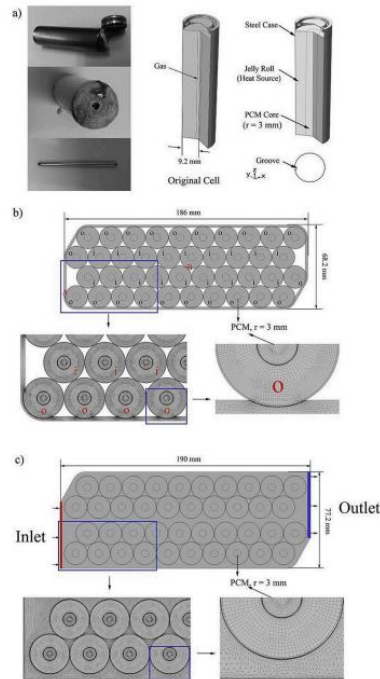


Figure 22 a) Illustrations of the internal structure of a disassembled 18650 cylindrical battery and the design of a PCM-embedded battery; b) Schematic of a passively cooled 40-cell battery pack; c) Schematic of a hybrid cooling design for the battery pack. [60]

In conclusion, compared with the traditional cooling methods, the PCM-based BTMS has the advantages of small space requirement and no energy consumption. PCMs include liquid-gas PCMs, solid-gas PCMs and liquid-gas PCMs. Thereinto, solid-gas PCMs and liquid-gas PCMs produce a large number of gases during the phase change process, and the volume of PCMs changes greatly. The solid-liquid phase change materials represented by paraffin are of small volume, suitable phase change temperature, large latent heat, non-toxic and cheap, which are the most suitable phase change materials for the BTMS. Under extreme conditions such as high temperature or high current, thermal runaway of the power lithium ion batteries will occur, which will result in safety problems. Therefore, it is necessary to optimize the physicochemical properties of PCMs and the BTMS structure to enhance the performance of the solid-liquid thermal management system. The enhanced PCMs coupled with different substances will be discussed in next section. [61]

2.8.3.3 Thermal Conductivity Enhancement (TCE) methods

There is plenty of experimental evidence which suggests that PCMs have low thermal conductivities, leading to small heat transfer rates during either charging and discharging. Therefore, thermal conductivity enhancement (TCE) methods are necessary to be implemented in the PCM TESS. These methods include fins, insertion of high conductivity material or particles (e.g. carbon nano-tubes, metallic rings, graphite or carbon matrices, brushes, chips), multi-tube configurations, micro or macro encapsulation. The aim of these methods is either to increase the heat exchange area or increase the effective heat conductivity. In this regards, Tian et al. [62] propose an interesting review of potential heat transfer rate improvement of different TCE methods, claiming that:

- Adding high conductivity elements (e.g. metal fins, beads, powders) leads to 60–150% increase of the overall thermal conductivity;
- Using porous media (e.g. carbon fibres, Expanded Graphite EG composites) leads to 81–272% increase of the overall thermal conductivity;
- Adopting metal foams with porosity in range 85–97% leads to increase slightly better;
- Using cascaded thermal energy systems (CTES) with 5 stages (i.e. 5 different PCMs) can increase the performance by up to 34.7%. Moreover, this method increases the stability of the outlet HTF temperature and leads to higher liquid fractions.

In this thesis, the main focus will be on the analysis of the improvement of the performance of PCM through the insertion of Fins in order to increase the heat exchange surface.

2.8.3.3.1 Fins

The general idea of fins is to increase the heat exchange area on the side of the low conductivity medium, i.e. PCM. It must however be taken into consideration that during melting processes natural convection of the liquid phase can further improve the heat transfer rate and this phenomenon must be taken into account when designing fins.

Sciacovelli et al. [63] present the optimisation of fin design as a TCE method for a PCM system. A shell-and-tube (S&T) storage system with Y shaped fins with different numbers of branches is optimised with CFD techniques, in order to find the best combination of base length and opening angle of the two branches (**Figure 23**). By means of optimisation procedures, it is possible to increase the thermal efficiency by 24%. Moreover, the authors suggest that the optimisation is a function of the operating time considered. For short operating times, the angle of the fins must be bigger than the ones used for long time periods. Therefore, transient operating conditions must be taken into account when proceeding with the optimisation. It must also be noted that typically the discharging process is slower than the charging one, due to the natural convection regime present in the melting phase.

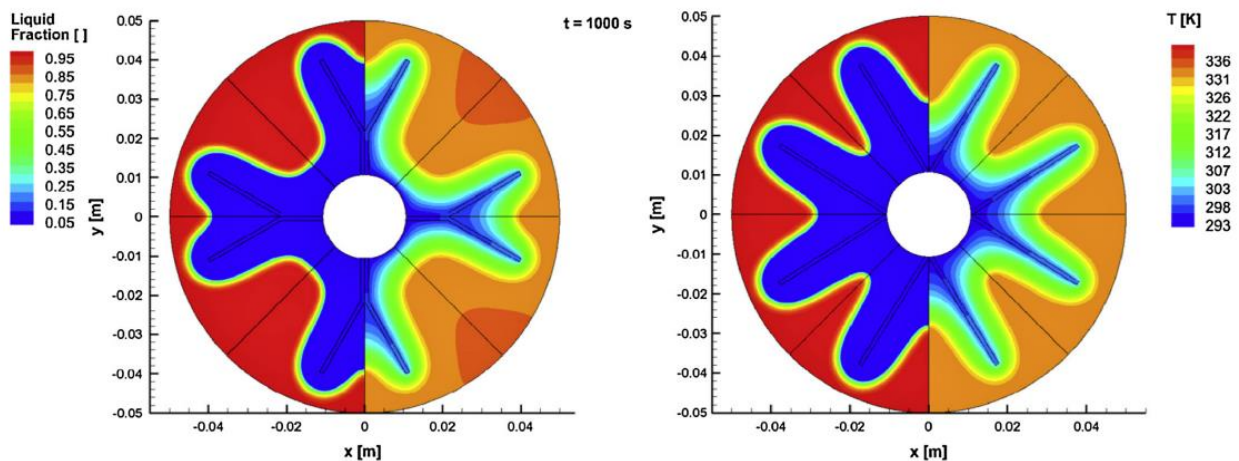


Figure 23 Optimization of Y shaped fins as TCE. Liquid fraction (half left) and Temperature (half right) profiles: initial (left) and optimal design (right).

Chapter 3 Physics of the problem

Since the performance and safety issues of Li-ion batteries are strongly linked to the temperature, it is of great significance to analyse the battery thermal behaviour (e.g. temperature profile) at cell and pack level. Despite the existence of other choices, experiments and numerical thermal simulations are the most prevalent methods. However, the experimental approach has its limitations. For instance, one experiment is only for a specific condition making it time-consuming and laborious to investigate the battery behaviours under different ambient environments and/or discharge rates. Additionally, the surface temperature cannot accurately indicate the maximum temperature of the battery due to the difference between the surface and the core. As the battery case is a sealed container, it is almost impossible to acquire the temperature data inside the battery using existent thermal detectors such as thermocouples. Comparatively, numerical simulations can be easily fitted to different conditions by altering the model parameters. It is also frequently used for the cell configuration optimization and the thermal management system design. The first step of numerical simulations is the establishment of battery thermal models which will be discussed below. This Chapter also reviews the literature about the commonly utilized electrochemical and equivalent circuit models for thermal analysis. The electrochemical and equivalent circuit models are always coupled with thermal models to gain a more accurate representation of the heat generation inside the battery. [64]

3.1 Thermal Model

During the charge/discharge process, heat is generated within the battery. The majority heat will be conducted from the internal portion to the surface and then dissipated by ambient air or through another coolant if an effective thermal management system is attached. The remaining energy is stored inside the battery. Thus, the building of battery thermal models is mainly about the selection of expressions including the energy balance equation, heat generation equation and boundary condition equation.

The energy balance equation is based on the energy conservation law and can be expressed as **Eq. 2** which gives the temperature distribution within the battery [27].

$$\rho C_p \frac{\partial T}{\partial t} = \frac{\partial}{\partial x} \left(\lambda_x \frac{\partial T}{\partial x} \right) + \frac{\partial}{\partial y} \left(\lambda_y \frac{\partial T}{\partial y} \right) + \frac{\partial}{\partial z} \left(\lambda_z \frac{\partial T}{\partial z} \right) + \dot{Q} \quad (2)$$

The term on the left-hand side represents the energy accumulated inside the battery while the right-side terms are the three-dimensional heat conduction and heat generation rate expressions respectively. It is also worth emphasizing that the abovementioned energy balance equation is under some assumptions for the simplification [27]. For example, the battery thermos-physical properties are regarded as independent of the temperature which is rational if being operated within a narrow temperature range. Besides, the convective heat transfer inside the battery is omitted as the flow velocity of electrolytes is greatly confined. The detailed three-dimensional simulation occupies massive computing resources, especially under intensive computation conditions. To reduce the complexity and simulation time, the temperature gradients in one or two directions may be ignored without compromise of simulation accuracy. Beyond that, lumped capacitance thermal models with the confinement of three dimensions are commonly employed as well. By assuming a uniform temperature distribution in all directions, **Eq. 3** can be expressed in the form as follow:

$$\frac{\partial(\rho C_p T)}{\partial t} = h_s A_s (T - T_{amb}) + \dot{Q} \quad (3)$$

The precondition of adopting the lumped model is that the Biot number is much lower than 0.1 (i.e. $B_i = hL/\lambda \ll 0.1$) [65]. That is to say, the requirement that either λ is much higher than the heat transfer coefficient h or the cell thickness is sufficiently small should be fulfilled.

The heat generation \dot{Q} of Li-ion batteries include the reversible heat and irreversible heat according to the production origins [66]. The reversible heat originates from the entropy change associated with electrochemical reactions. Thus, it is also known as reaction heat or entropic heat. The irreversible heat is comprised by active polarization heat and ohmic heat [67,68]. The polarization is the deviation between the cell open-circuit potential and the operating potential. At the solid-electrolyte interface, there is a resistance to hinder the charge transfer process. The energy that is needed to overcome the barrier during the lithium intercalation and the de-intercalation process is referred to as the active polarization heat [69]. The ohmic heat or joule heat is the energy loss caused by the

transport resistance in solid and electrolyte phases. Various equations have been introduced so far because of the intricacy of the heat generation process inside batteries. A localized heat generation equation is shown by **Eq. 4** which is derived from electrochemical analysis. The first term on the right side refers to the polarization heat and the second is the reaction heat. The third term is the joule heat because of resistance to the electronic conduction in the solid phase while the fourth and fifth terms are the ohmic losses due to the impedance to the ionic transport in the electrolyte phase.

$$\dot{Q} = a_s i_n (\phi_s - \phi_e - U_{OC}) + a_s i_n \left(T \frac{\partial U}{\partial T} \right) + \sigma^{eff} (\nabla \phi_s)^2 + k^{eff} (\nabla \phi_e)^2 + \frac{2R_g T k^{eff}}{F} (t_+^0 - 1) \left(1 + \frac{d \ln f_{\pm}}{d \ln c_e} \right) \nabla \ln c_e \cdot \nabla \phi_e \quad (4)$$

This equation gives a sophisticated and precise description of the heat generated inside the battery while its deficiency is that the containing excessive electrochemical parameters increase the computation cost. Therefore, a simplified form of the formula proposed by Bernardi et al. [70] from a thermodynamic perspective is widely used in the literature:

$$\dot{Q} = I(U_{OC} - V) - I \left(T \frac{dU_{OC}}{dT} \right) \quad (5)$$

In the above equation, the first term on right-hand side expresses the irreversible heat: ohmic heat inside the battery cell, transfer of over potential charges at the interface, and the limitations, where U_{OC} is the open circuit potential and V is the battery cell operating potential. The second term is the reversible heat term or the entropy generation term. The term (dU_{OC}/dT) is the entropy coefficient which is a function of density and the battery cell temperature. The term (dU_{OC}/dT) changes its sign in charging and discharging modes and it becomes zero at the time when there is no current. Low C-rate leads to reversible heat, while the high C-rate towards irreversible heat [71].

3.2 MSMD Approach

The ANSYS FLUENT software allows the resolution of the numerical model of the battery using an MSMD approach. The difficulty with modelling a lithium-ion (Li-ion) battery is due to its multi-domain, multi-physics nature. Vastly different length scales associated with different physics complicates the problem. When performing a thermal analysis, the goal is to determine the temperature distribution at the battery length scale. The physics governing the Li-ion transport occurs in the anode-separator-cathode sandwich layers (the electrode pair length scale). Li-ion transport in an active material occurs at the atomic length scale. The Multi-Scale Multi-Domain (MSMD) approach deals with different physics in different solution domains [72]. Battery thermal and electrical fields are solved in the CFD domain at the battery cell's scale using the following differential equations:

$$\frac{\partial \rho C_p T}{\partial t} - \nabla \cdot (k \nabla T) = \sigma_+ |\nabla \phi_+|^2 + \sigma_- |\nabla \phi_-|^2 + \dot{q}_{Ech} + \dot{q}_{short} + \dot{q}_{abuse} \quad (6)$$

$$\nabla \cdot (\sigma_+ \nabla \phi_+) = -(j_{Ech} - j_{short}) \quad (7)$$

$$\nabla \cdot (\sigma_- \nabla \phi_-) = (j_{Ech} - j_{short}) \quad (8)$$

where σ_+ and σ_- are the effective electric conductivities for the positive and negative electrodes, ϕ_+ and ϕ_- are phase potentials for the positive and negative electrodes, j_{Ech} and j_{short} are the volumetric current transfer rate and the electrochemical reaction heat due to electrochemical reactions, respectively, and \dot{q}_{Ech} and \dot{q}_{short} are the current transfer rate and heat generation rate due to battery internal short-circuit, respectively, and \dot{q}_{abuse} is the heat generation due to the thermal runaway reactions under the thermal abuse condition. For normal operation, \dot{q}_{abuse} is set to zero. The source terms are computed using an electrochemical submodel. If there is no internal short-circuit this term is equal to zero.

A wide range of electrochemical models, from simple empirically-based to fundamental physics-based, is available in the open literature. In ANSYS Fluent, the following electrochemical submodels are implemented:

- Newman, Tiedemann, Gu and Kim (NTGK) model
- Equivalent Circuit Model (ECM) model

- Newman Pseudo-2D (P2D) model

Electrochemical models, mainly used to optimize the physical design aspects of batteries, characterize the fundamental mechanisms of power generation, and relate battery design parameters with macroscopic (e.g., battery voltage and current) and microscopic (e.g., concentration distribution) information. However, they are complex and time consuming because they involve a system of coupled time-variant spatial partial differential equations a solution for which requires days of simulation time, complex numerical algorithms, and battery-specific information that is difficult to obtain, because of the proprietary nature of the technology. Mathematical models, mostly too abstract to embody any practical meaning but still useful to system designers, adopt empirical equations or mathematical methods like stochastic approaches to predict system-level behaviour, such as battery runtime, efficiency, or capacity. However, mathematical models cannot offer any I–V information that is important to circuit simulation and optimization. In addition, most mathematical models only work for specific applications and provide inaccurate results in the order of 5%–20% error. Electrical models, accuracy of which lies between electrochemical and mathematical models (around 1%–5% error), are electrical equivalent models using a combination of voltage sources, resistors, and capacitors for co-design and co-simulation with other electrical circuits and systems. There have been many electrical models of batteries, from lead-acid to polymer Li-ion batteries. Most of these electrical models fall under three basic categories: Thevenin, impedance and runtime-based models, as shown in **Figure 24** [73].

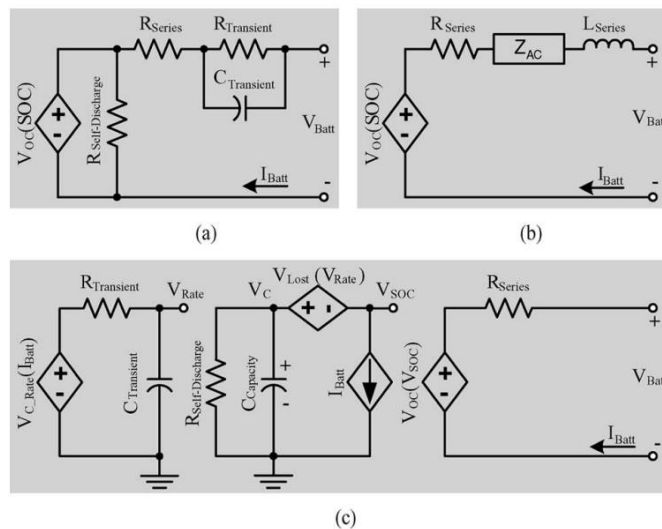


Figure 24 State of the art. (a) Thevenin, (b) impedance, and (c) runtime-based electrical battery models.

3.2.1 Chen’s Model

An accurate, intuitive, and comprehensive electrical battery model is proposed in **Figure 25**. On the left, a capacitor ($C_{capacity}$) and a current-controlled current source, inherited from runtime-based models, model the capacity, SOC, and runtime of the battery. The RC network, like that in Thevenin-based models, simulates the transient response. To bridge SOC to open-circuit voltage, a voltage-controlled voltage source is used. The proposed model is a blend of previous models whose unique combination of components and dependencies eases the extraction procedure, makes a fully Cadence-compatible model possible, and simultaneously predicts runtime, steady state, and transient response accurately and “on the fly,” capturing all the dynamic electrical characteristics of batteries: usable capacity ($C_{capacity}$), open-circuit voltage (V_{OC}), and transient response (RC network).

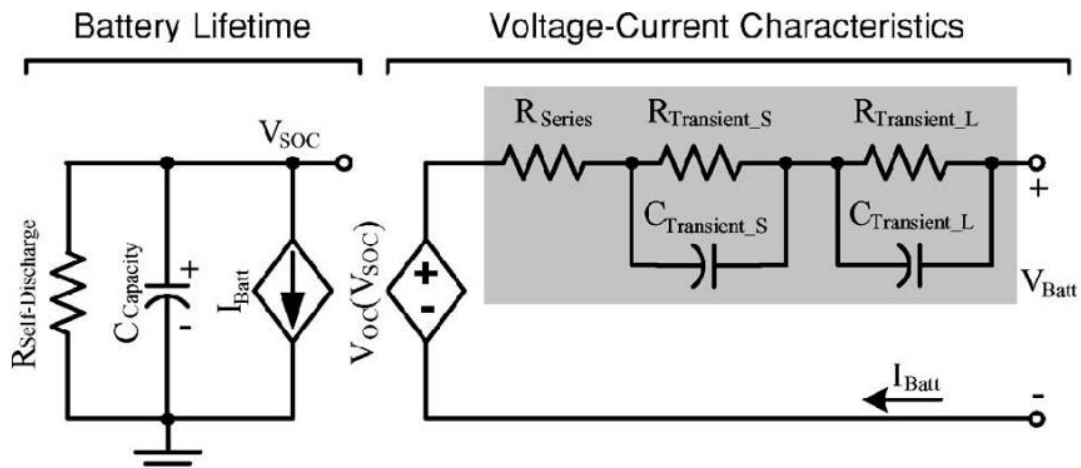


Figure 25 Proposed electrical battery model.

- **Usable Capacity:** assuming a battery is discharged from an equally charged state to the same end-of-discharge voltage, the extracted energy, called usable capacity, declines as cycle number, discharge current, and/or storage time (self-discharge) increases, and/or as temperature decreases, as shown in **Figure 26** (a) and (d). The phenomenon of the usable capacity can be modeled by a full-capacity capacitor ($C_{capacity}$), a self-discharge resistor ($R_{Self-Discharge}$), and an equivalent series resistor (the sum of R_{Series} , $R_{Transient_S}$ and $R_{Transient_L}$). Full-capacity capacitor

$C_{capacity}$ represents the whole charge stored in the battery, i.e., SOC, by converting nominal battery capacity in Ah to charge in coulomb and its value is defined as:

$$C_{capacity} = 3600 \cdot Capacity \cdot f_1(cycle) \cdot f_2(Temp) \quad (9)$$

where Capacity is the nominal capacity in Ah and $f_1(cycle)$ and $f_2(Temp)$ are cycle number- and temperature-dependent correction factors, shown in **Figure 26** (a) and (b). As seen from **Eq. 9**, $C_{capacity}$ will not change with current variation, which is reasonable for the battery's full capacity because energy is conserved. The variation of current-dependent usable capacity, shown in **Figure 26** (c), comes from different SOC values at the end of discharge for different currents owing to different voltage drops across internal resistor (the sum of R_{Series} , $R_{Transient_S}$ and $R_{Transient_L}$) and the same end-of-discharge voltage. When the battery is being charged or discharged, current-controlled current source I_{Batt} is used to charge or discharge $C_{capacity}$ so that the SOC, represented by V_{SOC} , will change dynamically. Therefore, the battery runtime is obtained when battery voltage reaches the end-of-discharge voltage. Self-discharge resistor $R_{Self-Discharge}$ is used to characterize the self-discharge energy loss when batteries are stored for a long time. Theoretically, $R_{Self-Discharge}$ is a function of SOC, temperature, and, frequently, cycle number. Practically, it can be simplified as a large resistor, or even ignored, according to the capacity retention curve shown in **Figure 26** (d), which shows that usable capacity decreases slowly with time when no load is connected to the battery.

- **Open Circuit Voltage:** Open-circuit voltage (V_{OC}) is changed to different capacity levels, i.e., SOC, as shown in **Figure 26** (e). The nonlinear relation between the open-circuit voltage (V_{OC}) and SOC is important to be included in the model. Thus, voltage-controlled voltage source V_{OC} (V_{SOC}) is used to represent this relation. The open circuit voltage is normally measured as the steady-state open circuit terminal voltage at various SOC points.
- **Transient Response:** In a step load current event, the battery voltage responds slowly, as shown in **Figure 26** (f). Its response curve usually includes

instantaneous and curve-dependant voltage drops. Therefore, the transient response is characterized by the shaded RC network in **Figure 26**. The electrical network consists of series resistor R_{Series} and two RC parallel networks composed of $R_{Transient_S}$, $C_{Transient_S}$, $R_{Transient_L}$, and $C_{Transient_L}$. Series resistor R_{Series} is responsible for the instantaneous voltage drop of the step response. $R_{Transient_S}$, $C_{Transient_S}$, $R_{Transient_L}$, and $C_{Transient_L}$ are responsible for short- and long-time constants of the step response, shown by the two dotted circles in **Figure 26** (f). Based on numerous experimental curves, using two RC time constants, instead of one or three, is the best tradeoff between accuracy and complexity because two RC time constants keep errors to within 1 mV for all the curve fittings. The detailed extraction methods can be found in [74]. Theoretically, all the parameters in the proposed model are multivariable functions of SOC, current, temperature, and cycle number. However, within certain error tolerance, some parameters can be simplified to be independent or linear functions of some variables for specific batteries. For example, a low-capacity battery in a constant-temperature application can ignore temperature effects, and a frequently used battery can ignore 5% per month self-discharge rate without suffering any significant errors.

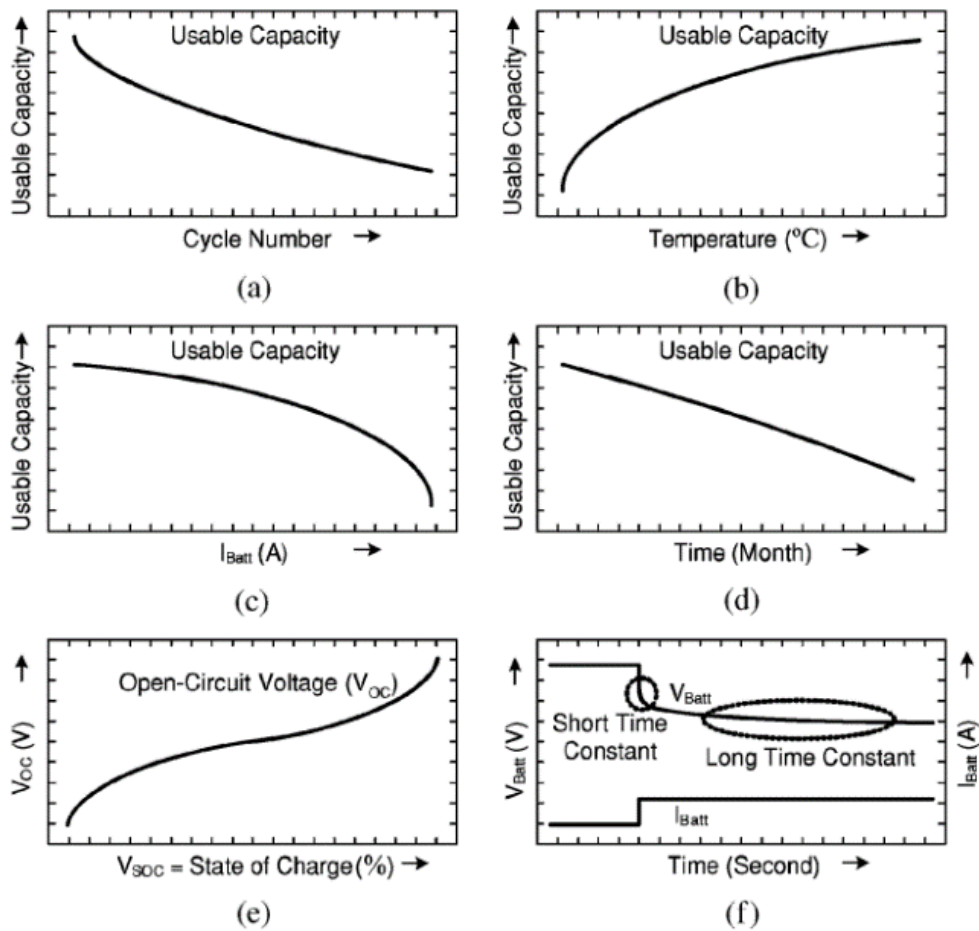


Figure 26 Typical battery characteristic curves of usable capacity versus (a) cycle number, (b) temperature, (c) current, and (d) storage time, as well as (e) open circuit voltage versus SOC and (f) transient response to a step load-current event.

3.2.1.1 Model Extraction

As mentioned in **Section 3.2.1**, all the parameters in the proposed model are multivariable functions of SOC, current, temperature, and cycle number. These functions make the model extraction (i.e., the fitting of multivariable functions or multidimensional lookup tables) complex and the test process (i.e., hundreds of cycle measurements at various temperatures) long. Therefore, some subordinate parameters are simplified or ignored not only because it eases validation but also because they have negligible effects in polymer Li-ion batteries, like usable capacity dependence on self-discharge (2%–10% per month) and cycle number (less than 10% capacity loss over 300 cycles); therefore, $R_{Self-Discharge}$ is set to infinity and $f_1(cycle)$ is set to one.

The extracted nonlinear open-circuit voltage [V_{OC} (V_{SOC})], series resistor (R_{Series}), and RC network ($R_{Transient_S}$, $C_{Transient_S}$, $R_{Transient_L}$, and $C_{Transient_L}$) are functions of SOC and discharge current. All the extracted RC parameters are approximately constant over 20%–100% SOC and change exponentially within 0%–20% SOC caused by the electrochemical reaction inside the battery. Small parameter differences among the curves for different discharge currents indicate that these parameters are approximately independent of discharge currents, which can simplify the model. Single-variable functions were used to represent these curves, as shown by: [73]

$$V_{OC}(SOC) = -1.031 \cdot e^{-35 \cdot SOC} + 3.685 + 0.2156 \cdot SOC - 0.1178 \cdot SOC^2 + 0.3201 \cdot SOC^3 \quad (10)$$

$$R_{Series}(SOC) = 0.1562 \cdot e^{-24.37 \cdot SOC} + 0.07446 \quad (11)$$

$$R_{Transient_S}(SOC) = 0.3208 \cdot e^{-29.14 \cdot SOC} + 0.04669 \quad (12)$$

$$C_{Transient_S}(SOC) = -752.9 \cdot e^{-13.51 \cdot SOC} + 703.6 \quad (13)$$

$$R_{Transient_L}(SOC) = 6.603 \cdot e^{-155.2 \cdot SOC} + 0.04984 \quad (14)$$

$$C_{Transient_L}(SOC) = -6056 \cdot e^{-27.12 \cdot SOC} + 4475 \quad (15)$$

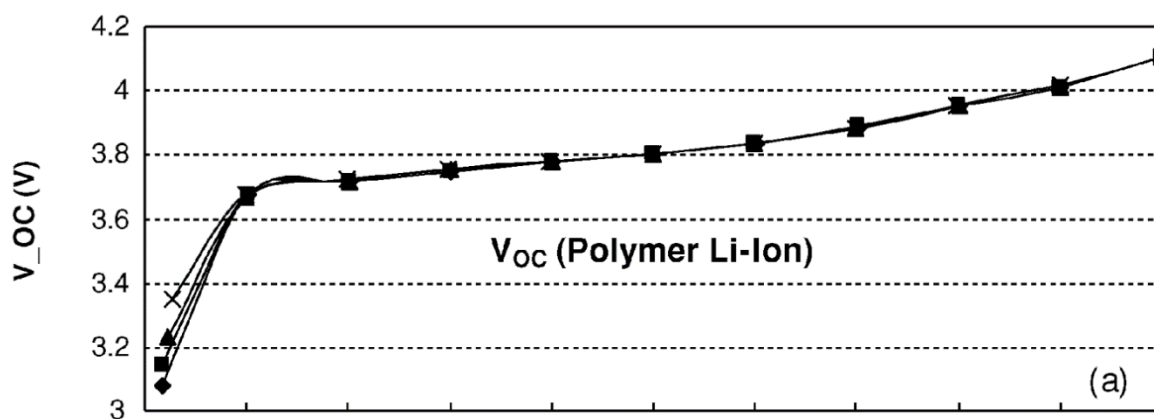


Figure 28 Open Circuit Voltage. [73]

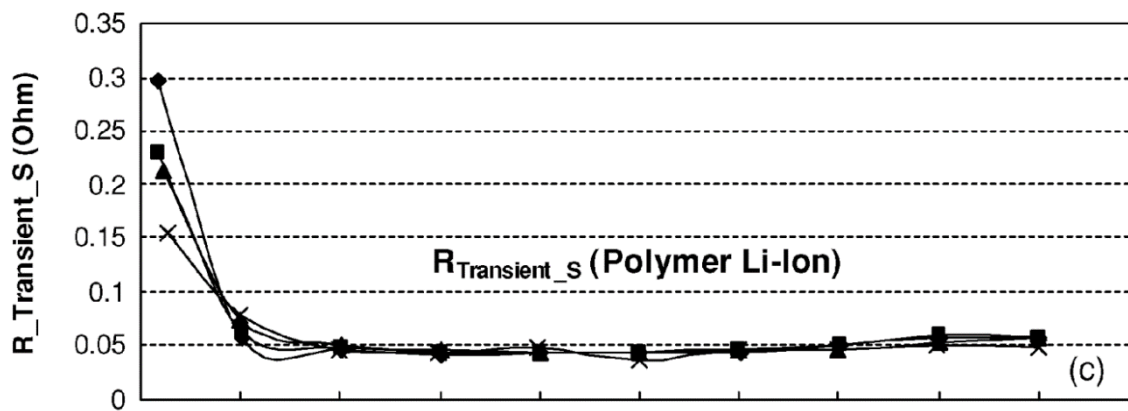


Figure 27 $R_{(Transient_S)}$. [73]

3.2.2 ECM in Ansys Fluent

In the Equivalent Circuit Model (ECM), battery electric behaviour is mimicked by an electrical circuit. ANSYS Fluent has adopted the six parameter ECM model following the work of Chen. In this model, the circuit consists of three resistors and two capacitors like in **Figure 29**.

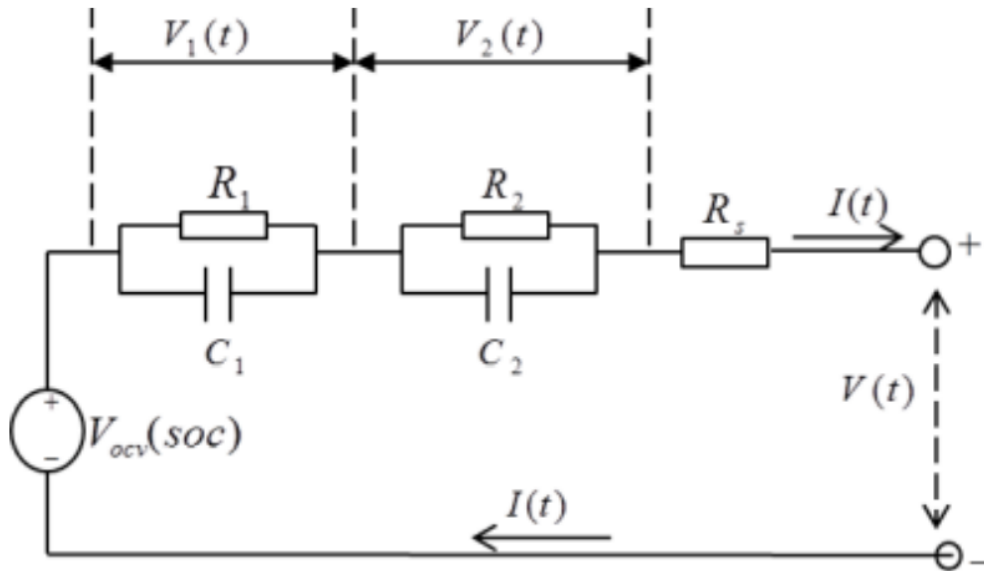


Figure 29 Electric Circuits Used in the ECM Model. [72]

The voltage-current relation can be obtained by solving the electric circuit equations:

$$V(t) = V_{ocv}(SOC) - V_1 - V_2 - R_s(SOC)I(t) \quad (16)$$

$$\frac{dV_1}{dt} = -\frac{1}{R_1(SOC)C_1}V_1 - \frac{1}{C_1(SOC)}I(t) \quad (17)$$

$$\frac{dV_2}{dt} = -\frac{1}{R_2(SOC)C_2}V_2 - \frac{1}{C_2(SOC)}I(t) \quad (18)$$

$$\frac{d(SOC)}{dt} = \frac{I(t)}{3600Q_{Ah}} \quad (19)$$

For a given battery, the open circuit voltage, resistors' resistances, and capacitors' capacitances are functions of the battery state of charge (SOC). These functions could be expressed in two different ways in ANSYS Fluent: the fifth order Polynomial form or the function form proposed by Chen. In this work the method based on the equations elaborated by Chen is adopted. **Chapters 4** and **5** will present a variation of the parameters because the original values proposed by Chen do not adapt to the thermal behaviour of the battery under consideration. The ANSYS FLUENT software, in fact, allows the user to modify the ECM parameters according to the form shown below.

$$R_S = a_0 + a_1 \exp[-a_2(SOC)] \quad (20)$$

$$R_1 = b_0 + b_1 \exp[-b_2(SOC)] \quad (21)$$

$$C_1 = c_0 + c_1 \exp[-c_2(SOC)] \quad (22)$$

$$R_2 = d_0 + d_1 \exp[-d_2(SOC)] \quad (23)$$

$$C_2 = e_0 + e_1 \exp[-e_2(SOC)] \quad (24)$$

$$V_{OCV} = f_0 + f_1(SOC) + f_2(SOC)^2 + f_3(SOC)^3 + f_4 \exp[-f_5(SOC)] \quad (25)$$

The source terms for **Equation 26** and **Equation 27** are computed as:

$$j_{Ech} = \frac{I}{Vol} \quad (26)$$

$$\dot{q}_{Ech} = \frac{I}{Vol} \left[V_{OCV} - (\varphi_+ - \varphi_-) - T \frac{dU}{dT} \right] \quad (27)$$

where Vol denotes the battery volume, I is the current, and V_{OCV} is the open circuit voltage.

3.3 PCM Problem

PCMs are used in different engineering fields, such as in the following: the thermal storage of building structures; building equipment, including domestic hot water; heating and cooling systems; electronic products; drying technology, waste heat recovery; refrigeration and cold storage; solar air collectors; solar cookers and Battery Thermal Management Systems. Using a CFD software to design a LHTES is expected to be an effective way to save money and time and to deliver optimization tools for maximum efficiency.

The mathematical formulation of a phase transient known as a phase change or moving boundary is governed by a partial differential equation that can be solved either analytically or numerically. The analytical solution of PCMs is problematic because of the nonlinear phase front interfaces, complex geometries, and nonstandard boundary condition; the few analytical studies available are on 1D cases with regular geometries and a standard boundary condition. Predicting the behaviour of phase change systems is difficult because of its inherent non-linear nature at moving interfaces, for which the displacement rate is controlled by latent heat lost or absorbed at the boundary [75]. The heat transfer phenomena in solid–liquid PCMs can be analysed using two main methods: the temperature-based and enthalpy-based methods. In the first method, temperature is considered a sole dependent variable. The energy conservation equations for the solid and liquid are written separately; thus, the solid–liquid interface position can be tracked explicitly to achieve an accurate solution for the problems.

$$\frac{\partial T_s}{\partial n} k_s = \frac{\partial T_l}{\partial n} k_l + \rho L k v_n \quad (28)$$

where T_s denotes the temperature in the solid phase, T_l denotes the temperature in the liquid phase, k_s is the thermal conductivity of the solid phase, k_l is the thermal conductivity of the liquid phase, n is the unit normal vector to the interface, and v_n is the

normal component of the velocity of the interface. L is the latent heat of freezing, as shown in **Figure 30**.

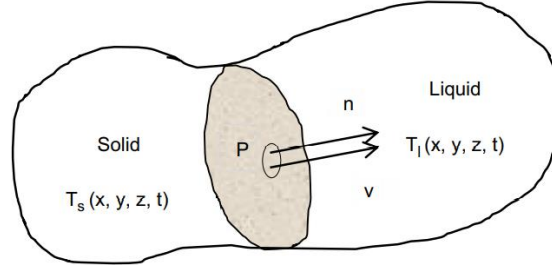


Figure 30 Solid–liquid interface for a multidimensional situation [76]

In the second method, the solid–liquid interface position need not be tracked. Researchers often use the enthalpy formulation because of the following advantages: (1) the governing equations are similar to the single-phase Eq.; (2) no explicit conditions need to be satisfied at the solid–liquid interface; (3) the enthalpy formulation involves the solution within a mushy zone, involving both solid and liquid materials, between the two standard phases; and (4) the phase change problem can be solved more easily [77]. The energy equation is expressed as:

$$\frac{\partial(\rho H)}{\partial t} + \nabla \cdot (\rho \bar{v} H) = \nabla \cdot (k \Delta T) + S \quad (29)$$

where ρ is the density of the PCM, \bar{v} is the fluid velocity, k is the thermal conductivity, H is the enthalpy, and S is the source term. The source term derives directly, in the present case, from the domain of the battery and its value is calculated as previously discussed. In the PCM zone it is zero since there is no heat generation. The effect of natural convection in the liquid PCM is neglected, thus the continuity and momentum equations are not necessary. The solidification process is dominated by heat conduction [63] and natural convection is present only at the beginning of the process. Consequently, after these hypotheses, the equation of the energy that resolves takes the following form:

$$\frac{\partial(\rho H)}{\partial t} = \nabla \cdot (k \Delta T) + S \quad (30)$$

3.3.1 PCM in Ansys Fluent

ANSYS FLUENT has a specific model that can simulate a range of different melting and solidification problems in engineering, including casting, melting, crystal growth, and solidification. The program can be used to solve the phase change that occurs at a single temperature (pure metals) or over a range of temperatures (mixture, alloy, and so on). The mathematical equations used to solve the solidification and melting models in Fluent depend on the enthalpy–porosity technique [78] and on the finite volume methods. In the former, the melt interface is not tracked explicitly. A quantity called liquid fraction, which indicates the fraction of the cell volume in liquid form, is associated with each cell in the domain. The liquid fraction is computed at each iteration based on enthalpy balance. The mushy zone is a region wherein the liquid fraction lies between 0 and 1. The mushy zone is modeled as a “pseudo” porous medium in which the porosity decreases from 1 to 0 as the material solidifies. When the material has fully solidified in a cell, the porosity becomes zero, resulting in the drop of velocities to zero.

The sensible enthalpy can be expressed as:

$$h = h_{ref} + \int_{T_{ref}}^T C_p \Delta T \quad (31)$$

$$H = h + \Delta H \quad (32)$$

where h_{ref} is the reference enthalpy at the reference temperature T_{ref} , C_p is the specific heat, ΔH is the latent heat content that may change between zero (solid) and 1 (liquid), L is the latent heat of the PCM, and γ is the liquid fraction that occurs during the phase change between the solid and liquid state when the temperature is $T_l > T > T_s$. Thus, γ may be written as [76]:

$$\gamma = \frac{\Delta H}{L} \quad (33)$$

$$\gamma = 0 \quad \text{if} \quad T < T_s$$

$$\gamma = 1 \quad \text{if} \quad T > T_l$$

$$\gamma = \frac{(T - T_s)}{(T_l - T_s)} \quad \text{if} \quad T_l > T > T_s$$

3.4 Boundary Conditions

In this section, boundary conditions are determined for all case studies that will be analysed in the following chapters. Depending on the case study, contour conditions may vary. During the process of simulation, the initial state was specified as follows:

$$t = 0; \quad T(x, y, z) = T_0$$

where T_0 is both the ambient temperature and the temperature of all the components constituting the geometry. The main case study present T_0 equal to 298 K, but are analysed in **Chapter 5** also T_0 equal to 273 K and 318 K. In the case with single cell, the interface between the cell walls and the external environment can be described as follows:

$$-k_{cell} \frac{\partial T}{\partial n} = h(T_{cell} - T_{amb}) \quad (34)$$

where k_{cell} represents the thermal conductivity of the cell, h is the convection coefficient, T_{cell} is the instantaneous temperature of the cell and T_{amb} represents the temperature of the external environment (constant value set during initialization).

In the second case, when two battery walls are in contact with the PCM, the boundary conditions take this form:

$$-k_{cell} \frac{\partial T_{cell}}{\partial n} = -k_{PCM} \frac{\partial T_{PCM}}{\partial n} \quad (35)$$

$$-k_{PCM} \frac{\partial T_{PCM}}{\partial n} = h(T_{PCM} - T_{amb}) \quad (36)$$

In the third case, with the addition of Heat Sinks and PCM, the interface between the contact regions is described by the following relationships:

$$-k_{cell} \frac{\partial T_{cell}}{\partial n} = -k_{Al} \frac{\partial T_{Al}}{\partial n} \quad (37)$$

$$-k_{Al} \frac{\partial T_{Al}}{\partial n} = -k_{PCM} \frac{\partial T_{PCM}}{\partial n} \quad (38)$$

$$-k_{PCM} \frac{\partial T_{PCM}}{\partial n} = h(T_{PCM} - T_{amb}) \quad (39)$$

It is useful to remember that the battery walls not involved in the contact have the same boundary condition described by the **Eq. 34**.

Finally, the case of the battery pack is studied, in which an Aluminum Case has been added. All the relationships described will be valid, but with the addition of the latter:

$$-k_{PCM} \frac{\partial T_{PCM}}{\partial n} = -k_{Al_case} \frac{\partial T_{Al_case}}{\partial n} \quad (40)$$

$$-k_{Al_case} \frac{\partial T_{Al_case}}{\partial n} = h(T_{Al_case} - T_{amb}) \quad (41)$$

For the walls of the cells in direct contact with the Aluminum Case will be worth the **Eq. 41** and the **Eq. 42**:

$$-k_{cell} \frac{\partial T_{cell}}{\partial n} = -k_{Al_case} \frac{\partial T_{Al_case}}{\partial n} \quad (42)$$

Chapter 4 Model development

In the previous chapter it was introduced the physics of the problem and the methodology used to simulate the heat generation for the active part of the single cell. In this section of the discussion, it is explained the generation of the mathematical model using the commercial software ANSYS FLUENT 2021 R2. In the following chapters, there will be reported the results obtained through simulation with the consequent discussion about the physical validity of the latter. This section summarizes what will be reported in Chapter 4. The first step is the simulation of the single cell by defining the geometry, the chemical and thermophysical characteristics of the cell, Mesh generation, model set-up setting. Secondly, changes implemented on the model will be presented, in order to analyze the different cooling techniques. Furthermore, in this section it will be explained the choices of materials (example, type of PCM adopted) and geometric parameters regarding the cooling system itself. In the last part of the chapter, it will be introduced the modeling system of the battery pack. A summary of the main working hypotheses, which led to the generation of the model, is presented here:

- The heat transfer from the terminal surfaces and ambient temperature is free convection;
- The boundary between the terminal and cell itself is “coupled” type boundary conditions which assures the continuity of the temperature across the defined boundary;
- The initial temperature is considered to be 298 K equal to the ambient temperature;
- The cell has orthotropic thermal conductivity;
- The specific heat for the cell is averaged;
- No flow filed for the liquid phase of PCM;
- Radiation is not considered.

4.1 Li-ion cell properties

The proposed model and the procedure for the identification of the parameters in the electrical equivalent circuit are applied to two Nickel Manganese Cobalt oxide (NMC) lithium-ion cells with nominal voltage and capacity 3.70 V and 59.3 Ah, respectively [79]. The cells have a pouch structure with same side terminals, and these represent a typical solution that is applied in the automotive applications. From the literature, it is possible, in addition, note that the capacity of the test cell varies according to temperature and discharge current as presented in **Table 1**. This type of behaviour is reflected in the variation of the parameters of the ECM as a function of temperature, as well as the SOC. Because of this, a sensitivity analysis of the parameters of the ECM model in relation to the variation of environmental conditions will be conducted in Chapter 5.

Table 1 Cell capacity at different operating temperatures and C-rates [Ah]. [79]

C-Rate	T [°C]			
	-20	0	25	40
1/3	48.9	56.1	60.4	60.6
1	51.4	55.1	59.3	60.6
2	3.7	18.3	50.1	39.0

4.2 Li-ion cell geometry

In the summary section, it was presented the typical structure of a cell type "pouch": constructed by stacking multiple layered sheets of anode-separator-cathode assemblies which are then inserted into a pouch, the pouch is then filled with electrolyte and sealed leaving the positive and negative terminals outside of the pouch. The material used for the pouch is a laminated aluminum film with a layer of polyamide on the outside and polyethylene on the inside to electrically insulate the casing material and prevent corrosion from the electrolyte. For this reason, it would be useful to realize a geometry of the cell characterized by layers of all the elements described. This type of approach could

lead to excessive computational expenditure due to the need to adopt a large number of elements and nodes in the generation of the mesh (making a good quality mesh for thin walls requires a high cost of calculation). For this reason, it was decided to significantly simplify the geometry of the model, by assigning to a single central body (Active zone) the thermophysical properties of each individual element characterizing the cell: these properties have been calculated using methodologies adopted by the literature and presented in the following sections.

The geometry of the cell was realized by using the Design Modeler, made available by the ANSYS FLUENT software. The dimensions of the cell have been reported by the literature, because of the need to validate, in the preliminary phase, the results obtained from the simulations with the experimental results reported in the literature. **Table 2** summarizes the fundamental values.

Table 2 Cell geometric characteristics. [79]

	Axial Directions		
Dimensions [mm]	X	Y	Z
Active Zone	95	300	14
Tab Zone	30	15	8

It is necessary to remember that, unlike the publication from which the model takes inspiration, in this case, the collecting Tab are placed on the same side of the active part. The temperature variation resulting from this assumption is presented in **Figure 31** and **Figure 32**; the temperature difference is minimal, moreover, the discharge current with which you want to validate the model is equal to 1C: the differences are less marked. Due to this, it has been possible considering the different arrangement of the Tabs as an ineffective aspect in the success of the validation.

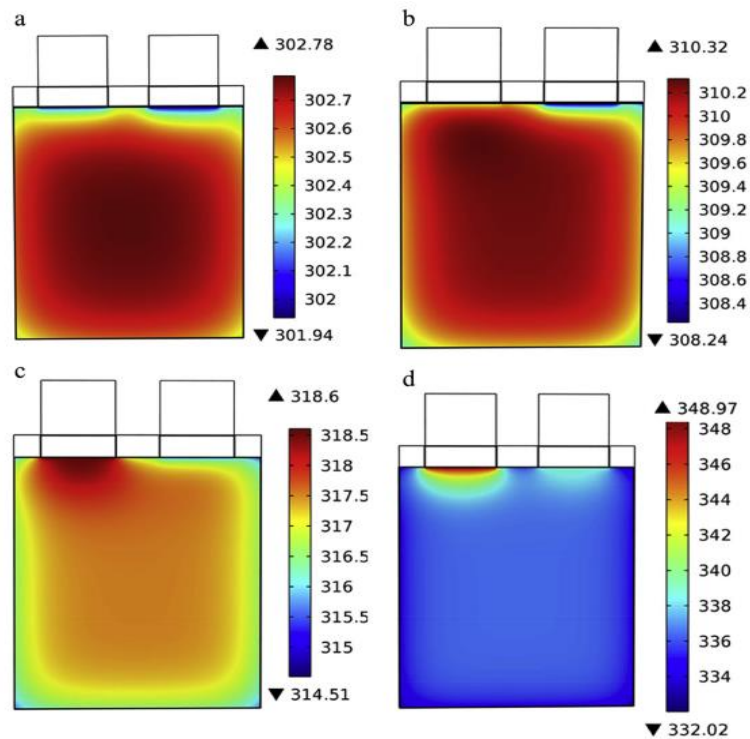


Figure 31 The temperature distributions of the center section under different rates. (a) 1C; (b) 3C; (c) 5C; (d) 10C. [80]

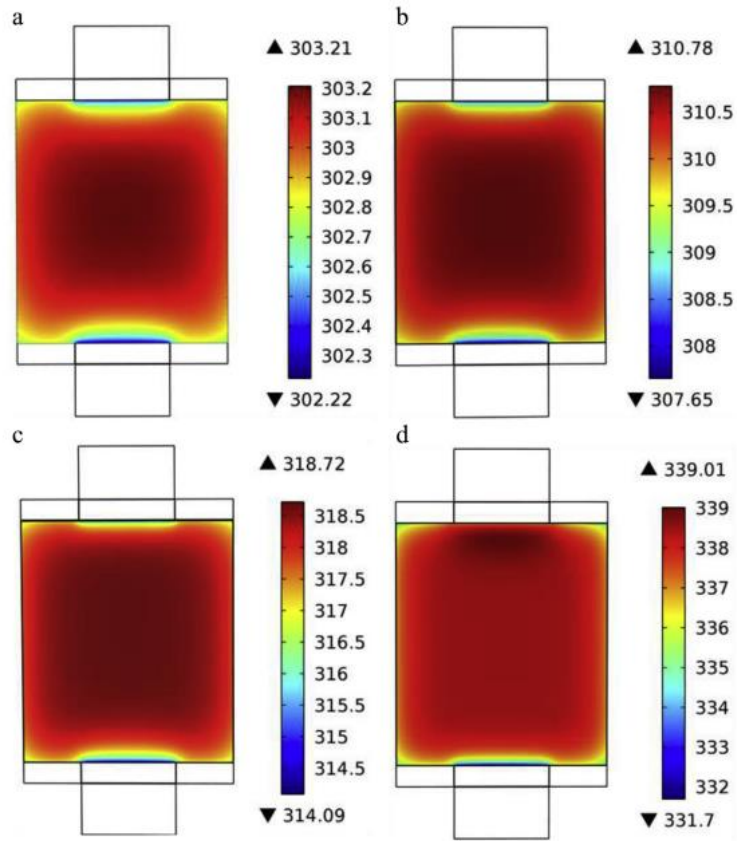


Figure 32 The temperature distribution of battery center section at different rates. (a) 1C; (b) 3C; (c) 5C; (d) 10C. [80]

Figure 33 shows the result obtained by the generation of the geometry of the cell through the use of the Design Modeler.

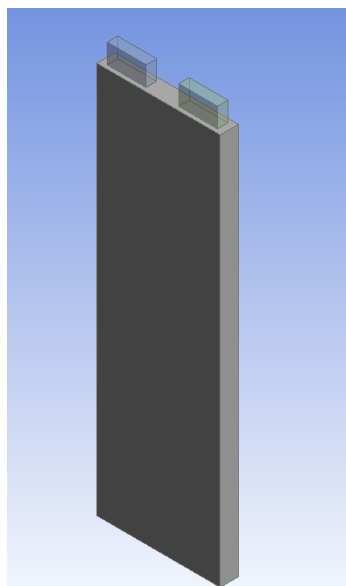


Figure 33 geometry of the cell.

4.3 Meshing

After creating the geometry, it is useful to make the mesh. For this purpose, the "Meshing" was used in dowry to the software ANSYS FLUENT 2021 R2.

The first step was to select CFDs as "Physic Preference" and Fluent in "Solver Preference" in order to obtain a mesh that would be more favourable to the software used for the simulation.

The very simplified battery structure allows to adopt a type of "structured" mesh. After assigning to all bodies the property of "solid", it is required generation of nodes and elements.

In the section "Mesh" it has been inserted a "Mesh Method" of realization called "Multizione" with which it is obtained a more ordered mesh, independent from the mapping of the adjacent elements. In addition, this method enables the choosing of the type of elements, useful to realize the assigned geometry. In the "Free Mesh Type" section, a "Hexa Dominant" mesh has been assigned. This method has been assigned to all parts of the cell (Active zone and Connecting Tab).

The criterion used to understand if the mapping generated by the software is suitable with the characteristics required by the simulation was one of the "Mesh Metric" made available by the program itself: "Element Quality". The more the element quality of the geometry is tending to 1, the more the mapping has been done correctly.

Last step for the definition of the Mesh was to assign a size to the elements called "Element Size" (measured in millimeters). This step is important because it determines both the quality of the mapping and the number of nodes and elements made. An excessively large "Element Size" leads to a reduced computation expense to the detriment of an unsophisticated mapping and with a very low "Element Quality". On the other hand, using a too small "Element Size" leads to excessive computational expenditure despite the excellent "Element Quality". Therefore, for completeness of treatment, it was conducted a "Grid Space Independency Test": the "Element Size" parameter was iteratively varied in order to obtain the best combination of a number of elements and "Element Quality".

In order to analyze the independence of the solution from the mesh, it has been taken into account the measurement of the average temperature trend of the active part, as shown in **Figure 36**. The iteration is considered concluded when the variation of the temperature parameter does not show excessive variations between two successive solutions.

Table 3 “Named Selection” of the elements.

Element	“Named Selection” Solid	“Named Selection” Surface
Active Zone	Active_Zone	Wall-Active_zone
Positive Terminal	Tab_positivezone	Wall-Tab_positivezone
Negative Terminal	Tab_negativezone	Wall-Tab_negativezone
Positive Tab		Tab_positive
Negative Tab		Tab_negative

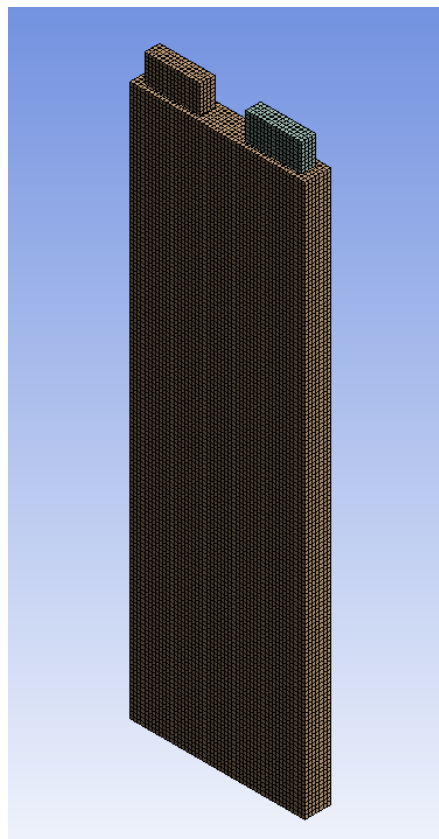


Figure 34 Mesh of the cell.

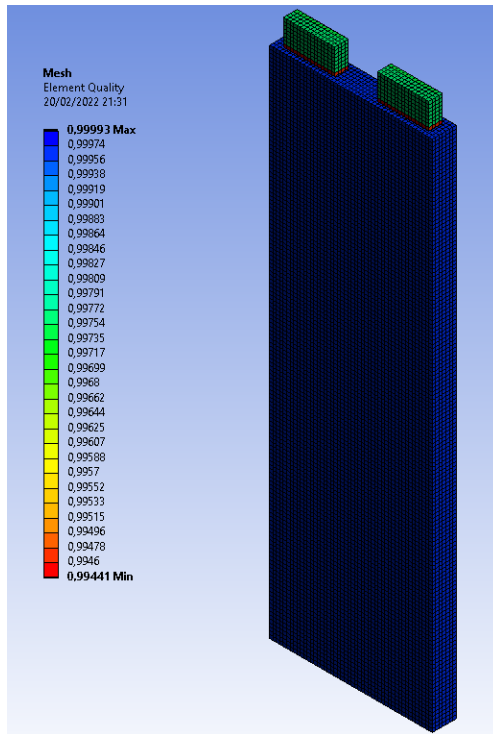


Figure 35 “Element Quality” of the cell.

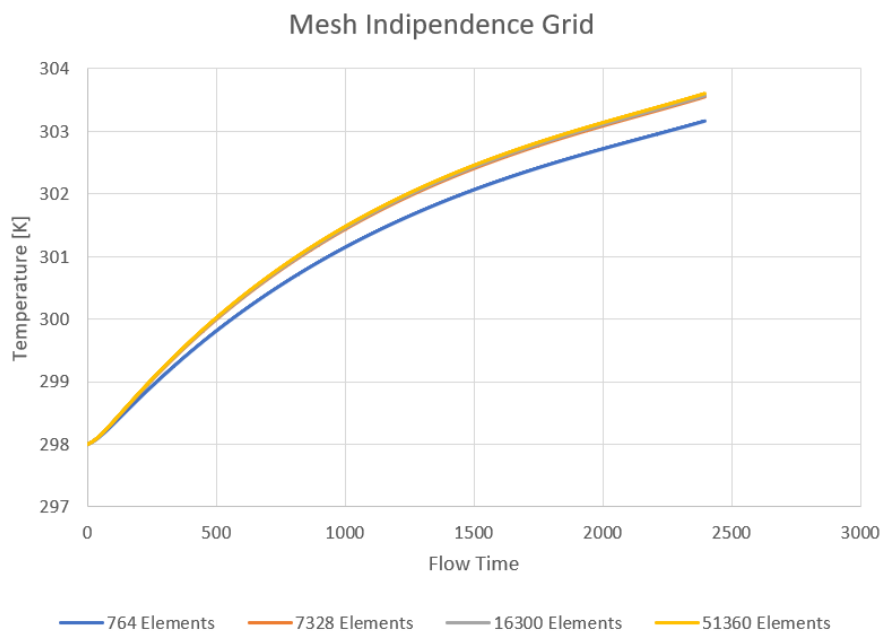


Figure 36 “Grid Space Independency Test” of the cell.

Figure 36 shows the "Mesh Independent Grid" and, in front of the results obtained, the choice of the "Element Size" fell on a value of 0.003 mm. The total number of elements and nodes is 16300 and 20526

4.4 Model Set Up

Once the mapping is set, the next step is to define the model set-up. In this section, there will be presented the steps that have been conducted for the assignment of the necessary parameters for the study of the thermal behaviour of the battery and battery combined with the PCM.

The ANSYS FLUENT software is designed to solve the equations in an iterative way; it is up to the user to assign these equations to the calculation system. In this case, the first equation is the NSF energy balance equation. As explained in Chapter 3, battery physics requires the addition of some terms to the budget equation. To achieve this, it is useful to load the add-on to study the cell within the software. Use the define/models/addon-module command and select "8. Dual-Potential MSMD Battery Model". To make the problem of PCM usable, it is useful to activate the "Solidification and Melting" section, which will automatically implement the flow equations in the three directions of space.

Once the "Dual-Potential MSMD Battery Model" is enabled, the user has the option to choose the most suitable electrochemical model for the case study (as already explained by ECM). Next, it is useful to define the current value at which is downloaded/loaded the cell. **Figure 37** shows the discharge value open to 1C, but other battery discharge conditions will be analysed during the sensitivity analysis. It is required to enter a nominal capacity value of the cell (Ah) and to adopt a range between maximum and minimum voltage (V) of battery operation. These values were derived from the literature [79] and reported in **Table 4**.

Nominal Cell Capacity [Ah]	59.3
C-Rate [Ah]	1
Min. Stop Voltage [V]	2.5
Max. Stop Voltage [V]	4.25

Table 4 Parameters in Model Option.

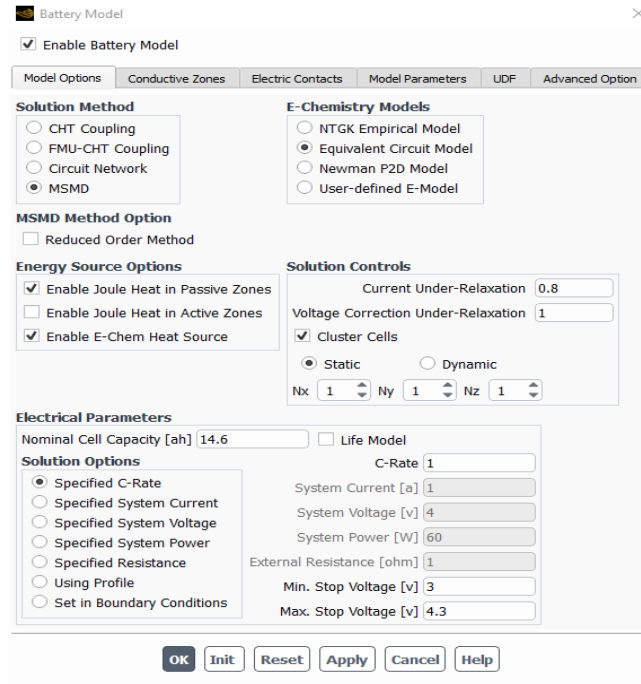


Figure 37 Model Option for MSMD Battery Model.

Continuing within the MSMD model, the elements responsible for electrical conduction are defined in the *Conductive Zones* tab. In particular, the active part, indicated by the named-selection "active-zone", has established itself as Active Components, while as Tab Components there are the two copper terminals ("tab_positivezone" for the positive terminal and "tab_negativezone" for the negative terminal). Finally, in the *Electric Contacts* tab, the two "tab_positive" and "tab_negative" surfaces were assigned as external connectors, positive and negative respectively. Regarding the section "Electric contact resistance" reserves the right to read the **Section 4.9**.

4.4.1 ECM Parameters

In the section were presented the parameters of the Chen model and the software provides the user the implementation of these default parameters as shown in **Figure 38**.

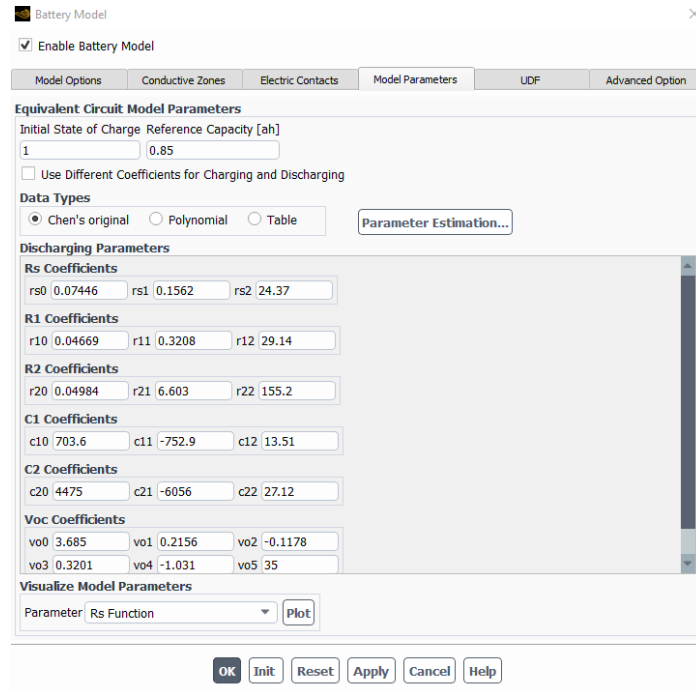


Figure 38 Chen's model parameters for MSMD Battery Model.

If these parameters had been adopted, without making any changes related to this case study, no satisfactory results would have been obtained for the validation of the experimental trend of the voltage and temperature curves. Therefore, below, there are the graphs representing the experimental voltage and temperature curves that have been analysed and the results obtained by the simulation if no changes had been made to the standard parameters of the Chen model.

In **Figure 39** is reported the temperature trend obtained on the battery in question with the use of Chen parameters.

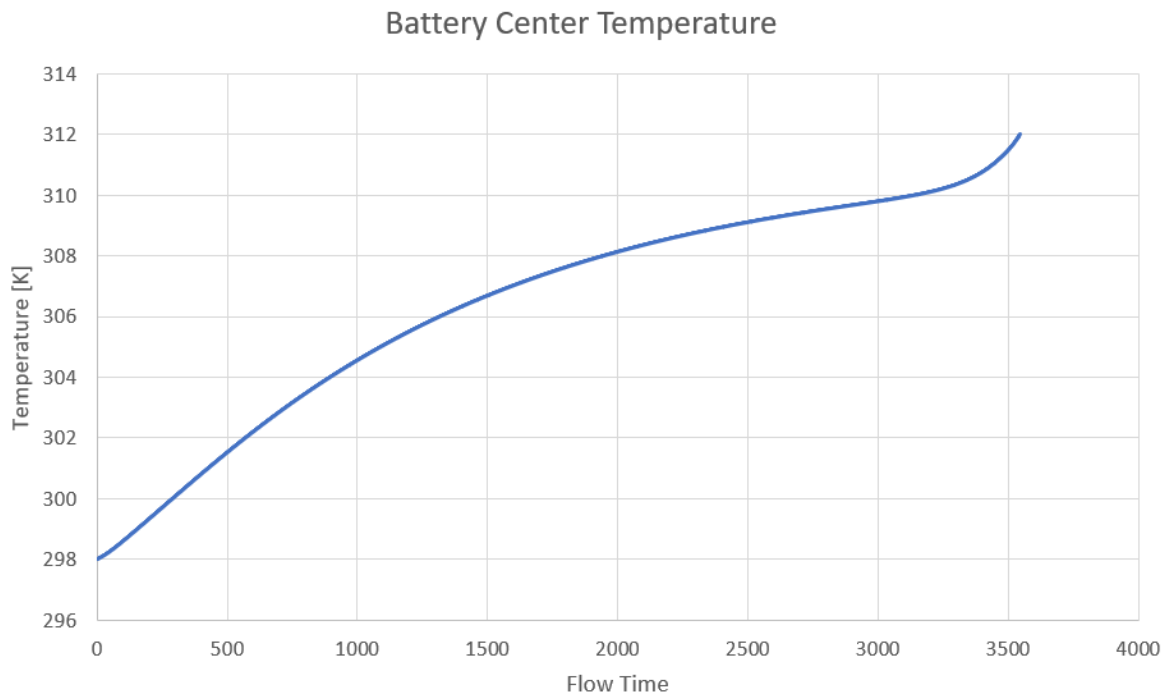


Figure 39 Battery Center Temperature @ 25 °C and 1 C-rate.

The temperature and voltage trends obtained by experimental tests are shown below in **Figure 40**

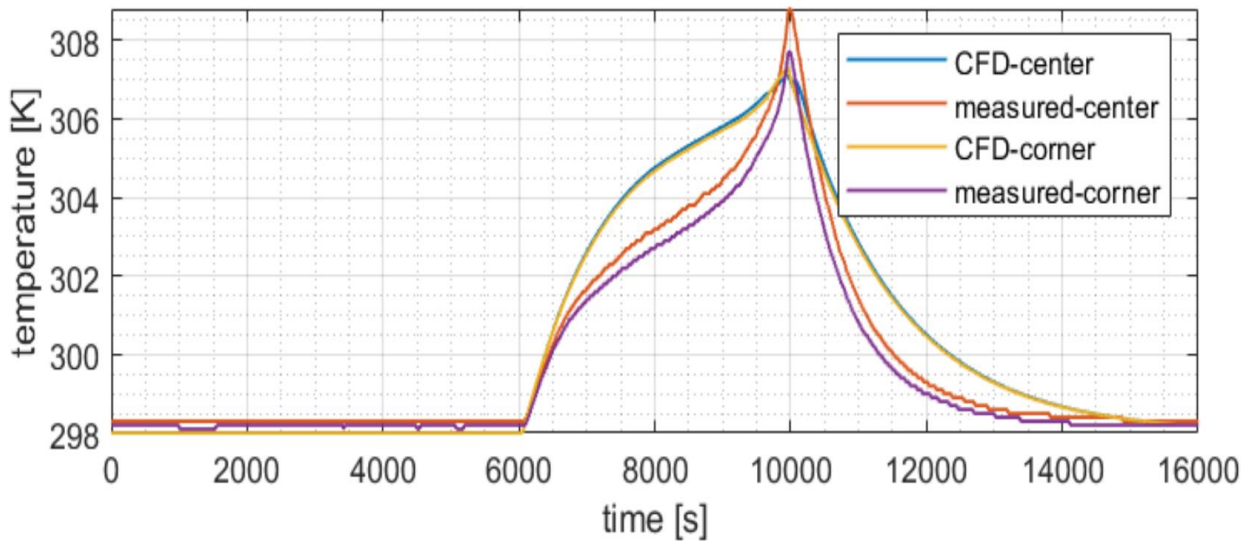


Figure 40 Temperature comparison @ 25 °C and 1 C-rate. [81]

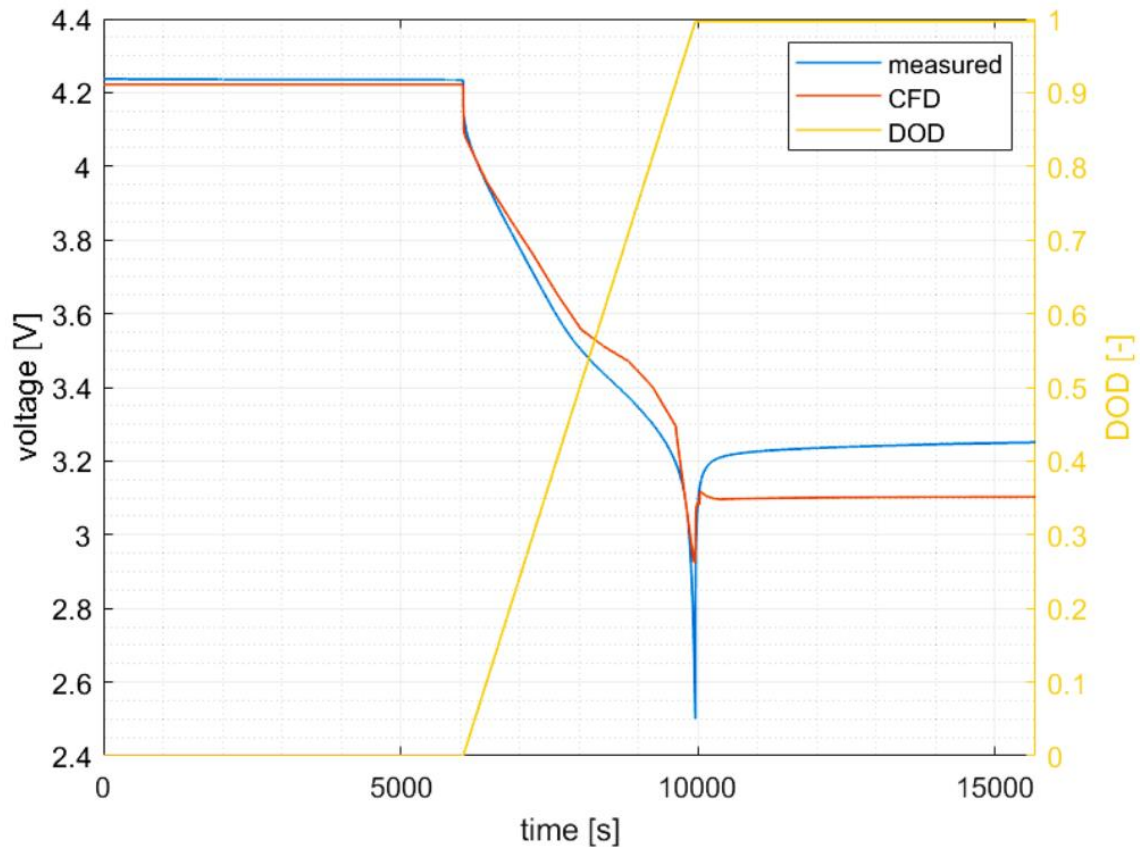


Figure 41 Voltage comparison @25°C and 1 C-rate. [81]

As is appreciable from the figures, there is a clear difference in the temperature trend of the measured center in **Figure 40** and the center of the battery simulated with the use of Chen parameters in **Figure 39**. The use of these parameters does not allow to obtain the typical temperature trend for large cells size.

One of the limitations of Chen's model is that it is only applicable for an assigned temperature value, allowing parameters to vary exclusively with the progress of the charging state. The physical reality of the problem, however, is quite different because the variations in these parameters depend both on the SOC and on temperature changes. It can be seen in Fig the trend of the parameter "*R_Series*" (Ω) depending on the state of charge. The most significant variation is obtained in the area ranging from 0 to 10 % of the battery charge. This type of behaviour is consistent with the experimental temperature trend proposed in Fig. In the final phase of the discharge, therefore, an exponential increase of the resistance value is obtained, which is reflected in the sharp increase in temperature.

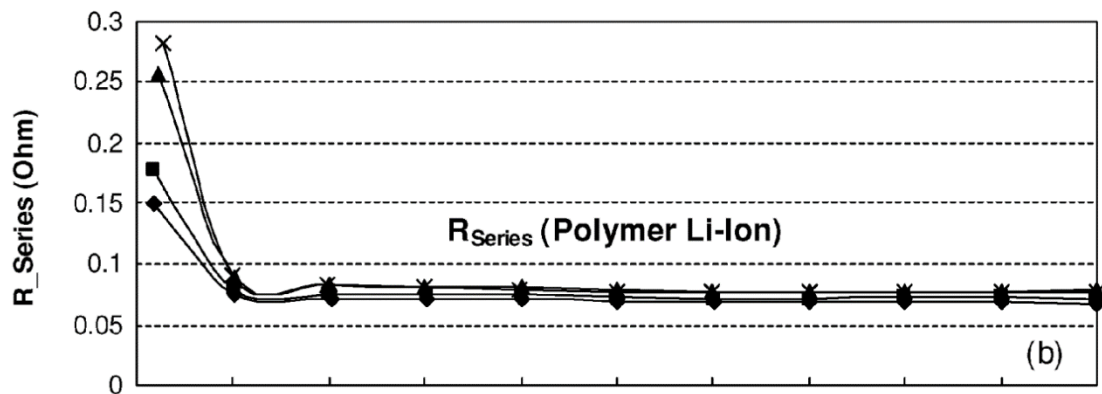


Figure 42 Extracted parameter of the polymer Li-ion battery at room temperature. [73]

As reported in the Overview chapter of the Lithium-ion battery problem, the operating range of the cells is between 80 and 20% of the charge. The range has to ensure the stability of the electrochemical reactions inside the cell and avoid inconveniences such as excessive temperature rises (leading to catastrophic phenomena such as the Thermal Runaway) and the possibility of decay of the nominal capacity of the latter. Against this, it is possible to say that, in operating conditions, the real responsible for the variation of the parameters of the ECM model is the operating temperature of the cell. Below there are the Figures in which it is possible to appreciate, through representations of three-dimensional diagrams, the variation of the parameters of the ECM with single-branch configuration RC.

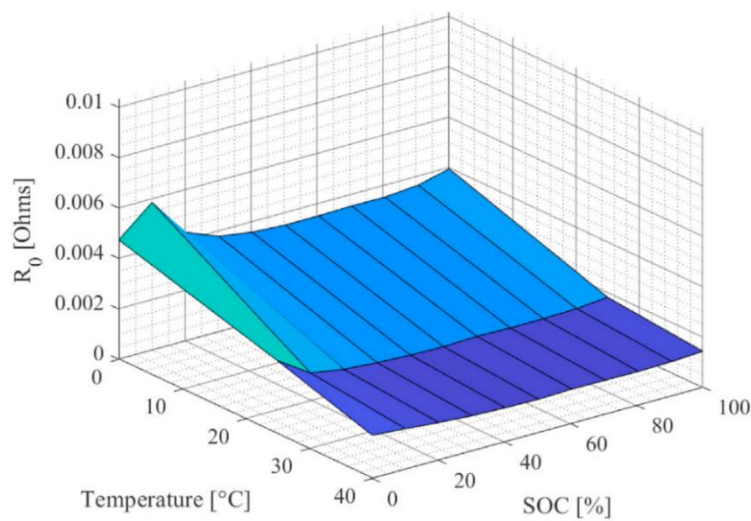


Figure 43 Average values of R0. [79]

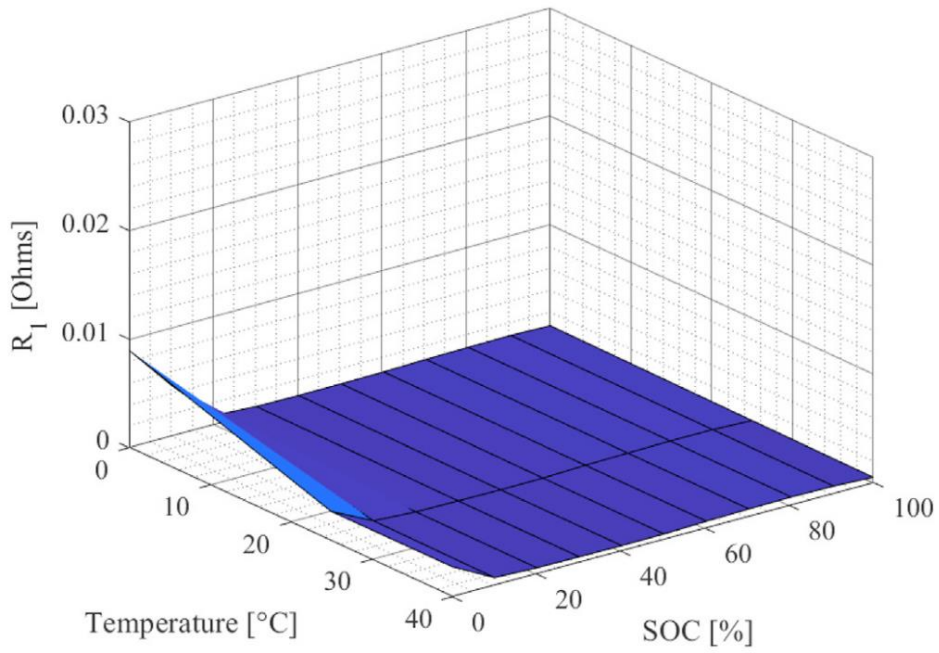


Figure 44 Average values of R_1 . [79]

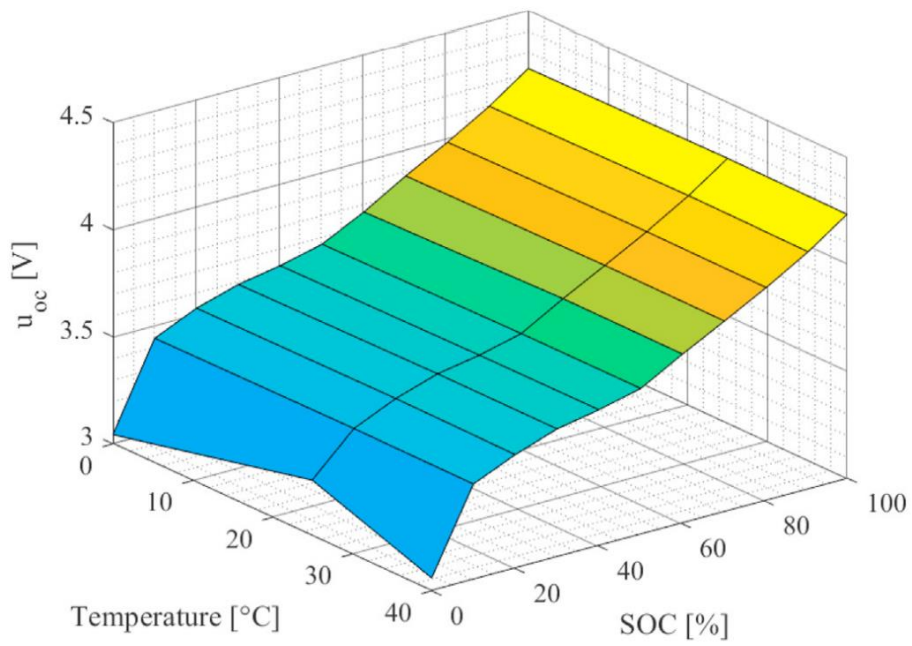


Figure 45 Average values of U_{oc} [V]. [79]

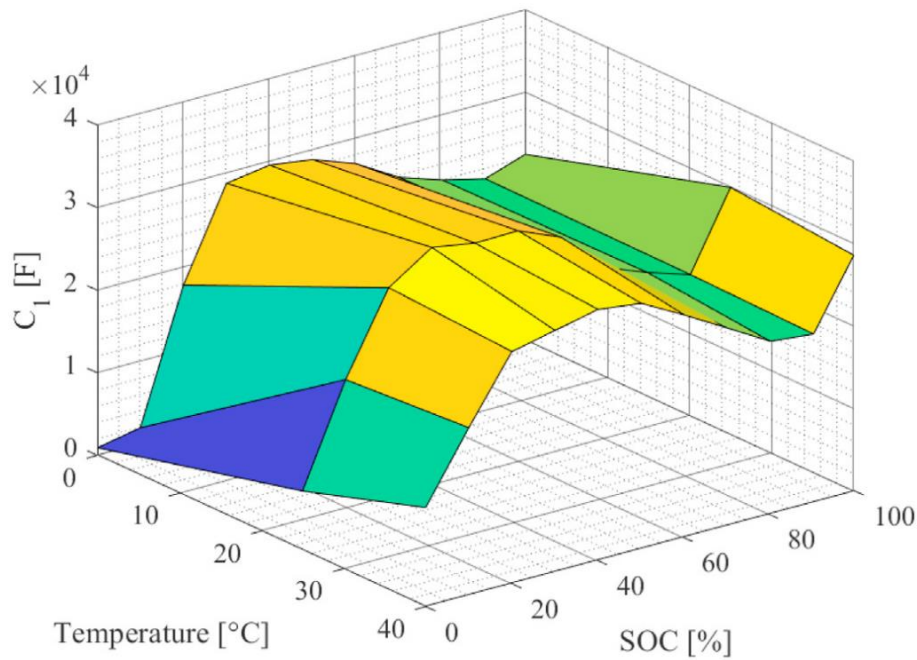


Figure 46 Average values of C1 [F]. [79]

The main observation concerns the development of the "*R_Series*" parameter, as previously done. The greatest variation compared to the operating temperature is obtained with this parameter, which is the main responsible for the thermal behaviour of the battery. At a relatively low operating temperature values (in the order of 0 °C) the resistance value is much greater than the operating range of 20 °C.

In addition, it is possible to observe how, at low temperatures, the sensitivity of the parameter, compared to the change in the state of charge, is more pronounced. A similar behaviour is not to be considered negligible and will be treated in the sensitivity analysis of the ECM parameters that will be described in the following chapters.

The ANSYS FLUENT software provides the user with the possibility to enter the parameters of the ECM model in matrix format with the "Table" functionality in the "Model Parameters" section. The implementation of the parameters in this format involves an excessive increase in computational expenditure and the instability of the resolution of the energy equation; a behaviour recognized and generated by the difficulty of the software to instantly read the temperature value after iteration and interpolate simultaneously all the values of the ECM model as a function of SOC and T. To solve this problem, ANSYS suggests adopting a "Under Relaxion-Factor", whose optimal value

must oscillate between 1 and 0.8. Following some tests conducted on the simulation, in the present case, given the complexity of the model, the value of optimal URF is 0.5. It is a value too low that is in contrast with the indications given by the manufacturer of the Software.

As it can be seen from **Figure 40** the operating range of the battery under examination, during a complete discharge cycle at 1C, is around 10 °C. Because of this, it was possible to make an approximation: consider as a basis the Chen model with only the variation of the parameters as a function of the SOC. In the first case a set-up of battery temperature of 298 K is considered, later, for completeness of treatment, a sensitivity analysis of the ECM parameters was carried out as a function of the variation of the ambient temperature conditions.

4.5 Cooling Systems

In the introductory section, a reference was made to the purpose of this research work: to minimize the maximum temperature value attainable by the battery and to optimize the temperature distribution within the cell; Key features to achieve maximum battery life under ideal operating conditions. Therefore, to reach the goal, it was decided to study how different cooling systems are going to affect the thermal behaviour of the battery components (active zone and collecting tab).

4.5.1 Heat Sinks geometry

In **Chapter 2**, several techniques for improving the performance of the passive cooling system using PCM have been described. In order to increase the heat exchange surface between the active part and the phase change material, it is possible to use aluminum structures called heat sinks.

Heat sinks are rigid structures composed of a heat sink plate that represents the supporting structure on which the fins are welded. The latter have a rectangular profile, whose dimensions are strictly at the discretion of the user who requests its use. Assigning a correct value to the size of the rectangular profile was one of the most interesting aspects of the realization of the combined model between heat sink and the cell.

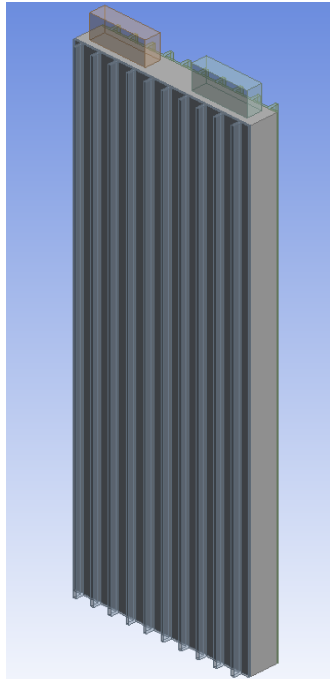


Figure 47 Battery with Heat Sinks geometry.

The heat sinks presented in **Figure 47** have been realized through the use of the "Design Modeler" tool made available by the ANSYS software. The image shows the geometric details that have been described above. The characteristic dimensions are shown in the **Table 5** below.

	Dimensions [mm]			
	Thickness	Length	Height	Spacing
Heat sink Plate	95	1	300	-
Heat sinks	1.5	4	300	9.5

Table 5 Dimensions of heat sinks and heat sinks plate.

The choice of size was predominantly arbitrary, but inevitably conditioned by the physical and computational limitations of the problem. First, it is useful to remember that the analysed system has the only purpose of illustrating what is the effect of the insertion of a surface of a material with high thermophysical properties such as Aluminum. It was necessary to limit the size of the heat sink plate and the fins themselves in order not to present an excessive cooling effect. Since the real focus of the problem is to demonstrate how the increase of the heat exchange surface improves the cooling performance when using PCM. In contrast to this, the size characteristics must not be reduced excessively, as it wants to ensure a good stability of the software in solving the problem: very thin volumes do not allow a correct mapping of the geometry.

As it can be seen from **Figure 47**, the plates that serve as support to the fins have been laid on the faces of the cell, leaving free the narrow sides and the base of the latter.

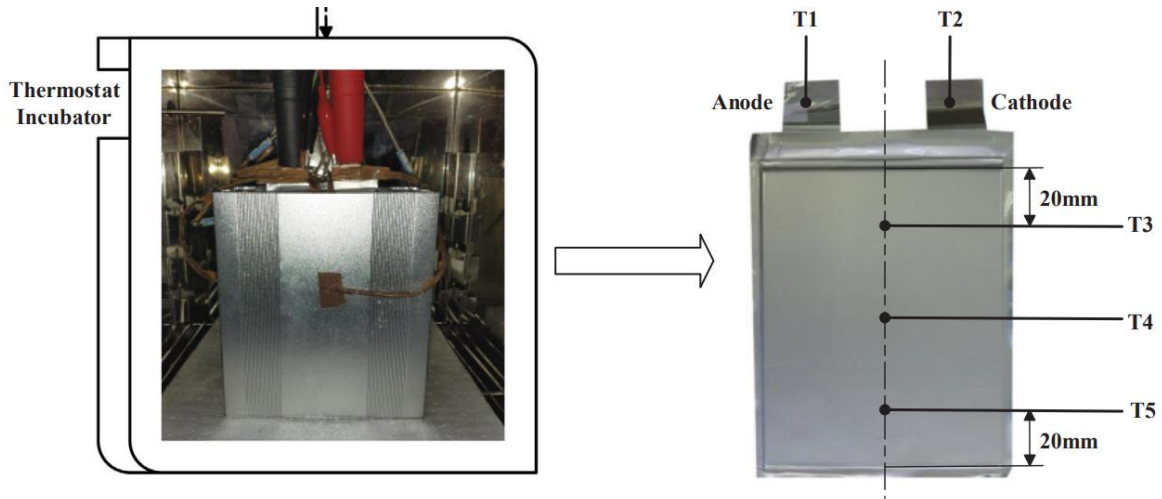


Figure 48 Sketch of the experimental system and thermocouples locations in single battery. [82]

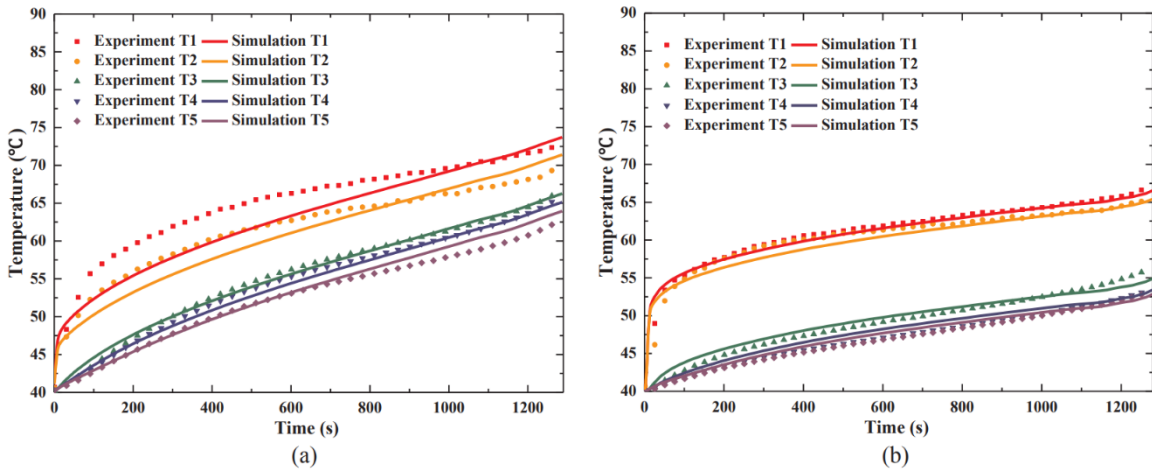


Figure 49 Comparisons of the inhomogeneous temperature contours and evolution history obtained from prediction and measure during 3C discharge under different thermal management modes: (a) natural convection, (b) heat sink without PCM. [82]

It is possible to notice the useful effect that the heat sinks generate on the temperature trend. The figures represent temperature curves obtained by attaching thermocouples to the pouch cell at the points indicated in **Figure 48**. A significant decrease of the battery surface temperature was observed from natural convection, using the heat dissipation materials. The temperature of T3 for natural convection was 66.4 °C, as shown in Fig. Comparatively, the temperature of T3 in the case of heat sink without PCM was 56.1 °C due to the improvement of the surface heat transfer capability, as indicated in **Figure 49** [82].

4.5.1.1 Heat sinks meshing

Moreover, in the development of the model consisting of the battery and fins, it was also necessary to adopt a "Multizone" mapping method, applied to all the components constituting the geometry. In order to obtain a mesh that had the best possible value of "Element Quality", it was necessary to opt for a resizing of the only area affected by heat sinks through the use of "Body Sizing" made available by the ANSYS tool.

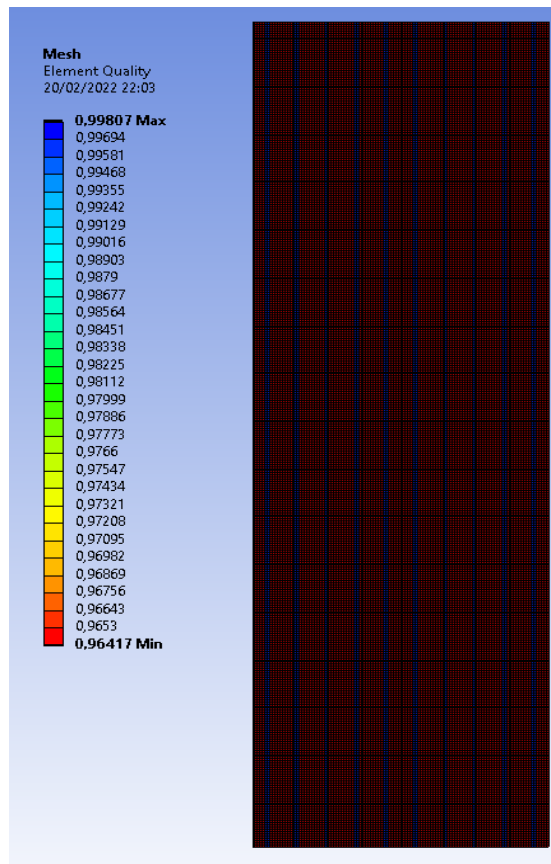


Figure 50 Element Quality” of the Heat Sinks.

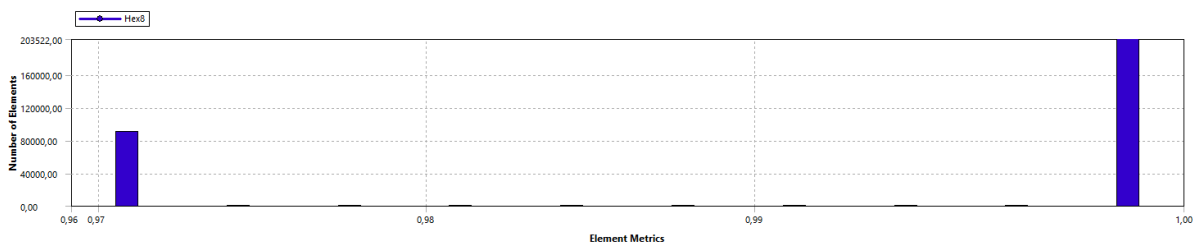


Figure 51 “Mesh Metric” of the Heat Sinks.

Unlike the case analysed for the individual battery, in this case it was necessary to identify new contact zones. As noticeable in **Table 6**, not all the surface of the battery is subject to natural convection, but there are areas in contact with the heat sinks that delegate convection to the latter. All this is demonstrated by the variation of the boundary conditions reported previously.

Element	“Named Selection” Solid	“Named Selection” Surface
Active Zone	Active_Zone	Wall-Active_zone_conv
Heat sink Front	Heat_Sink_Front	Wall-Heat_sink_Front_conv
Heat sink Rear	Heat_Sink_Rear	Wall-Heat_sink_Rear_conv

Table 6 “Named Selection” of the elements.

4.5.2 PCM

The main objective of this thesis paper is to analyse the effect that a passive cooling system has on the thermal behaviour of the lithium-ion cell. To observe the influence that the application of heat sinks has on this cooling system, it is useful to initially analyse the only effect of PCM applied to the body of the battery.

In **Figure 52** it is presented the geometry, realized through the "Design Modeler", which sees the application of the cooling material in the same position of application of the heat sinks. Therefore, the outer and lower sides of the cell, subject to the effect of natural convection, were left "free". **Table 7** shows the characteristic dimensions of the PCM blocks placed symmetrically on the battery with respect to its Y axis.

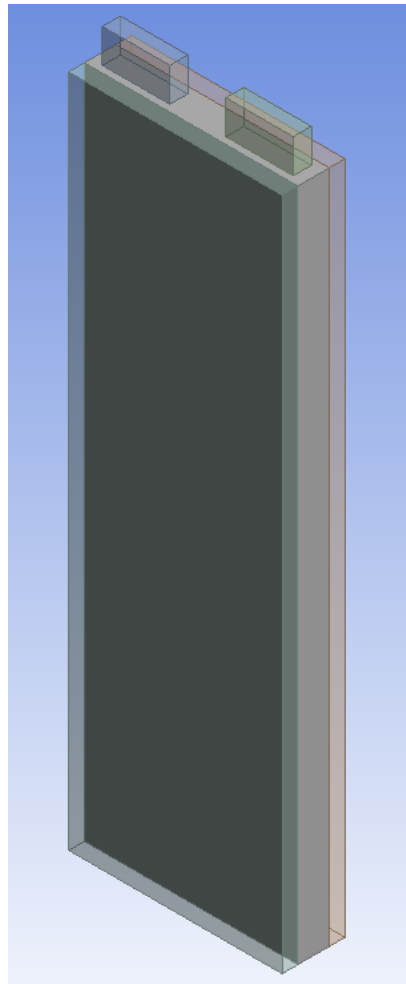


Figure 52 Battery with pure PCM geometry.

	Axial Directions		
Dimensions [mm]	X	Y	Z
PCM	95	300	7

Table 7 PCM geometric characteristics.

The choice of the thickness of the PCM was made because of the desire to demonstrate that the effect of the application of the phase change material only, can lead to a better useful effect than the application of the heat sinks only. In the following chapters, it will also be exposed the influence that the variation of the thickness of PCM leads to the cooling effect.

In **Figure 53** are shown the images, taken from the literature, which demonstrate what is the effect, of the application of the material to phase change, about the temperature trend of the battery. Immediately after an initial sharp increase in temperature, in the case with the application of pure PCM a ceiling of the curve is noted. This behaviour is given by the absorption of the latent heat of liquefaction of the material at phase change. During the phase passage, as is well known, PCM does not change its temperature, unless effects due to impurities contained in the material itself. Such impurities affect the constancy of the temperature of beginning and end liquefaction, but with a range that varies at more than about 2 °C: $T_{SOLIDUS}$ different from $T_{LIQUIDUS}$. If it were possible to obtain a material without processing "defects", it would result in a sharp flattening of the temperature curve due to the absorption of latent heat.

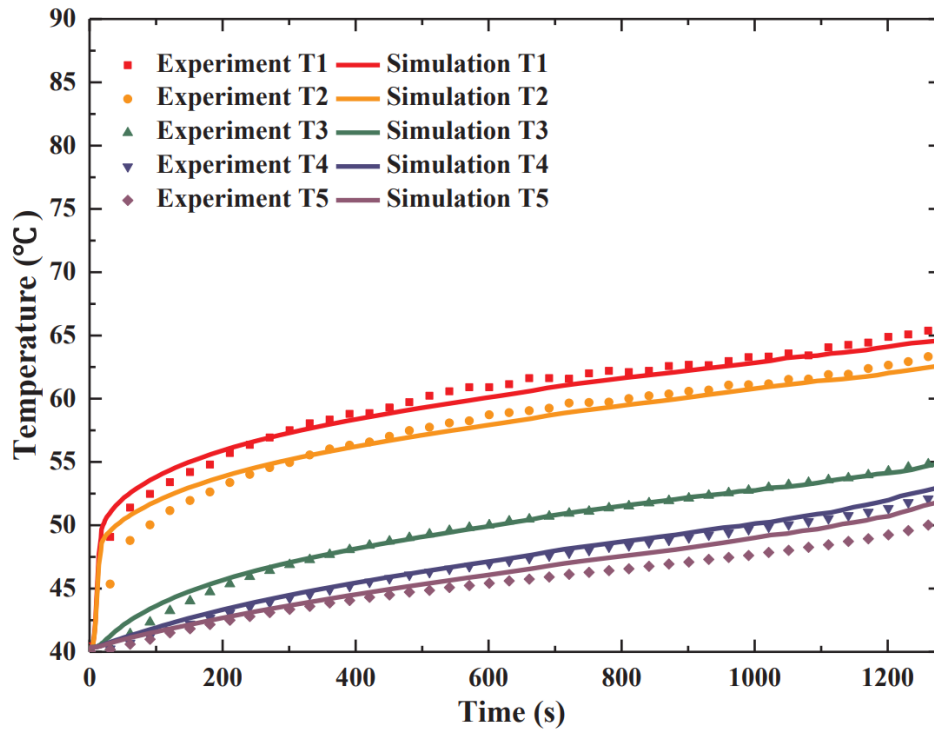


Figure 53 Comparisons of the inhomogeneous temperature contours and evolution history obtained from prediction and measure during 3C discharge under thermal management mode: pure PCM. [82]

Figure 53 shows that there is not a total flattening of the curve as this tends to grow with monotonous trend even after the application of the material. In any case, it is clearly visible that the inclination of the tangent to the curve is greatly reduced.

If the cooling effect is given by the latent heat of liquefaction [kJ/kg], then the greater the thickness of the material, the greater the effect that will be obtained by cooling. This is partly true and verifiable from the sensitivity analysis of the parameters that will be explained in **Chapter 5**.

4.5.2.1 PCM Meshing

As in the case of the application of heat sinks, also in this model it was necessary to define the contact regions between PCM and Active zones. The PCM is subject to cooling by natural convection, so the walls of the PCM not in contact with the battery have been declared as "PCM wall convection". Unlike the previous case, however, the very simple geometry of the material blocks permits to operate with a value of "Element Size" standardized for the entire geometry. It also guarantees an optimal value of "Element Quality" with a lower number of nodes and elements.

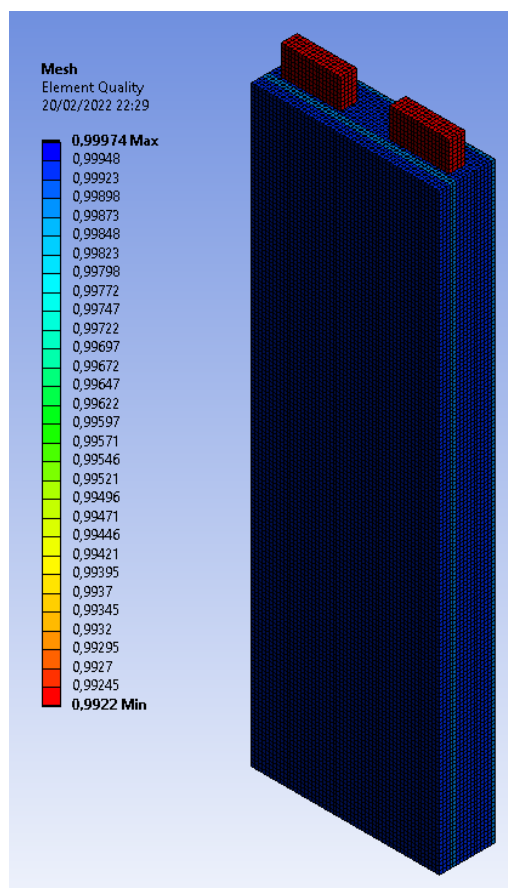


Figure 54 "Element Quality" of the Battery with Pure PCM

4.5.3 PCM with Heat Sinks

The **Section 2.8.3.3** of **Chapter 2** describes the methods to increase the efficiency of the passive cooling system. The most convenient, from the point of view of the simplicity of design, cost and implementation, is the one that involves the use of heat sinks to obtain an increase in the heat exchange surface.

In this case study it was decided to simulate, as a last step, a system that provides for a lithium-ion cell cooled with a combined system of PCM and heat sinks. In order to demonstrate the veracity of the effect that the increase of the exchange surface has on the thermal behaviour of the battery, it was decided to adopt a geometry that was the perfect combination of the two described above. In this way, leaving the characteristic dimensions of the components unchanged, the combined effect could be verified without any alteration of the results.

Figure 56 shows the geometry created by the "Design Modeler". For the same thickness, the proportion of the volume of PCM present in this case is reduced due to the presence of the fins.

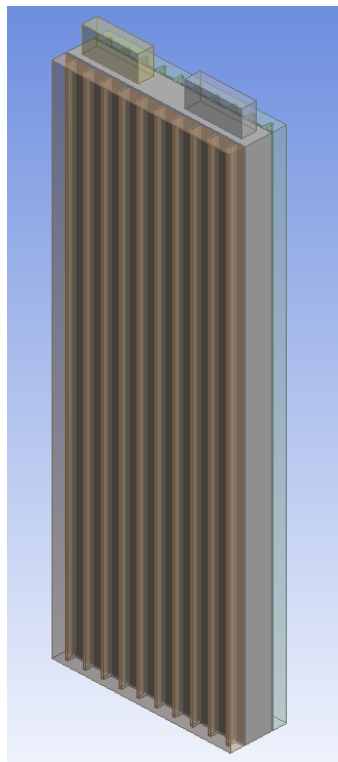


Figure 56 Battery with PCM and Heat Sinks geometry.

The results obtained from the simulation will be presented at a later stage in Chapter 5, for the time being, it will only be illustrated what is the effect that is expected to be obtained from the application of the combination of cooling systems. In **Figure 57** are presented the curves that represent the trend of temperature and liquid fraction for the two different application cases: pure PCM and PCM-Fin structure.

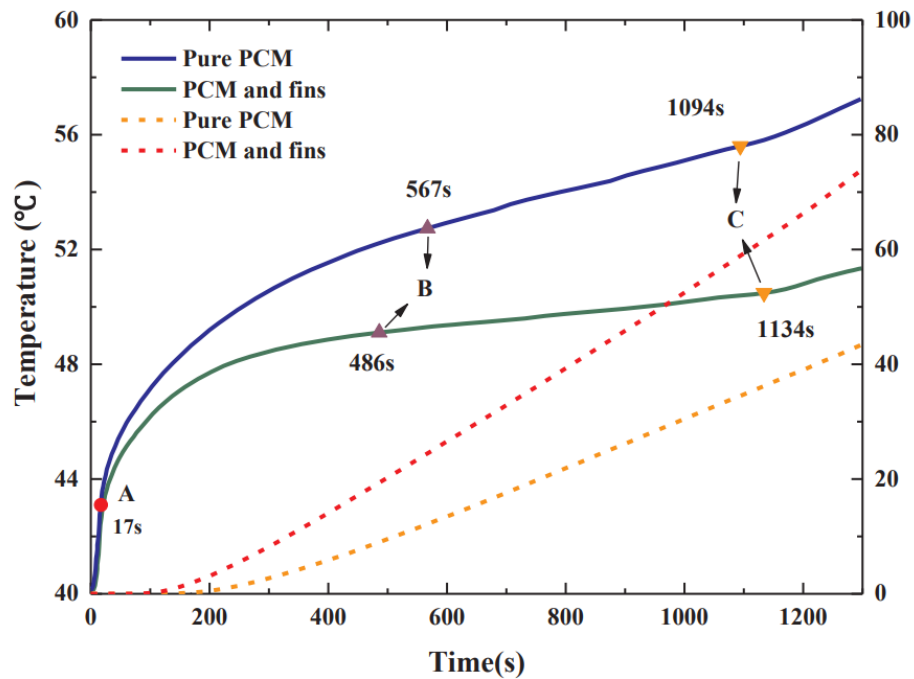


Figure 57 Evolution of T_{max} and PCM liquid fraction. [82]

In comparison with pure PCM, PCM-fin structure can enhance the heat exchange area of PCM by uniformly allocating straight fins into PCM, but it will decrease the volume of PCM between two baseplates. **Figure 57** shows the evolution of T_{max} and PCM liquid fraction under the cases of pure PCM and PCM-fin structure during 3C discharge. It is observed that T_{max} of PCM-fin structure was greatly reduced by attaching fins, while the liquid fraction of PCM eventually was 72.37%, nearly twice the value of the pure PCM case at the end of discharging. By examining the representative time points, Point A, B, and C were identified in the curve of T_{max} for the case of PCM-fin structure. It can be found that the time to reach Point A was the same in both cases as shown in **Figure 57**. The reason lies in that the edge of the PCM layer contacting with the aluminum baseplate firstly absorbed heat released by the batteries in the initial stage of discharge, such process is independent of the fin structure. The liquid fraction can be found as nearly zero at Point

A which was the same as the case of pure PCM. However, as T_{max} continued to exceed the minimum temperature of phase transition, the case of PCM-fin structure reduced the battery temperature ramp-up rate at the same discharge condition. The time of Point B was also advanced comparing to the pure PCM case. The reason is that the heat can be timely transferred into the deeper layers of PCM through the conduction of fins. The BC segment in which T_{max} grew linearly was almost forming the temperature plateau in the case of PCM-fin structure, whose temperature rise was merely $1.3\text{ }^{\circ}\text{C}$. The heat released by the batteries can be absorbed by the whole layers of PCM during the discharge, and the availability of latent heat is greatly augmented, when the exchange heat area is increased by the fins. Although the introduction of fins slightly reduces the PCM volume, the fins influence the thermal behaviour of PCM due to improved heat conduction and natural convection [82].

4.5.3.1 PCM with Heat Sinks meshing

Like the previous cases, the geometry mapping was done using the "Multizone" method. To obtain an optimal "Element Quality" value for the body of the fins, it was carried out an ad hoc "Body Sizing". All this was done with the purpose of optimizing the computational expenditure of the problem.

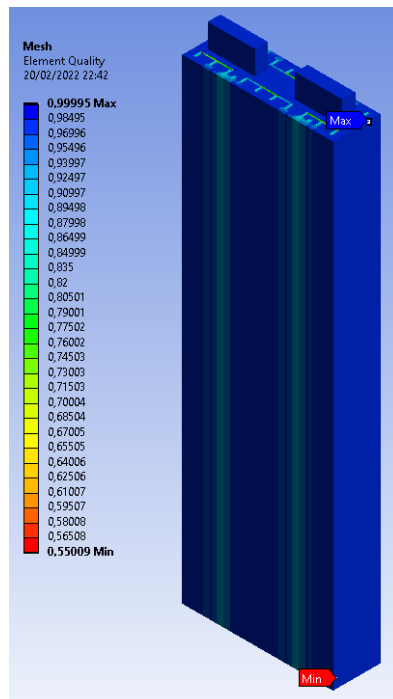


Figure 58 Element Quality” of the Battery with PCM and Heat Sinks.

Figure 58 shows the geometry mapping and the "Element Quality" distribution along the geometry.

In this case too, the lateral and lower walls of the cell are subject to natural convection. Below is the table with the identification of the contact regions in addition to the assignment of free convection conditions.

Element	“Named Selection” Solid	“Named Selection” Surface
Active Zone	Active_Zone	Wall-Active_zone_conv
Heat sink Front	Heat_Sink_Front	Wall-Heat_sink_Front_conv
Heat sink Rear	Heat_Sink_Rear	Wall-Heat_sink_Rear_conv
PCM Front	PCM_Front	Wall-PCM_Front_conv
PCM Rear	PCM_Rear	Wall-PCM_Rear_conv

Table 8 “Named Selection” of the elements.

4.6 Materials

Of significant importance is the assignment of thermophysical properties for the components that make up the geometry. In this section, then, the best techniques for assigning properties for the cell and the type of PCM will be studied.

4.6.1 Thermophysical Properties of the cell

As previously explained, in the present thesis it is analysed a lithium-ion cell that has a "pouch" structure. In **Figure 59** is presented a stratigraphy, representing the typical internal structure belonging to a pouch cell: alternating layers composed in order of aluminum bag, positive or negative electrode collector, positive or negative electrode material and finally a separator. The structure repeats itself throughout the development of the cell thickness by alternating the collector materials and positive and negative electrodes.

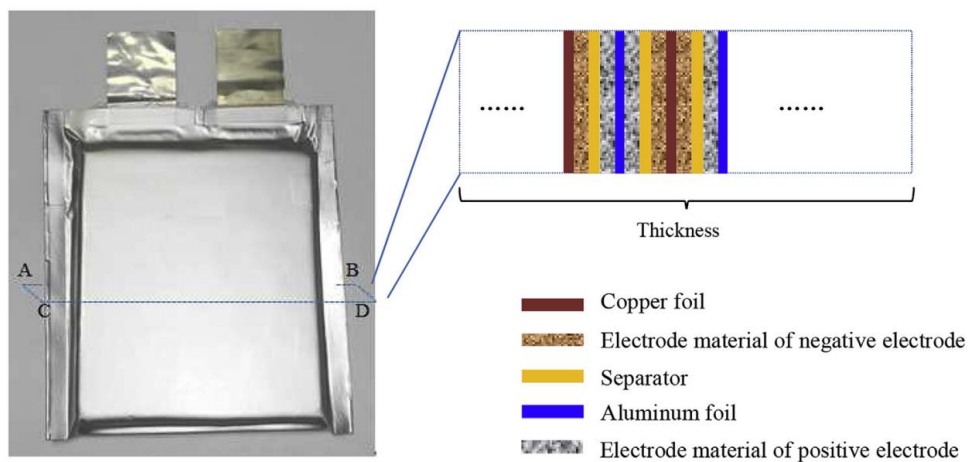


Figure 59 A sample 3.2 V/10 Ah LFP aluminum-laminated battery. [80]

The alternation of layers is not directly achievable on the geometry developed in the model; in fact, it can be noted that the active part of the cell is realized as a single block. The ANSYS FLUENT software makes available to the user the possibility to assign the thermo-physical parameters of a component by making them vary with the temperature change. An example could be the specific heat $C_p(T)$, which is clearly a parameter dependent on temperature change according to a polynomial function. In this case, however, it is useful to pursue the hypothesis that the thermo-physical parameters of the cell are invariant compared to temperature, as the variation of the latter over time

falls within the order of magnitude of tens of degrees. A different discussion will be conducted when it comes to the determination of parameters for the PCM.

Given this first hypothesis, it is useful to calculate in detail the thermal conductivity, density, specific heat and diffusivity of the cell. An incorrect interpretation of these parameters may lead to a simulation with results that do not conform to the experimental trend.

In the numerical analysis, these parameters are applied when the control volume is across the interface. The product value of density and heat capacity is calculated, based on the volume of each component as follows:

$$\rho C_p = \frac{\sum_i \rho_i C_{p,i} V_i}{\sum_i V_i} \quad (43)$$

where V denotes the volume of a specific component. The thermal conductivity at the interface should be determined based on connection between components and the contact resistance of the interface. Fortunately, the effect of contact resistance on the effective thermal conductivity is insignificant in this case, because most of the pores and gaps are filled with liquid electrolyte, and the thermal conductivity of the liquid electrolyte is comparable with that of the materials, such as the separator and the electrode, in the core region [80]

Since lithium-ion batteries are made up of multiple-layers of different materials which are divided by electrolyte, the heat conductivity coefficient of the battery is anisotropic. According to the basic principle of heat transfer, the heat transfer can be divided into heat transfers that are in parallel and in series. [83]

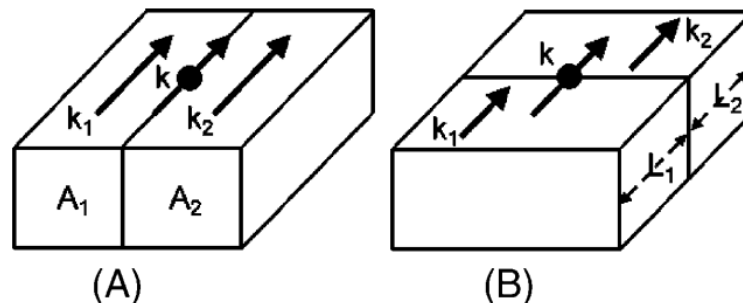


Figure 60 Schematic representation of the effective thermal conductivity at the interface. The elements are connected in (A) parallel; (B) series. [83]

The mean heat conductivity coefficient in parallel can be determined by **Equation 44** and that in series can be determined by **Equation 45**.

$$\lambda_x = \lambda_z = \frac{\lambda_p L_{x_p} + \lambda_n L_{x_n} + \lambda_s L_{x_s}}{L_y} \quad (44)$$

$$\lambda_y = \frac{L_y}{\frac{L_{x_p}}{\lambda_p} + \frac{L_{x_n}}{\lambda_n} + \frac{L_{x_s}}{\lambda_s}} \quad (45)$$

λ_x , λ_y and λ_z are the heat conductivity coefficients of the battery materials at the directions of x, y and z, respectively; L_p , L_n and L_s are, respectively, the anode slice, cathode slice and the heat conductivity coefficient of diagram inside the battery.

Because the control volume is extremely small in comparison with the volume of each component, adopting the above equations to estimate the physical properties works well. [83]

The UDS diffusivity is used by Ansys in the active area instead of the electric conductivity in order to consider both materials: the collector and the electrode. To calculate the values of uds0 and uds1 **Equation 46** was used. Where uds0 is the diffusivity of the positive side, σ is the electric conductivity, δ is the thickness and the subscripts c and e are for collector and electrode respectively. A similar equation was used to estimate uds1. [81]

$$UDS_0 = \frac{0.5\sigma_c^p \delta_c^p + 0.5\sigma_e^p \delta_e^p}{\delta_{total}} \quad (46)$$

All the formulations presented in this Section require the explicit knowledge of quantities such as volume and thickness of the individual layers constituting the geometry of the lithium ion NMC cell. Such accuracy in knowledge of cell data could not be obtained from the review done in the literature. Because of this objective lack of data, it was decided to assign to the active part of the cell a series of parameters taken from the literature. To choose a reference to follow, it was mainly considered the chemistry characterizing the positive electrode of the cell and the characteristic size of the cell. A careful analysis of the literature has led to the choice of the parameters that are presented in **Table 10**; taken from an experimental study based on the characterization of a lithium-

ion cell used in Heavy Duty Hybrid applications. The analysed cell is also with "pouch" structure. [87]

	Dimensions (WxHxT) [mm]	Weight [g]	Chemistry
Pouch cell	150x100x6.67	237	NMC

Table 9 Specification of the pouch cell used for the experiments. [87]

	Axial Directions		
	X	Y	Z
Thermal Conductivity [W/(mK)]	23	31.6	0.74
Specific Heat [J/(kgK)]	1091		
Density [kg/m³]	1930		

Table 10 Specification of the pouch cell used for the simulation. [87]

The most relevant data that led to the choice of this reference was battery chemistry (NMC), which is the most relevant data according to geometric characteristics. In the **Equations 44** and **45** (for the calculation of thermal conductivity) it is required the knowledge of the thickness of the individual layers of material, but these are determined in a general way according to the type of chemistry of the cell. Therefore, the overall thickness of the cell does not play a fundamental role in the calculation of these parameters. A different matter if the calculation of the product between density and specific heat of the cell is considered: the **Equation 43** requires the knowledge of the volume of the individual layers, which depends on the geometric characteristics of the layer itself. In this case it was necessary to make an approximation, accepting the difference between the data and the physical reality of the problem. However, the problem

is solved by re-adapting the parameters of the ECM model as explained in the **Section 4.4**.

The ANSYS FLUENT software allows the user to enter the thermal conductivity values in the form "Orthotropic" as presented in **Figure 61**.

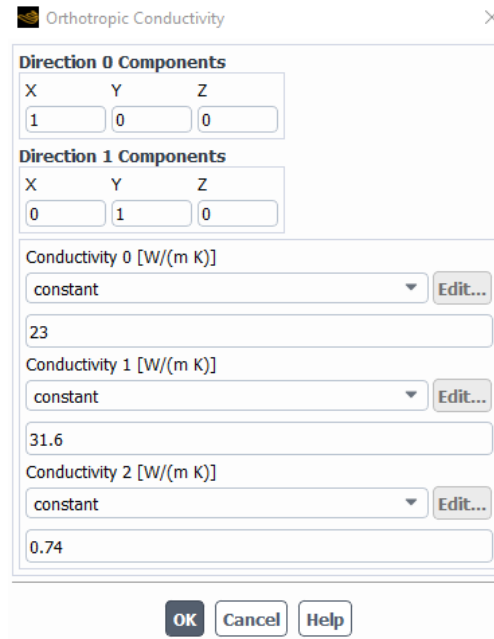


Figure 61 Orthotropic Conductivity.

In this way it is possible to distinguish the different values of conductivity in the three directions of space. Along directions X and Y, the values have a similar order of magnitude, while in the direction of the thickness Z there is a value with a smaller order of magnitude.

For the calculation of UDS diffusivity, the data taken from literature were considered: $119e04$ [S/m] for positive electrode and $983e03$ [S/m] for negative electrode. In this case too, it is possible to set the UDS Diffusivity according to the type of electrode.

4.6.2 Passive components materials

In addition to assigning the thermophysical properties of the active part, it is useful to assign the respective materials to the passive components of the geometry. In this case study, the "passive" components are the battery collecting tabs and the heat sinks. In the **Table 11** and **Table 12** are presented the thermophysical properties, obtained from the literature, of Aluminum (material of heat sinks) and Copper (material of Tabs).

Properties	Al Values
Thermal Conductivity [W/(mK)]	160
Specific Heat [J/(kgK)]	903
Density [kg/m³]	2700
Electrical Conductivity [S/m]	3.83e07

Table 11 Specification of the Al used for the simulation. [84]

Properties	Cu Values
Thermal Conductivity [W/(mK)]	400
Specific Heat [J/(kgK)]	385
Density [kg/m³]	8900
Electrical Conductivity [S/m]	Ansys User Defined Function

Table 12 Specification of the Al used for the simulation. [84]

4.6.3 PCM selection for the application

Properties like congruent melting, neglected super-cooling due to their self-nucleating ability and compatibility with other materials like container materials (corrosivity and possible reactions) are advantages of organic PCMS. As explained earlier, inorganic materials have a high latent heat of fusion, and their density is two times higher than organic materials. This property gives them the advantage of small volume and compactness, but incongruent melting and some corrosion and toxic properties make them unfavourable to use in sensitive cases like the current research. For instance, sodium hydroxide, as a salty hydrate PCM has a good thermal conductivity and less volume change, but it is very toxic and has corrosive properties. Therefore, it cannot be considered as a thermal storage material here [85]. For eutectics, the main part of their compound is inorganic materials which hold the same problems of inorganic materials in eutectics. In order to narrow down the selection, with respect to properties of PCMs, iso-paraffin is not applicable to this research, because these PCMs have the disadvantage of temperature variations during freezing. This is in contrast with the assumption that constant temperature is needed to have effective thermal management in battery. For non-paraffin materials, like fatty acid, their high costs, which can be as high as 2 times other PCMs is the main disadvantage of this group of organic materials comparing with paraffin organics. Characteristics such as incongruent melting, high latent heat of fusion, and no corrosivity lead to the selection of organic, paraffin wax PCM. The disadvantage of low thermal conductivity can be improved by certain methods like encapsulation or embedding the PCM inside a graphite matrix and other methods. By considering the operating temperature, the melting point of Eicosane is large to be used for cooling the Li-ion cells. From the same category, normal-Octadecane is selected for the current study. Its melting point is around 27.7 °C which makes it more suitable for the current application and for controlling the temperature and was selected to use for experiments.

A table showing the main values of the thermophysical properties of some phase change materials is shown in **Figure 62**.

Compound	Reference(s)	Melting temp. T_m (°C)	Heat of fusion, λ (kJ kg ⁻¹)	Specific heat capacity, C_p (kJ kg ⁻¹ K ⁻¹)	Thermal conductivity, k (W m ⁻¹ K ⁻¹)	Density, ρ (kg m ⁻³)
Water-ice	[66-70]	0	335	4.2	2.4 (liquid) 0.6	1000
GR25	[74]	23.2-24.1	45.3	1.2 (solid) 1.2 (liquid)	-	-
RT25-RT30	[72,73]	26.6	232.0	1.80 (liquid) 1.41 (solid)	0.18 (liquid) 0.19 (solid)	749 (liquid) 785 (solid)
n-Octadecane	[55,56,74-79]	27.7	243.5	2.66 (liquid) 2.14	0.148 (liquid) 0.190 (solid)	785 (liquid) 865 (solid)
CaCl ₂ ·6H ₂ O	[66,80,81]	29.9	187	2.2 (liquid) 1.4 (solid)	0.53 (liquid) 1.09 (solid)	1530 (liquid) 1710 (solid)
Rubitherm RT	[37]	-	-	-	-	-
Na ₂ SO ₄ ·10H ₂ O	[50,80,81]	32, 39	180	2.0 (liquid) 2.0 (solid)	0.15 (liquid) 0.3 (solid)	1460 (solid)
Paraffin wax	[72,80,81]	32-32.1	251	1.92(solid) 3.26(liquid)	0.514 (solid) 0.224 (liquid)	830
Capric acid	[82,83]	32	152.7	-	0.153 (liquid)	878 (liquid) 1004 (solid)
Polyethylene glycol 900 (PEG900)	[84]	34	150.5	2.26 (liquid) 2.26 (solid)	0.188 (liquid) 0.188 (solid)	1100 (liquid) 1200 (solid)
Lauric-palmitic acid (69:31) eutectic	[85]	35.2	166.3	2.41 (liquid) 1.77 (solid)	-	-
Lauric acid	[82,85-87]	41-43	211.6	2.27(liquid) 1.76(solid)	1.6	1.76(solid) 0.862 (liquid)
Stearic acid	[61,87-89]	41-43 (67-69)*	211.6	2.27 (liquid) 1.76 (solid)	1.60 (solid)	862 (liquid) 1007 (solid)
Medicinal paraffin	[60]	40-44	146	2.3 (liquid) 2.2 (solid)	2.1 (liquid) 0.5 (solid)	830 (solid)
Paraffin wax	[90]	40-53	-	-	-	-
P116-Wax	[55,60,80,81]	46.7-50	209	2.89 (liquid) 2.89 (solid)	0.277 (liquid) 0.140 (solid)	786 (solid)
Merck P56-58	[53]	48.86-58.06	250	2.37 (liquid) 1.84 (solid)	-	-
Commercial paraffin wax	[94]	52.1	243.5	-	0.15	809.5 (solid) 771 (liquid)
Myristic acid	[35,58,95]	52.2	182.6	-	-	-
Paraffin RT60/RT58	[93,94]	55 to 60	214.4-232	0.9	0.2	775 (liquid) 850 (solid)
Palmitic acid	[83,85,87,89,92,95]	57.8-61.8	185.4	-	0.162 (liquid)	850 (liquid) 889 (solid)
Mg(NO ₃) ₂ ·6H ₂ O	[71,88]	89	162.8	-	0.490 (liquid) 0.611 (solid)	1550 (liquid) 1636 (solid)
RT100	[96]	99	168	2.4 (liquid) 1.8 (solid)	0.2 (liquid) 0.2 (solid)	770 (liquid) 940 (solid)
MgCl ₂ ·6H ₂ O	[71,97]	116.7	168.6	2.61 (liquid) 2.25 (solid)	0.570 (liquid) 0.704 (solid)	1450 (liquid) 1570 (solid)
Erythritol	[50,98-100]	117.7	339.8	2.61(liquid) 2.25(solid)	0.326 (liquid) 0.733 (solid)	1300 (liquid) 1480 (solid)
Na/K/NO ₃ (0.5/0.5)	[54,65]	220	100.7	1.35	0.56	1920
ZnCl ₂ /KCl (0.319/0.681)	[54,65]	235	198	-	0.8	2480
NaNO ₃	[54,65]	310	172	1.82	0.5	2260
KNO ₃	[54,65]	330	266	1.22	0.5	2110
NaOH	[54,65]	318	165	2.08	0.92	2100
KOH	[54,65]	380	149.7	1.47	0.5	2044
ZnCl ₂	[54,65]	280	75	0.74	0.5	2907
LiF-CaF ₂ (80.5:19.5) mixture	[101]	767	816	1770 (liquid) 1.770 (liquid)	1.70 (liquid) 3.8 (solid)	2390 (liquid) 2390 (solid)

- Not available.

Figure 62 Thermophysical properties of PCMs investigated for different applications. [86]

A paraffin was chosen because of the reasons given above. In **Figure 63** are listed the main types of paraffins and the normal-Octadecane is the best for this thesis work given the operating range of the liquefaction temperature.

	C number	ρ	T_m	h_m	E_{vol}	Price (Min)	Price (Max)
n-Tetradecane	14	764	5.5	228	48.39	8.27	10.33
n-Pentadecane	15	769	10	205	43.79	9.13	11.42
n-Hexadecane	16	770	16.7	237.1	50.71	7.89	9.86
n-Heptadecane	17	777	21.7	213	45.97	8.70	10.88
n-Octadecane	18	777	28	244	52.66	7.60	9.49
n-Nonadecane	19	786	32	222	48.47	8.25	10.32
n-Eicosane	20	792	36.7	246	54.12	7.39	9.24
n-Henicosane	21	792	40.2	200	44.00	9.09	11.36
n-Docosane	22	794	44	249	54.92	7.28	9.10
n-Tricosane	23	797	47.5	232	51.36	7.79	9.73
n-Tetracosane	24	799	50.6	255	56.60	7.07	8.83
n-Pentacosane	25	812	49.4	238	53.68	7.45	9.31
n-Hexacosane	26	803	56.3	256	57.10	7.00	8.76
n-Heptacosane	27	802	58.8	236	52.58	7.61	9.51
n-Octacosane	28	807	61.6	253	56.71	7.05	8.82

Units: Melting Temperature T_m (°C), Specific Latent Heat h_m (kJ/kg), Density ρ (kg/m³), Energy Density E_{vol} (kWh/m³), Price (£/kWh)

Figure 63 Paraffins properties. [29]

4.6.3.1 PCM parameters

For the phase change materials region, the thermo-physical properties of PCM are dependent on the state of PCM. Thereinto, the specific heat capacity (C_p) of PCM can be described as follows [82]

$$\begin{aligned}
 C_p &= C_{PCMS} & T_{PCM} &\leq T_S \text{ (solid phase)} \\
 C_p &= (1 - \theta)C_{PCMS} + \theta C_{PCML} + \frac{L_{PCM}}{T_L - T_S} & T_S &< T_{PCM} < T_L \text{ (solid - liquid phase)} \\
 C_p &= C_{PCML} & T_{PCM} &\geq T_L \text{ (solid phase)}
 \end{aligned} \tag{47}$$

where C_{PCMS} , C_{PCML} and L_{PCM} are heat capacity of solid PCM, heat capacity of liquid PCM and latent heat of PCM. T_{PCM} , T_S and T_L respectively stand for the temperature of PCM, the initial temperature of phase transition and the end temperature of phase transition. θ represents the volume fraction of liquid PCM, which is described as follows:

$$\theta = \frac{T_{PCM} - T_S}{T_L - T_S} \tag{48}$$

Considering the operating temperature of the cycle, the organic normal Octadecane is selected. Solidus and liquidus temperatures also depend on the materials purity. Based on the literature review, the considered values for n-Octadecane are:

$$T_{liquidus} = 303.15K \text{ and } T_{solidus} = 301.15K.$$

The thermal conductivity and density in the Mushy Phase are defined as follows [88]:

$$k = \frac{k_S + k_L}{2} \tag{49}$$

$$\rho = \frac{\rho_S + \rho_L}{2} \tag{50}$$

dynamic viscosity value was derived from the literature under conditions of 0.1 MPa at a temperature of 323.15 K and corresponds to $2.460 \text{ mMPa} \cdot \text{s}$ [89].

In ANSYS FLUENT, there is an option to enter input data as discrete numbers. Thus, once the variations of the considered property are known, the values can be entered to the software. In the piecewise polynomial option, which is available in the software, the abrupt increase of properties can lead to divergence. (For example, specific heat has a very low value, namely, 2150 J/kgK for solid phase and at phase change stage, roars to a very large number of 114640 J/kgK. This step-wise behaviour may cause instability in the simulation which should be noticed).

The "piecewise polynomial" function was also used to implement the variation of dynamic viscosity, density and thermal conductivity as a function of temperature. **Figure 64** shows the effect of the step function on the specific heat flow.

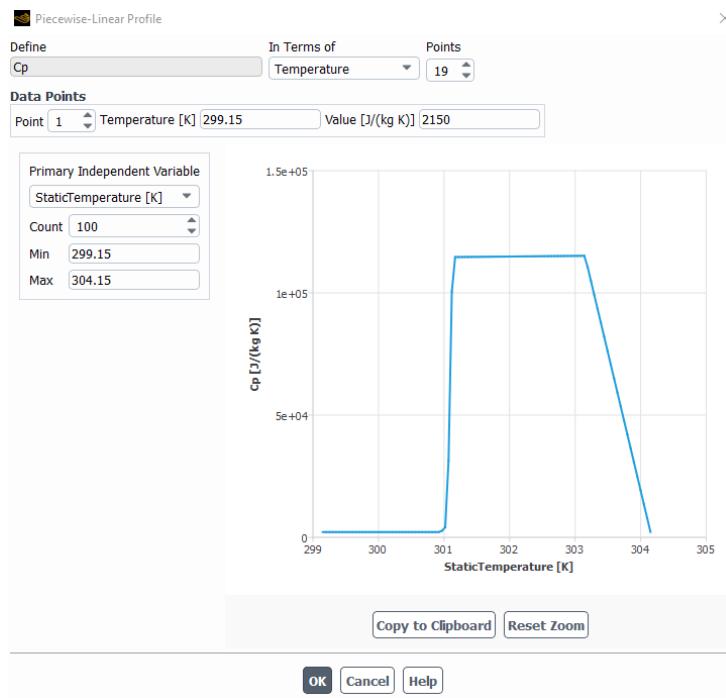


Figure 64 Piecewise-Linear Profile of Specific Heat

For the present treatment, it was decided to divide the temperature range in which PCM operates into 19 segments. The results obtained by applying the Equations for the calculation of specific heat, density, thermal conductivity and dynamic viscosity are reported in **Table 13**.

T [K]	Thermal Conductivity [W/mK]	Density [kg/m³]	Viscosity [mPa*s]	Specific Heat [J/kgK]
299.15	0.385	814	1	2150
300.15	0.385	814	1	2150
300.65	0.385	814	1	2150
300.95	0.385	814	1	2150
301.05	0.385	814	1	5000
301.13	0.385	814	1	114640
301.15	0.255	769	0.025	114640
301.2	0.255	769	0.025	114653
301.25	0.255	769	0.025	114666
301.35	0.255	769	0.025	114692
301.55	0.255	769	0.025	114744
301.75	0.255	769	0.025	114796
301.95	0.255	769	0.025	114848
302.05	0.255	769	0.025	114874
302.25	0.255	769	0.025	114926
302.35	0.255	769	0.025	114952
302.95	0.255	769	0.025	115108
303.15	0.152	724	0.00246	115160
304.15	0.152	724	0.00246	2140

Table 13 PCM Thermophysical properties.

Normal-Octadecane as the selected PCM for this research can be found in two categories: Technical grade and pure PCM. In the literature, latent heat of fusion for this material is considered 225 kJ/kg.

4.7 Boundary Conditions

The next step of the CFD analysis is the setting of thermal boundary conditions for the cell walls and terminal surfaces. An example of the procedure to be followed for assigning boundary conditions is presented below. In particular, it is analysed the simplest case of the model for the single cell. The walls of the active part and of the Tabs are lapped by air and, having neglected the term radiative, the only boundary condition that is considered is the convective one.

The next step is to select the outer surface of the cell indicated by the named-selection "wall-active_zone". Within the zone name "wall-active_zone" the Thermal tab has been selected and natural convection has been set as the boundary condition (**Figure 65**). The necessary parameters for natural convection are the convective thermal exchange coefficient, h (W/m²K), and the temperature of the outside air, T (K). Same procedure is performed for the walls of collecting Tab.

The heat transfer coefficient was set to 10 W/(m²K), while the free stream temperature was set to 298 K. The convective heat transfer coefficient was evaluated according to the typical operating conditions that are present in climatic chambers where the cells are tested. A fan is typically adopted to recirculate the air and keep the temperature constant; the typical values of the flow velocity were used to assess the aforementioned values of the heat transfer coefficient [81].

The application of boundary conditions in all other case studies follows the procedure just explained, with the difference that the walls involved vary from case to case and are declared as seen in the Meshing section (for example "Heat Sinks wall convection")

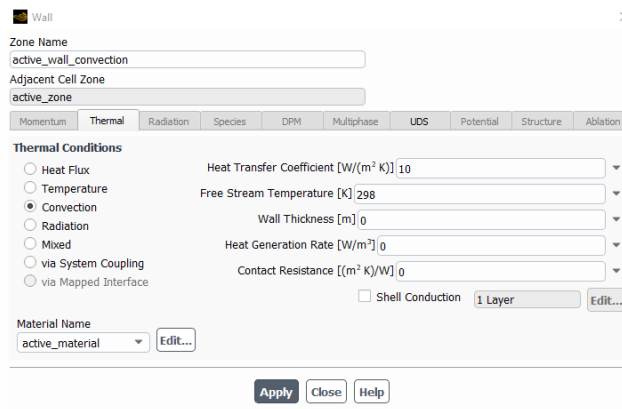


Figure 65 "Active_wall_convection" ANSYS.

4.8 Solution

The SIMPLE scheme was selected as solution method. The initial temperature was set to 298 K. A fixed time stepping method was used under run calculation. Time step size was defined 0,6 s and the number of time steps were determined based on the different C-rates till the complete discharge of the cell. Convergence criteria was set to absolute with a residual threshold equal to 10^{-6} for all the monitored calculation variables (energy, uds0 and uds1 equations). The temperatures were registered at different cell positions, as shown in **Figure 66**, in order to correspond to the temperatures measured during the test campaign. As mentioned in the introductory section of this chapter, the resolution of the equations by the software is limited only to energy equations, uds0 and uds1 because, to lighten the computational expenditure, it was decided not to solve the equations of turbulence and flow (as regards the PCM study).

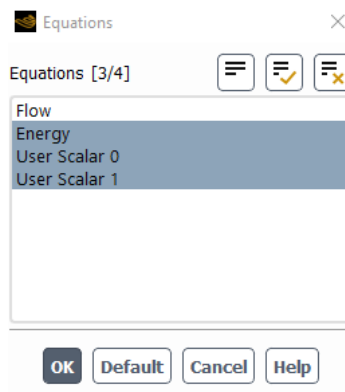


Figure 67 Equations solved in ANSYS.



Figure 66 Positions of the temperature sensors on the cell (frontside and backside, up and down respectively). [81]

4.9 Contact resistance

In the section "Mesh interface" the contact regions concerned were highlighted and, in particular, those that concern the contact between active zone and collecting Tab. It operates with a contact type "Coupled" to ensure temperature continuity.

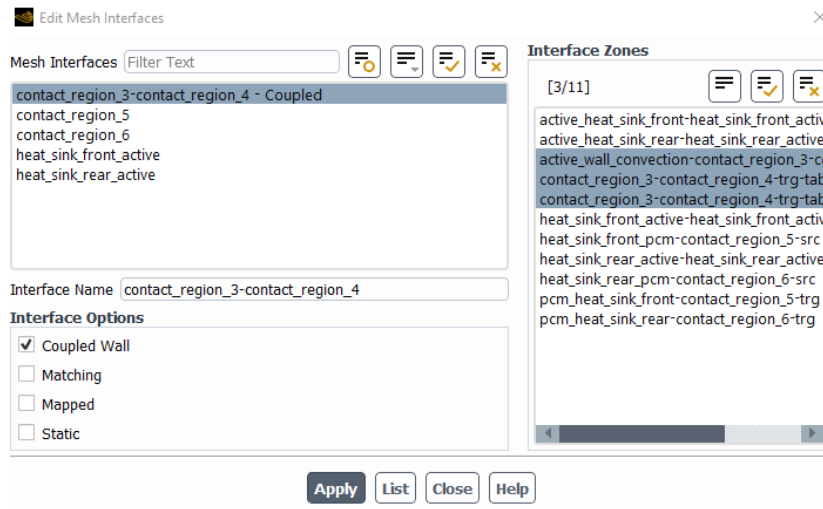


Figure 68 "Coupled wall" in Mesh Interfaces.

The electrical contact resistance between the battery tab and the leading cable is generally ignored in the literature. The contact resistance was an adjustable variable to provide the best agreement between the simulated and the measured temperatures. The adjusted contact resistance was a comparable value with the tab resistance, which indicates the heating effect of the contact resistance cannot be ignored [91].

The heat generation rate in the current collecting tabs owing to ohmic and electrical contact resistances, q , can be obtained from the following expression: [90]

$$q = (r + r_c)i^2 \quad (51)$$

where r is the resistivity ($\Omega \text{ m}$) of the current collecting tab, r_c is the resistivity ($\Omega \text{ m}$) of the electrical contact between the current collecting tab and the lead wire connecting the battery cell and the external cycler, and i is the current density with respect to the cross sectional area of the current collecting tab (A m^{-2}). One note when using **Eq. 51** is that the nonzero value of r_c is given only to the edge of the current collecting tab that is in contact with the lead wire; otherwise, the value of r_c would be zero and the heat

generation rate in the current collecting tabs would only have contributions from ohmic resistance. **Table 14** shows contact resistance values from the literature.

Parameter (unit)	Electrode	Value
r [Ω m]	Positive	2.8e-08
	Negative	1.7e-08
r_c [Ω m]	Positive	1.6e-07
	Negative	4.1e-08

Table 14 Meters related to the heating of current collecting tabs.

The ANSYS software allows the user to insert contact resistors in the section of the MSMD Battery Model. It is specified that, in this case study, the only value that is assigned is r_c because of the contact between tab and the active part. The contact resistances are declared with a different unit of measurement (Ω m²) compared to the literature.

In order to overcome this difference, it was decided to adapt the values derived from the literature to the current units of measurement. In the transition from Ω *m to Ω *m² the original value multiplied by the characteristic length of the Tabs (expressed in mm). As is logical to expect, a substantial variation in the order of magnitude of the resistances has been achieved. In **Table 15**, the contact resistance values for this case study are presented. The contact resistance value of the positive Tab is about an order of magnitude greater than that of the negative Tab; this leads to expect a greater warming of that region as presented in **Figure 70**

Parameter (unit)	Electrode	Value
r_c [Ω m]	Positive	2.6e-09
	Negative	4.8e-10

Table 15 Parameters related to the heating of current collecting tabs.

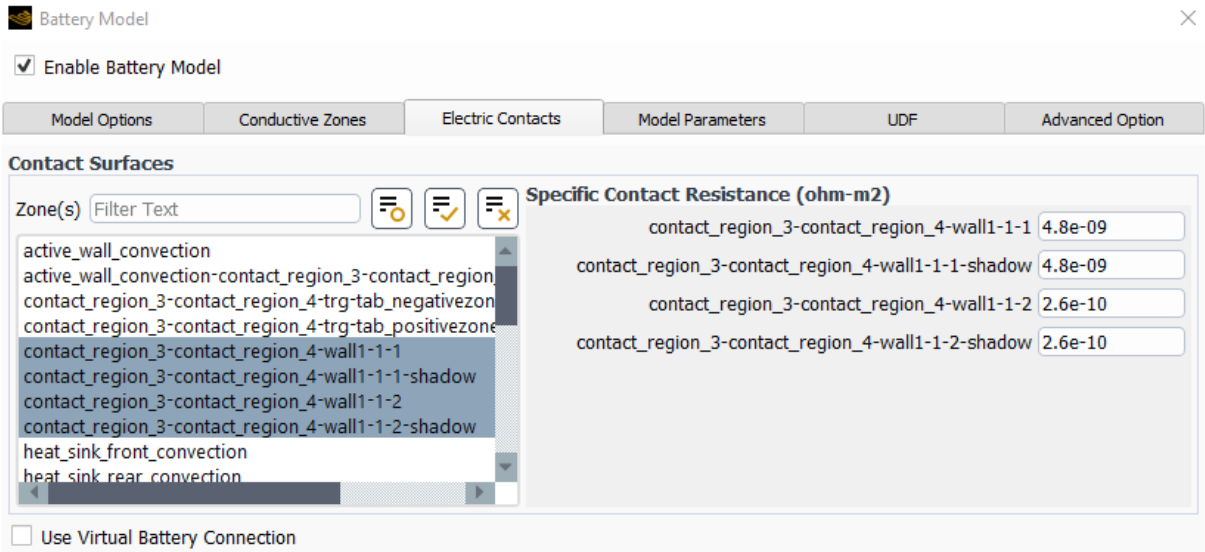


Figure 69 Electric contacts resistance.

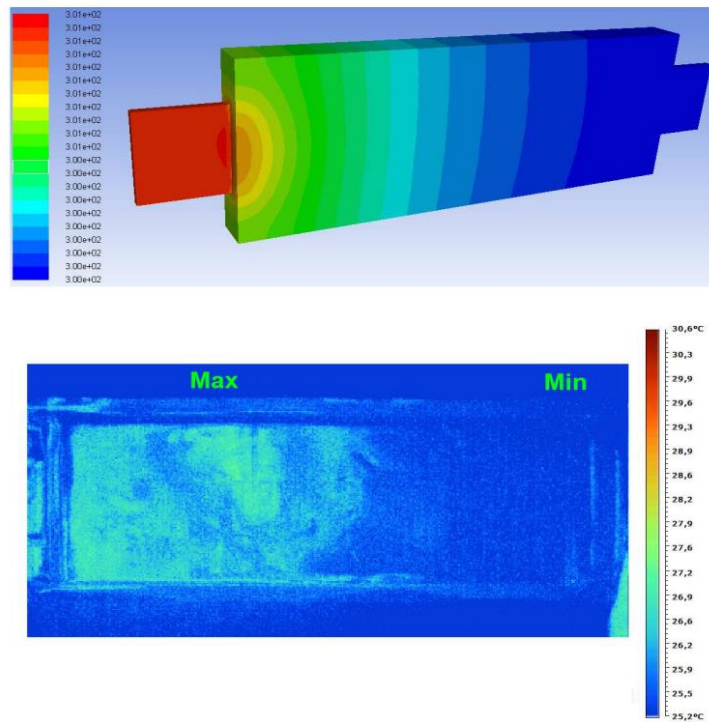


Figure 70 Comparison the temperature field (real measured and simulated).

4.10 Battery Pack

The last section of this chapter concerns the generation of the battery pack study. The configuration adopted is a 1P3S that simply provides three batteries connected in series. A series cell arrangement ensures a voltage of the entire module equal to the sum of the nominal voltage of the individual cells. The configuration type is not inspired by real applications because, in this case, it has been designed for the sole purpose of demonstrating the effect of sensitivity analysis on the thermal behaviour of cells.

All input for model generation, which has been explained in the previous paragraphs, remains valid. For this reason, in this section, it is shown only the generation of the geometry as well as the study of the mesh of a single case.

The geometry of the simplest case analysed, concerns a pattern of three batteries arranged in an equally spaced series of 4 mm. All the walls have natural convection as the only cooling system. Unlike the case with a single cell, in **Figure 71** it is noticeable the presence of elements of connection between the Tabs: such elements are defined "Busbar". In a series connection the busbars connect a negative Tab to a positive Tab alternately. As shown in **Figure 71**, the first link concerns the negative Tab of cell 1 with the positive Tab of cell 2, The second link concerns the negative Tab of cell 2 with the positive Tab of cell 3. The material with which the busbars are made is the same used for Tab, or Copper (Cu).

4.10.1 Battery Pack Geometry

Below is the **Figure 72** representing the battery pack with the presence of the PCM. Unlike the previous case, it is also clear the presence of an "Aluminum Case" that acts as a container for the sealing of the material at phase change at the time of liquefaction. The thickness of the case is 1.5 mm, while the thickness of the PCM is 8 mm. The choice of such thickness has been made in an arbitrary way with the scope to verify in phase of sensitivity analysis which is the better configuration.

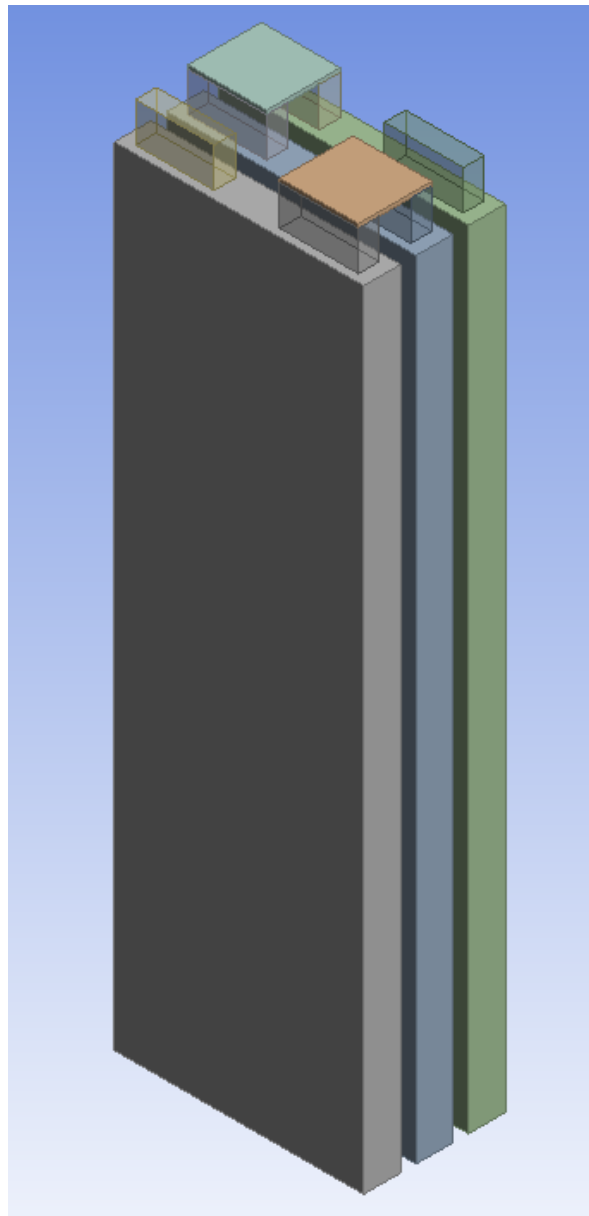


Figure 71 Battery Pack geometry.

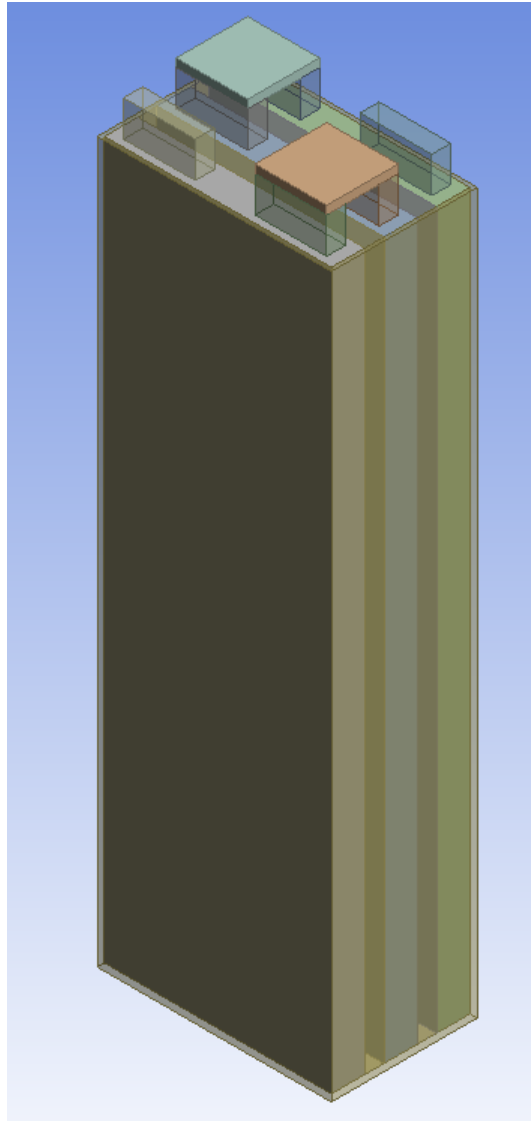


Figure 72 Battery Pack with PCM geometry.

Last step concerns the generation of module geometry with the addition of heat sinks. In **Figure 73** the structure of the heat sinks is presented, which is different from the case study of the single cell: the heat sinks are connected both sides of the plates. The length of the heat sinks extends throughout the thickness of the material at phase change.

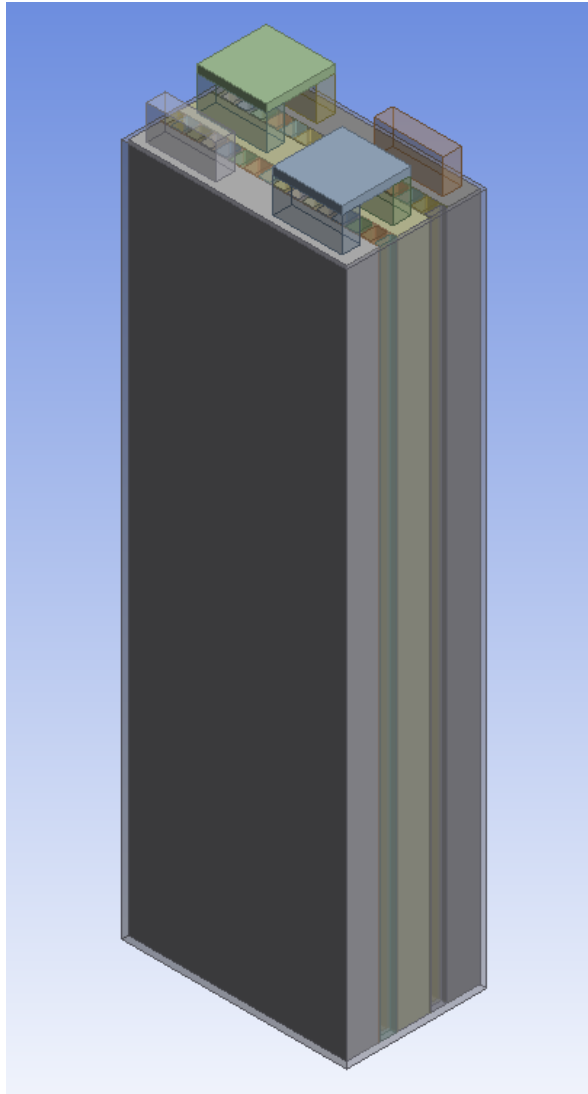


Figure 73 Battery Pack with PCM and Heat sinks geometry.

4.10.2 Battery pack Meshing

As mentioned above, also in the case of the battery pack a "Multizone" method is used for the realization of the mapping. In order to obtain an acceptable "Element Quality" value, a "Body Sizing" of the body of the fins has been performed because the complex geometry requires an accurate study of the dimension of the elements.

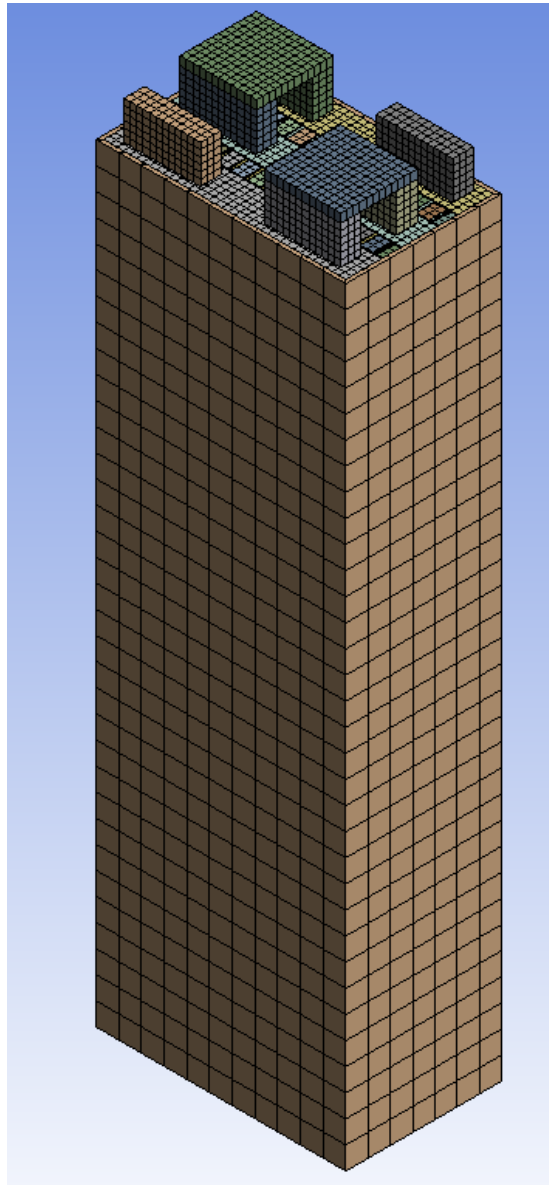


Figure 74 Battery Pack with PCM and Heat sinks Mesh.

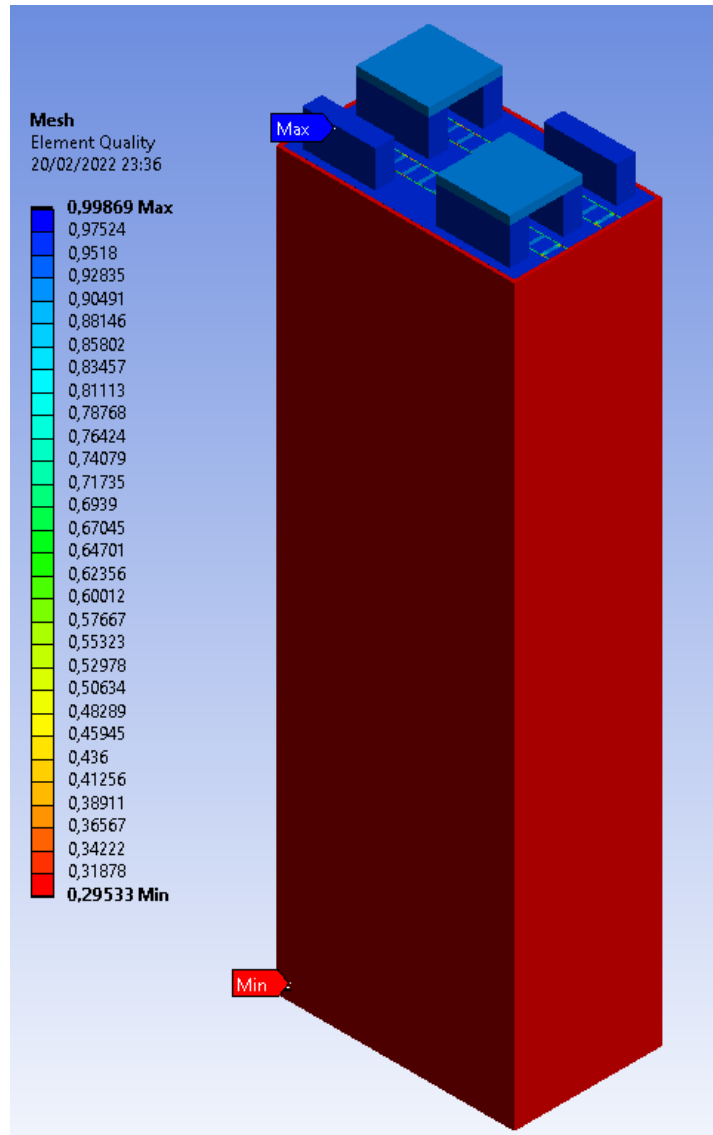


Figure 75 Battery Pack with PCM and Heat sinks “Element Quality”.

Chapter 5 Results and Discussion

In **Chapter 4**, the development of the numerical model for the lithium-ion cell was presented. This chapter will present the results obtained from the transient analysis for the battery and all the cooling systems previously presented. In particular, the first part of the Chapter will be discussed the validation of the numerical model based on the comparison with the experimental data. The effects of the variation of the discharge current (n-C Rate) and the operating temperature on the ECM parameters will then be analysed. The identification of the so-called "hot spots" justifies the need to adopt functional cooling systems to avoid the generation of catastrophic events such as the Thermal Runaway. In addition, the results of the thermal behaviour of the battery subject to cooling systems will be presented with particular attention to the comparison between the latter. In the final part, however, the transient behaviour of the battery pack is analysed with the related sensitivity analysis on parameters such as the thickness of the PCM layer, the thickness of the fins and spacing of the latter.

5.1 Model Validation

The validation process consists of the comparison between the data obtained at the experimental level and those obtained from the numerical model through CFD simulation. In this thesis, a comparative analysis of the temperature and voltage trend of the single cell has been conducted. To carry out this task, reference was made to the temperature trend of two characteristic points of the cell: the central part of the surface and the area adjacent to the positive tab, as shown in **Figure 76**. As regards the voltage trend, was taken as a reference the average trend of the active part of the cell. Specifically, the analysis was conducted with a discharge current of 1-C at a T_0 temperature of 25 °C (temperature of the external environment and of all the components of the battery being initialized).

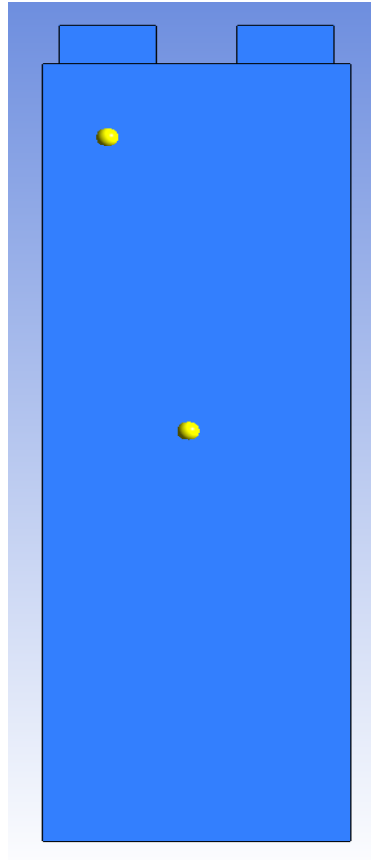


Figure 76 Identification of measuring points.

The results of the experimental analysis are reported in **Figure 77** and **Figure 78** and are taken from the literature [81]. The experimental voltage curve, referred to in this study, is the one coloured in blue. The temperature curves representing the thermal behaviour of the cell are those declared as "center measured" and "corner measured". The graphs are developed as a function of the discharge time (in this case 3600 s).

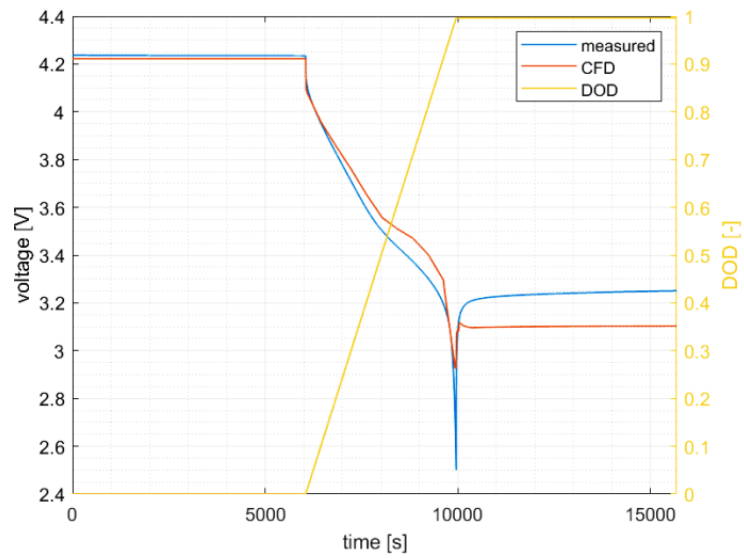


Figure 77 Voltage comparison @25°C and 1 C-rate.

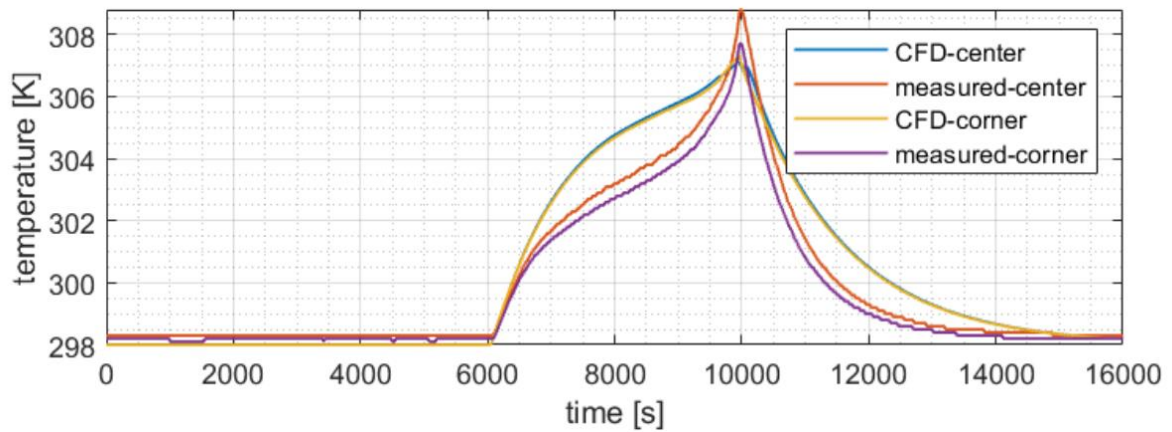


Figure 78 Temperature comparison @25°C and 1 C-rate.

As mentioned in **Chapter 4**, for the realization of the numerical model, reference was made to the ECM model, developed by Chen among others, adapting these parameters to the present case study. For the implementation on the ANSYS software, please refer to the reading of the **Section 4.4.1**. In this paragraph, a **Table 16** with all the parameters used is presented.

V_{OC}	f_0	f_1	f_2	f_3	f_4	f_5
	3.685	-0.16	-0.2	0.925	-0.93	10.5
R_S	a_0	a_1	a_2	-	-	-
	0.032	0.157	10.5	-	-	-
R_1	b_0	b_1	b_2	-	-	-
	0.038	0.235	14.6	-	-	-
C_1	c_0	c_1	c_2	-	-	-
	703.6	-651.6	21.5	-	-	-
R_2	d_0	d_1	d_2	-	-	-
	0.013	0.338	12.5	-	-	-
C_2	e_0	e_1	e_2	-	-	-
	4475	-6056	28.4	-	-	-

Table 16 ECM Parameters in ANSYS FLUENT.

The following Figures represent the comparison between the experimental and the simulation data.

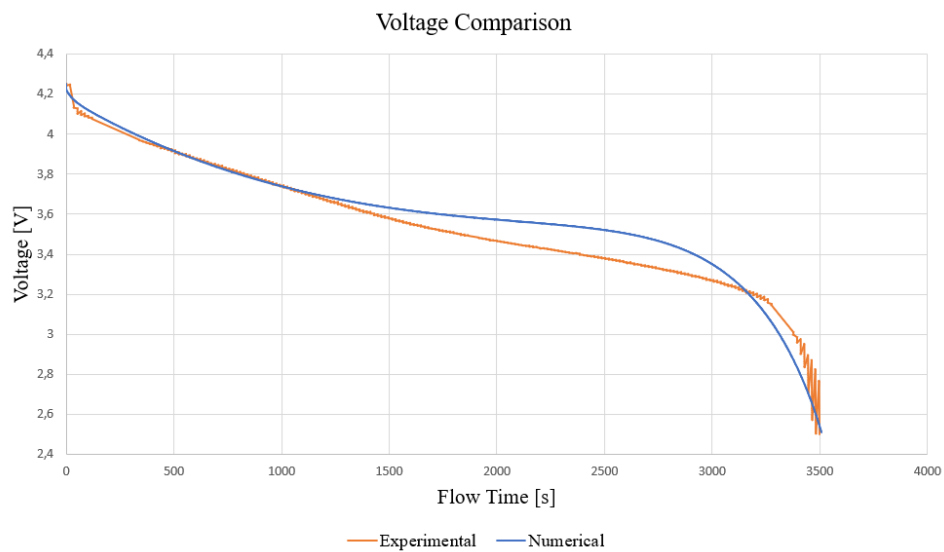


Figure 79 Voltage Comparison @25°C and 1C Rate.

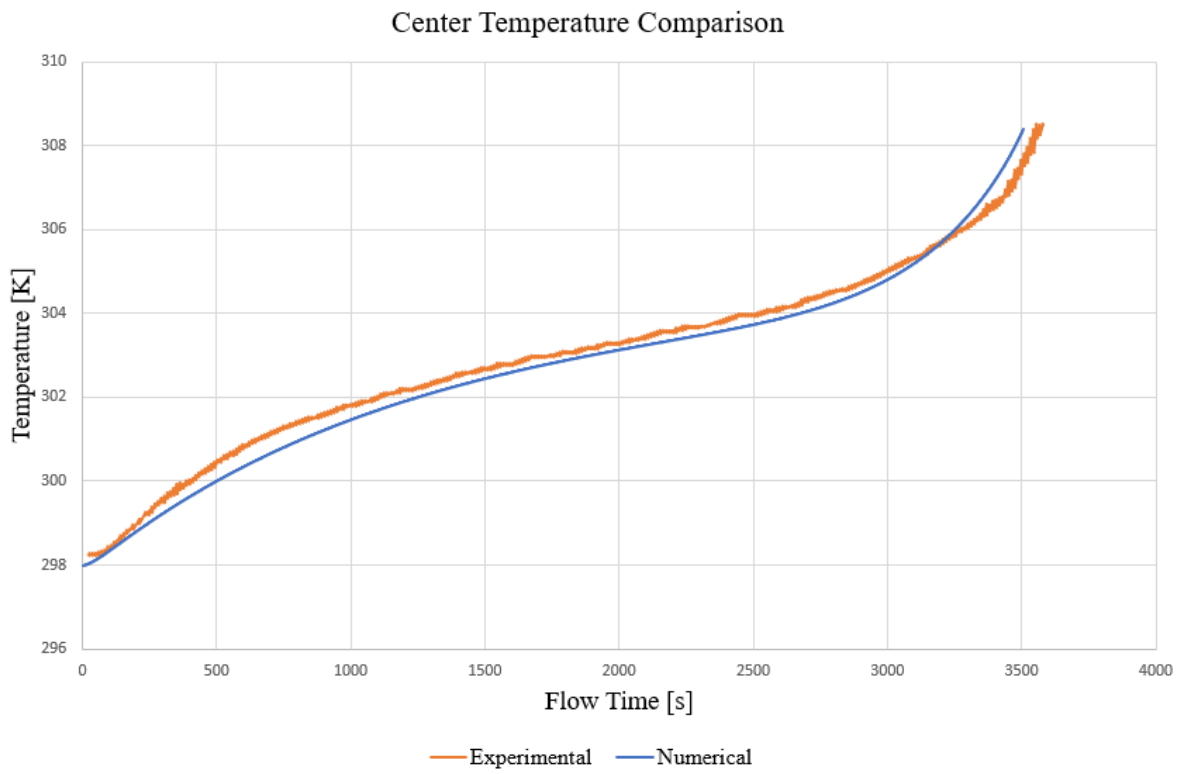


Figure 81 Center Temperature Comparison @25°C and 1C Rate.

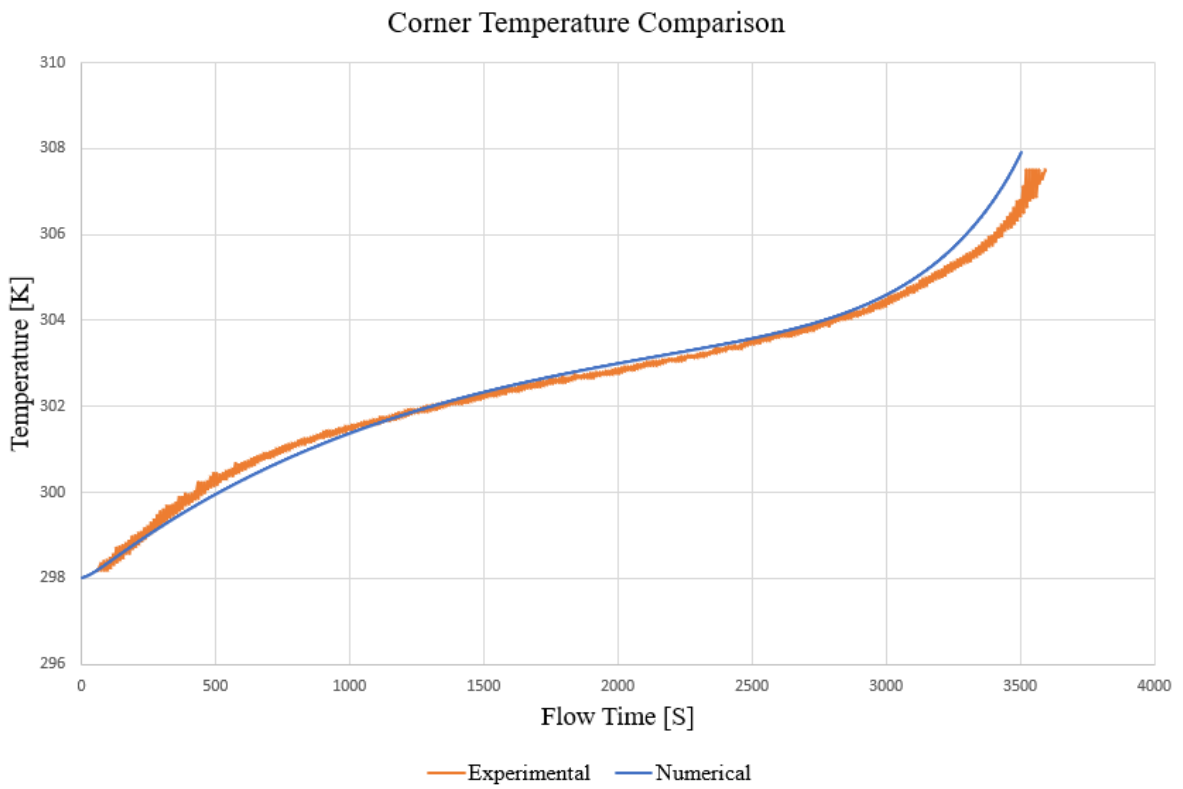


Figure 80 Corner Temperature Comparison @25°C and 1C Rate.

The figures show the time trend of the above-stated quantities. Attention should be paid to the values presented in the final part of the simulation: the canonical discharge time should have been 3600 s, but in this case, the simulations are automatically interrupted at a time of 3520 s. The reason for this behaviour lies in the fact that, depending on the ECM parameters from the state of charge of the battery, in the final phase of the discharge these parameters grow exponentially generating instability in the resolution of characteristic equations. In the phase between 3500 and 3600 s the state of charge is between 3% and 0%: values to be considered categorically avoidable in a real operation of the battery (the optimal range of charge is considered between 80% and 20%). For this reason, this defect in the simulation can be considered negligible.

The average quadratic error (MSE) method is used to assess the goodness of the performance provided by the model. This method is based on a comparison between the expected values (experimental values) and the obtained values (model values). The report for the calculation of the root mean quadratic error is given:

$$MSE = \frac{\sum_{i=1}^n (\hat{x}_i - x_i)^2}{n} \quad (52)$$

Where \hat{x}_i represents the value of the data taken from the experiment, while x_i represents the data obtained from the simulation. The more the value of MSE tends to 0, the more the numerical model has provided results consistent with the experimentation. To carry out this type of analysis, the entire development grid in time (Flow Time 3600 s) was discretized into 25 samples. From the analysis of these 25 characteristic points, the value of the MSE was calculated first for the temperature curve of the center of the battery and then for the curve of the average voltage of the latter. For completeness of treatment they come, of continuation, brought back two Tables with the 7 that introduces the greater discrepancy between the data attended and those obtained. The **Table 17** refers to the analysis conducted for the temperature curve of the center of the battery.

Flow Time [s]	x_i [K]	\hat{x}_i [K]	$(\hat{x}_i - x_i)$ [K]	$(\hat{x}_i - x_i)^2$ [K ²]
500	300.018	300.51	0.492	0.242
1000	301.47	301.79	0.3	0.09
1500	302.45	302.65	0.2	0.04
2000	303.13	303.31	0.18	0.0324
2500	303.73	303.99	0.26	0.0676
3000	304.81	304.98	0.17	0.0289
3500	308.38	307.97	-0.41	0.1681

Table 17 parameters for the calculation of Center temperature MSE.

The final value of the MSE for the temperature curve of the center of the Battery is 0.12 K²: a value that is very close to the optimal value 0. From the **Table 17** it is noticed that the Points with the greatest discrepancy are those that represent the initial and final part of the Simulation. The highest heat generation values were obtained under both extreme conditions of the DOD, as confirmed by the literature [92]. These two peaks can be associated with cellular supercapacity; in other words, this means that the cell is not working at equilibrium and requires more energy than expected thermodynamically; this extra energy is eventually lost as heat. In particular, the first peak may be associated with the activation overvoltage, then the additional energy required to activate the reaction, while the second peak may be related to the concentration overvoltage, i.e. the depletion of the charge vectors on the electrode surface. This is due to the slow diffusion of the charge carriers, which can be explained by the change in the concentration difference between the electrolyte and the electrode surface. The highest heat output is generated around 0% of SOC. The temperature difference may be related to the determination of the actual limit conditions (thermal convection coefficient), in particular it can be said that the actual convection coefficient in the experimental tests was not available, but it was probably higher than the one used to model the heat exchange. [81]

The **Table 18** refers to the analysis carried out for the trend of the average voltage of the active part.

Flow Time [s]	x_i [V]	\hat{x}_i [V]	$(\hat{x}_i - x_i)$ [V]	$(\hat{x}_i - x_i)^2$ [V ²]
500	3.914	3.914	0	0
1000	3.73	3.74	0.01	0.0001
1500	3.63	3.57	-0.06	0.0036
2000	3.57	3.47	-0.1	0.01
2500	3.52	3.37	-0.15	0.0225
3000	3.34	3.27	-0.07	0.0049
3500	2.5	2.6	0.1	0.01

Table 18 Parameters for the calculation of voltage MSE.

The final value of the MSE for the battery voltage curve is $0.0413 V^2$: a value strongly tending to 0. This means that the curve obtained by the numerical model simulates the experimental trend in an optimal way. Also in this case, however, the greater discrepancy is obtained in the final phase of the simulation. The last aspect can be related to the fact that not enough experimental data was available to estimate the electrical model parameters in operating conditions with a SOC lower than 10%. However, it should be pointed out how this particular operating region is usually avoided in order to Prolong the battery life.

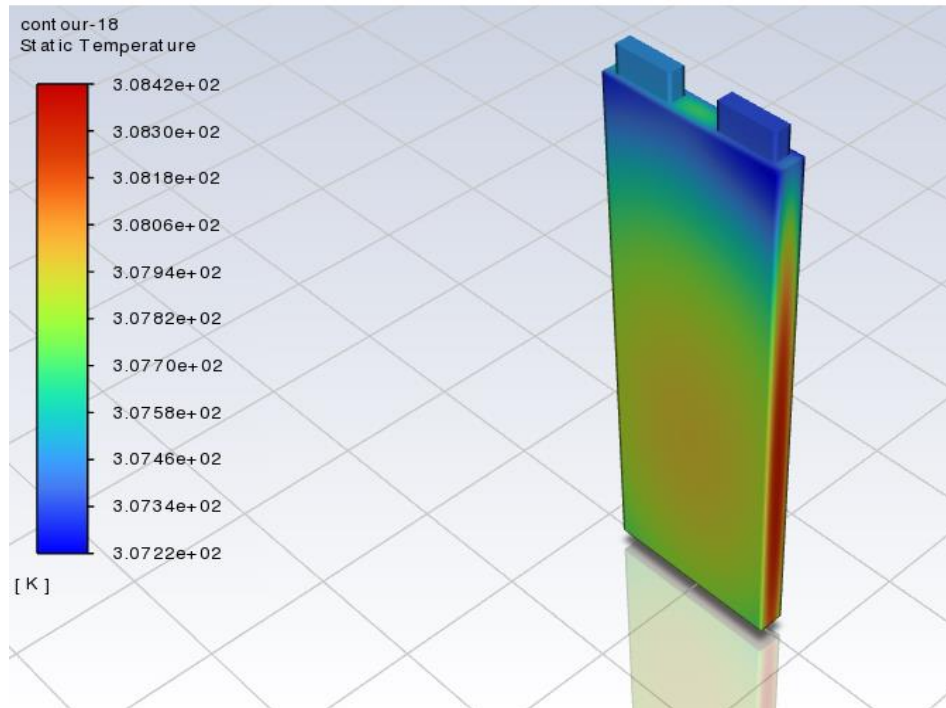


Figure 82 Battery contour of Temperature @25°C and 1C Rate (3600 s)

Figure 82 shows the temperature contour of the cell at the end of the simulation. The analysis of the identification of the hot spots of the battery is addressed in the following sections, as well as the study of the maximum temperature difference of the cell. At this stage it is useful to note that one of the two Tabs (positive Tab) has a temperature value higher than the other. This type of behaviour was announced in the section dedicated to the determination of contact resistances (**Chapter 4**). The values of these resistances have been obtained from an iterative analysis in order to obtain the best combination between a correct temperature trend (with less MSE possible) and the possibility to adequately visualize the declared behaviour.

5.2 Ambient temperature and C-rates effects

This Section presents the study on the thermal behaviour of the battery at different conditions of environmental temperature (and initialization T_0) and discharge current. In particular, the battery will be analysed under discharge conditions 1-C but with an ambient temperature of 0 °C and 45 °C. The second analysis concerns the variation of the discharge current: in this case a system with a discharge current of 2-C and with room temperature 25 °C.

As presented in the previous chapter, the parameters of the ECM model do not depend solely on the state of charge (SOC). Specifically, it is useful to remember that, in a range of charge ranging from 90% to about 10%, the influence of the SOC on the parameters of the model is almost nil. In opposition to this type of behaviour there is a strong dependence of the parameters on the temperature state of the system. Proof of this is the change in the capacity of the battery itself according to the change in environmental conditions (as can be seen in the **Table 1**).

The first analysis concerns the thermal behaviour of the battery with T_0 equal to 0 °C. Unlike what was done in the previous section, in this case the temperature trend affected is that of the T_{max} of the active part. The validation of the model with the experimental data concerns only the comparison of the maximum temperature reached by the cell at the end of the discharge. The simulated value is derived from literature [81]. The main purpose of this type of study is to demonstrate the effect of temperature change on the parameters of the numerical model. For this reason, below, is presented the that summarizes the parameters implemented on the simulation software.

Table 19 ECM Parameters in ANSYS FLUENT @0 °C.

V_{oc}	f_0	f_1	f_2	f_3	f_4	f_5
	3.685	-0.16	-0.2	0.925	-0.93	10.5
R_S	a_0	a_1	a_2	-	-	-
	0.098	0.511	14.2	-	-	-
R_1	b_0	b_1	b_2	-	-	-
	0.081	0.438	12.1	-	-	-
C_1	c_0	c_1	c_2	-	-	-
	703.6	-651.6	21.5	-	-	-
R_2	d_0	d_1	d_2	-	-	-
	0.073	0.425	10.2	-	-	-
C_2	e_0	e_1	e_2	-	-	-
	4475	-6056	28.4	-	-	-

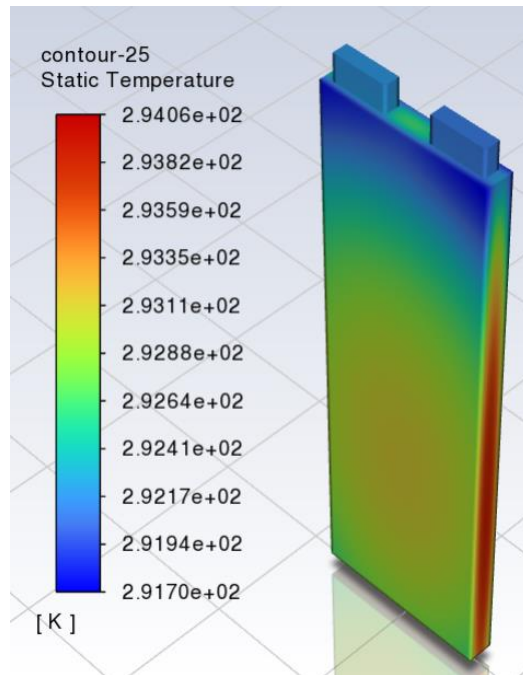


Figure 83 Battery contour of Temperature @0°C and 1C Rate (3600 s)

The value of T_{max} obtained from the literature corresponds to 294 K. In the Figure just presented the value of T_{max} stands at 294.06 K, demonstrating the goodness of the performance of the simulation. By observing the values of the ECM parameters for this case study, an increase can be noted for R_s , R_1 and R_2 . These three parameters are the main responsible for the increase in temperature of the cell. Behaviour of this type had been previously announced in **Chapter 4**; observing the **Figure 43** can be noticed as, assigned a reference to 25 °C, decreasing of temperature the parameter increases conspicuously. The energy and power dissipated increased considerably at low ambient temperature because of the Increase of the battery internal resistance. Electric vehicles limitations and reduced performance in cold weather are well known. The energy released should be used to uniformly heat the battery until the optimum working conditions are reached.

In the **Table 19** it is useful to observe that all the other parameters have remained identical. The reality is that the trend of the voltage curve should also change due to changing environmental conditions. There is no precise indication of this type of variation in the literature references, which is why this analysis was not considered necessary. In addition, in **Figure 45** there is a change in the value of U_{OC} as a function of temperature as well as the SOC. The observed variation, unlike resistance, is much less marked than dependence on SOC. Because of this, the voltage variation could be considered negligible.

The second analysis concerns the thermal behaviour of the battery with T_0 equal to 45 °C. Also, in this case the temperature trend concerned is that of the T_{max} of the active part. The validation of the model with the experimental data concerns only the comparison of the maximum temperature reached by the cell at the end of the discharge. The simulated value is derived from literature [81]. Below is the **Table 20** that summarizes the parameters implemented on the simulation software.

V_{oc}	f_0	f_1	f_2	f_3	f_4	f_5
	3.685	-0.16	-0.2	0.925	-0.93	10.5
R_S	a_0	a_1	a_2	-	-	-
	0.032	0.14	10.5	-	-	-
R_1	b_0	b_1	b_2	-	-	-
	0.036	0.23	14.5	-	-	-
C_1	c_0	c_1	c_2	-	-	-
	703.6	-651.6	21.5	-	-	-
R_2	d_0	d_1	d_2	-	-	-
	0.009	0.326	12.5	-	-	-
C_2	e_0	e_1	e_2	-	-	-
	4475	-6056	28.4	-	-	-

Table 20 ECM Parameters in ANSYS FLUENT @45°C.

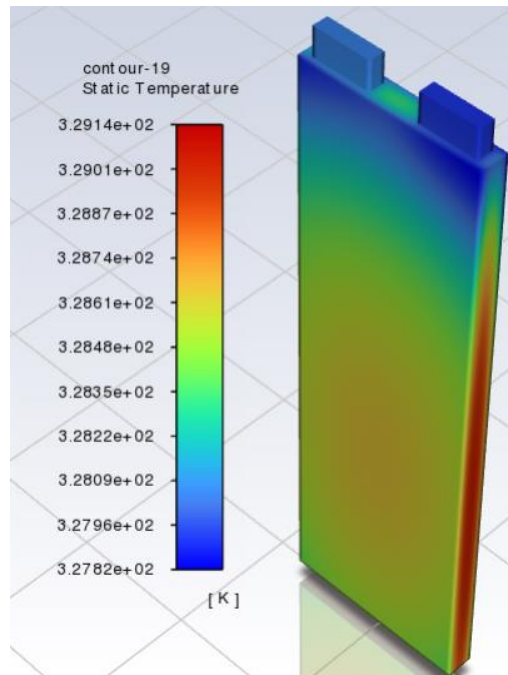


Figure 84 Battery contour of Temperature @45°C and 1C Rate (3600 s)

The value of T_{max} obtained from the literature corresponds to 329.1 K. In the Figure just presented the value of T_{max} stands at 329.14 K, demonstrating the goodness of the performance of the simulation. By observing the values of the ECM parameters for this case study, a decrease can be noted for R_s , R_1 and R_2 . Looking at **Figure 43**, it can be seen that, with a reference to 25 °C, the parameter decreases moderately as the temperature rises. It can also be seen that high temperatures do not have an instantaneous impact on the performance of the cell. In particular, the heat generated, and the consequential total energy remained almost constant, but a temperature above the suggested limit, higher than 50 °C, was reached. High temperatures should be avoided: they deteriorated the chemical structure of the electrodes and in some cases produce the decomposition of the electrolyte; so, they have a long-term impact by decreasing the cells state of health. In this specific case, it has been demonstrated that natural convection is not enough to maintain the safety conditions of a single cell. More intense cooling strategies need to be adopted.

Concerning the T_0 value for the respective cases, it can be noted that the case with an ambient temperature of 0 °C has an increase in the maximum temperature of the battery that is around 21 °C. In the second case, on the other hand, the maximum temperature increase is about 11 °C. In addition, in the first case, there is a temperature gradient (ΔT) of the active part of about 2.89 °C: a value significantly higher than the 1.32 °C of the case with T_0 45 °C. The behaviours described above confirm the above: working at high temperatures leads to a long-term deterioration of the battery, while the excessive increase of the internal resistances of the battery at low operating temperatures can lead to problems, such as poor battery efficiency, already in the short term. In both cases, however, it is necessary to avoid reaching this type of conditions by adopting appropriate heating and cooling systems of the battery.

The last case study for this Section concerns the variation of the discharge current. In particular, from the literature it is derived the value of T_{max} that the active part reaches at the end of the discharge process with constant current 2-C. The temperature value T_0 is given at the start of the study condition. Also, in the case of the variation of the discharge current it is useful to evaluate the change of capacity of the cell (see **Table 1**)

as well as the change of the ECM parameters. Below, then, is the **Table 21** with the identification of the parameters implemented on the ANSYS FLUENT software.

V_{oc}	f_0	f_1	f_2	f_3	f_4	f_5
	3.685	-0.16	-0.2	0.925	-0.93	10.5
R_S	a_0	a_1	a_2	-	-	-
	0.032	0.122	10.5	-	-	-
R_1	b_0	b_1	b_2	-	-	-
	0.038	0.225	14.5	-	-	-
C_1	c_0	c_1	c_2	-	-	-
	703.6	-651.6	21.5	-	-	-
R_2	d_0	d_1	d_2	-	-	-
	0.013	0.328	12.5	-	-	-
C_2	e_0	e_1	e_2	-	-	-
	4475	-6056	28.4	-	-	-

Table 21 ECM Parameters in ANSYS FLUENT @25°C and 2-C Rate.

Following Chen's Model, the variation of the discharge current causes a slight change in the parameters of the model [73]. A variation that mainly affects the exponential terms of Chen's functions, which undergo a slight decrease (in the order of 10^{-2}). The value of T_{max} obtained from the literature corresponds to 318.6 K. The value obtained from the simulation stands on 318.64 K as evidence of the goodness of the simulation. Unlike the previous case studies, for the variation of the discharge current a graph (**Figure 85**) is presented in which the trend in time of the maximum temperature of the active part of the cell is plotted. This choice is given by the fact that the discharge condition 2-C Rate will be used for the subsequent analysis of cooling systems. For the presentation of the Contour of temperature, please refer to the reader to the next Section, in which the themes

of the identification of hot spots and the temperature difference in the cell itself will be addressed.

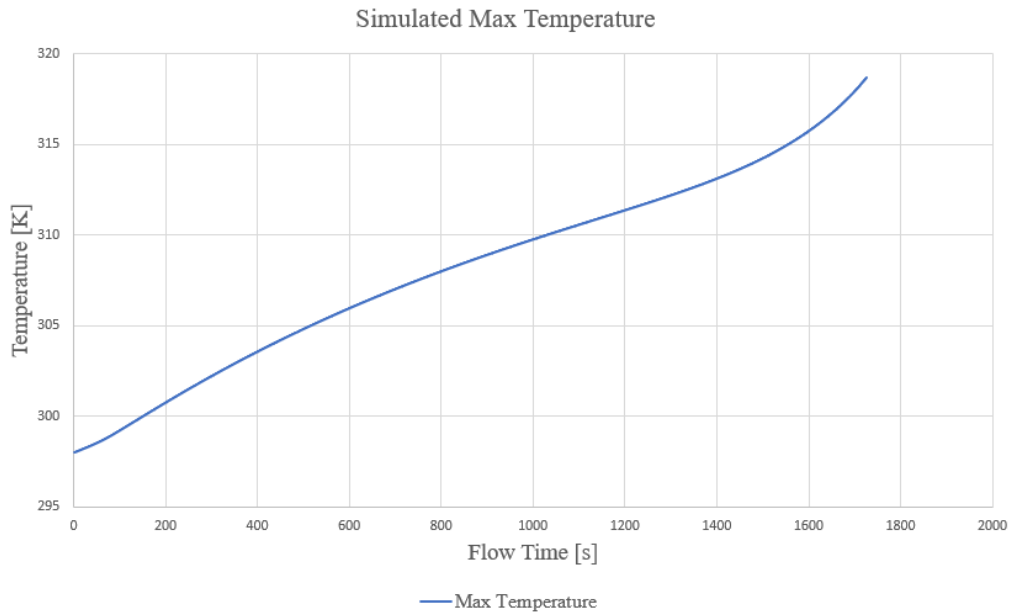


Figure 85 Simulated Max Temperature @25°C and 2C Rate.

.Also in this case, as in the previous analysis with discharge current 1C, the trend of the temperature curve presents the typical behaviour of large batteries. There is, in fact, a high-temperature increase in the final part of the discharge (or simulation). Having adopted a discharge equal to 2-C Rate, the total time of simulation should be 1800 s. Also in this case, as already explained above, the divergence of the values of the circuit model, due to low values of SOC, involves an automatic interruption of the equation resolution by the system. In this case, the simulation goes no further than 1740 s. The 60 s that would complete the simulation involve a charge phase between 2% and 0%: a range of operation that does not compete with the ideal operating conditions for a hybrid vehicle.

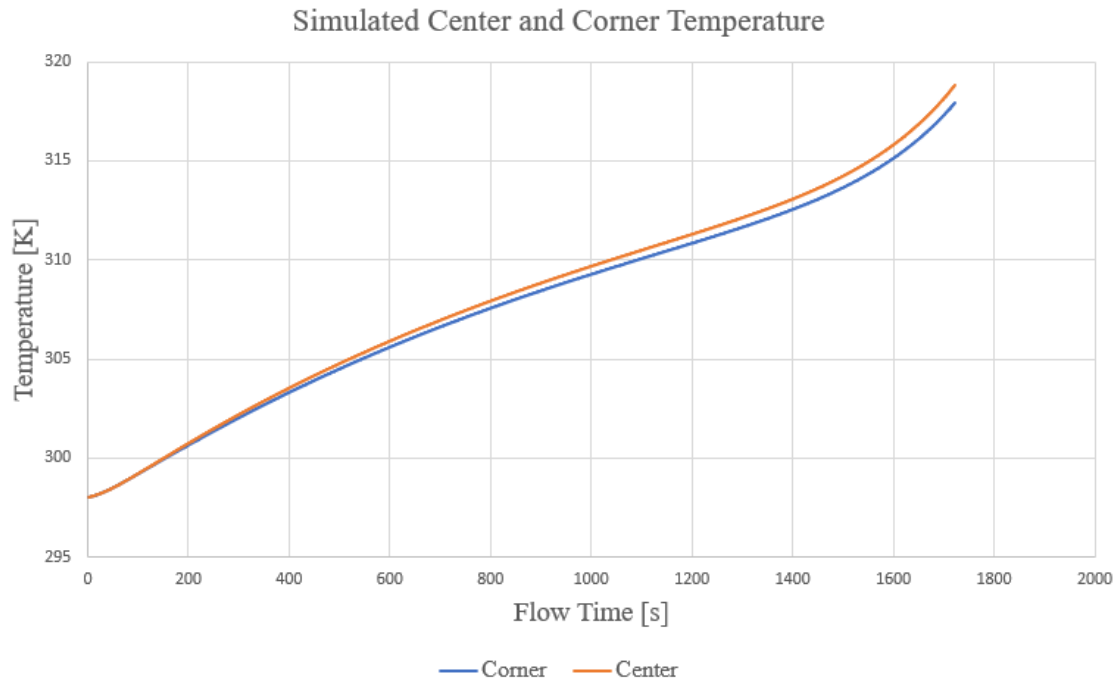


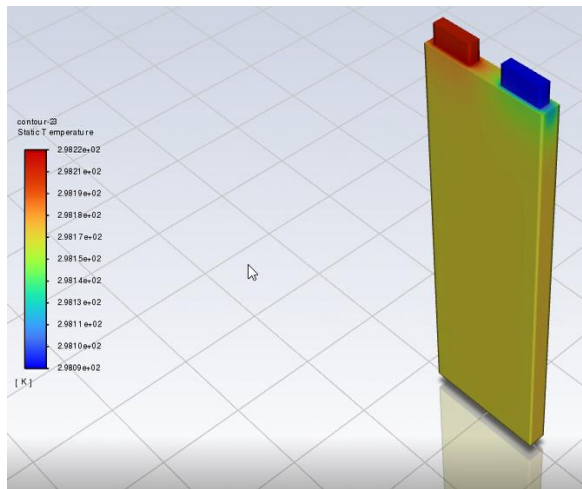
Figure 86 Simulated Corner and Center Temperature @25°C and 2C Rate.

5.3 Hot spots identification

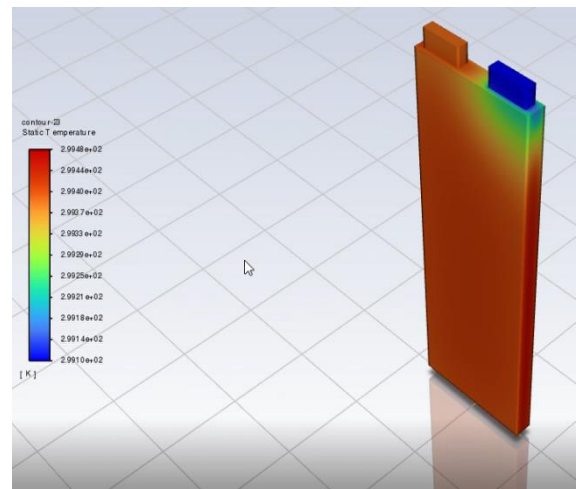
As already amply explained in the previous chapters, one of the main problems of the batteries garlic Li-ion lies in the high difference of Temperature between the parts that compose them. For this reason, in this Section, the identification of the hottest and coldest points of the battery itself is discussed. Initially, only the case of the single battery is presented subject to simple natural convection (with discharge current 1-C and 2-C Rate); later, in the following sections, will be presented the positive contribution that cooling systems have on limiting the temperature difference first on the single cell and then on the whole battery pack.

It is interesting how, through a transient analysis, it is possible to appreciate the thermal behaviour of the battery throughout the operating cycle. The ANSYS FLUENT software allows the user to create an animation of the simulation in time. In particular, for this case study, the Contour animation of the temperature of the cell subjected to a discharge current of 2-C Rate is realized. **Figure 87** shows the Contour of battery temperature in 4 significant moments: (a) 15 seconds after the start of the discharge; (b) 102 seconds after

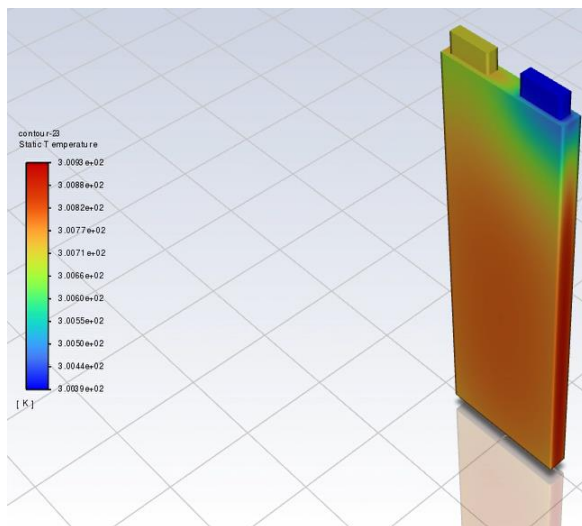
the start of the simulation; (c) 300 seconds after the start of the simulation; (d) 1083 seconds after the start of the simulation.



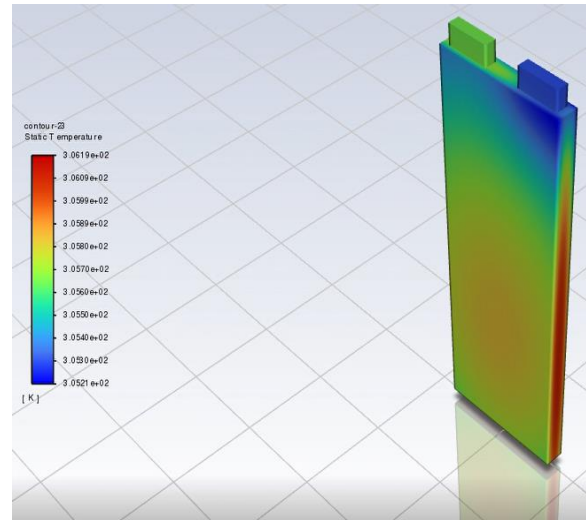
(a)



(b)



(c)



(d)

Figure 87 Simulated Temperature Contour at different time steps @25°C and 2C Rate.

From the figures just reported it is possible to appreciate the thermal behaviour of the cell. In the initial phase of the discharge (a) the greater concentration of heat is localized on the positive Tab, while the "colder" region turns out to be that of the negative Tab. Shortly after the start of the simulation (b), the heat begins to spread evenly over the entire volume of the active part. The only exception is given by the region adjacent to the negative Tab: an expected behaviour, given by the fact that in that region have been set contact resistances with an order of magnitude smaller. In the third phase (c) a loss of

homogeneity in the distribution of heat and therefore of temperature is detected. In the last snapshot (d) all regions of the battery have assumed a heat distribution that will be very similar to the final configuration, obtained for a discharge time of about 1800 s.

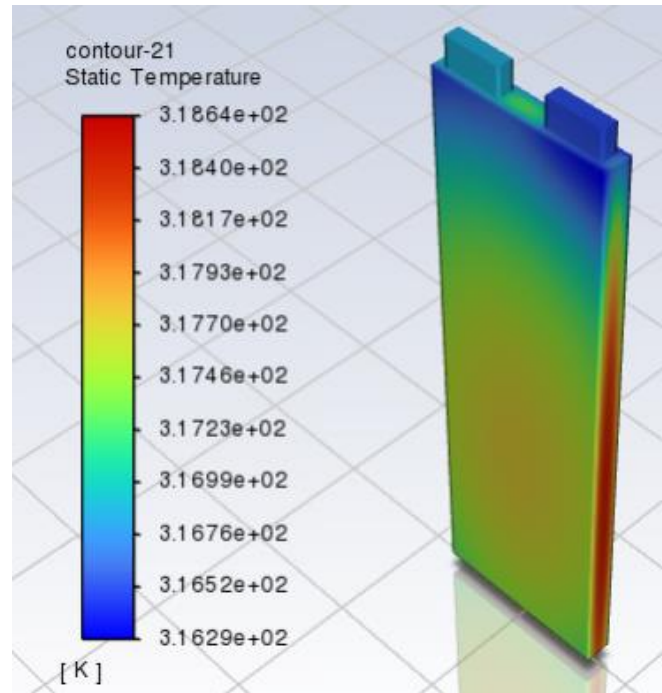


Figure 88 Simulated Temperature Contour at 1800 s @25°C and 2C Rate.

Figure 88 shows the temperature distribution obtained at $t = 1800$ s (2C-Rate discharge cycle). The surface hot spots of the cell are the lateral sides; the regions with lower temperature are the connectors, as shown in **Figure 88**. In this case, it is possible to appreciate that the core temperature is the highest cell temperature, which confirms the importance of LIBs models to avoid thermal runaway and guarantee safety. Critical temperature monitoring, such as the measurement of the core temperature, is extremely difficult. So, it should be accurately modelled. From these results two main aspects can be commented:

- the cooling system design must introduce a strategy with a higher heat exchange coefficient on the cell lateral sides;
- the response of the cooling system should carefully consider the thermal inertia phenomena.

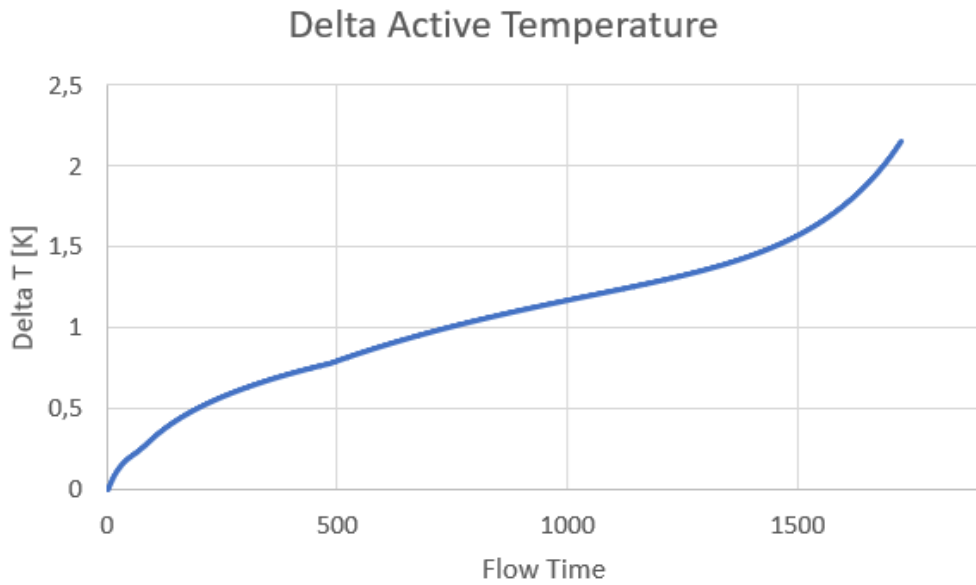


Figure 89 Delta active Temperature @25°C and 2C Rate.

The curve presented in **Figure 89** was obtained by calculating the maximum and minimum temperature value of the active part of the cell. The minimum temperature value of the Negative Tab has also been taken into account, but it has been verified that the greatest temperature difference is found in the active part only. The time trend of the temperature difference shows what has already been said: in the final part of the discharge process there is an increase in the instability of the processes inside the battery. All this leads to a sudden rise in the temperature gradient in the battery itself. In the case of the discharge current equal to 2C Rate, the maximum ΔT is 2.35 °C. In the case with a discharge current equal to 1C Rate, the maximum gradient is 1.2 °C.

5.4 Cooling systems performance

Chapter 4 introduced the main geometrical characteristics of cooling systems adopted to limit temperature growth. Summarizing the types adopted, in this Section will be presented three cooling techniques: cooling with fins, with pure PCM and with the combination of PCM and heat sinks. For the geometrical configuration of the systems, please refer to the Sections of the previous chapter, in which the hypotheses and the generation of models are explained. To further demonstrate the ability of the proposed design in terms of efficiency, effectiveness and accuracy in controlling the temperature of the battery, a series of numerical simulations were conducted for different discharge conditions (1C and 2C Rate).

5.4.1 Heat Sinks performance

The first case in the analysis is that of the addition of the cooling metal fins on the surfaces of the cell. The fins, in turn, are subject to natural convection, as well as the surfaces of the active part not affected by contact with heat sinks. Below are the **Figure 90** and **Figure 91** representing the temperature trend of the known points of the cell and the Contour of temperature obtained at the end of the discharge phase (discharge current 1C Rate).

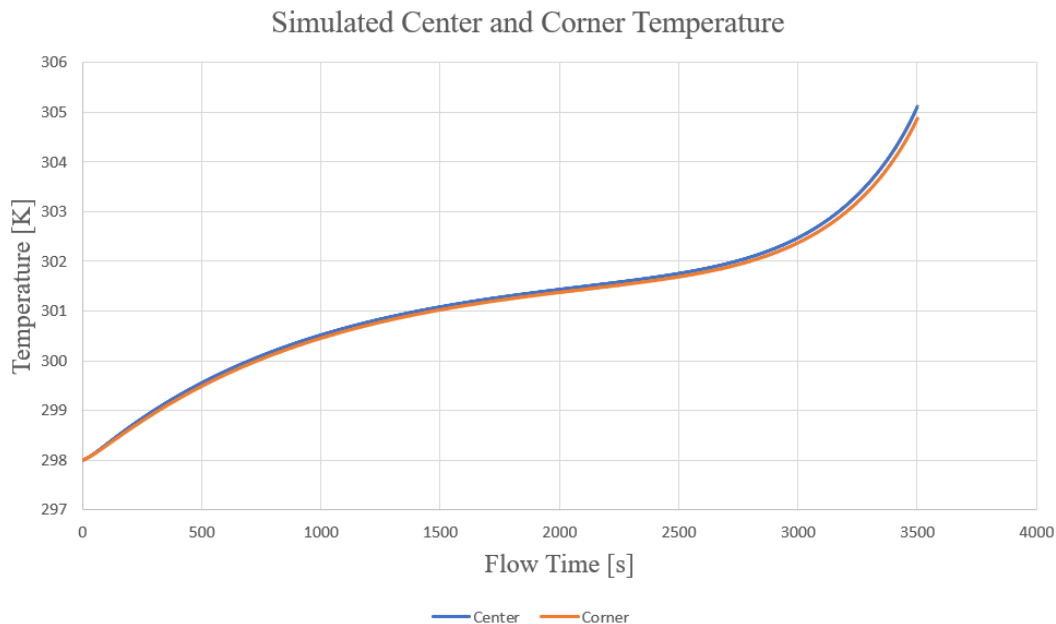


Figure 90 Simulated Temperature with Heat Sinks @25°C and 1C Rate.

A significant decrease of the battery surface temperature was observed from natural convection to using the heat dissipation materials. The center temperature for natural convection was 35.4 °C. Comparatively, the temperature in the case of heat sink without PCM was 32.1 °C due to the improvement of the surface heat transfer capability. Compared to the case without Heat Sinks, the temperature trend suffers a maximum peak reduced by 9.26% which corresponds in absolute terms to an overall reduction of 3.27 °C. It should be noted, moreover, that the temperature increase in the initial phase of the discharge is limited compared to the case with only natural convection. After 1000 s of simulation, in this case the temperature reaches about 300.5 K. In the case with natural convection cooling, after 1000 s of discharge, the battery exceeds 301.5 K approaching 302 K. It should also be considered that the two curves follow an almost identical time trend, being superimposed for more than two-thirds of the simulation. In the final phase, there is a natural detachment of the curves given by the instability of the processes inside the cell for SOC values tending to 0%. It can, therefore, be said that, in addition to allowing the global lowering of the battery temperature, this cooling system has provided greater uniformity to the temperature distribution for most of the discharge time.

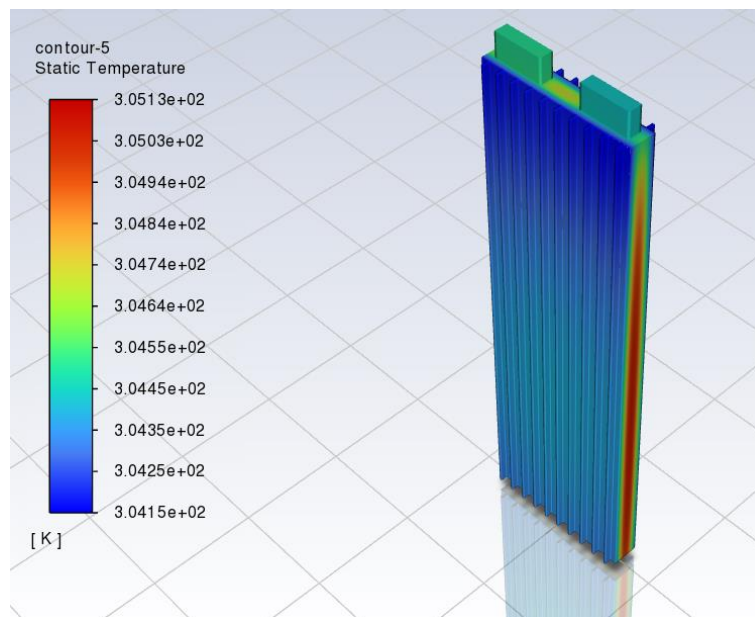


Figure 91 Simulated Temperature Contour at 3600 s @25°C and 1C Rate.

From the Contour of temperature, it is possible to observe that the warmest region always remains the lower part of the cell, testified by the fact that the fins presented a higher temperature in that area. In this case, the graph relating to the temperature difference as a function of time is not presented because the trend is similar to that shown above. This

does not alter the fact that the absolute value of the temperature difference has to be analysed. Also in this analysis, the peak of temperature difference of the active part is obtained at the end of the simulation. The value of the maximum temperature difference is equal to 0.88 °C: a reduction of 27% compared to the 1.2 °C obtained in the case with only natural convection.

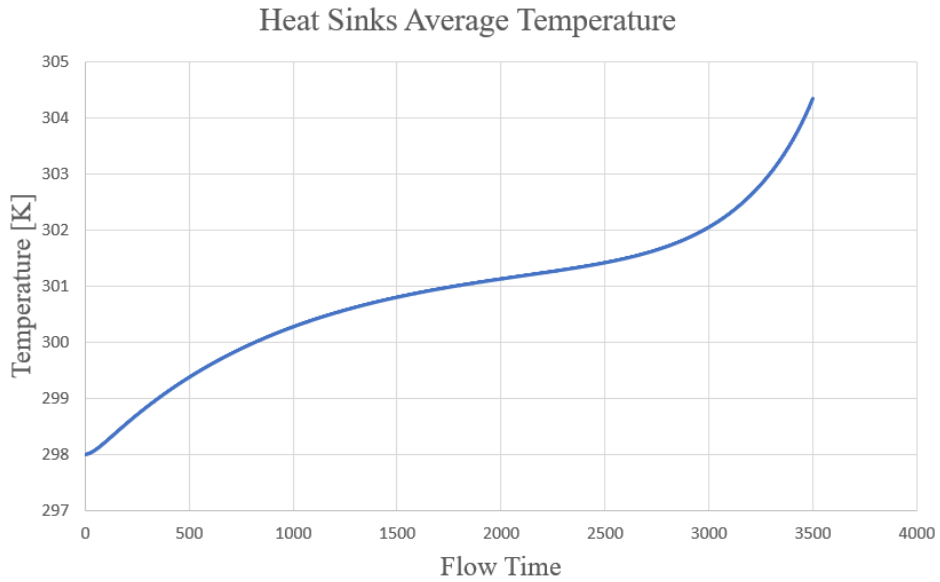


Figure 92 Simulated average Heat Sinks Temperature @25°C and 1C Rate.

Below are the **Figure 93** and **Figure 96** representing the temperature trend of the known points of the cell and the Contour of temperature obtained at the end of the discharge phase (discharge current 2C Rate).

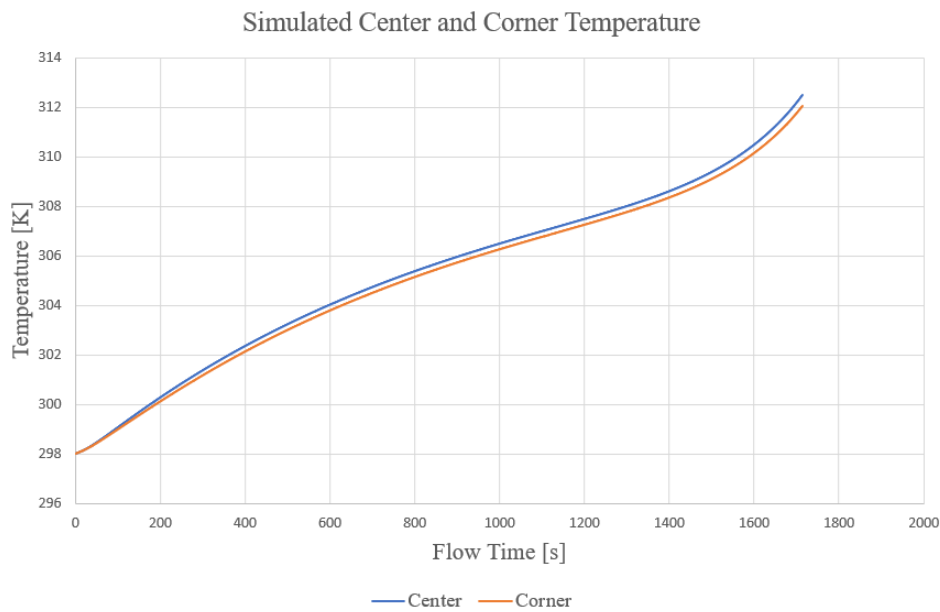


Figure 93 Simulated Temperature with Heat Sinks @25°C and 2C Rate.

The center temperature for natural convection was 45.64 °C. Comparatively, the temperature in the case of heat sink without PCM was 39.5 °C due to the improvement of the surface heat transfer capability. Compared to the case without Heat Sinks, the temperature trend undergoes a maximum peak reduced by 13.45% which corresponds in absolute terms to an overall reduction of 6.14 °C. Compared to the case with discharge current 1C, the curve is detached from the start of the simulation.

The **Figure 94** shows the battery temperature contours with the fins in 4 significant moments: (a) 15 seconds after the start of the discharge; (b) 102 seconds after the start of the simulation; (c) 300 seconds after the start of the simulation; (d) 650 seconds after the simulation begins.

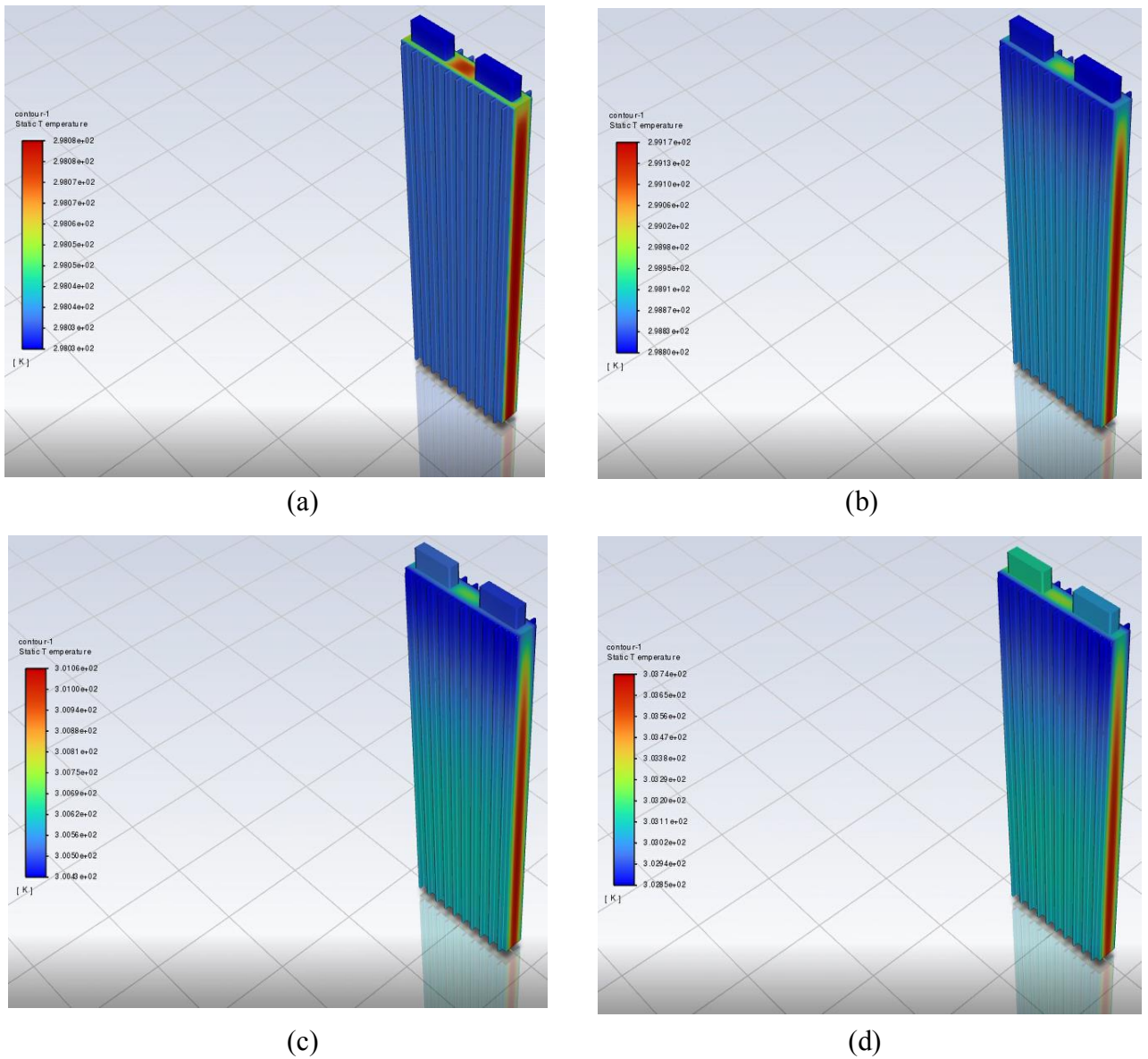


Figure 94 Simulated Temperature Contour at different time steps @25°C and 2C Rate.

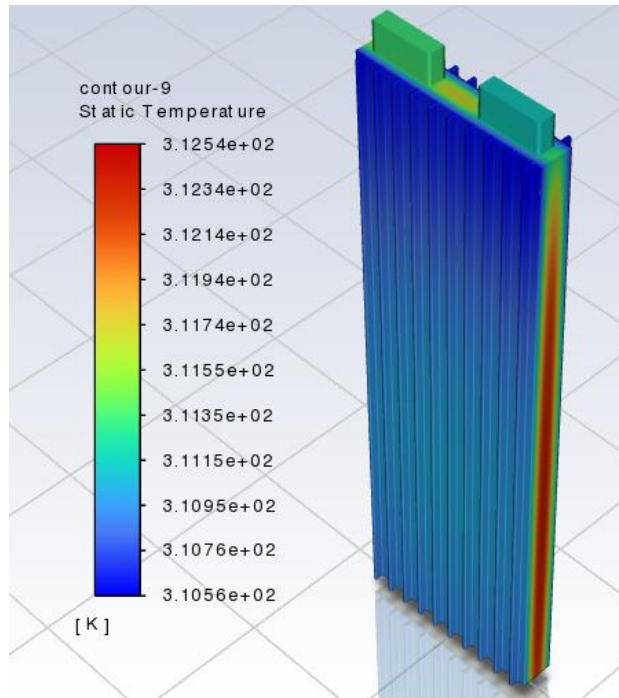


Figure 96 Simulated Temperature Contour at 1800 s @25°C and 2C Rate.

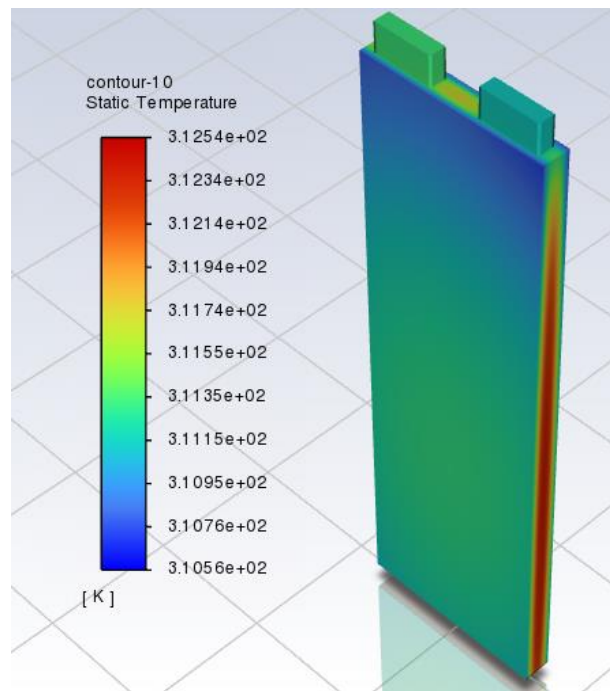


Figure 95 Simulated Temperature Contour without Heat Sinks at 1800 s @25°C and 2C Rate.

Also in this analysis the peak of temperature difference of the active part is obtained at the end of the simulation. The value of the maximum temperature difference is equal to 1.79 °C: a reduction of 23.8% compared to 2.35 °C obtained in the case with only natural convection.

5.4.2 Pure PCM performance

The second case under analysis is the addition of phase change material blocks on the cell surfaces. The blocks, in turn, are subject to natural convection, as well as the surfaces of the active part not affected by contact with the material. Below are the **Figure 97** and **Figure 99** representing the temperature trend of the known points of the cell and the Contour of temperature obtained at the end of the discharge phase (discharge current 1C Rate).

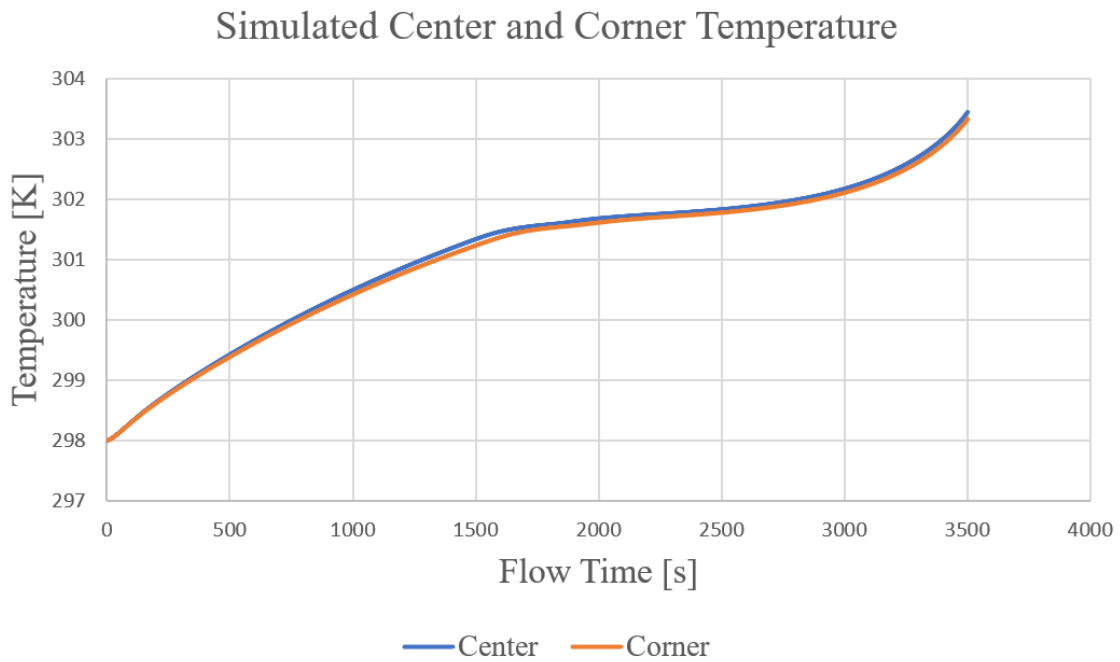


Figure 97 Simulated Temperature with PCM @25°C and 1C Rate.

The first difference that can be noticed compared to the cases previously analysed is the temperature trend over time. At about 1600 seconds from the beginning of the discharge, the temperature increases, which lasts for more than 3000 seconds. A similar behaviour indicates that at that moment the material has begun to change its state. The latent heat of phase change "absorbs" the heat generated by the battery not allowing an increase in temperature of the latter. Attributing to the characteristics of heat absorption with high latent heat, pure PCM module restricted the temperature of the center under 30.45 °C. The center temperature for natural convection was 35.4 °C. Compared to the case without PCM, the temperature trend suffers a maximum peak reduced by 13.9% which

corresponds in absolute terms to an overall reduction of 4.95 °C. It should also be considered that the two curves follow a trend in time that is almost identical, being superimposed all the time in the simulation. Even in the final phase there is no natural detachment of the curves given by the instability of the processes inside the cell for SOC values tending to 0%. It can, therefore, be said that, in addition to allowing the global lowering of the temperature of the battery, this cooling system has provided a greater uniformity of the temperature distribution than the case analysed above.

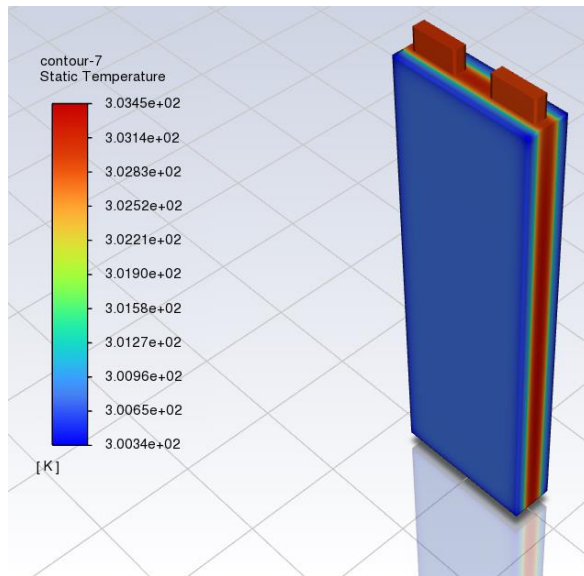


Figure 99 Simulated Temperature Contour with PCM at 3600 s @25°C and 1C Rate.

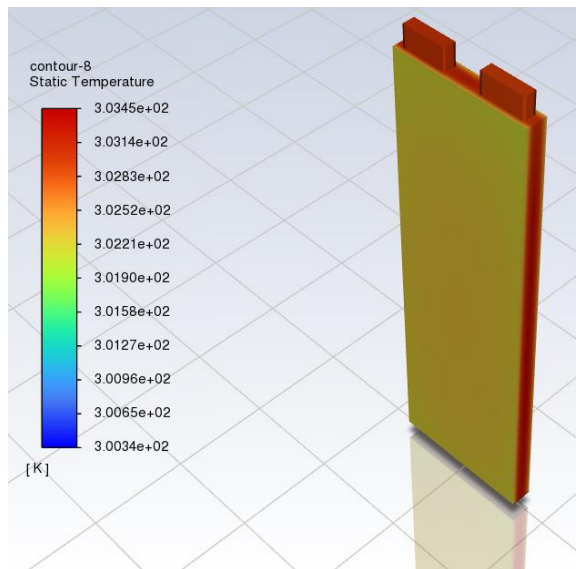


Figure 98 Simulated Temperature Contour without PCM at 3600 s @25°C and 1C Rate.

Contrary to what happens with the Heat Sinks, in this case the temperature difference between the positive and negative Tabs is almost completely canceled. It is possible to say that the influence of the contact resistances is negligible. In addition, unlike in cases with only natural convection and convection with fins, adding the material to phase change has a long uniformity in the Y direction of heat distribution. The greatest temperature difference occurs between the outer surface and the center of the active part (along the Z direction of the geometry). The maximum temperature difference is found at the end of the discharge phase and corresponds to about 1.05 °C: a reduction of 14% compared to 1.2° C obtained in the case of natural convection only. The temperature difference obtained with the Heat Sinks is better in absolute terms, but the uniformity of the heat obtained along the Y direction is not comparable. In addition, with the use of PCM a lowering of the maximum temperature value is achieved.

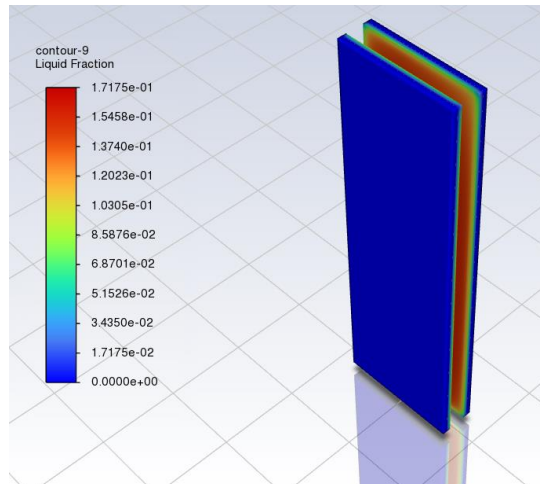


Figure 100 Simulated Liquid Fraction Contour at 3600 s @25°C and 1C Rate.

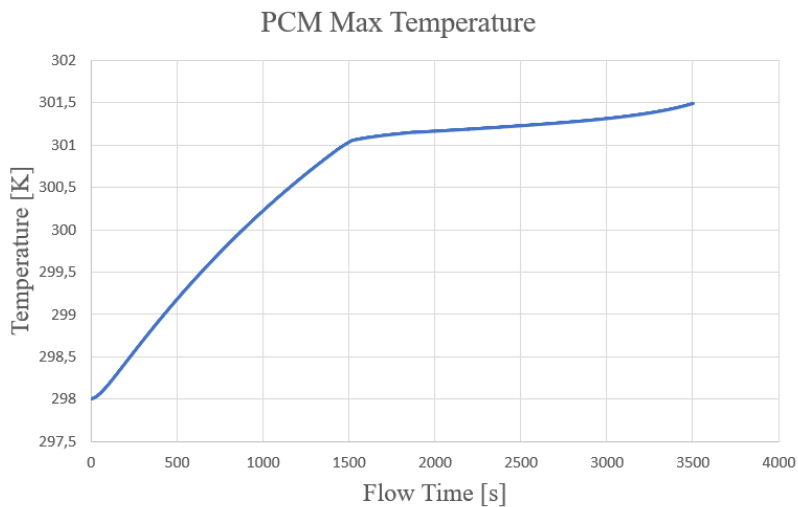


Figure 101 Simulated Max PCM Temperature @25°C and 1C Rate.

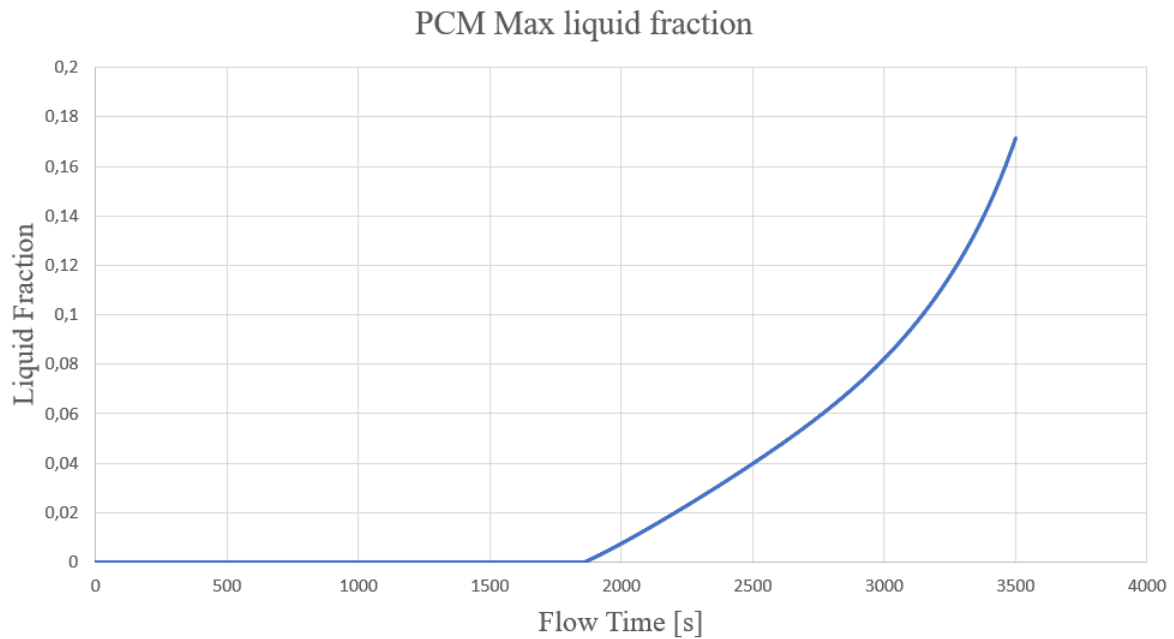


Figure 102 Simulated Max PCM liquid fraction @25°C and 1C Rate.

Figure 101 shows the time trend of the maximum temperature reached by the PCM during the discharge. As in the case of the temperature trend of the characteristic points of the battery, at a time of about 1500 seconds the curve undergoes a ceiling due to the beginning of the phase change. Remember that the liquefaction start temperature has been set in the ANSYS software equal to 301.15 K (corresponding to about 1500 s in the case with 1C Rate download). It is known that, during a phase change, the temperature remains constant. This type of behaviour belongs to pure substances (no more mixtures substances). In **Chapter 4**, reference was made to the impossibility of obtaining a commercial PCM free of impurities. It is explained, therefore, the necessity to have an end-liquefaction temperature equal to 303.5 K and a maximum temperature trend of the PCM not constant during the phase passage. The maximum percentage of liquid formed is 17.15%: it means that in no zone of the block there is pure liquid phase.

Below are the **Figure 103** and **Figure 106** representing the temperature trend of the known points of the cell and the Contour of temperature obtained at the end of the discharge phase (discharge current 2C Rate).

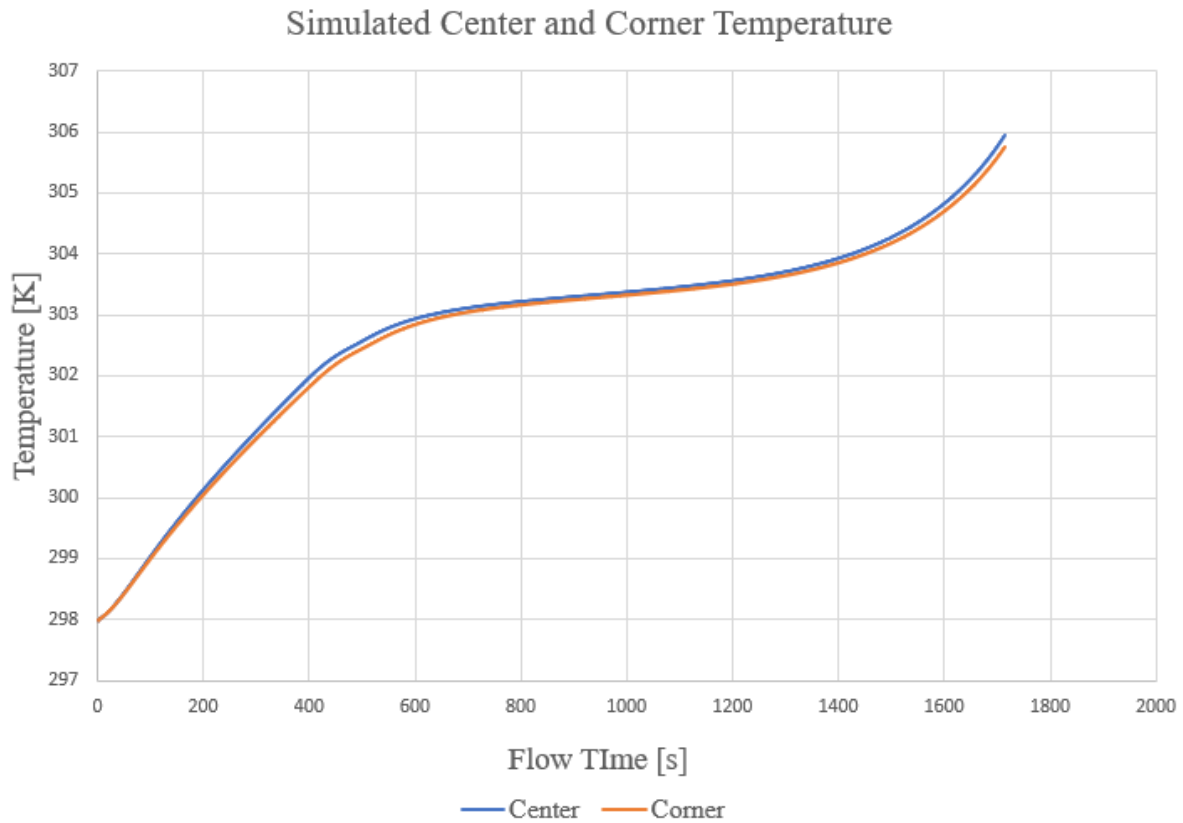


Figure 103 Simulated Temperature with PCM @25°C and 2C Rate.

The center temperature for natural convection was 45.64 °C. Attributing to the characteristics of heat absorption with high latent heat, pure PCM module restricted the temperature of the center under 32.94 °C. Compared to the case without PCM, the temperature trend suffers a maximum peak reduced by 27.82% which corresponds in absolute terms to an overall reduction of 12.7 °C. Unlike what happens in the case with discharge current 1C, the start of the liquefaction phase is strongly anticipated to 600 seconds from the beginning of the simulation. A predictable and consistent behaviour with the reality of the problem. Consequently, the time curve of the PCM Max liquid fraction will also show a growth that starts earlier than in case 1C, as presented in the **Figure 105** below.

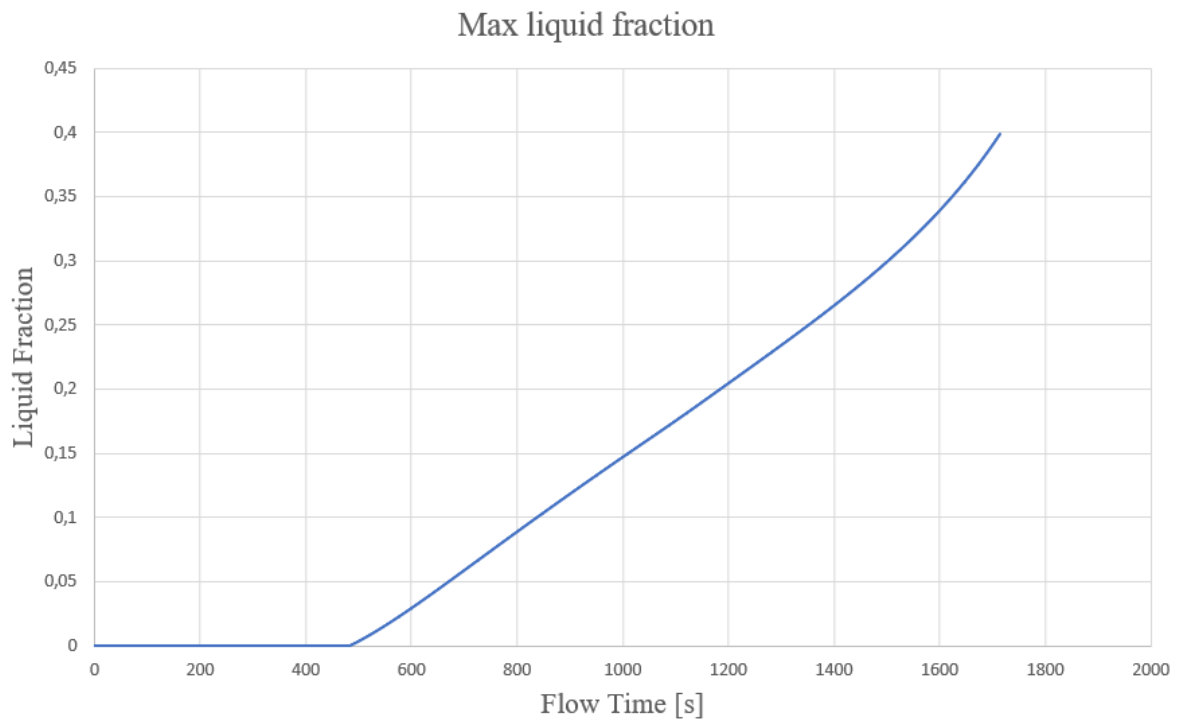


Figure 105 Simulated Max PCM liquid fraction @25°C and 2C Rate.

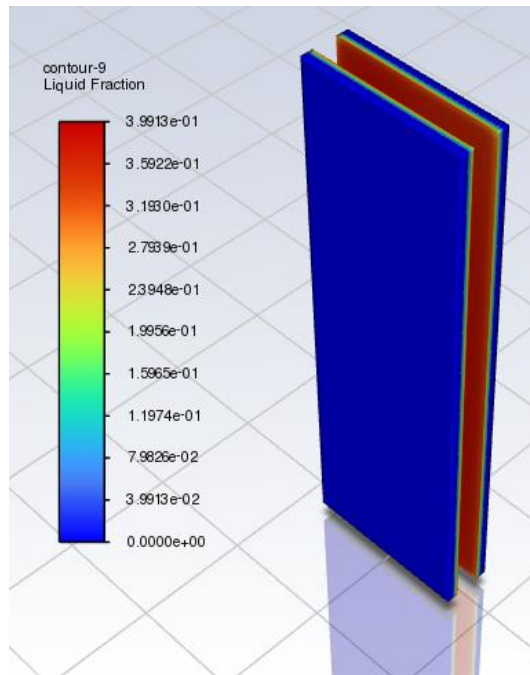


Figure 104 Simulated PCM liquid fraction Contour at 1800 s and 2C Rate.

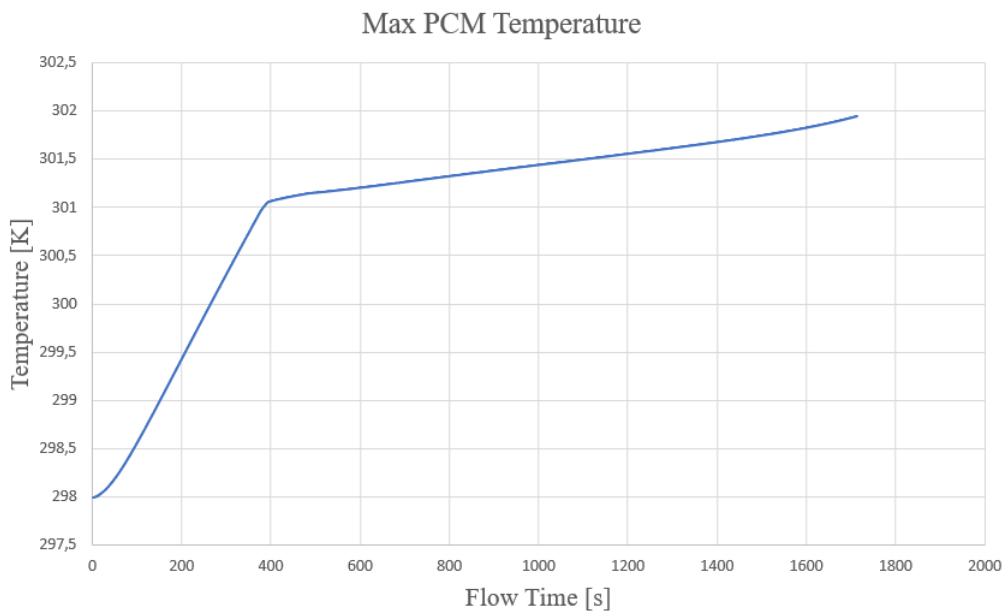


Figure 107 Simulated Max PCM Temperature @25°C and 2C Rate.

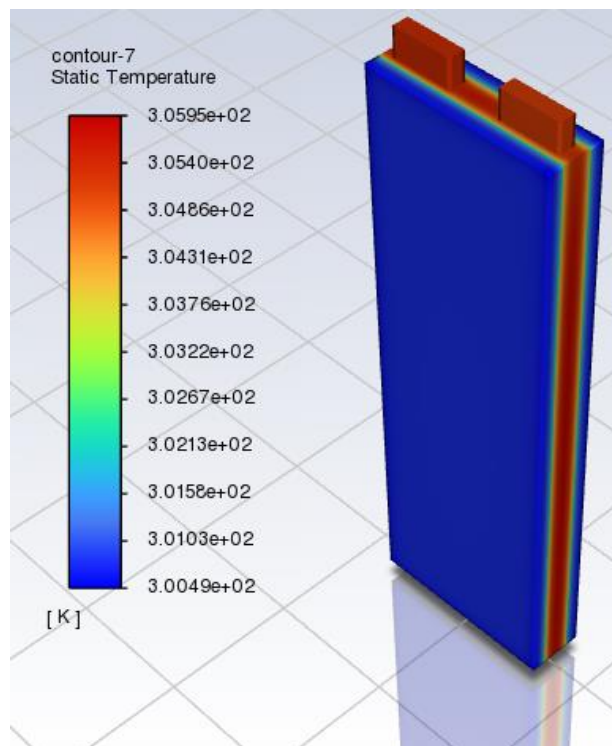


Figure 106 Simulated Temperature Contour with PCM at 1800 s @25°C and 2C Rate.

The greatest temperature difference occurs between the outer surface and the center of the active part (along the Z direction of the geometry). The maximum temperature difference is found at the end of the discharge phase and corresponds to about 1.97 °C: a reduction of 16.2% compared to the 2.35 °C obtained in the case with only natural convection.

5.4.3 PCM-Fin structure performance

The last case study for the single-cell concerns the implementation of a PCM-Fin structure as a cooling method. The thickness of PCM remains unchanged compared to the case analysed above: a choice was made to better visualize the effect of the fins on the thermal behaviour of the battery and the material itself. In comparison with pure PCM, a PCM-fin structure can enhance the heat exchange area of PCM by uniformly allocating straight fins into PCM, but it will decrease the volume of PCM between two baseplates. In this section, the thermal behaviours of PCM-fin structure during discharge were analysed and compared to further confirm the effect of fins structure on thermal performance.

Below are the **Figure 108** and **Figure 110** representing the temperature trend of the known points of the cell and the Contour of temperature obtained at the end of the discharge phase (discharge current 1C Rate).

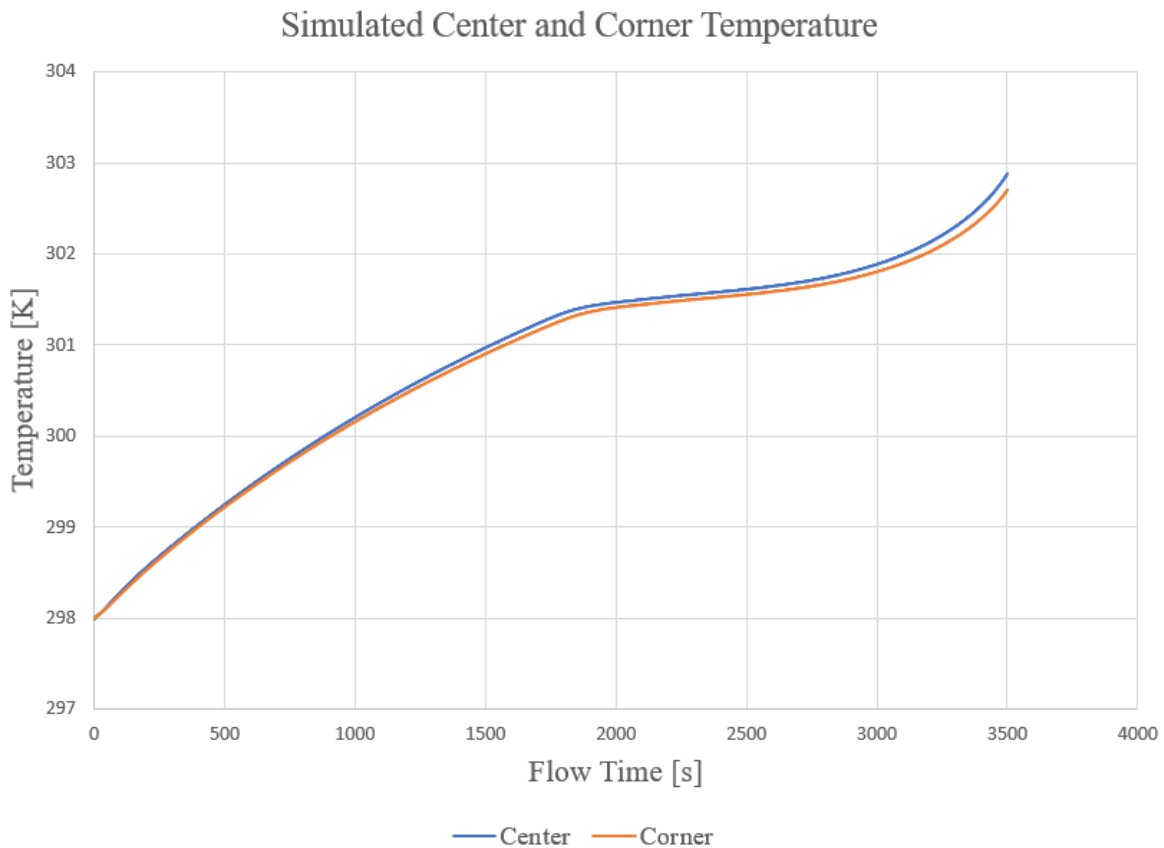


Figure 108 Simulated Temperature with PCM-Fin structure @25°C and 1C Rate.

In comparison with other cooling methods, the rate of temperature rise with PCM-fin structure is the slowest for the same discharge rate. Such result demonstrates the

efficiency of PCM-fin structure in controlling the temperature of battery. For the final temperature rise of each discharge process, the one with PCM-fin structure demonstrates its superiority over that with the other three cooling methods in the effectiveness of heat dissipation. PCM-Fin structure restricted the temperature of the center under 29.88 °C. The center temperature for natural convection was 35.4 °C. Compared to the case without PCM, the temperature trend suffers a maximum peak reduced by 15.6% which corresponds in absolute terms to an overall reduction of 5.52 °C.

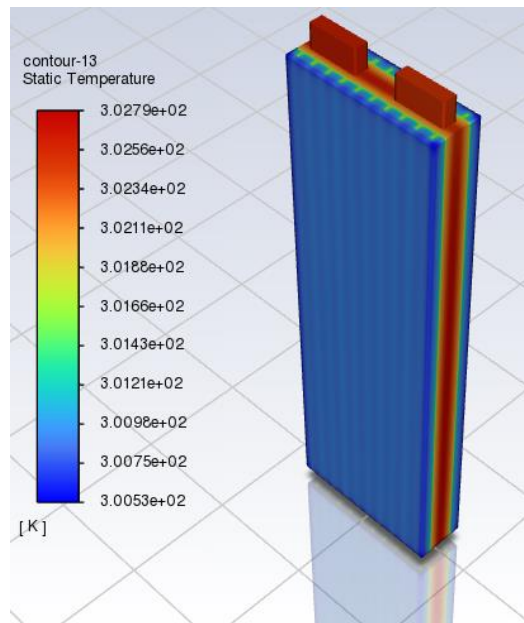


Figure 110 Simulated Temperature Contour with PCM-Fin structure at 3600 s @25°C and 1C Rate.

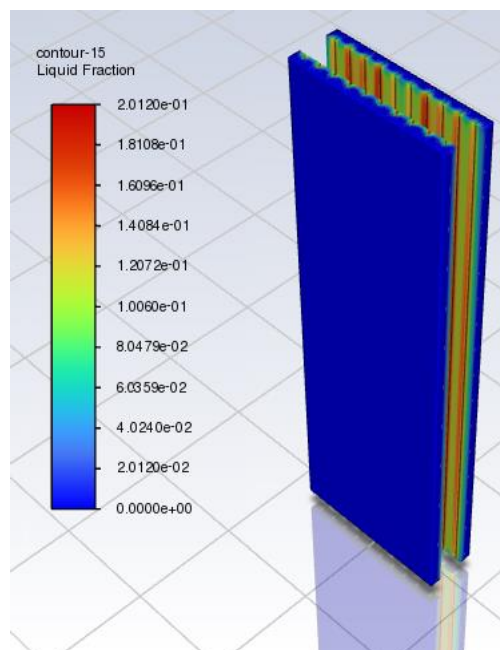


Figure 109 Simulated PCM-Fin structure liquid fraction Contour at 3600 s and 1C Rate.

Also in this analysis the peak of temperature difference of the active part is obtained at the end of the simulation. The value of the maximum temperature difference is 0.81 °C: a reduction of 32.5% compared to 1.2 °C obtained in the case of natural convection only.

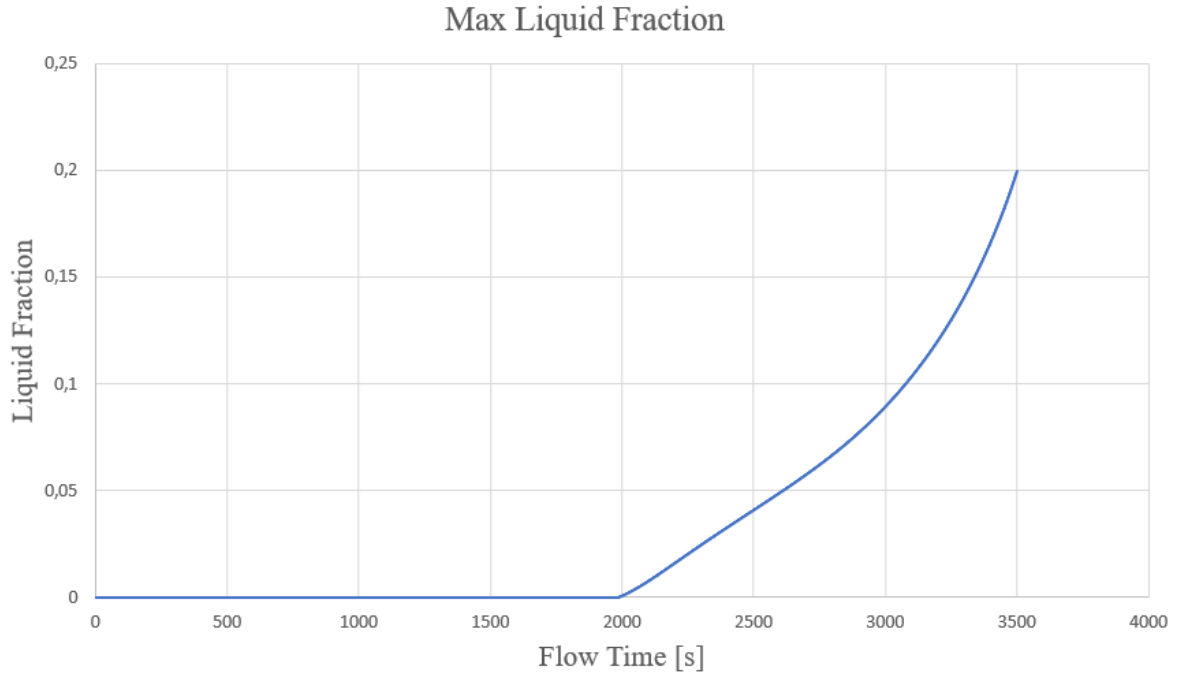


Figure 111 Simulated Max PCM-Fin structure liquid fraction @25°C and 1C Rate.

Thanks to the introduction of the finned system, an increase of 3 percentage points can be observed on the fraction of liquid formed during the discharge.

A more detailed analysis of the difference between pure PCM and PCM-Fin structure is conducted in the 2C discharge current case study. Below are **Figure 112** and **Figure 113** representing the temperature trend of the known points of the cell and the Contour of temperature obtained at the end of the discharge phase (discharge current 2C Rate).

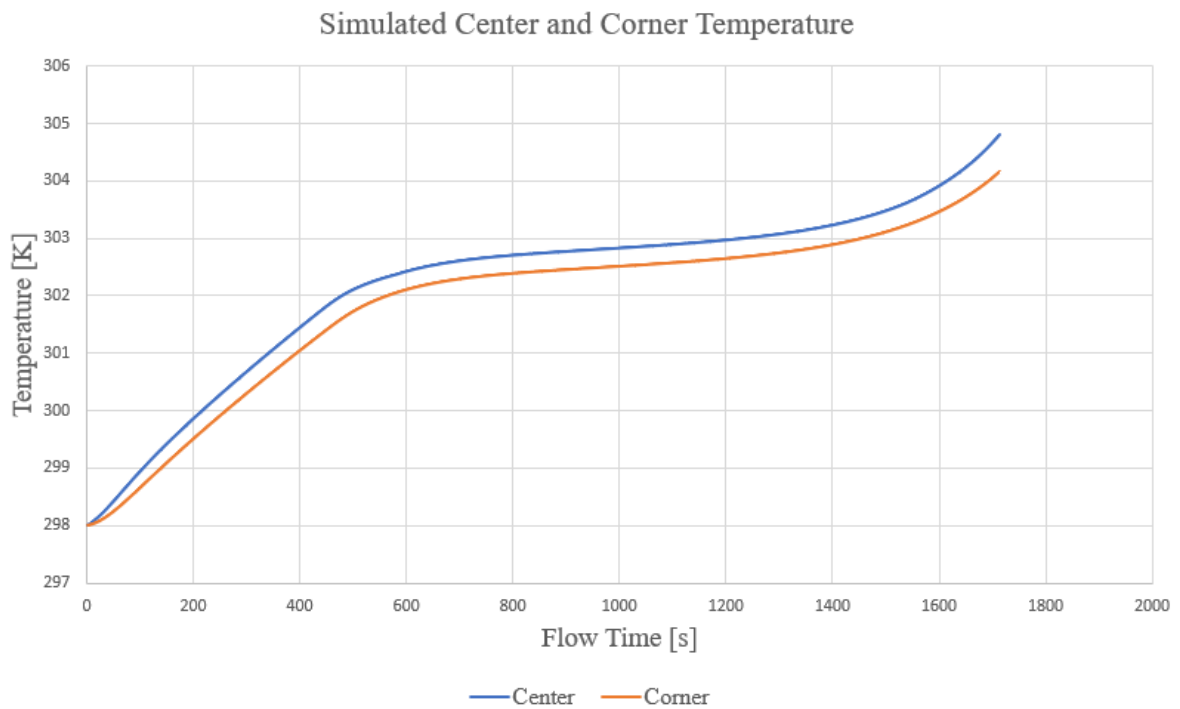
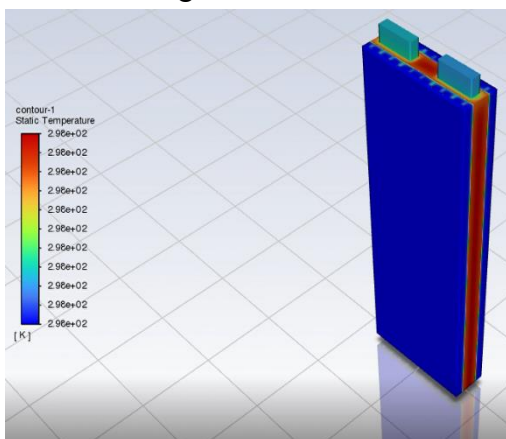


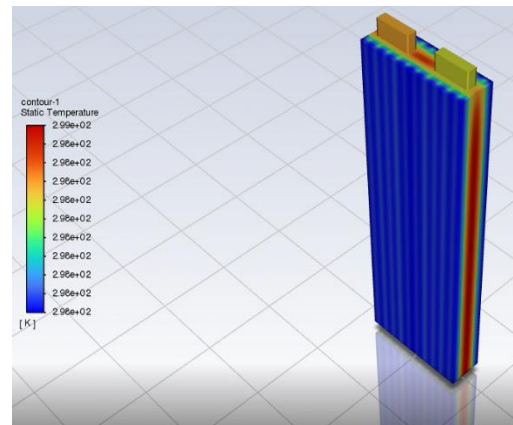
Figure 112 Simulated Temperature with PCM-Fin structure @25°C and 2C Rate.

PCM-Fin structure restricted the temperature of the center under 31.81 °C. The center temperature for natural convection was 45.64 °C. Compared to the case without PCM, the temperature trend suffers a maximum peak reduced by 30.3% which corresponds in absolute terms to an overall reduction of 13.83 °C.

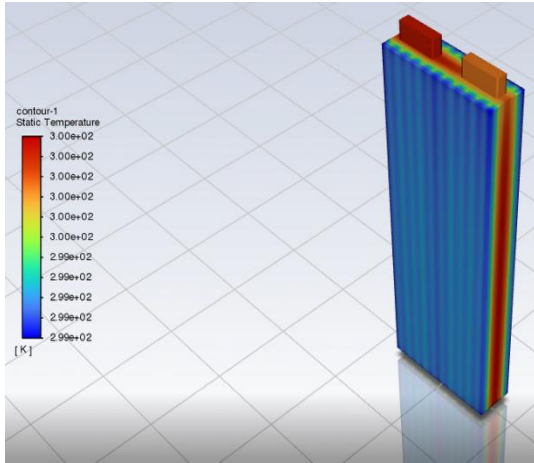
Figure 114 shows the battery temperature contours with the fins in 4 significant moments: (a) 15 seconds after the start of the discharge; (b) 102 seconds after the start of the simulation; (c) 300 seconds after the start of the simulation; (d) 650 seconds after the simulation begins.



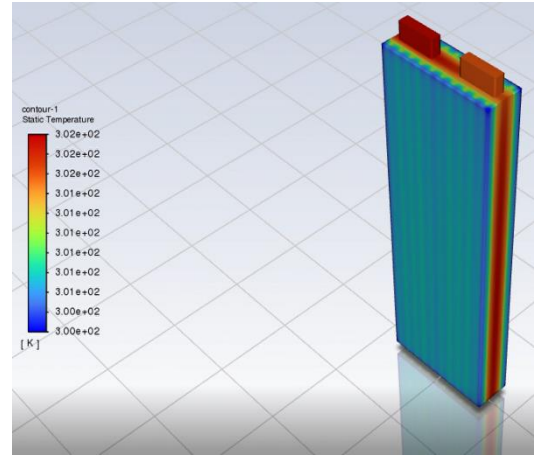
(a)



(b)



(c)



(d)

Figure 114 Simulated Temperature Contour with PCM-Fin structure at different time steps @25°C and 2C Rate.

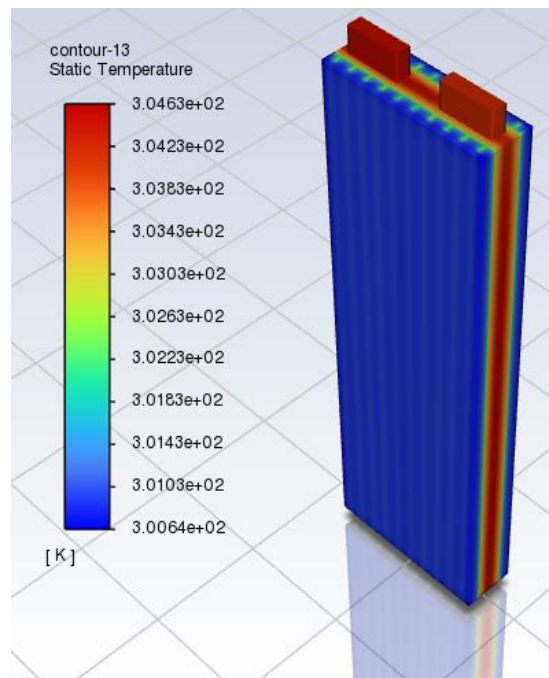


Figure 113 Simulated Temperature Contour with PCM-Fin structure at 1800 s @25°C and 2C Rate

Also in this analysis the peak of temperature difference of the active part is obtained at the end of the simulation. The value of the maximum temperature difference is equal to 1.57 °C: a reduction of 33.2% compared to 2.35 °C obtained in the case with only natural convection.

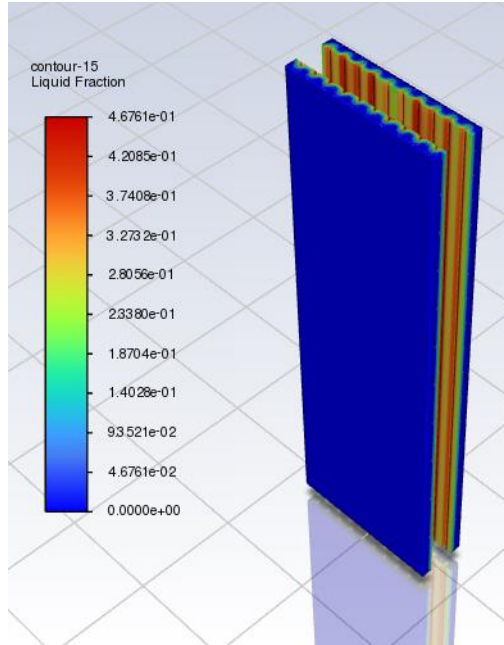


Figure 116 Simulated PCM-Fin structure liquid fraction Contour at 1800 s and 2C Rate.

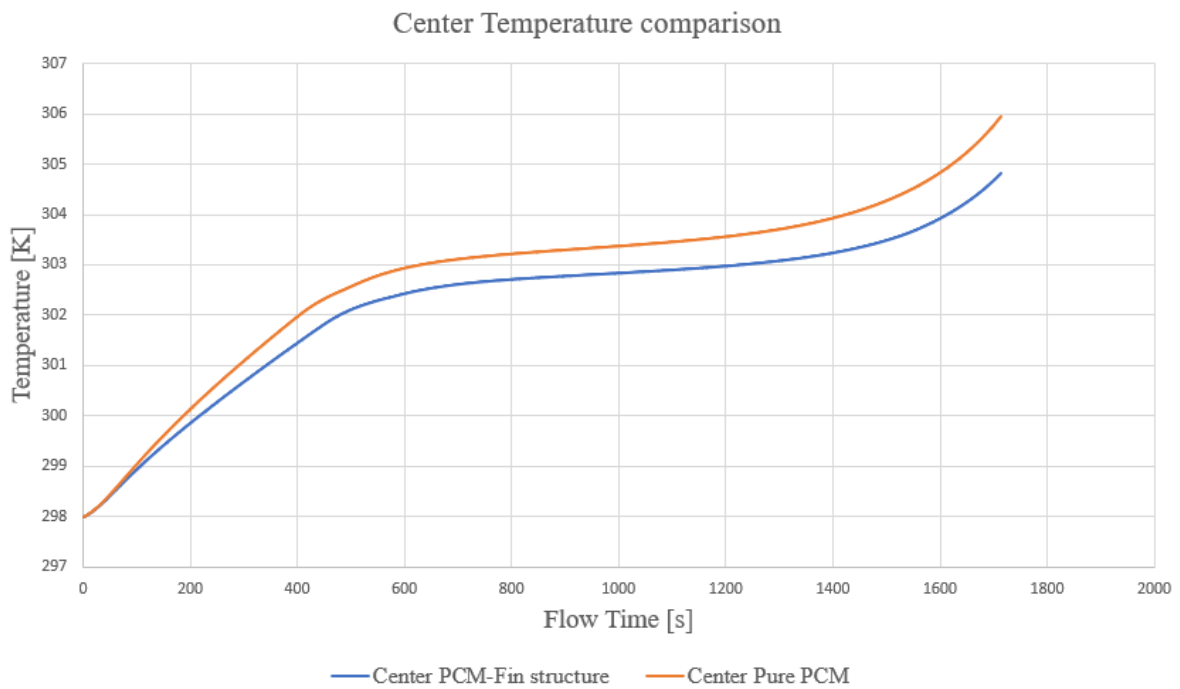


Figure 115 Comparison of Center Temperature for pure PCM and PCM-Fin structure @25°C and 2C Rate.

Figure 115 demonstrates the evolution of center Temperature under the cases of pure PCM and PCM-fin structure during 2C discharge. It is observed that Temperature of PCM-fin structure was reduced by attaching fins. By examining the representative time points, it can be found that the time to reach 299 K was the same in both cases as shown in **Figure 115**. The reason lies in that the edge of PCM layer contacting with the

aluminum baseplate firstly absorbed heat released by the batteries in the initial stage of discharge, such process is independent of the fin structure. However, as Center Temperature continued to exceed the minimum temperature of phase transition, the case of PCM-fin structure reduced the battery temperature ramp-up rate at the same discharge condition. The time to reach melting Temperature was also reduced comparing to the pure PCM case. The reason is that the heat can be timely transferred into the deeper layers of PCM through the conduction of fins. The phase change segment in which Center Temperature grew linearly was almost forming the temperature plateau in the case of PCM-fin structure, whose temperature rise was merely 1.2 °C. Although the introduction of fins slightly reduces the PCM volume, the fins influence the thermal behaviour of PCM due to improved heat conduction and natural convection. In particular, PCM-fin structure further enhanced the thermal performance of the battery by restraining the temperature rise in the mid-late discharging process.

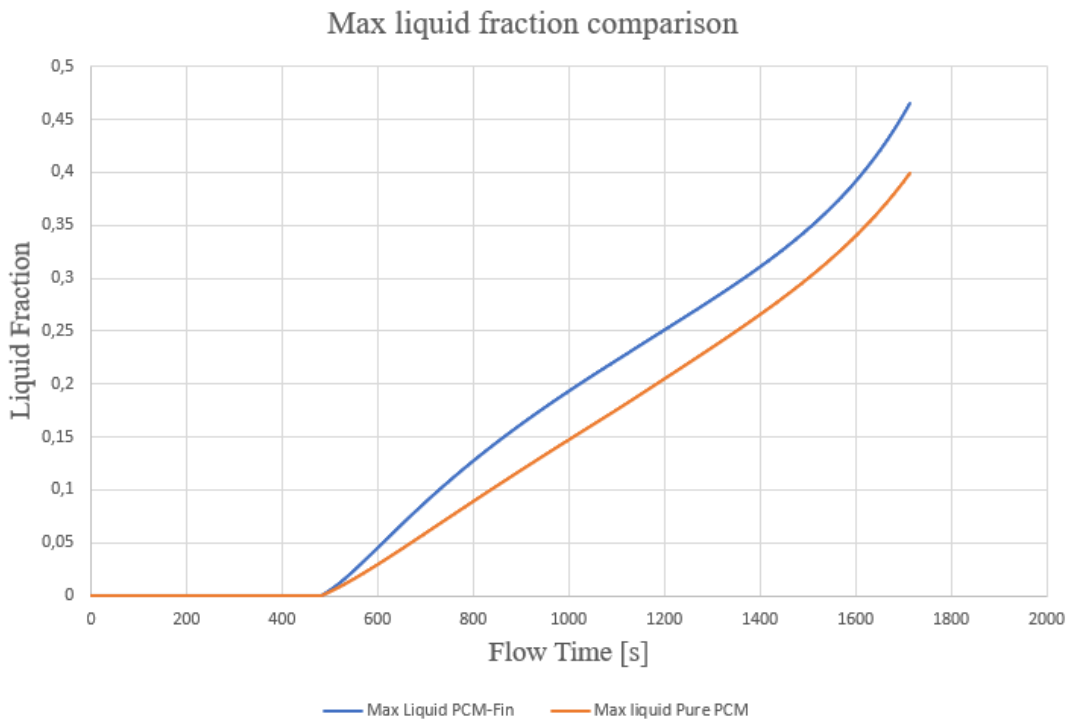


Figure 117 Comparison of Max liquid fraction for pure PCM and PCM-Fin structure @25°C and 2C Rate.

The final PCM liquid fraction achieved to 46.5% and was much higher than that of the pure PCM case, which was 39.3%. It demonstrates that PCM-fin structure can significantly improve the thermal performance of battery

1C Discharge Rate	T_{max} [°C]		ΔT_{max} [°C]	
Natural Convection	35.43		1.2	
Cooling Methods	T_{max} [°C]	Performance	ΔT_{max} [°C]	Performance
Heat Sinks	32.1	-9.3%	0.88	-27%
Pure PCM	30.4	-13.9%	1.05	-14.3%
PCM-Fin Structure	29.9	-15.6%	0.81	-32.5%

Table 22 Summary of the performance of the various cooling systems with 1C discharge current.

2C Discharge Rate	T_{max} [°C]		ΔT_{max} [°C]	
Natural Convection	45.64		2.35	
Cooling Methods	T_{max} [°C]	Performance	ΔT_{max} [°C]	Performance
Heat Sinks	39.5	-13.45%	1.79	-23.9%
Pure PCM	32.9	-27.8%	1.97	-16.2%
PCM-Fin Structure	31.8	-30.3%	1.57	-33.2%

Table 23 Summary of the performance of the various cooling systems with 2C discharge current.

5.5 Battery Pack performance

After analyzing the performance of the single cell, it is useful to observe what happens by placing in series 3 Li-ion cells. The geometrical characteristics and the mesh have been previously presented in **Chapter 4**. In this section, the results obtained from the simulations of the battery pack subject to simple natural convection, cooling with pure PCM and with PCM-Fin structure. Unlike what has been done for the single cell, in this case, a sensitivity analysis of the main geometric parameters characterizing the cooling systems will also be performed. The purpose is to monitor the effect of these parameters on the maximum temperature and the maximum temperature difference of the package.

Below are the **Figure 118** and **Figure 119** representing the maximum temperature trend of the battery pack and the Contour of temperature obtained at the end of the discharge phase (discharge current 1C Rate).

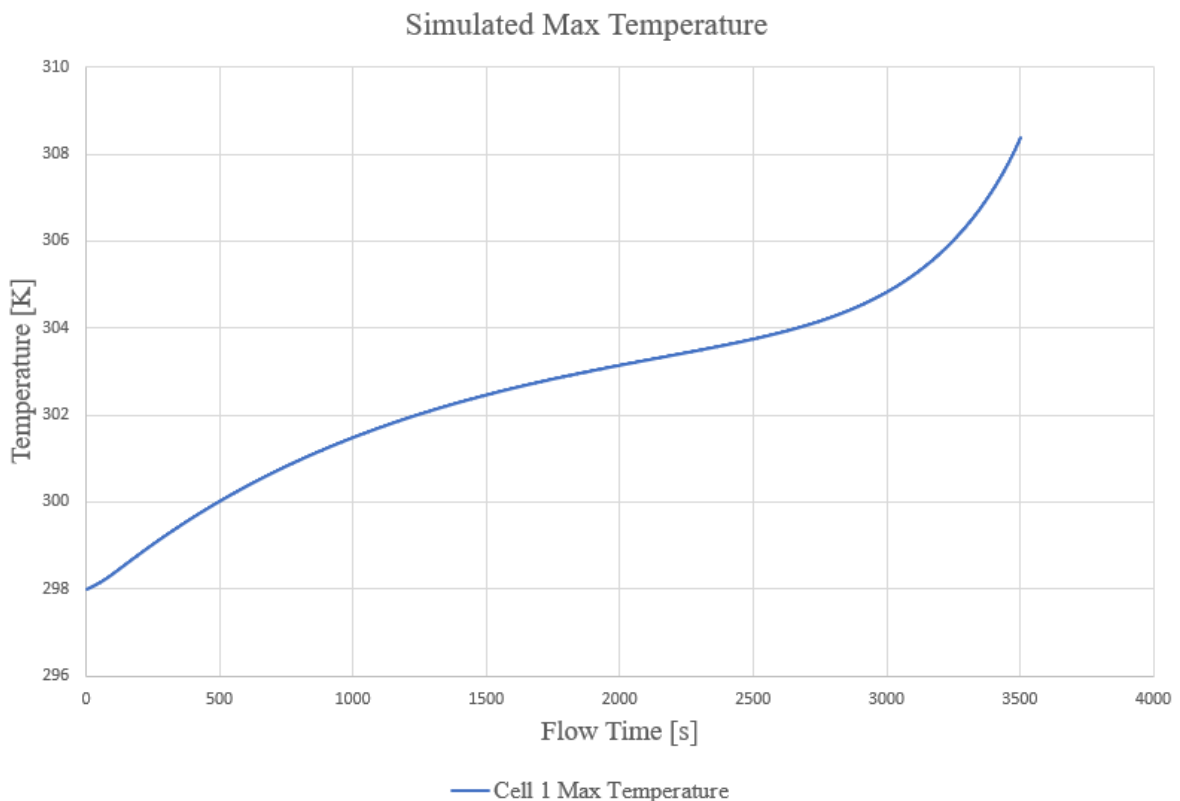


Figure 118 Simulated Max Temperature @25°C and 1C Rate.

In the Legend of the graph above it is indicated that the curve represents the maximum temperature of the first cell. The reason lies in the fact that, of the three cells, the maximum temperature is reached in the first. The difference in temperature compared to

the other two is in the order of tenths of a degree. For this reason, it was decided to conduct an analysis solely on the first cell. The temperature trend, however, is not dissimilar to that obtained in the case of the single cell.

More attention should be paid to the temperature difference in the battery pack, for this the Temperature Contour is presented.

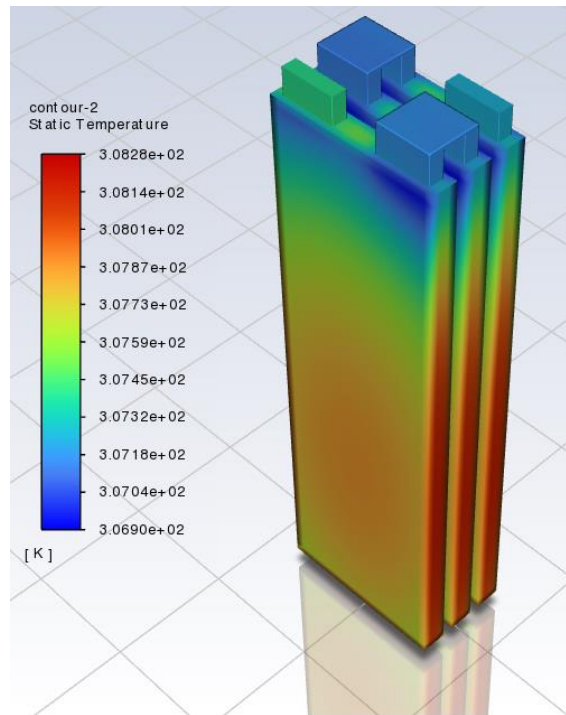


Figure 119 Simulated Battery Pack Temperature Contour at 3600 s @25°C and 1C Rate.

Again, the influence of the contact resistances between positive and negative Tab is reflected in a visible temperature difference. Compared to what was said in the case of the single cell, there are no additional considerations to do. The maximum temperature is 35.28 °C and the maximum temperature difference is 1.38 °C.

Below are the **Figure 120** and **Figure 122** representing the maximum temperature trend of the battery pack and the Contour of temperature obtained at the end of the discharge phase (discharge current 2C Rate).

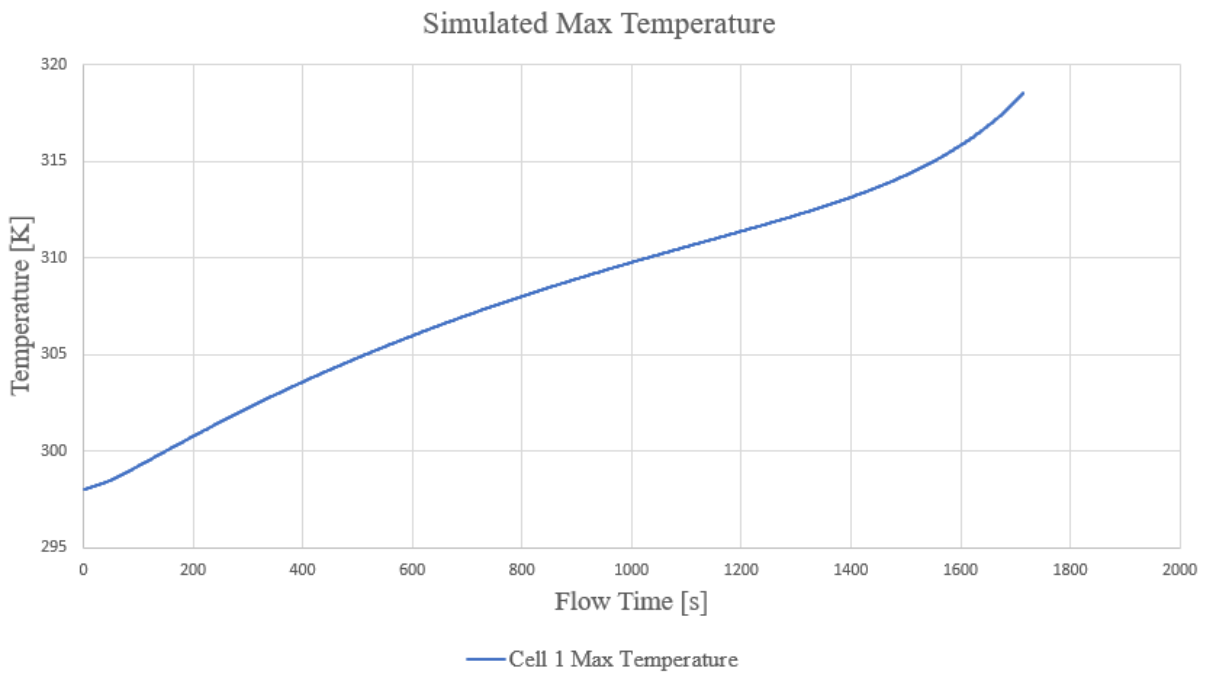
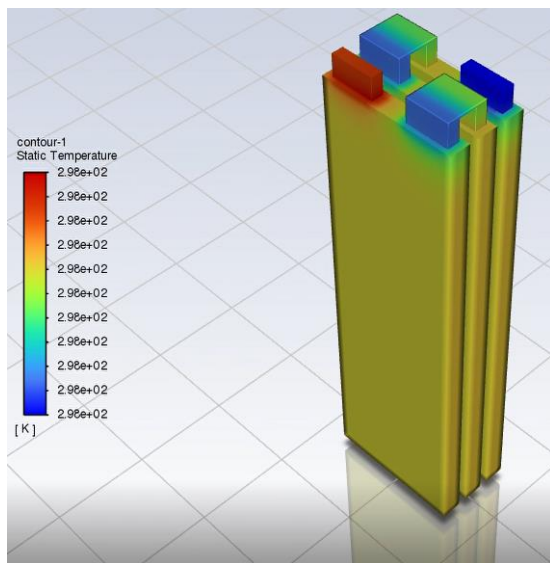
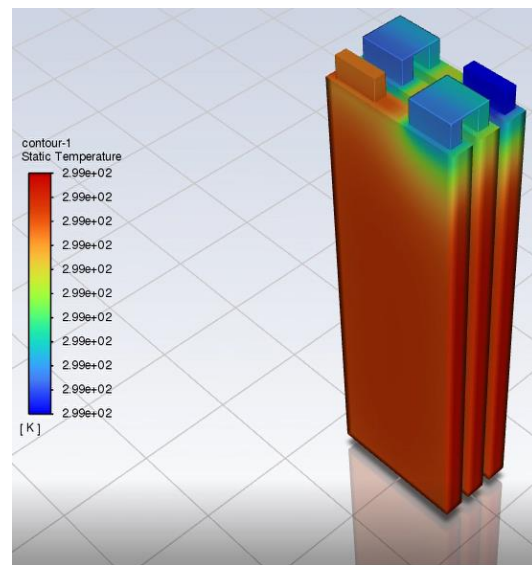


Figure 120 Simulated Max Temperature @25°C and 2C Rate.

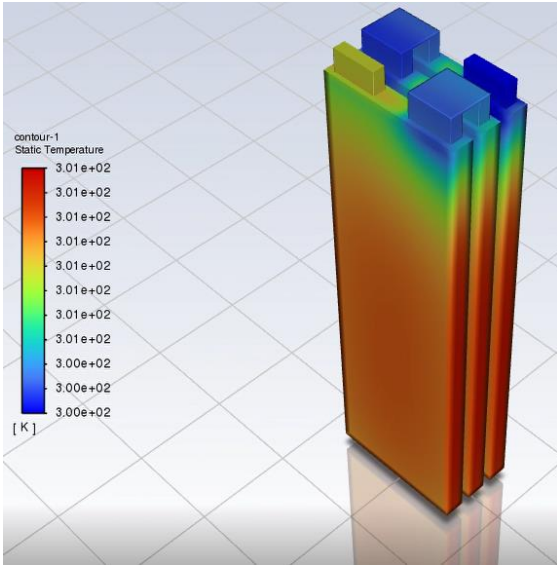
Figure 121 shows the temperature contours of the battery pack in 4 significant moments: (a) 15 seconds after the start of the discharge; (b) 102 seconds after the start of the simulation; (c) 300 seconds after the start of the simulation; (d) 650 seconds after the simulation begins.



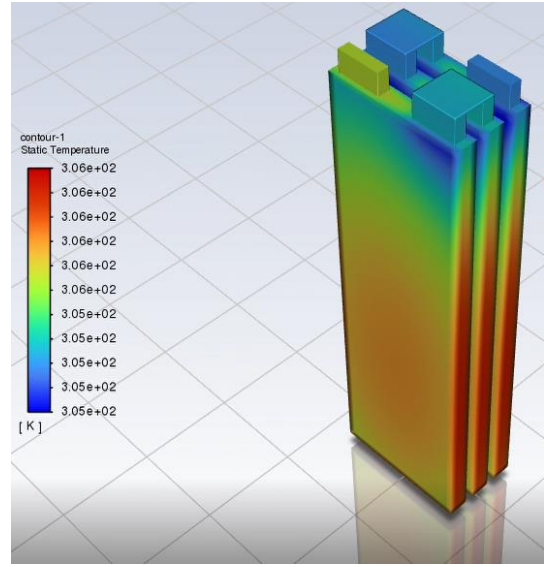
(a)



(b)



(c)



(d)

Figure 121 Simulated Battery Pack Temperature Contour at different time steps @25°C and 2C Rate.

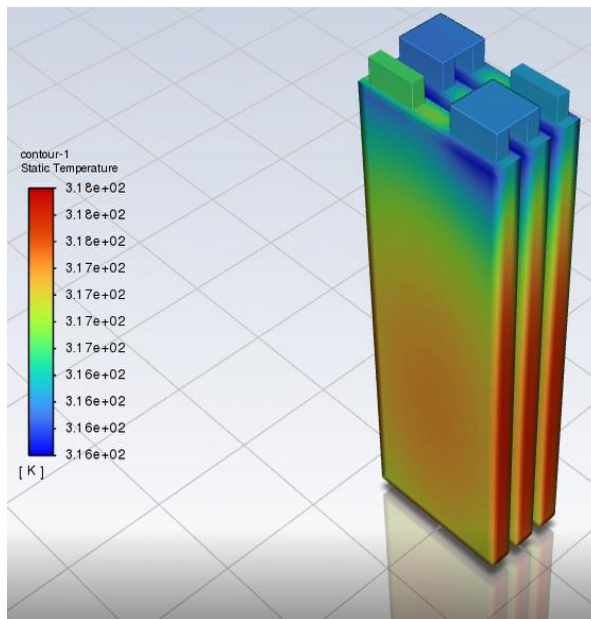


Figure 122 Simulated Battery Pack Temperature Contour at 1800 s @25°C and 2C Rate.

The maximum temperature value is 45.71 °C and the maximum temperature difference is 2.52 °C.

5.5.1 Battery Pack with pure PCM performance

The first method of cooling that is analysed is that which involves the insertion of blocks of phase change material between the active parts of the cells. The blocks have a thickness of 8 mm and this measure has been taken as a reference following a sensitivity analysis that will be presented in the following sections. Unlike the case with a single cell, in the design of the battery pack was inserted an aluminum case as a coating of the entire module: a choice dictated by the need to create a structure that accurately reflects the reality of the problem. In addition, the addition of the Case increases the heat exchange of the surfaces of the batteries not involved by contact with PCM. This ensures a clear reduction of the temperature difference in the entire module.

All aspects related to the physics of the PCM problem, such as the effect on the trend of temperature curves, have been described in the previous sections. This section shows the results of the application of PCM blocks on the walls of the battery pack cells.

Below are the **Figure 123** and **Figure 124** representing the maximum temperature trend of the battery pack and the Contour of temperature obtained at the end of the discharge phase (discharge current 1C Rate).

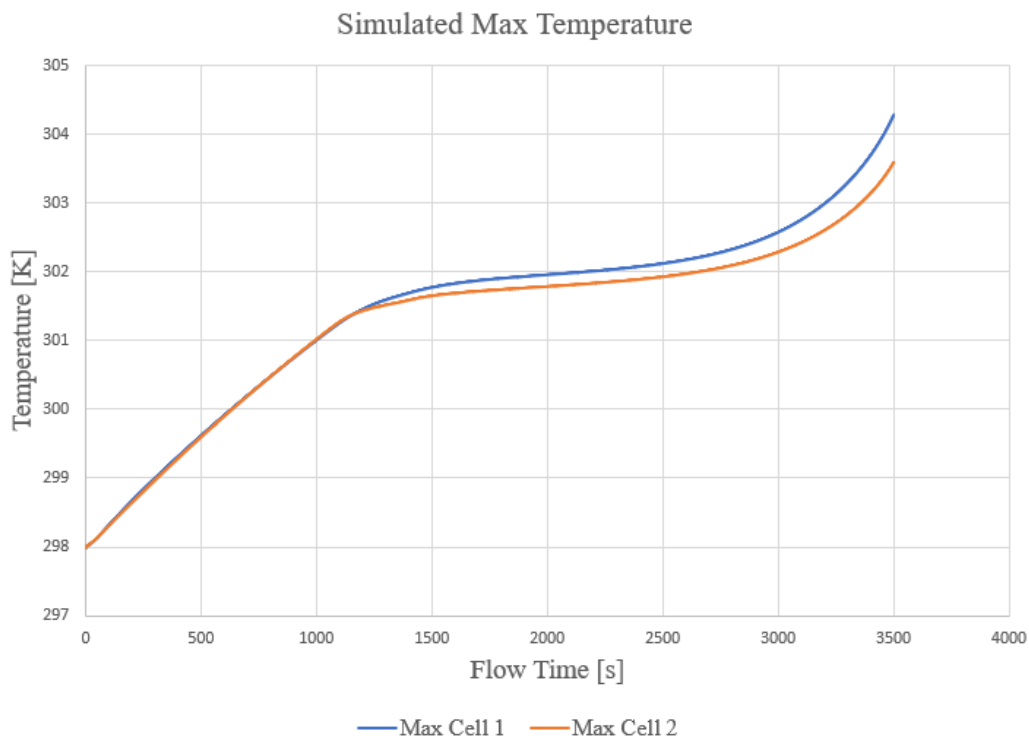


Figure 123 Simulated Battery Pack Max Temperature with PCM @25°C and 1C Rate.

Compared to the case with single cell, the phase of beginning liquefaction is anticipated in terms of time. The reason for the described behaviour is that the single block of PCM is adjacent to two cells (unlike the case with single-cell). In addition, the two curves represent the maximum temperature trend of two adjacent cells. At the beginning of the phase change, cell 2 undergoes a less marked temperature increase than cell 1. This is due to the fact that cell 2 is adjacent to two continuous blocks of PCM, while cell 1 has on one side a block of material and on the other is in direct contact with the Aluminum Case. The max temperature of the module for natural convection was 35.28 °C. Attributing to the characteristics of heat absorption with high latent heat, pure PCM module restricted the max temperature under 31.28 °C. Compared to the case without PCM, the temperature trend undergoes a maximum peak reduced by 11.33% which corresponds in absolute terms to an overall reduction of 4 °C. The physics of the problem is observable by the Contour of temperature shown below.

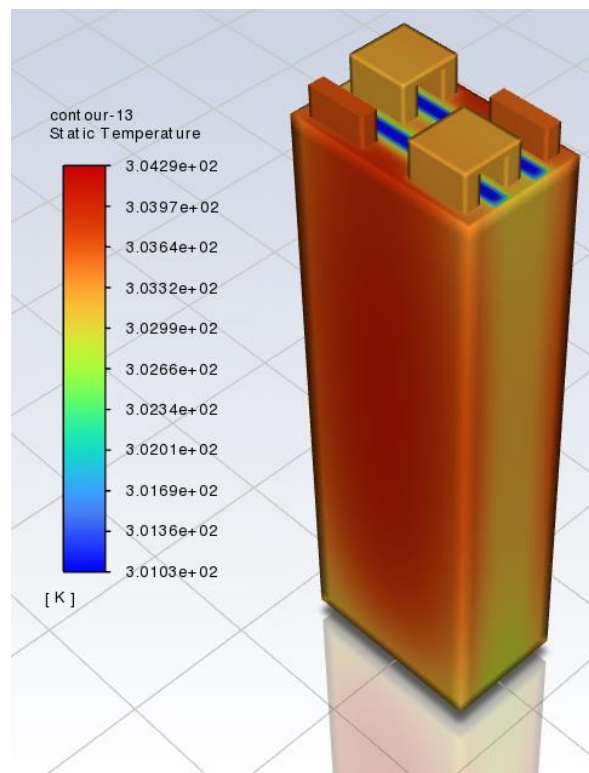


Figure 124 Simulated Battery Pack Temperature Contour with PCM at 3600 s @25°C and 1C Rate.

The temperature difference between the positive and negative Tabs is almost completely cancelled. It is possible to say that the influence of the contact resistance is negligible. In addition, unlike in natural convection-only cases, adding phase change material results in long uniformity in the Y direction of heat distribution. The biggest temperature difference

occurs between cell 1 and cell 2. The reason lies in the physics of the problem, which sees cell 2 subject to increased cooling. The maximum temperature difference is found at the end of the discharge phase and corresponds to about 1.55 °C: an increase of 12% compared to 1.38 °C obtained in the case with only natural convection. A reduction that is on differences of tenths of a degree but, compared with the overall reduction of maximum temperature, can be considered an additional useful effect.

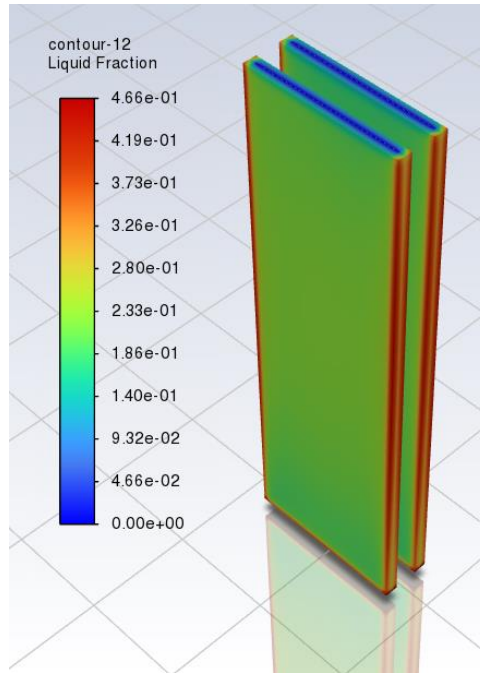


Figure 126 Simulated Battery Pack Liquid Fraction Contour at 3600 s @25°C and 1C Rate.

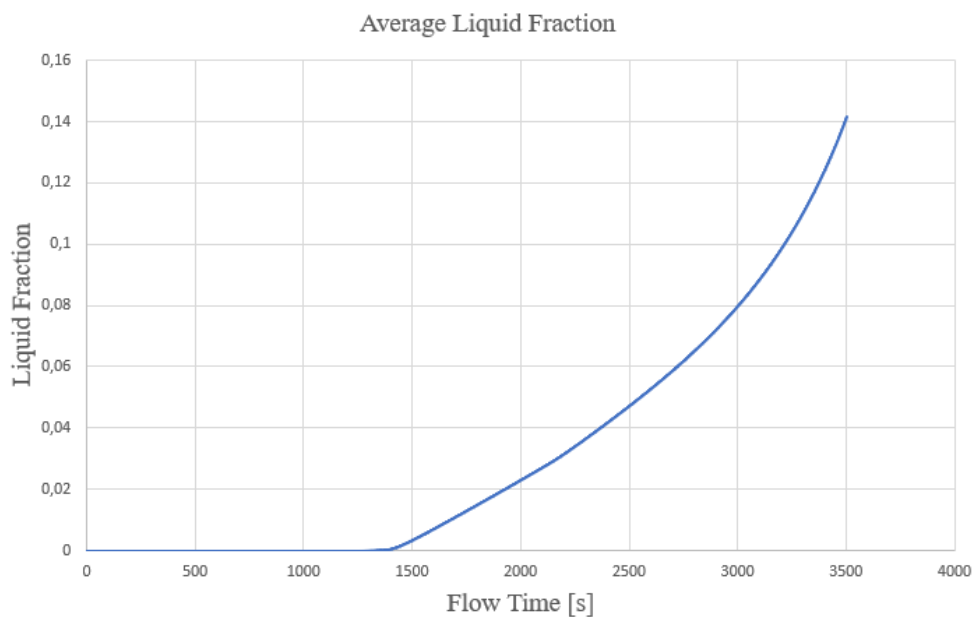


Figure 125 Simulated Battery Pack Average PCM liquid fraction @25°C and 1C Rate.

Below are the **Figure 127** and **Figure 128** representing the maximum temperature trend of the battery pack and the Contour of temperature obtained at the end of the discharge phase (discharge current 2C Rate).

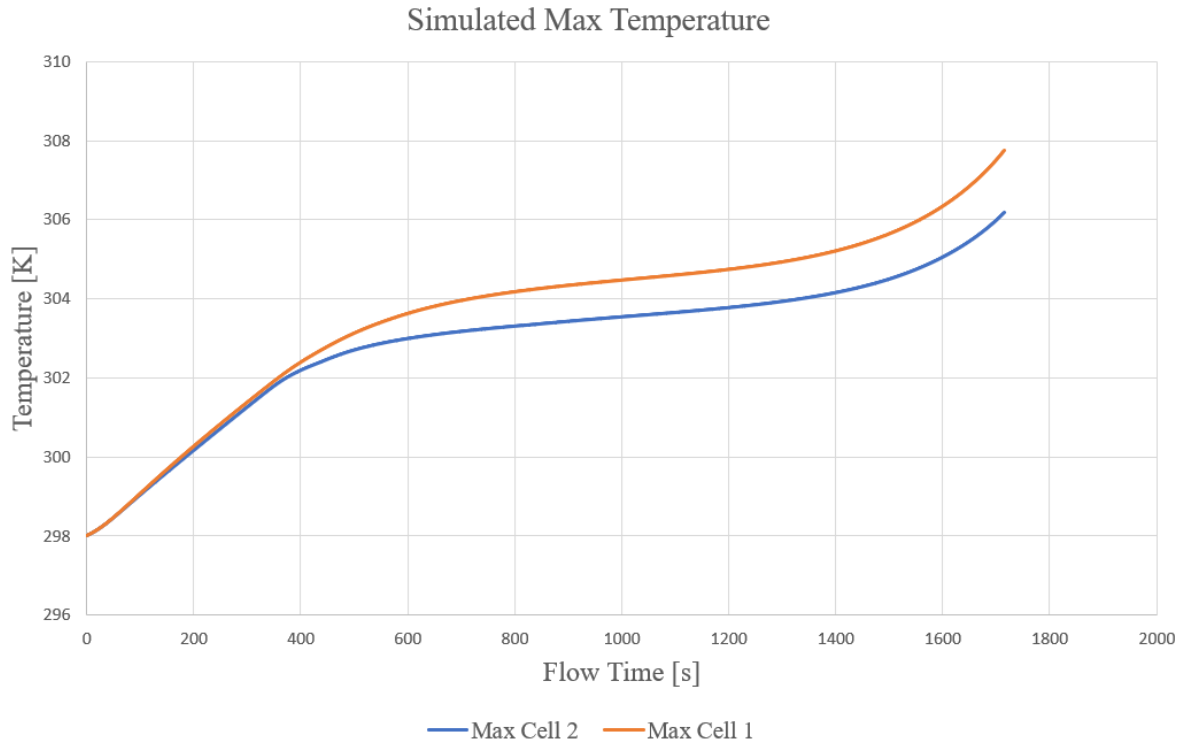


Figure 127 Simulated Battery Pack Max Temperature with PCM @25°C and 2C Rate

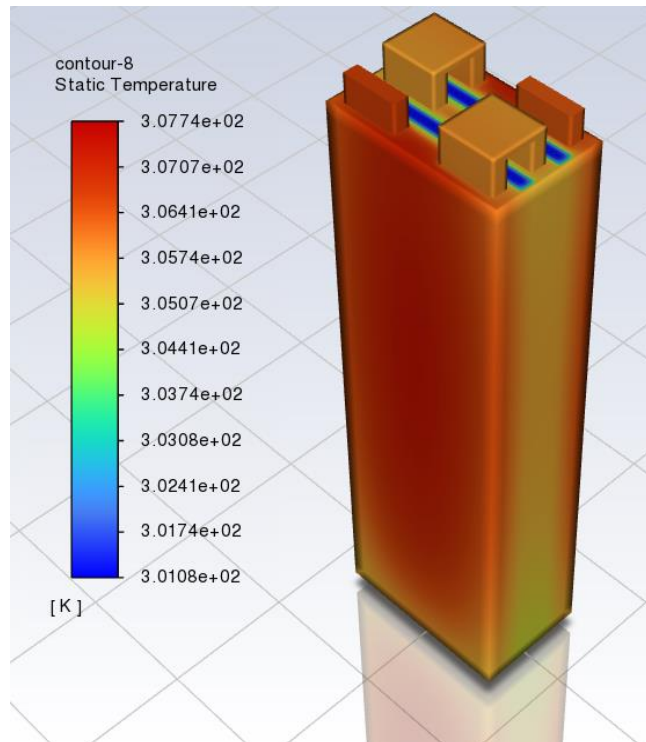


Figure 128 Simulated Battery Pack Temperature Contour with PCM at 1800 s @25°C and 2C Rate.

The max temperature of the module for natural convection was 45.71 °C. Attributing to the characteristics of heat absorption with high latent heat, pure PCM module restricted the max temperature under 34.74 °C. Compared to the case without PCM, the temperature trend suffers a maximum peak reduced by 24% which corresponds in absolute terms to an overall reduction of 11 °C.

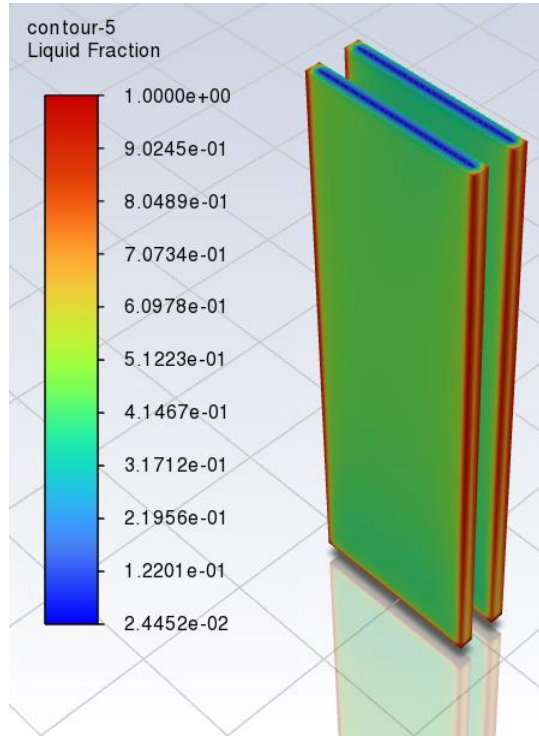


Figure 130 Simulated Battery Pack Liquid Fraction Contour at 1800 s @25°C and 2C Rate.

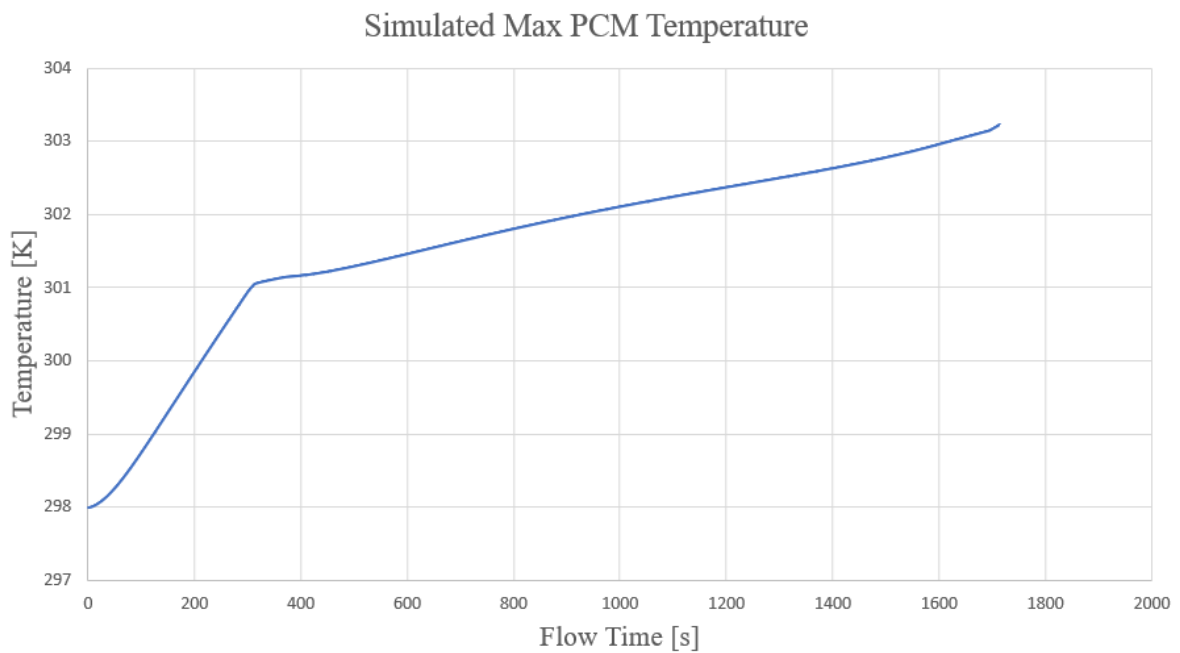


Figure 129 Simulated Battery Pack Max PCM Temperature @25°C and 2C Rate.

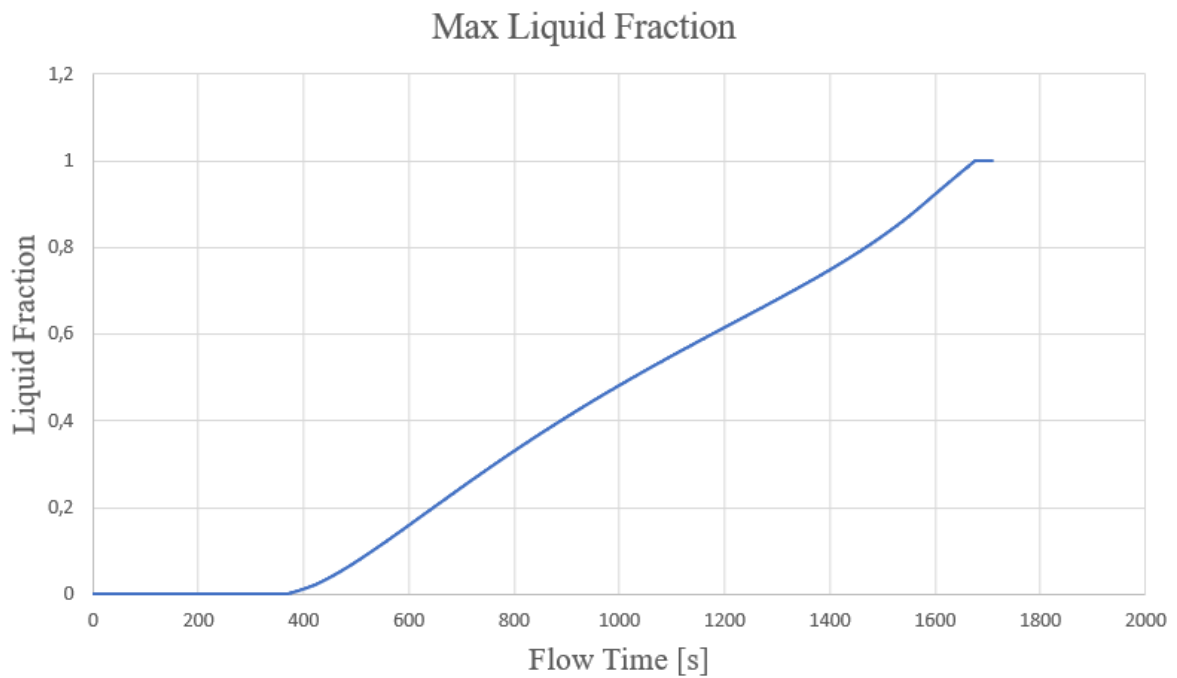


Figure 131 Simulated Battery Pack Max PCM liquid fraction @25°C and 2C Rate.

In this case, at 1700 seconds of simulation, a part of the PCM has reached the complete phase change and as **Figure 131** shows, the temperature trend undergoes a sudden increase. It seems to observe the behaviour of a material that, exceeding the temperature value of the limit curve, is overheated following a hypothetical isobar.

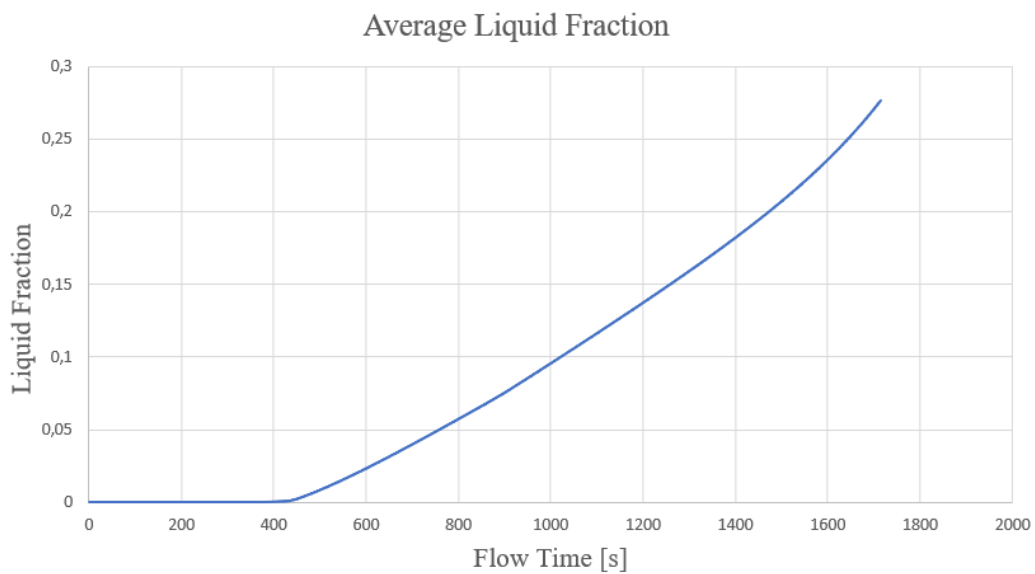


Figure 132 Simulated Battery Pack Average PCM liquid fraction @25°C and 2C Rate.

5.5.2 Effect of PCM thickness

In this section, the effect of different PCM thicknesses was investigated. The influence of PCM thicknesses with 5 mm, 8 mm and 11 mm were simulated. **Figure 133** and **Figure 134** illustrate the temperature contours of the battery module with different PCM thicknesses at the end of 2C discharge. Apparently, with the augment of PCM thickness from 5 mm to 11 mm, the temperature distribution was remarkably improved.

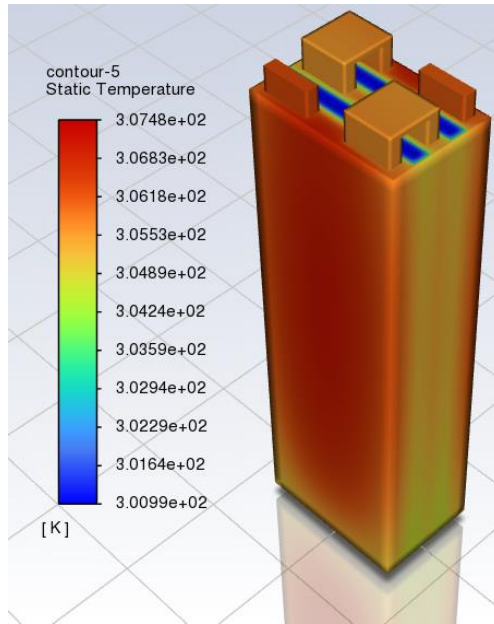


Figure 134 Simulated Battery Pack Temperature Contour with 11 mm PCM at 1800 s @25°C and 2C Rate.

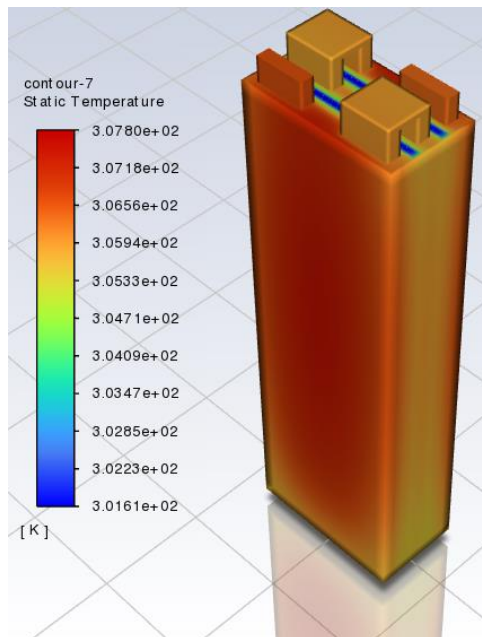


Figure 133 Simulated Battery Pack Temperature Contour with 5 mm PCM at 1800 s @25°C and 2C Rate.

Figure 135 shows the maximum temperature of the central cell under different PCM thicknesses at the end of 2C discharge.

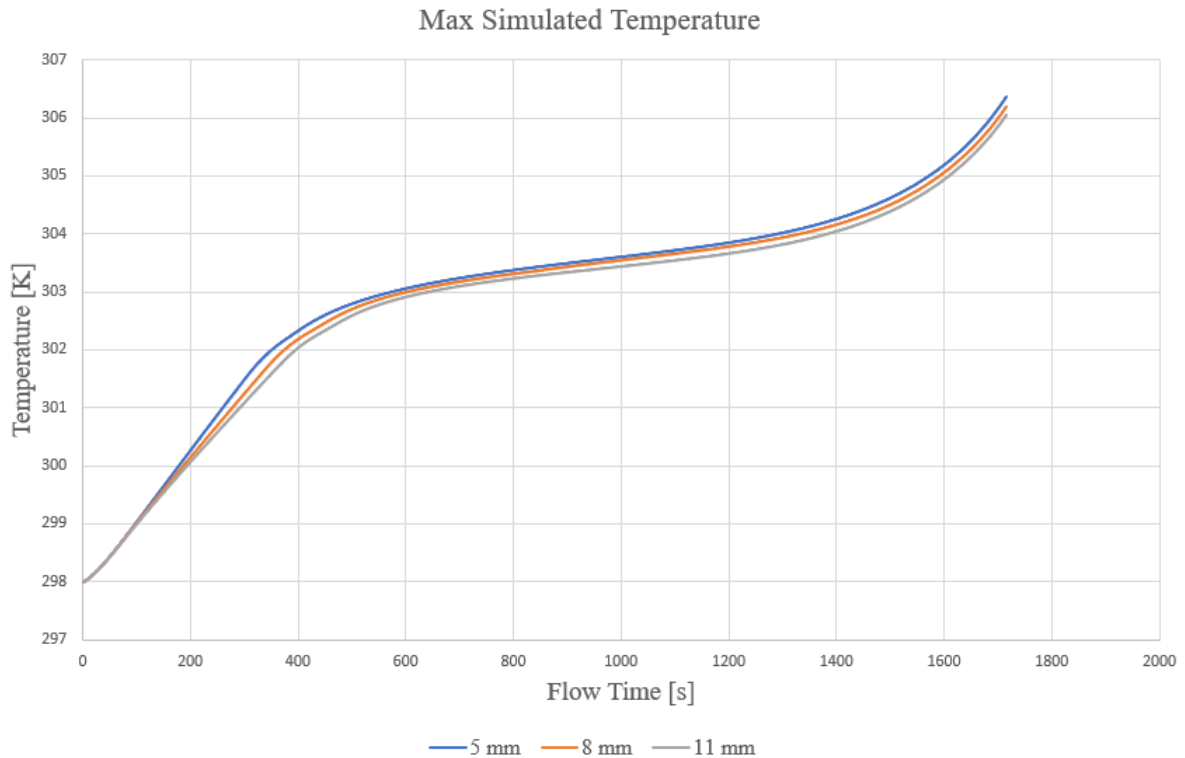


Figure 135 Simulated Battery Pack Max Temperature with different PCM thickness @25°C and 2C Rate.

Figure 136 shows the temperature difference (ΔT_{max}) of battery module at the end of 2C discharge. When the thickness was 5 mm, the maximum temperature of the cell was 33.7 °C and the temperature difference of battery module was 3.35 °C. When the thickness was 8 mm, the maximum temperature of the cell was 33.15 °C and the temperature difference of the battery module was 3.25 °C. For the case of $h = 11$ mm, the maximum temperature of the cell decreased to 33.05 °C, and the temperature difference was limited in 3.22 °C, which means $h = 11$ mm can maintain the suitable temperature performance. Therefore, the PCM with a thickness of 5 mm is not sufficient for controlling the temperature rise of the battery. As the PCM thickness increased, the maximum temperature of the central cell and the temperature difference of the battery module were in the desired temperature range. As the thickness of PCM increases, the influence of PCM on the maximum temperature becomes increasingly rare. It is not necessary to continue increasing the thickness, as the difference between $h=8$ mm and $h=11$ m is only one-tenth of a degree. Results are consistent with those from literature analysis [82].

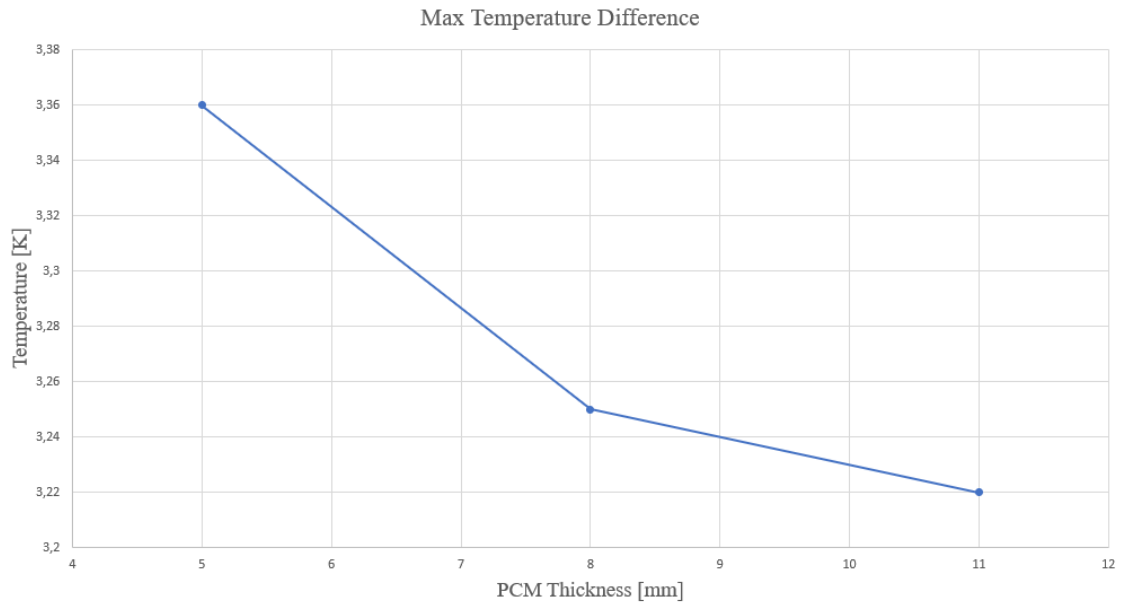


Figure 136 Simulated Battery Pack Max Temperature difference (ΔT_{max}) with PCM Thickness @25°C and 2C Rate.

Figure 137 shows that the maximum PCM liquid fraction in $h = 5$ mm was 100%, which means that the PCM has completely melted in the final stage of discharge. It indicates that in this case, a rapid accumulation of heat in the later period and rapid temperature rise of the battery occurred. Further increasing the thickness, the maximum temperature difference tends to a constant value.

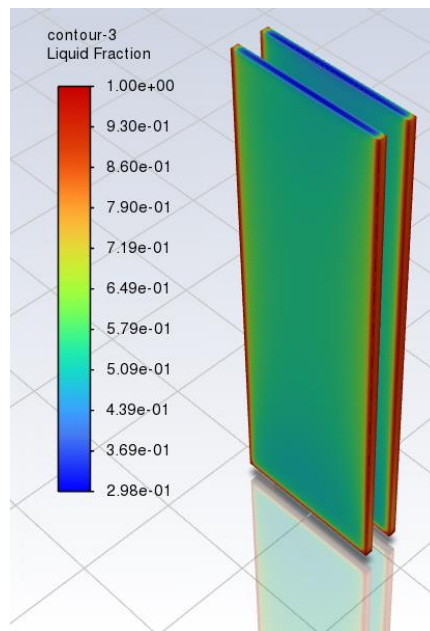


Figure 137 Simulated Battery Pack Liquid Fraction Contour with 5 mm PCM at 1800 s @25°C and 2C Rate.

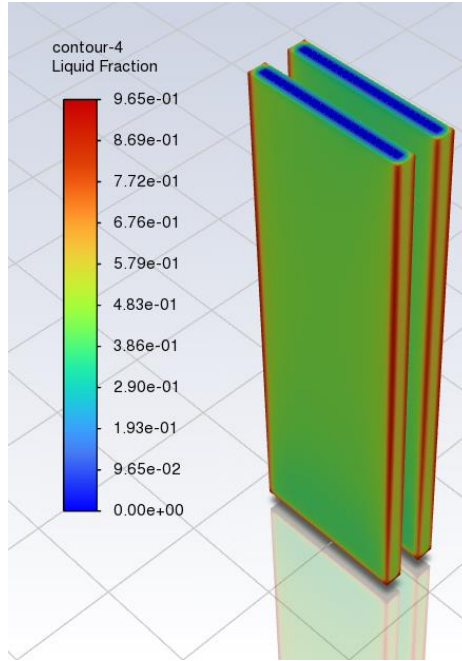


Figure 139 Simulated Battery Pack Liquid Fraction Contour with 11 mm PCM at 1800 s @25°C and 2C Rate.

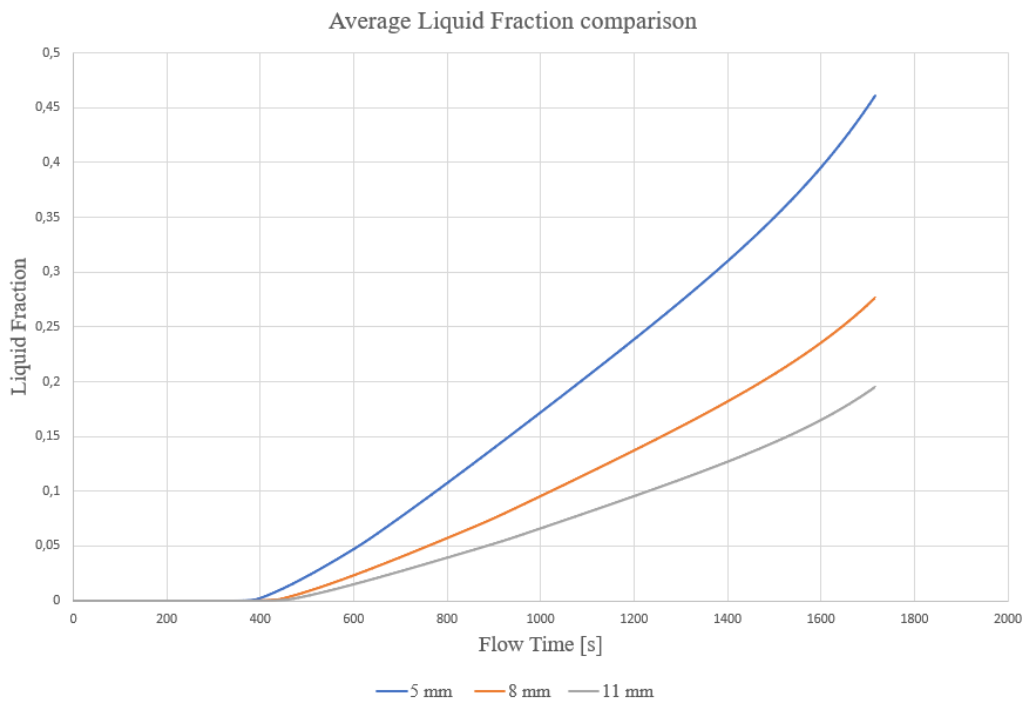


Figure 138 Simulated Battery Pack Average liquid fraction comparison with PCM Thickness @25°C and 2C Rate.

Such results imply that although the thicker PCM can lead a lower temperature and temperature differences of batteries, the effect of the thicker PCM than 11 mm in this study is minor. In addition, the thicker the PCM is, the heavier and more complex the structure of heat sink is, as well as higher cost in the practical applications. Consequently, these results imply that a PCM thickness of 8 mm is enough in this study.

5.5.3 Battery Pack with PCM-Fin structure performance

The second method of cooling that is analysed is the one that involves the insertion of PCM-Fin structure between the active parts of the cells. The PCM blocks have a thickness of 8 mm and the fin configuration is the same that is used for the analysis of the individual battery. These measures were taken as a reference following a sensitivity analysis which will be presented in the following sections.

All aspects related to the physics of the PCM problem, such as the effect on the trend of temperature curves, have been described in the previous sections. This section shows the results of the application of the PCM-Fin structure on the walls of the battery pack cells.

Below are **Figure 140** and **Figure 141** representing the maximum temperature trend of the battery pack and the Contour of temperature obtained at the end of the discharge phase (discharge current 1C Rate).

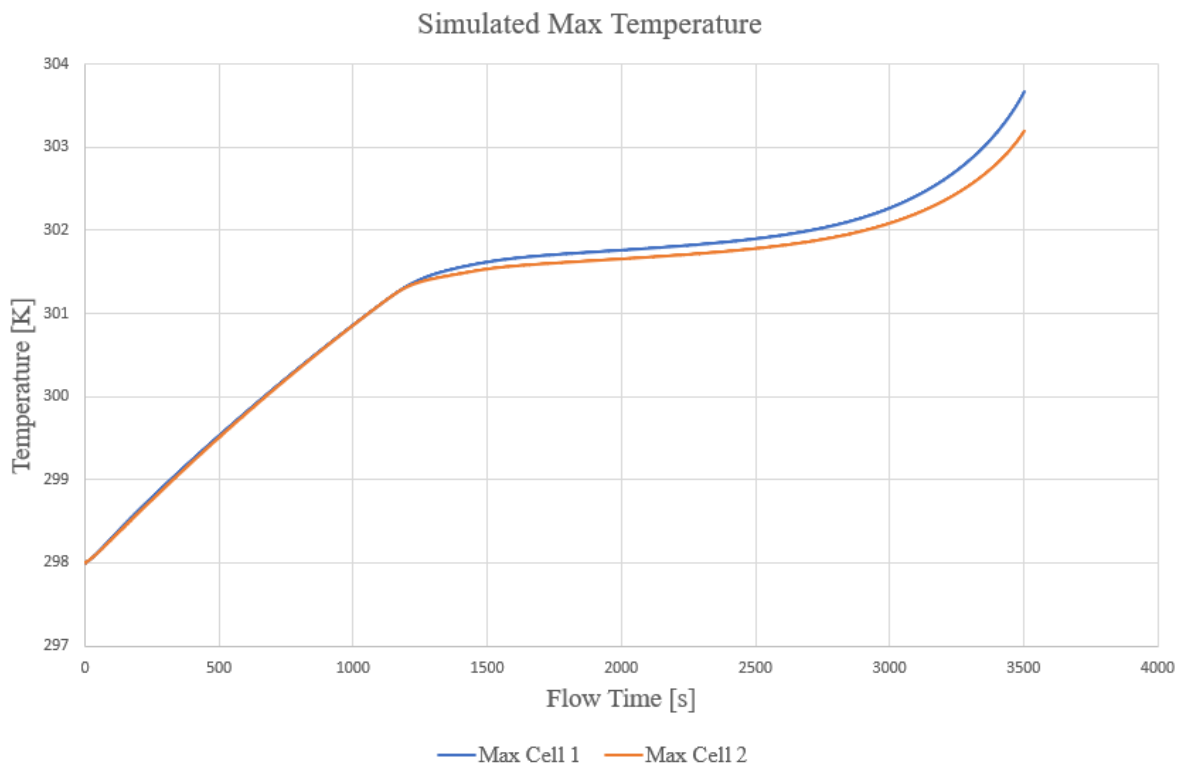


Figure 140 Simulated Battery Pack Max Temperature with PCM-Fin Structure @25°C and 1C Rate.

The max temperature of the module for natural convection was 35.28 °C. Attributing to the characteristics of heat absorption with high latent heat, pure PCM module restricted the max temperature under 30.67 °C. Compared to the case without PCM-Fin, the

temperature trend suffers a reduced maximum peak of 13.1% which corresponds in absolute terms to an overall reduction of 4.61 °C. The physics of the problem is clearly observable by the Contour of temperature below.

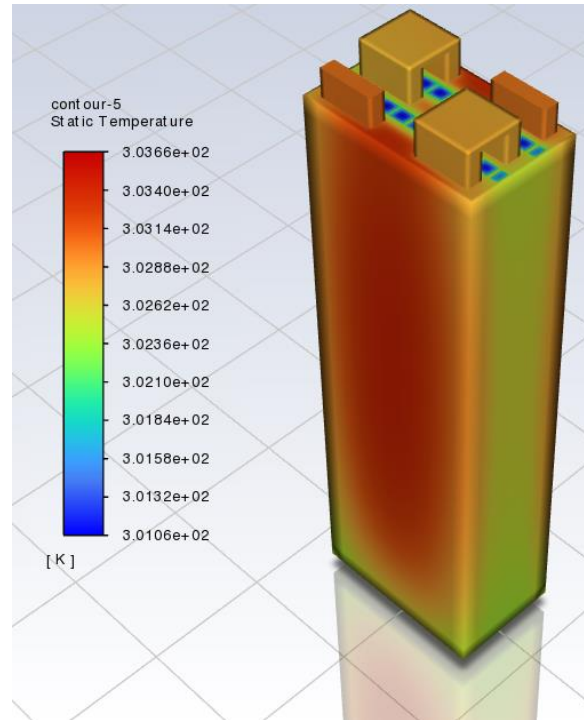


Figure 141 Simulated Battery Pack Temperature Contour with PCM-Fin structure at 3600 s @25°C and 1C Rate.

The biggest temperature difference occurs between cell 1 and cell 2. The reason lies in the physics of the problem, which sees cell 2 subject to increased cooling. The maximum temperature difference is found at the end of the discharge phase and corresponds to about 1.25 °C: a reduction of 9.5% compared to 1.38 °C obtained in the case of natural convection only. A reduction that is on differences of tenths of a degree but, compared with the overall reduction of maximum temperature, can be considered an additional useful effect.

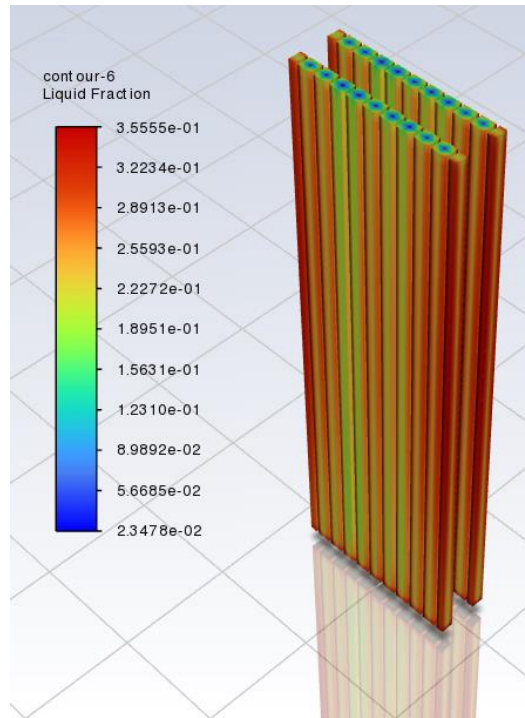


Figure 143 Simulated Battery Pack Liquid Fraction Contour with PCM-Fin structure at 3600 s @25°C and 1C Rate.

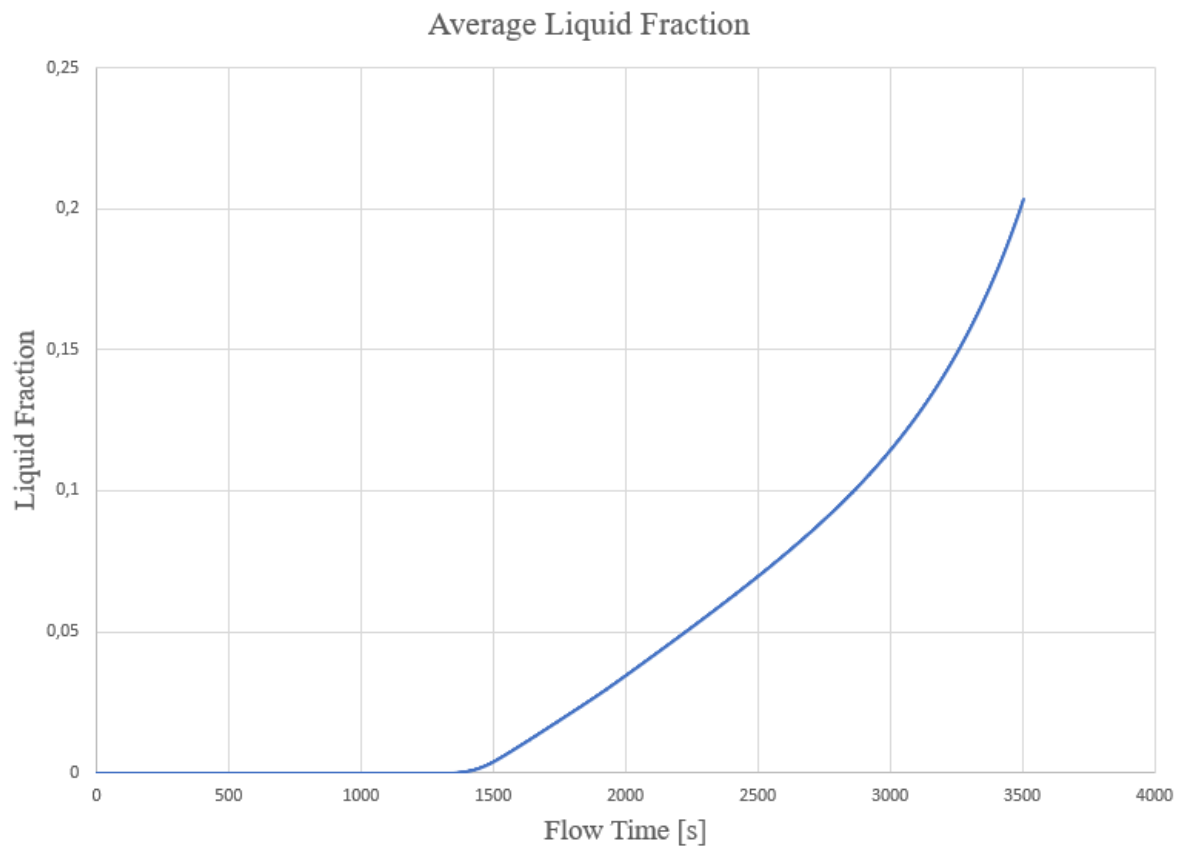


Figure 142 Simulated Battery Pack with PCM-Fin structure Average PCM liquid fraction @25°C and 1C Rate.

The maximum liquid fraction value is lower than in the case of Pure PCM, but the average distribution of liquid fraction at the end of the simulation is 7 percentage points higher in the case of the PCM-Fin structure. The reason lies in the greater uniformity of heat distribution given by the presence of heat sinks. The non-homogeneity of the Contour representing the liquid fraction is due to problems related to the mesh of the Heat Sinks.

Below are **Figure 144** and **Figure 146** representing the maximum temperature trend of the battery pack and the Contour of temperature obtained at the end of the discharge phase (discharge current 2C Rate).

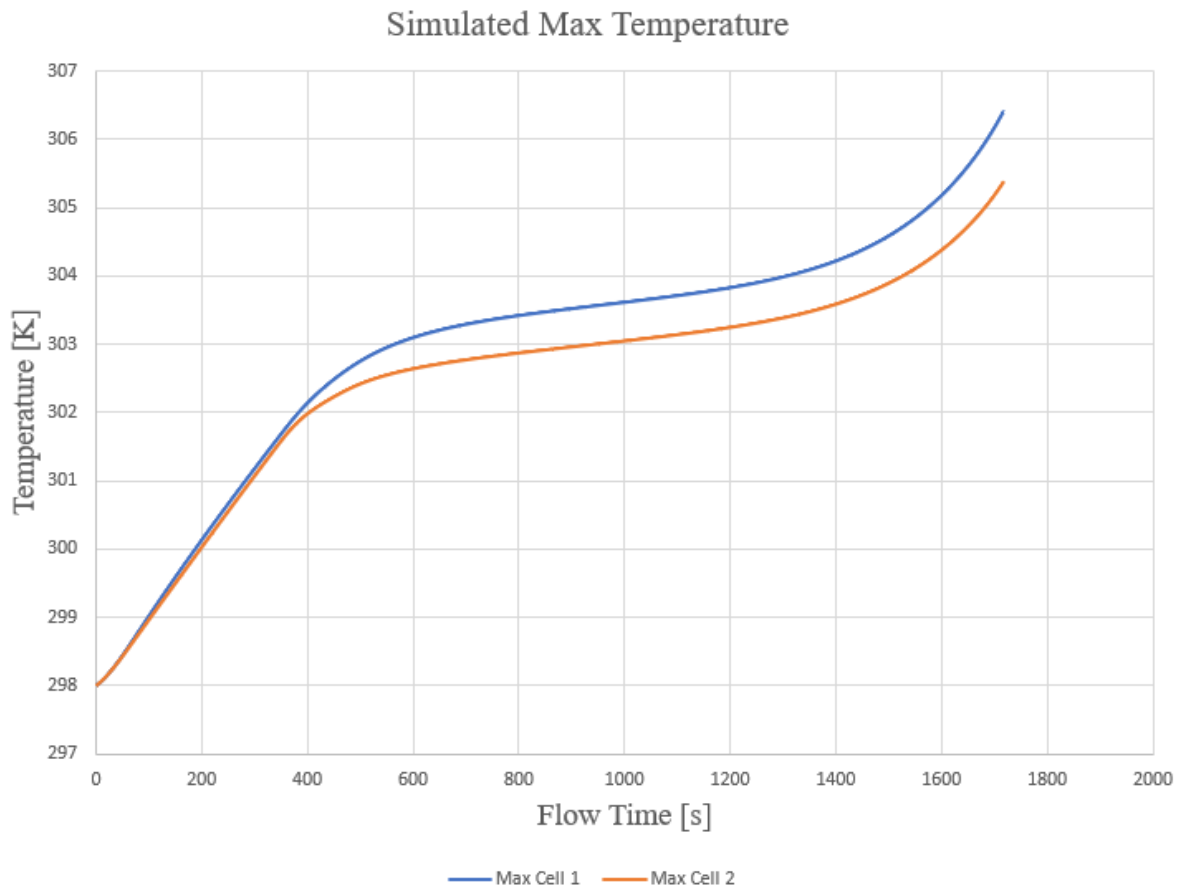


Figure 144 Simulated Battery Pack Max Temperature with PCM-Fin Structure @25°C and 2C Rate.

The max temperature of the module for natural convection was 45.71 °C. Attributing to the characteristics of heat absorption with high latent heat, pure PCM module restricted the max temperature under 33.4 °C. Compared to the case without PCM-Fin, the temperature trend suffers a reduced maximum peak of 26.9%, which corresponds in absolute terms to an overall reduction of 12.31 °C. The physics of the problem is observable by the Contour temperature shown below.

Figure 145 shows the temperature contours of the battery pack in 4 significant moments of time: (a) 15 seconds after the start of the discharge; (b) 102 seconds after the start of the simulation; (c) 300 seconds after the start of the simulation; (d) 650 seconds after the simulation begins.

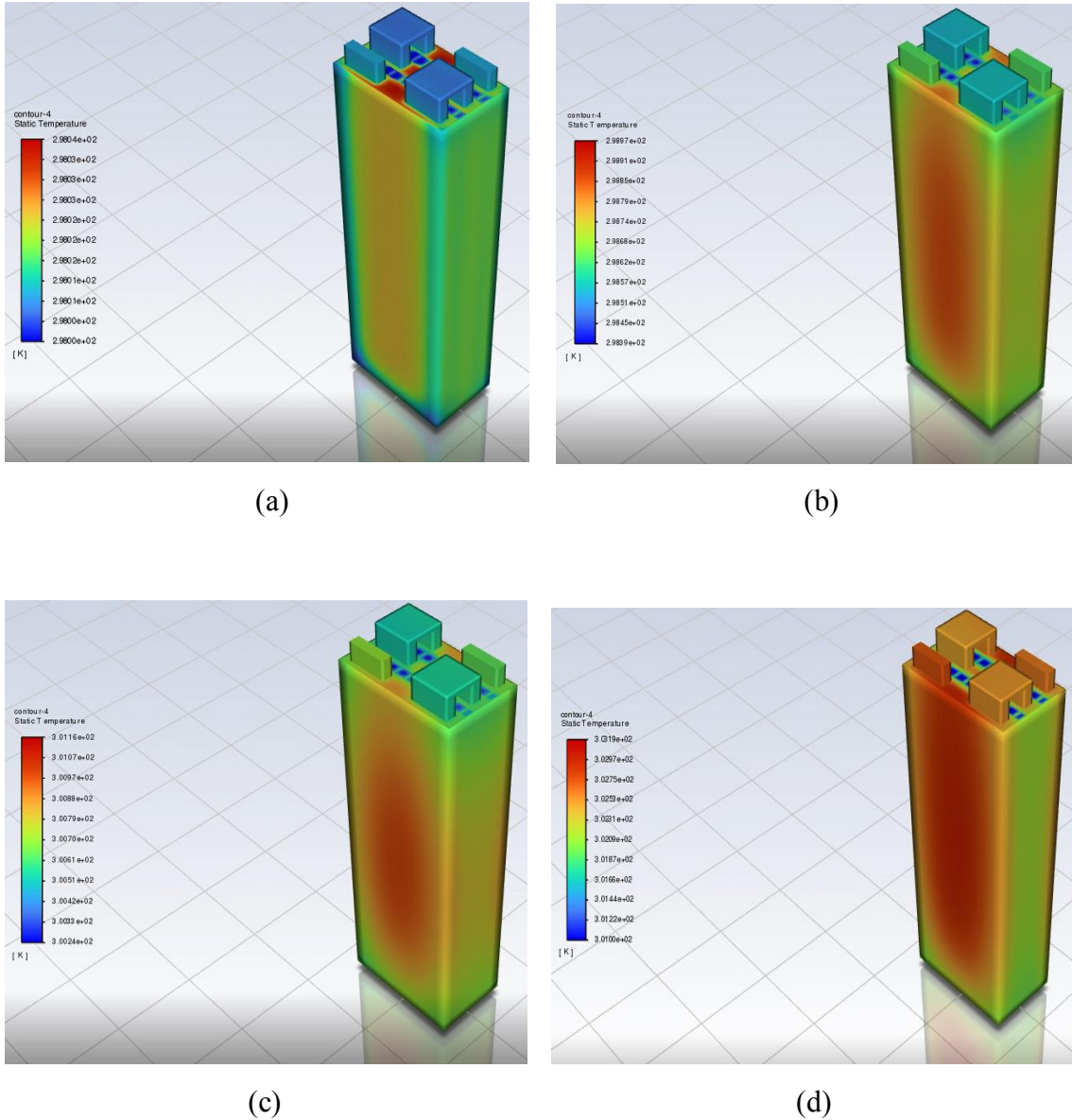


Figure 145 Simulated Battery Pack with PCM-Fin structure Temperature Contour at different time steps @25°C and 2C Rate.

The biggest temperature difference occurs between cell 1 and cell 2. The reason lies in the physics of the problem, which sees cell 2 subject to increased cooling. The maximum temperature difference is found at the end of the discharge phase and corresponds to about

2.7 °C: an increase of 7.1% compared to 2.52 °C obtained in the case with only natural convection. This slight increase is due to the high efficiency of the PCM-Fin structure system, which leads to a high cooling of cell number 2.

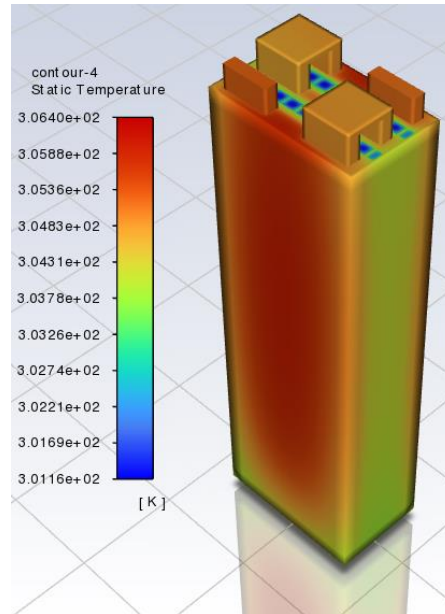


Figure 146 Simulated Battery Pack Temperature Contour with PCM-Fin structure at 1800 s @25°C and 2C Rate.

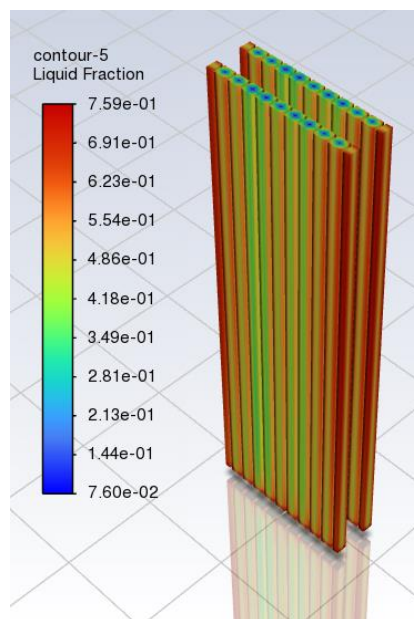


Figure 147 Simulated Battery Pack Liquid Fraction Contour with PCM-Fin structure at 1800 s @25°C and 2C Rate.

The maximum liquid fraction value is lower than in the case of Pure PCM, but the average distribution of liquid fraction at the end of the simulation is 14 percentage points higher in the case of the PCM-Fin structure. The reason lies in the greater uniformity of heat distribution given by the presence of heat sinks. The non-homogeneity of the Contour representing the liquid fraction is due to problems related to the mesh of the Heat Sinks.

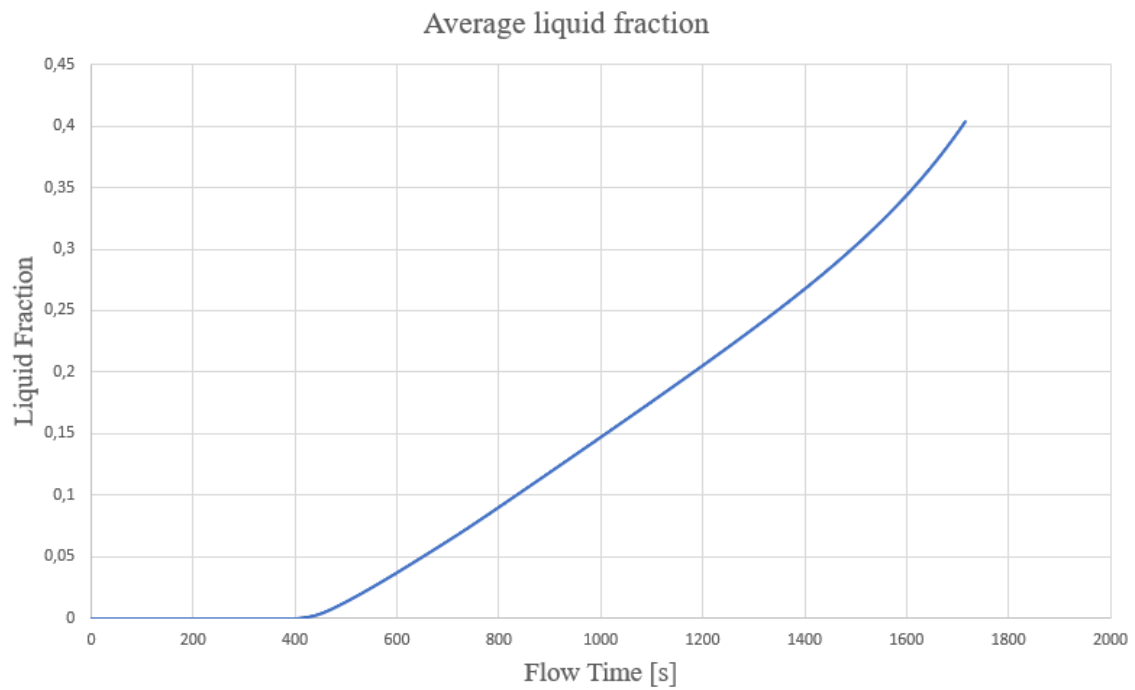


Figure 148 Simulated Battery Pack with PCM-Fin structure Average PCM liquid fraction @25°C and 2C Rate.

1C Discharge Rate	T_{max} [°C]		ΔT_{max} [°C]	
Natural Convection	35.28		1.38	
Cooling Methods	T_{max} [°C]	Performance	ΔT_{max} [°C]	Performance
Pure PCM	31.3	-11.3%	1.55	+12%
PCM-Fin Structure	30.6	-13.1%	1.25	-9.5%

Table 24 Summary of the performance of the various Battery Pack cooling systems with 1C discharge current.

2C Discharge Rate	T_{max} [°C]		ΔT_{max} [°C]	
Natural Convection	45.71		2.52	
Cooling Methods	T_{max} [°C]	Performance	ΔT_{max} [°C]	Performance
Pure PCM	34.75	-24%	3.25	+28%
PCM-Fin Structure	33.4	-26.9%	2.7	+7.1%

Table 25 Summary of the performance of the various Battery Pack cooling systems with 2C discharge current.

5.5.4 Effect of fin thickness and spacing

Another case study concerns a sensitivity analysis conducted on geometric parameters of the fins. PCM-fin structure can effectively increase the heat exchange area of PCM to effectively enhance the heat transfer in the PCM. In this section, the design of fin structure including fin thickness (l) and fin spacing (d) was investigated to find the best dimension to restrain the temperature rise of cells. Below is the table that summarizes the fin thickness (l) used to conduct the analysis.

	Case 1 [mm]	Case 2 [mm]	Case 3 [mm]
Fin Thickness (l)	1.5	2	2.5

Table 26 Fin thickness.

The case with a blade thickness of 1.5 mm corresponds to the one previously analysed. Consequently, in this section a comparison will be made between the values already obtained and those that could be obtained by varying the thickness of the fins.

Figure 149 and Figure 150 show the temperature Contours of the battery module with different fin thicknesses at the end of 2C discharge. Compared to this case, other cases with fins got the better temperature performance for the batteries with the function of utilizing the latent heat in central section of PCM layer.

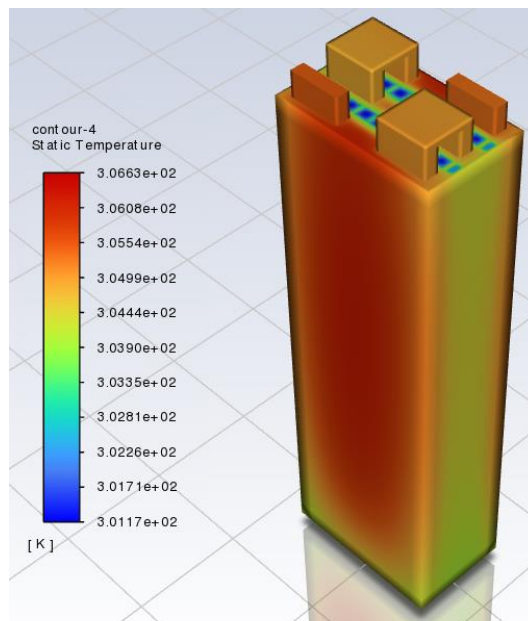


Figure 149 Simulated Battery Pack Temperature Contour with 2mm Fin thickness at 1800 s @25°C and 2C Rate.

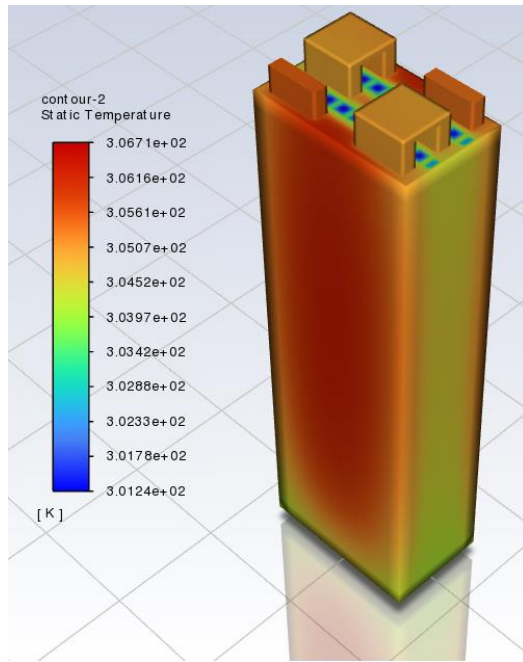


Figure 150 Simulated Battery Pack Temperature Contour with 2.5mm Fin thickness at 1800 s @25°C and 2C Rate.

Figure 151 demonstrates the distribution of T_{max} in the battery module under different fin thicknesses at the end of 2C discharge, and **Figure 152** shows the maximum temperature difference (ΔT_{max}) of battery module.

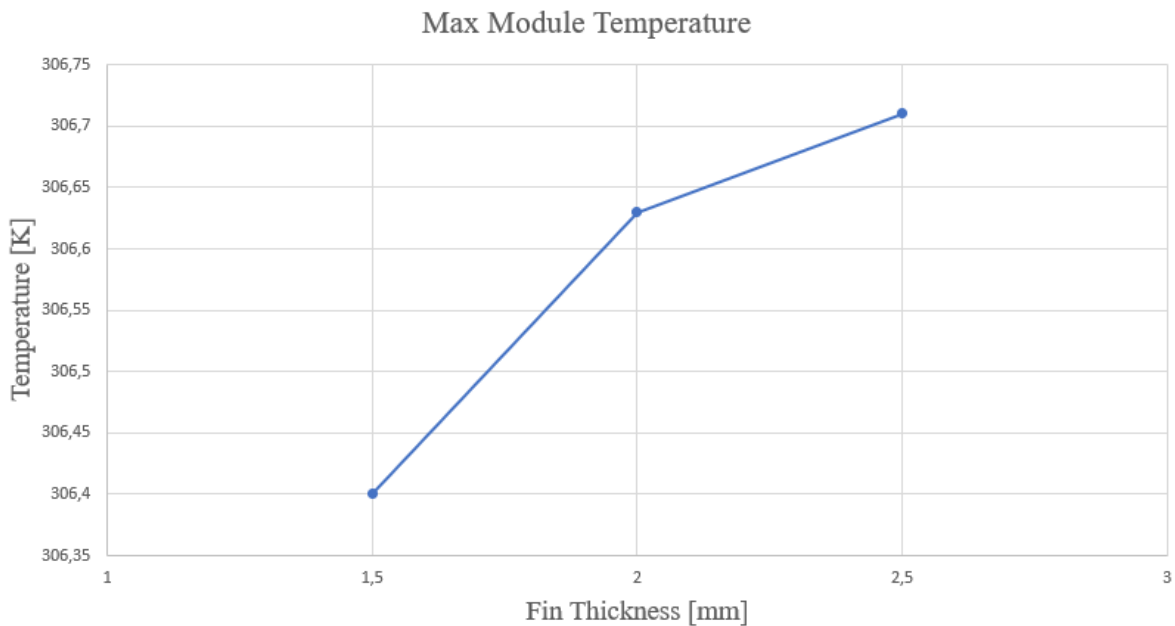


Figure 151 Simulated Battery Pack Max Temperature (T_{max}) with Fin thickness @25°C and 2C Rate.

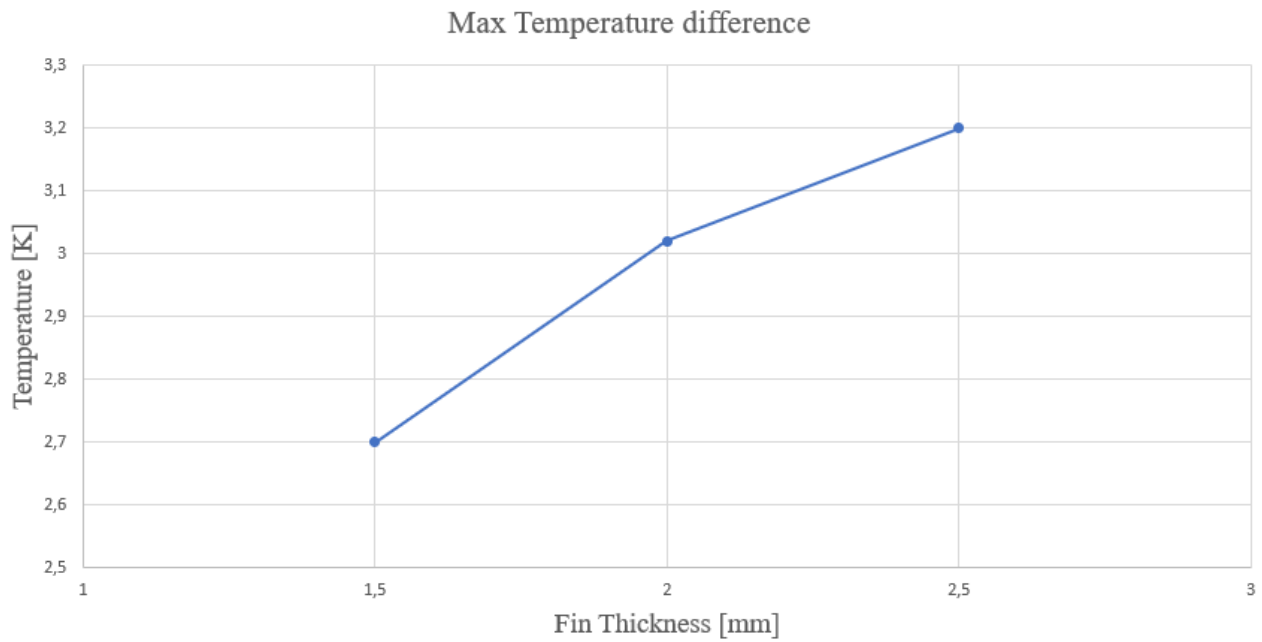


Figure 152 Simulated Battery Pack Max Temperature difference (ΔT_{max}) with Fin thickness @25°C and 2C Rate

With the decrease of fin thickness, T_{max} and ΔT_{max} decreased, specially ΔT_{max} and the maximum temperature of the module were well controlled under 5 °C and 35 °C, when (l) was 1.5 mm. These results illustrate that although thicker fin can enhance thermal conduction, the increasing fin thickness inevitably leads to a decrease in the volume of PCM within a heat sink of fixed width and thickness. Consequently, it results in a corresponding reduction in the amount of heat that the PCM can absorb (**Figure 153** and **Figure 154**). When the fin spacing is constant, the smaller fin thickness, the more number of fins than the thicker fin could increase the heat exchange area with PCM, thus the performance of heat dissipation is improved [82]. The results obtained are also reflected in the analysis in the literature [82]. As shown in **Figure 150**, it was observed that the temperature distribution was inconsistent in every case, which presented the situation of high temperature appearing in the edge of battery module and low temperature emerging at the middle part. It is caused by the arrangement of the heat sinks, cells in edge of battery module were only equipped with heat sink with fin on one side, while the middle cells contacted with heat sinks on both sides.

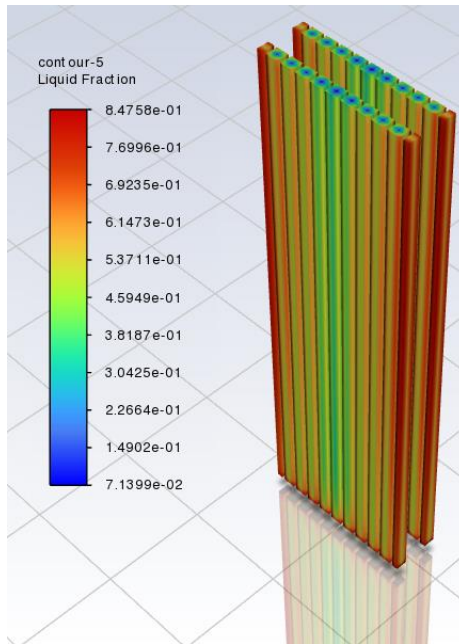


Figure 153 Simulated Battery Pack Liquid Fraction Contour with 2 mm Fin thickness at 1800 s @25°C and 2C Rate.

In the **Figure 155** the trend in time of the average liquid fraction is presented for cases with different thickness of the fins. As shown above, the thicker fin configuration has the highest average liquid fraction throughout the simulation. A greater thickness of the fins leads to a greater heat exchange surface. This aspect, combined with the smaller fraction of PCM in the cooling block, inevitably leads to an increase in the fraction of solid material that is partially transformed into liquid.

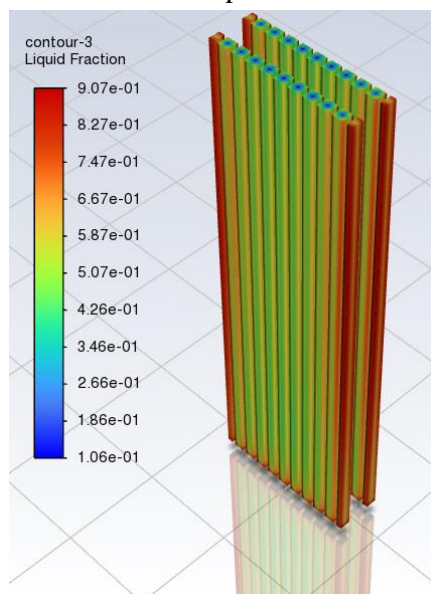


Figure 154 Simulated Battery Pack Liquid Fraction Contour with 2.5 mm Fin thickness at 1800 s @25°C and 2C Rate.

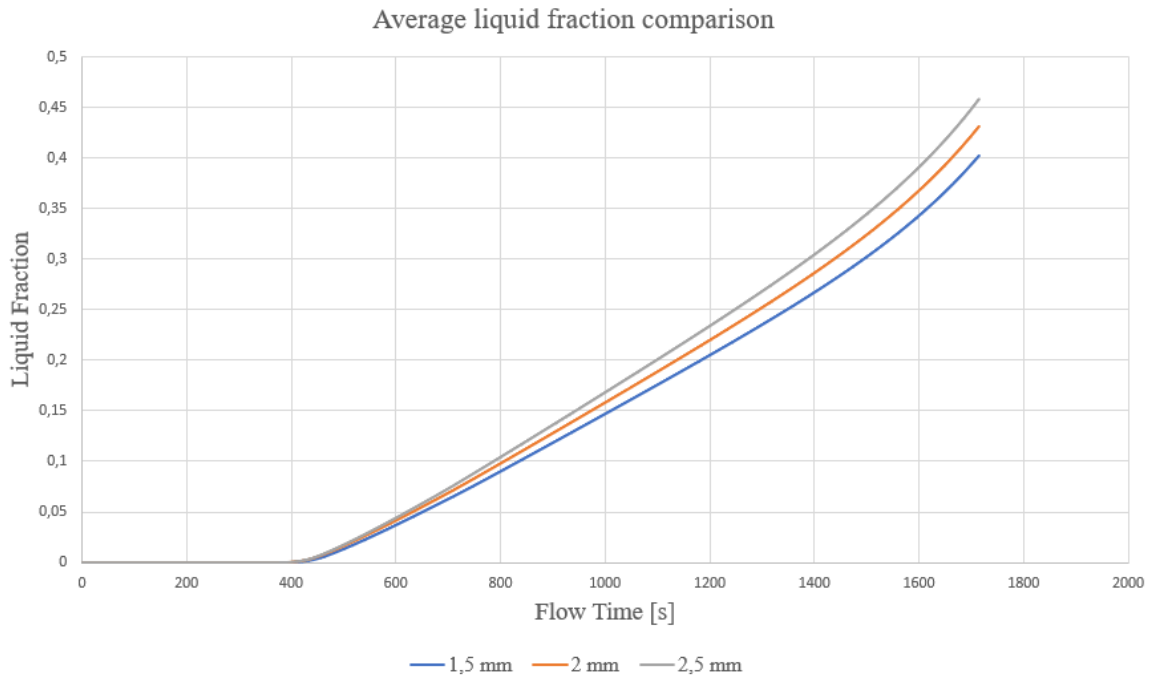


Figure 155 Simulated Battery Pack Average liquid fraction comparison with Fin thickness @25°C and 2C Rate.

In PCM-fin structure, the fin spacing (d) is another important factor. Three types of fin spacing, which changed from 9.5 mm to 4.75 mm and $l = 1.5$ mm was chosen to study the influence on the fin spacing. As listed in **Table 27**, it can be seen that the decrease of fin spacing leads to the increase of fin number.

	Case 1 [mm]	Case 2 [mm]	Case 3 [mm]
Fin Spacing (d)	9.5	6.3	4.75
Fin number	10	15	20

Table 27 Fin number and spacing.

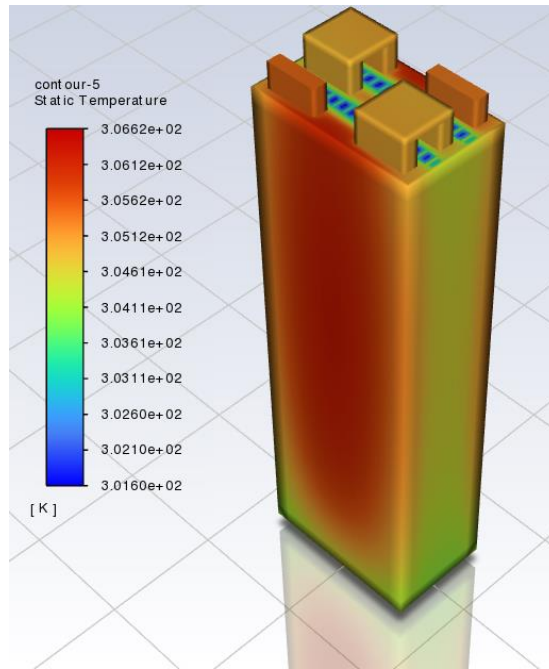


Figure 157 Simulated Battery Pack Temperature Contour with 15 Fins at 1800 s @25°C and 2C Rate.

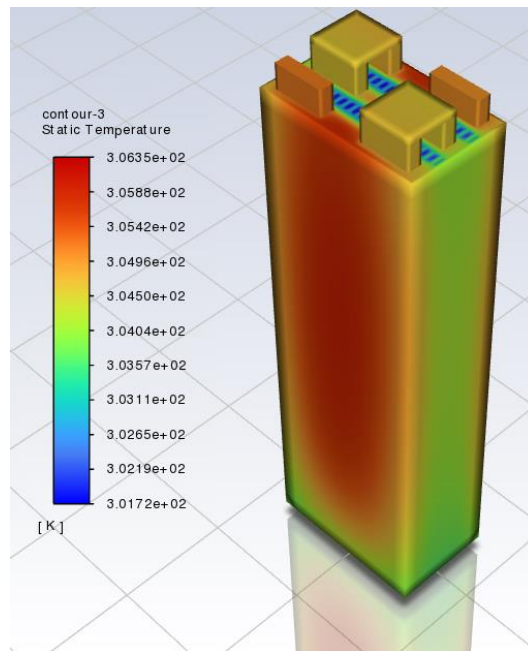


Figure 156 Simulated Battery Pack Temperature Contour with 20 Fins at 1800 s @25°C and 2C Rate.

Figure 158 displays the distribution of T_{max} in the battery module under different fin spacing at the end of 2C discharge, and **Figure 159** illustrates the maximum temperature difference (ΔT_{max}) of battery module. It can be seen that the change of temperature distribution with the decrease of fin spacing was nonlinear. At first, T_{max} increased

gradually with the decrease of fin spacing from 9.5 mm to 6.3 mm. Although the increased fin numbers lead to the increase of the heat transfer area, it also causes the excessive reduction of the volume of PCM. Meanwhile, the liquid fraction of PCM rapidly increased at the end of discharge because of the reduction in latent heat of PCM. It reveals that the negative influence of decreasing volume of PCM is more significant than the positive effect of increasing the heat transfer area on thermal performance of the module. The configuration with 20 Fins has the best performance in terms of T_{max} . It is because that the latent heat of PCM can be better utilized due to the reduction of fin spacing improving the heat exchange area with PCM. Compared to all other sensitivity analysis, in this case the aspect related to T_{max} is in contrast with the evidence reported in the literature [82]. On the other hand, the very good cooling effect from the 20 Fins configuration leads to a higher ΔT_{max} value than the other two cases. The reason lies in the fact that the cells placed at the ends are subject to contact with only one cooling plate, while the central cell is in contact with two plates simultaneously. This last result, instead, is qualitatively in line with the analyses drawn from literature [82].

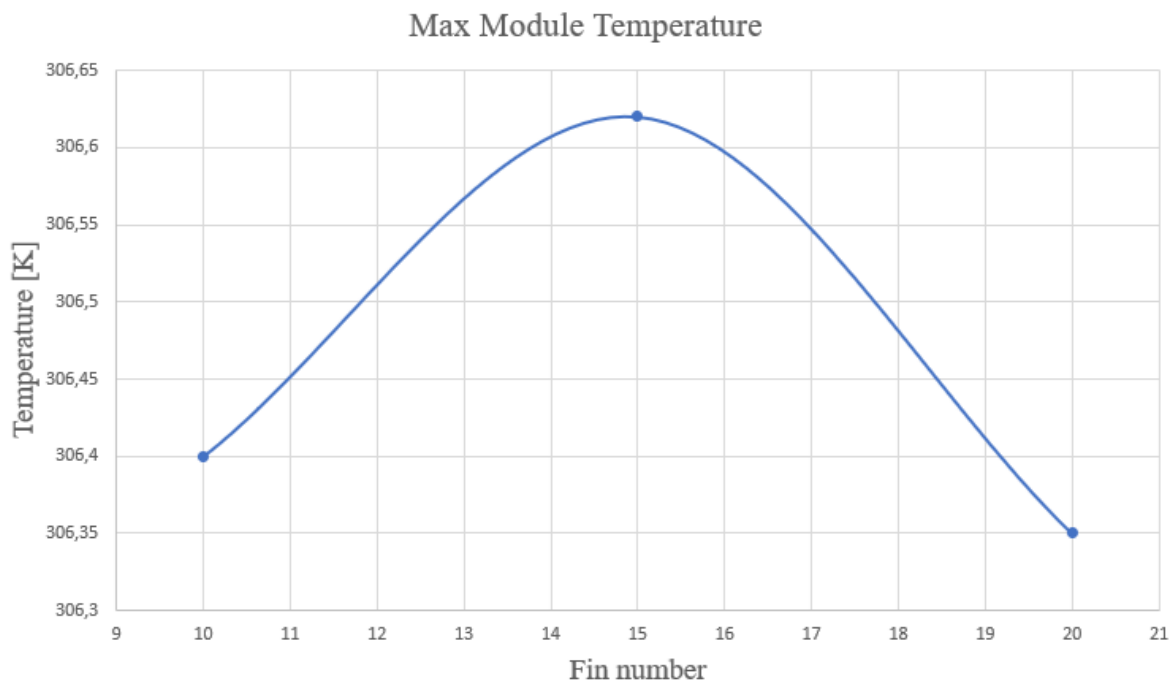


Figure 158 Simulated Battery Pack Max Temperature (T_{max}) with Fin Spacing @25°C and 2C Rate.

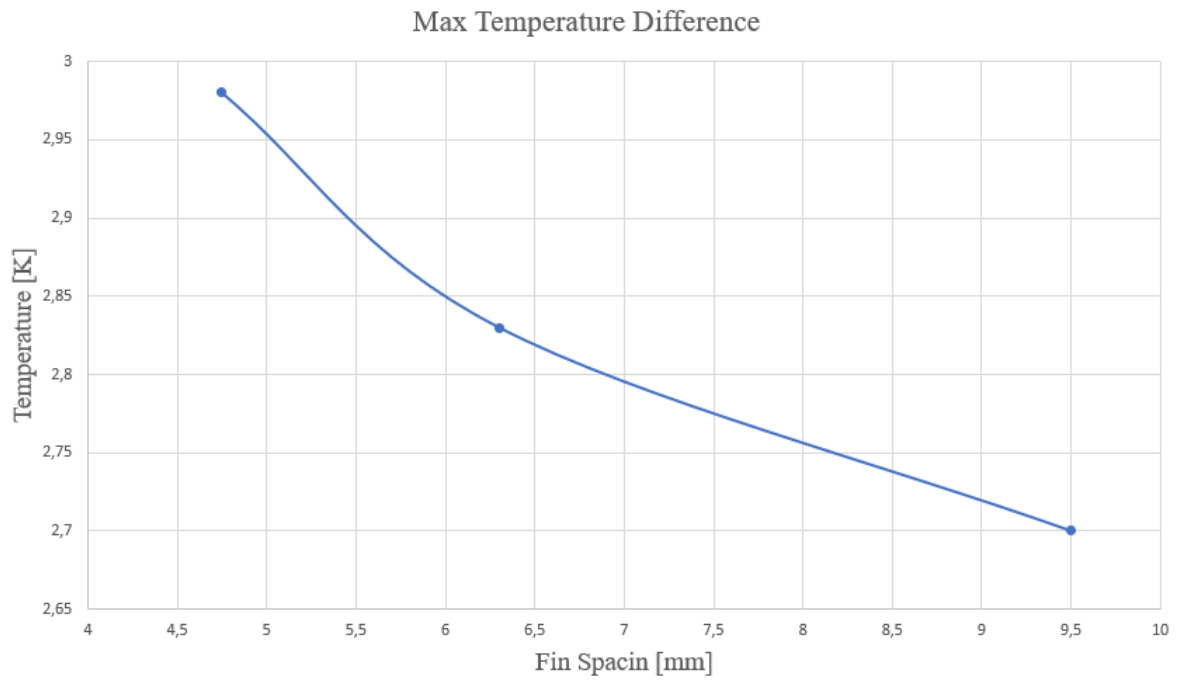


Figure 159 Simulated Battery Pack Max Temperature difference (ΔT_{max}) with Fin Spacing @25°C and 2C Rate.

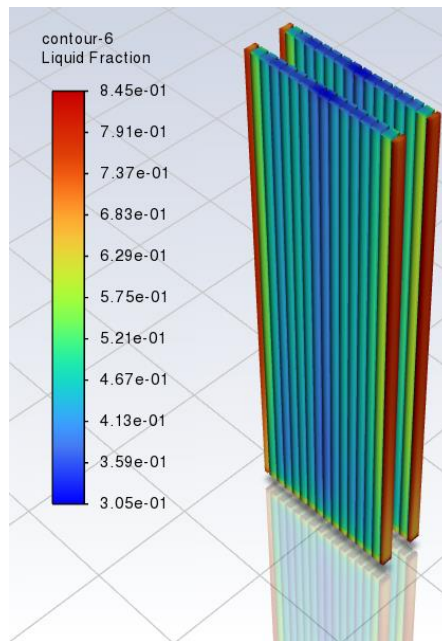


Figure 160 Simulated Battery Pack Liquid Fraction Contour with 6.3 mm Fin Spacing at 1800 s @25°C and 2C Rate.

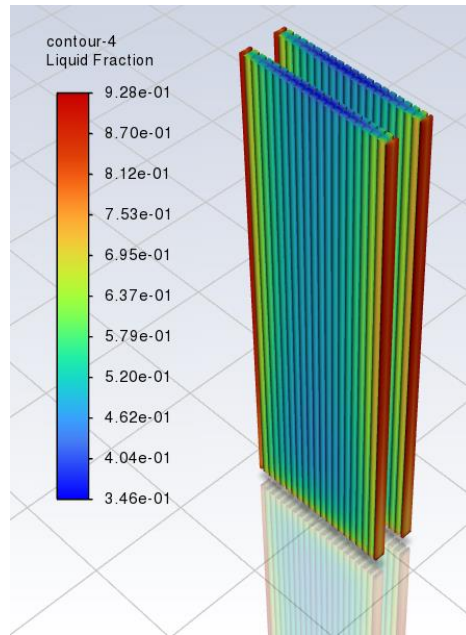


Figure 161 Simulated Battery Pack Liquid Fraction Contour with 4,75 mm Fin Spacing at 1800 s @25°C and 2C Rate.

Meanwhile, the liquid fraction of PCM rapidly increased at the end of discharge because of the reduction in latent heat of PCM. It reveals that the negative influence of decreasing volume of PCM is more significant than the positive effect of increasing the heat transfer area on thermal performance of the module. Therefore, the results demonstrate that the configuration with the fin spacing of 4.75 mm has more advantage in controlling the temperature rise of the battery module than other cases. In contrast, the performance of ΔT_{max} in the case with $d = 6.3$ mm is better than $d = 4.75$ mm, and it also reduces the difficulty of manufacturing process compared to the cases with 4.75 mm.

5.5.5 Effect of the number of plates

In the last section of **Chapter 5** the effect of the increase in the number of cooling plates for the battery pack is presented. In all previous studies, the number of plates was determined as $n - 1$, where n indicates the number of cells involved in the package configuration. This type of approach, as discussed above, leads to an increase in the unevenness of the temperature distribution between the cells. The reason for this was that only one of the three batteries came into contact with the cooling system on both sides. In this further analysis the effect of the insertion of $n + 1$ cooling plates inside the battery pack is studied. In this way, all cells are involved by cooling on both surfaces. The effects that will be presented in this Section concern the maximum temperature reached by the cells, the maximum value of liquid fraction of the various layers of PCM and the direct comparison of these parameters with the previous configurations. In order to conduct the study, a modification was made to the most efficient cooling system analysed above. The latter turned out to be the one with PCM-Fin Structure (10 metal fins with a thickness of 1.5 mm fins).

The first analyses presented are those concerning 1C discharge current.

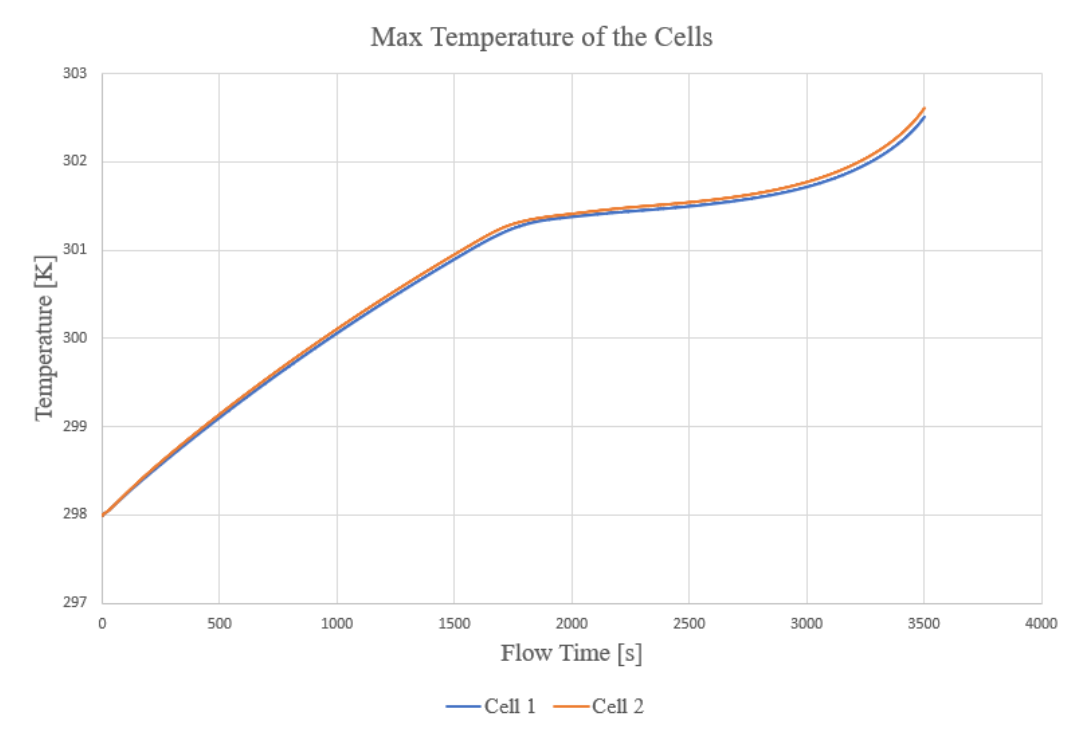


Figure 162 Simulated Battery Pack Max Temperatures with 4 Plates PCM-Fin Structure @25°C and 1C Rate.

Figure 162 above shows the time trend of the maximum temperature of the central cell (Cell 2) and the most external one (Cell 1). It is important to note that, unlike the case with only two cooling plates, in this analysis the two curves coincide throughout the discharge time. Moreover, unlike the previous case, the maximum temperature of the first cell is always lower than the central one. A behaviour diametrically opposed to that studied in the first analysis. The reason can be given by the fact that Cell 1 is in direct contact with two cooling plates, one of which is in contact only with one cell; consequently, the plate being exposed to contact with only one thermal source (Cell 1) will show a latent heat saturation of the PCM later than a plate in contact with two thermal sources. All this brings a better effect on the overall cooling of the cell. In addition, the plate in question has a surface in contact with the Aluminum Case which, in turn, is involved in a process of pure natural convection. This effect produces an increase in the heat dissipation accumulated in the cooling plate. The absolute value of temperature reached by the first cell at the end of the discharge is 29.5 °C: a reduction of 3.8% compared to 30.6 °C achieved with the system with only 2 plates. The Cell 2 also undergoes a decrease in temperature to reach 29.6 °C: a reduction of 2% compared to the 30.2 °C of the case with 2 cooling plates.

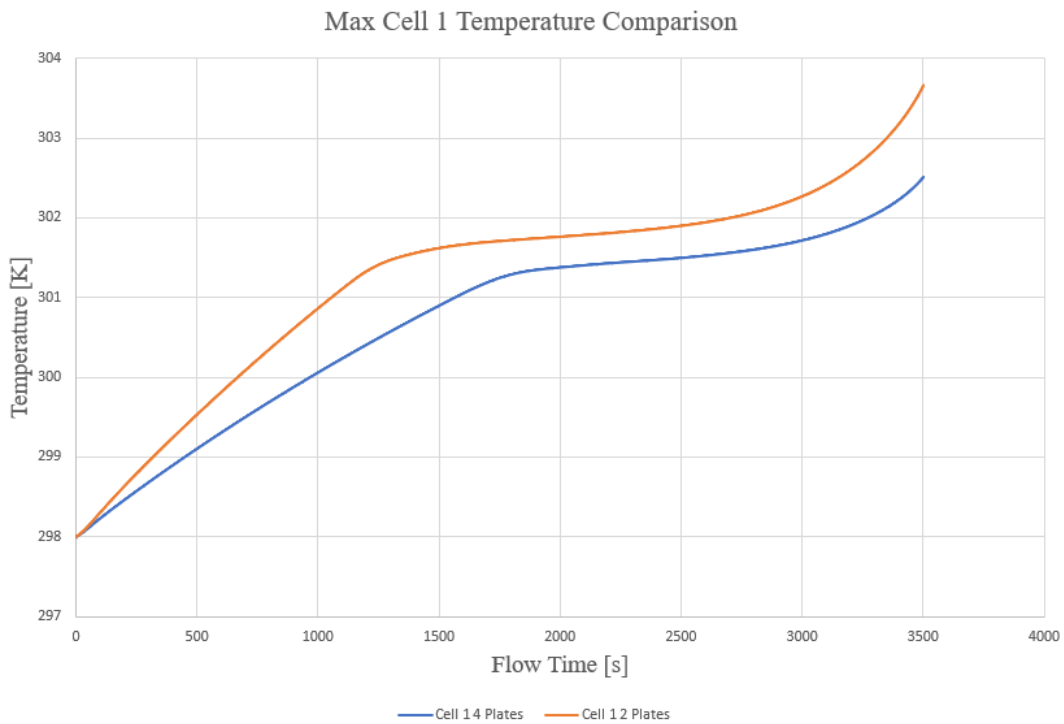


Figure 163 Simulated Battery Pack Max Temperature Comparison with 2 and 4 Plates @25°C and 1C Rate.

In **Figure 163** the comparison between the maximum temperature curves of Cell 1 subject to 2 and 4 cooling plates is shown. The reduction of the maximum temperature of the cell has already been exposed previously. What is interesting to note is the time in which the melting temperature of the PCM is reached (301.15 K). In the case of 2 cooling plates, this temperature is reached in a time of about 1300 s. In the case with 4 plates, the melting start time is about 1800 s: a time delay of 500 s. The effect obtained leads to a delay of the process of completion of melting of the material, which results in a better use of the latent heat available to the PCM.

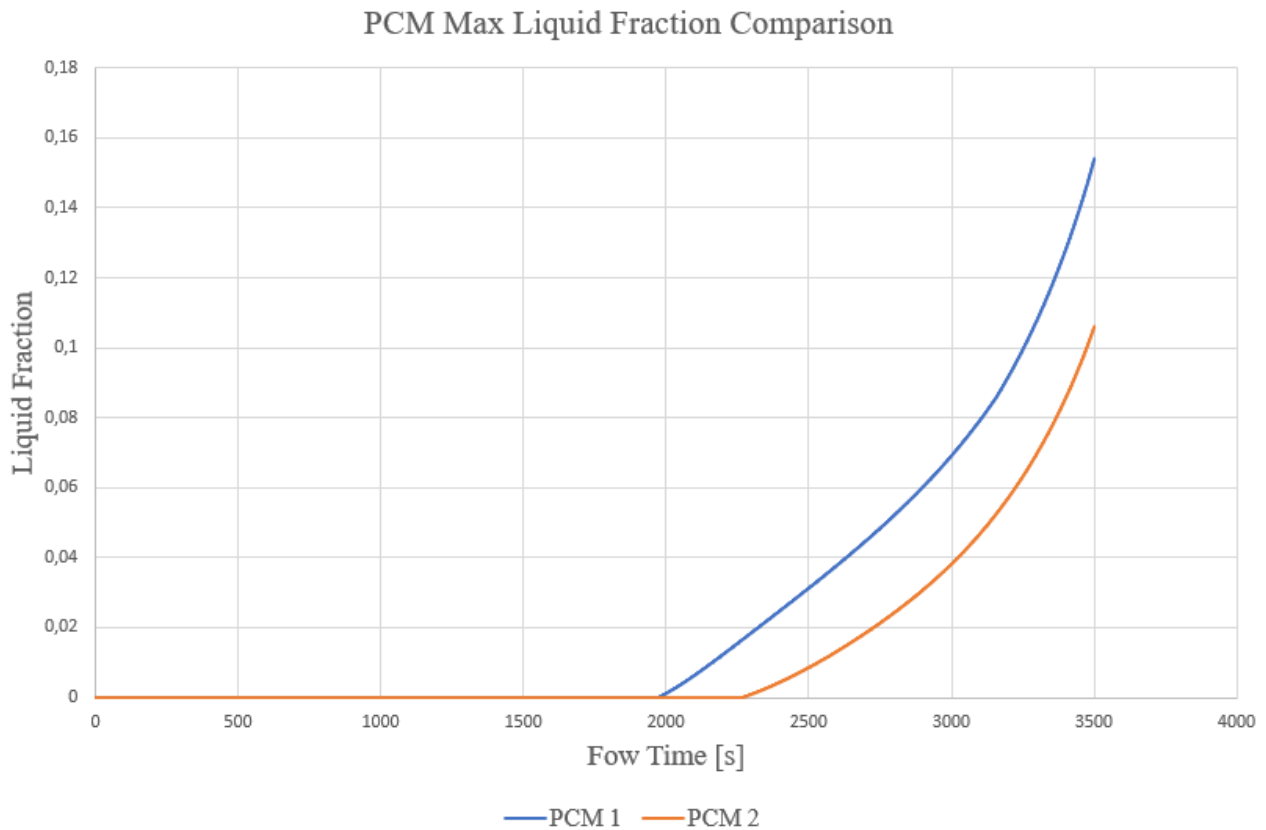


Figure 164 Simulated Max Liquid Fraction of PCM 1 and PCM 2 @25°C and 1C Rate.

Figure 164 shows the trend in time of the maximum fraction of liquid formed in the two cooling plates. PCM 1 refers to the layer in contact with two cells. PCM 2 refers to the layer in contact with one cell. PCM 1 inevitably has a higher liquid fraction value as the heating of the material is given by two thermal sources (Cell 1 and Cell 2). The fraction of liquid formed in the first layer is 15.7%, while for the second layer the maximum reached is 10.8%.

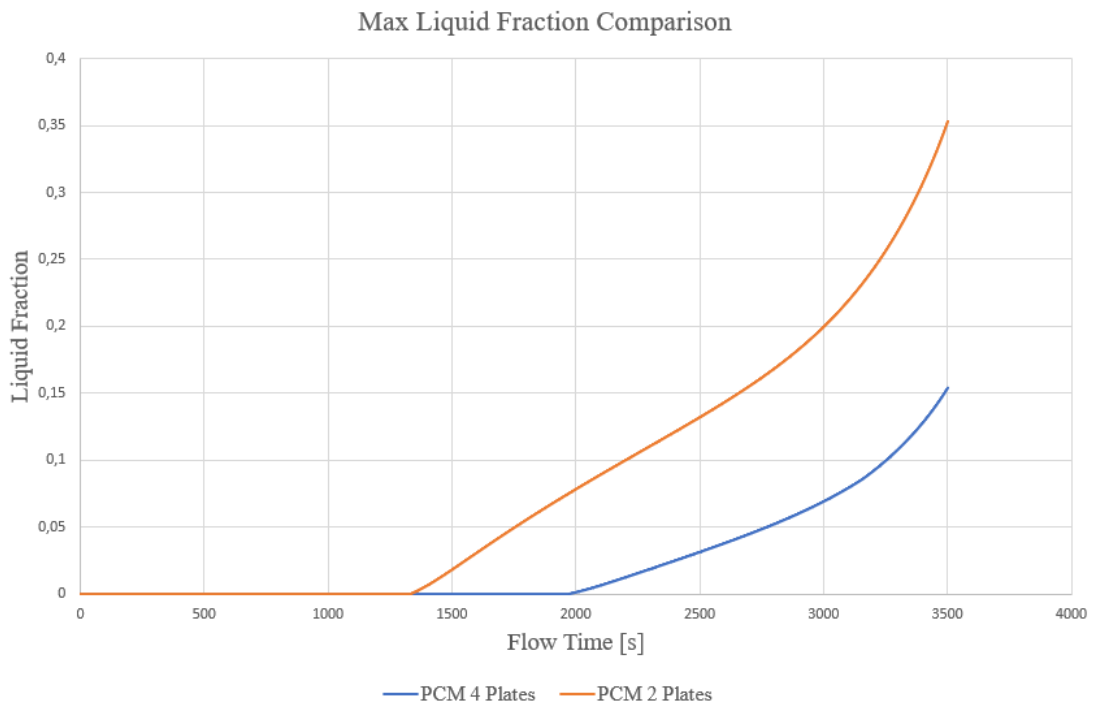


Figure 165 Simulated Max Liquid Fraction Comparison with 2 and 4 Plates @25°C and 1C Rate.

The graph presented in **Figure 165** shows the comparison between the maximum fraction of liquid reached by the layer, in contact with two cells (PCM 1), in the case of 2 and 4 cooling plates. The first observation that can be made concerns the maximum value reached by the two curves. In the case with 4 cooling plates the maximum value is 15.7% (as previously reported), while in the case of 2 cooling plates the maximum is 35.8%. The considered layer is the same and is in contact with the same cells. The reason for such a high difference (about 20 percentage points) is given by the different nature of thermal sources. In the case with 2 cooling plates the Cell 1 is in contact with only one layer, for this it provides a contribution in terms of heat much more important than the case with 4 plates. The addition of an additional layer in contact with the Cell 1 means that the heat generated by the latter is significantly reduced: the proof is that the maximum temperature of Cell 1 is even lower than that of Cell 2. A second aspect to consider is the time of beginning phase change: the case with 2 plates begins the liquefaction 700 s about before the case with 4 plates. This aspect should not be underestimated as the use of multiple layers could lead to a wider operating range, especially in cases with discharge currents above 1 or 2 C.

In **Figure 166** and **Figure 167** it is possible to appreciate the Contour of temperature and liquid fraction of the analysed system. In addition to the Contour, **Figure 166** shows the different geometry adopted to conduct this last analysis.

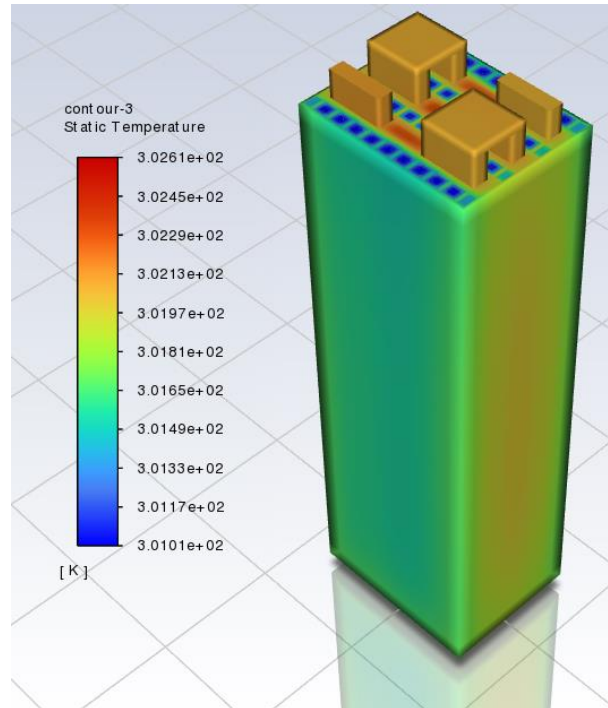


Figure 166 Simulated Battery Pack Temperature Contour with 4 PCM-Fin structure at 3600 s @25°C and 1C Rate.

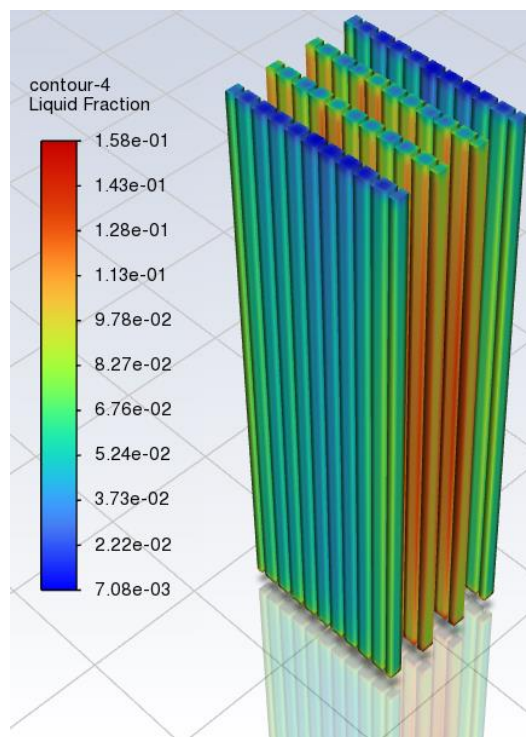


Figure 167 Simulated Battery Pack Liquid Fraction Contour with 4 PCM-Fin structure at 3600 s @25°C and 1C Rate.

The biggest temperature difference occurs between Cell 1 and Cell 2. The reason lies in the physics of the problem, which sees Cell 1 subject to increased cooling. The maximum temperature difference is found at the end of the discharge phase and corresponds to about 0.92 °C: a reduction of 26.4% compared to 1.25 °C obtained in the case with only 2 plates.

The second analysis presented is that concerning 2C discharge current. All the considerations presented in the case with discharge current 1C have the same value from the qualitative point of view.

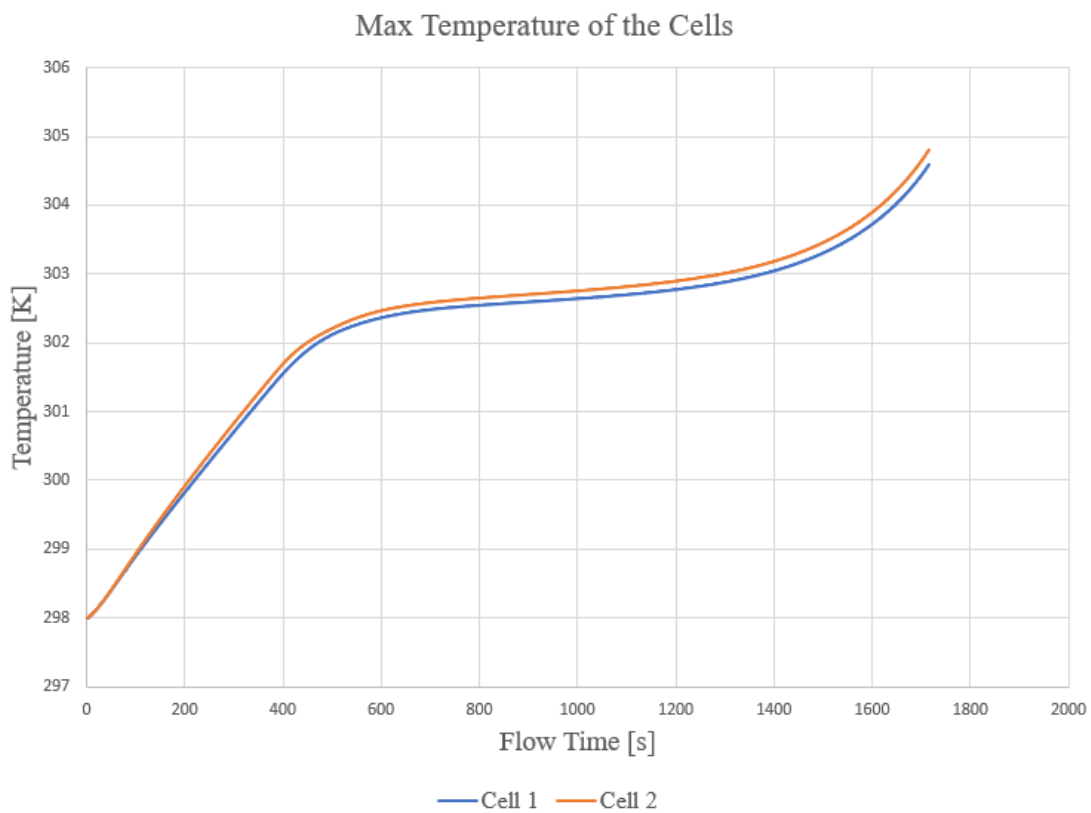


Figure 168 Simulated Battery Pack Max Temperatures with 4 Plates PCM-Fin Structure @25°C and 2C Rate.

The absolute value of temperature reached by the first cell at the end of the discharge is 31.6 °C: a reduction of 5.4% compared to 33.4 °C reached with the system with only 2 plates. The Cell 2 also undergoes a decrease in temperature to reach 31.8 °C: a reduction of 1.7% compared to the 32.37 °C of the case with 2 cooling plates.

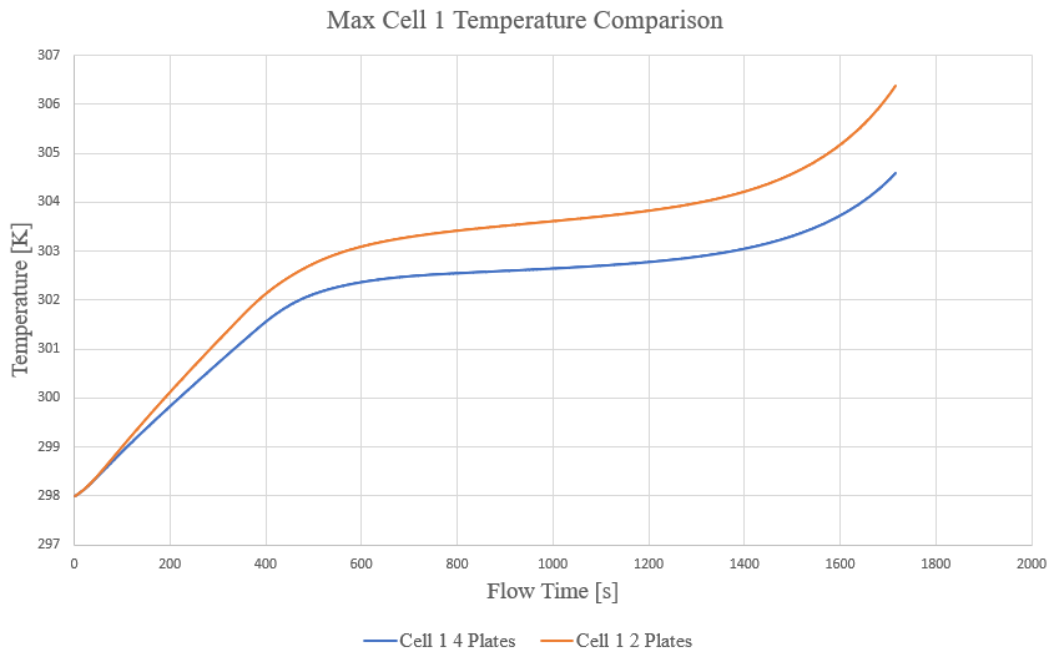


Figure 169 Simulated Battery Pack Max Temperature Comparison with 2 and 4 Plates @25°C and 2C Rate.

Unlike the case with 1C discharge, in this case there is no delay in the process of starting melting of the material.

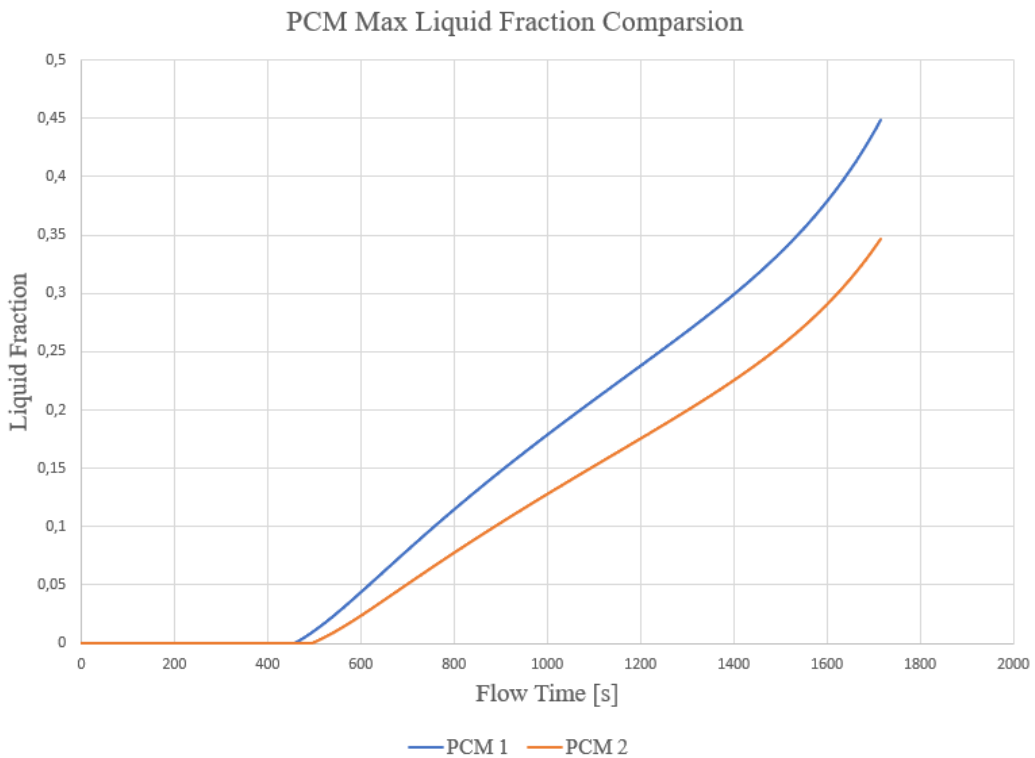


Figure 170 Simulated Max Liquid Fraction of PCM 1 and PCM 2 @25°C and 2C Rate.

Figure 171 shows the trend in time of the maximum fraction of liquid formed in the two cooling plates. PCM 1 refers to the layer in contact with two cells. PCM 2 refers to the layer in contact with only one cell. PCM 1 inevitably has a higher liquid fraction value as the heating of the material is given by two thermal sources (Cell 1 and Cell 2). The fraction of liquid formed in the first layer is 45%, while for the second layer the maximum reached is 34.9%.

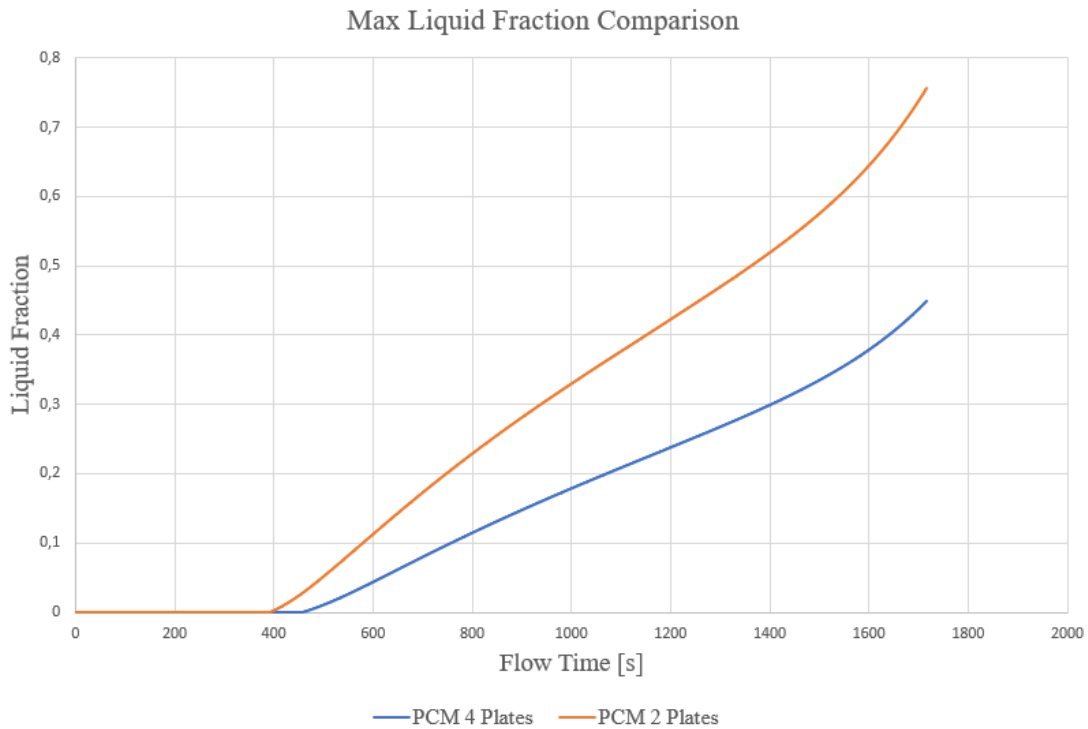


Figure 171 Simulated Max Liquid Fraction Comparison with 2 and 4 Plates @25°C and 2C Rate.

The graph presented in **Figure 171** shows the comparison between the maximum fraction of liquid reached by the layer, in contact with two cells (PCM 1), in the case of 2 and 4 cooling plates. One observation that is possible concerns the maximum value reached by the two curves. In the case with 4 cooling plates the maximum value is 45% (as previously reported), while in the case of 2 cooling plates the maximum is 75%. The considered layer is the same and is in contact with the same cells. The reason for such a high difference (about 30 percentage points) is given by the different nature of thermal sources. In the case with 2 cooling plates the Cell 1 is in contact with only one layer, for this it provides a contribution in terms of heat much more important than the case with 4 plates. The

addition of an additional layer in contact with the Cell 1 causes the heat generated by the latter to be significantly reduced: the demonstration is that the maximum temperature of Cell 1 is even lower than that of Cell 2.

In **Figure 173** and **Figure 172** it is possible to appreciate the Contour of temperature and liquid fraction of the analysed system. In addition to the Contour, **Figure 173** shows the different geometry adopted to conduct this last analysis.

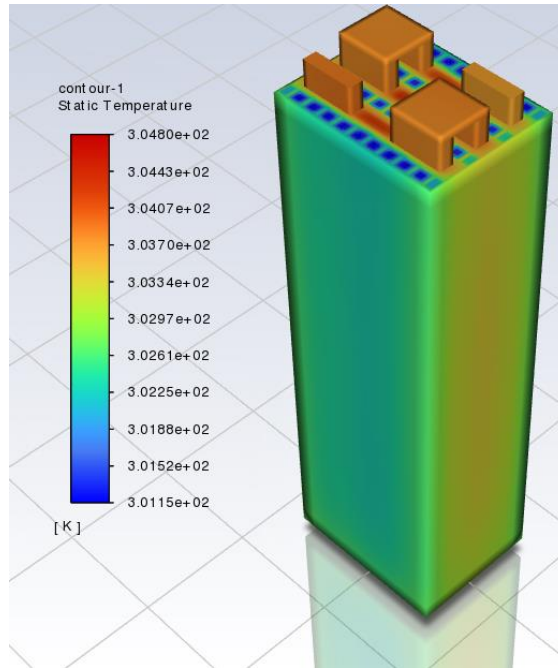


Figure 173 Simulated Battery Pack Temperature Contour with 4 PCM-Fin structure at 1800 s @25°C and 2C Rate.

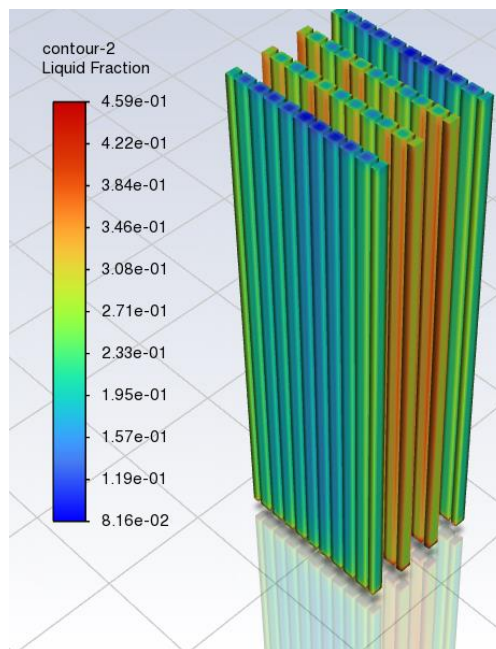


Figure 172 Simulated Battery Pack Liquid Fraction Contour with 4 PCM-Fin structure at 1800 s @25°C and 2C Rate.

The biggest temperature difference occurs between Cell 1 and Cell 2. The reason lies in the physics of the problem, which sees Cell 1 subject to increased cooling. The maximum temperature difference is found at the end of the discharge phase and corresponds to about 2.07 °C: a reduction of 23.3% compared to 2.7 °C obtained in the case with only 2 plates.

Chapter 6 Conclusions

A CFD electro-thermal model of a li-ion pouch cell was implemented in Ansys/Fluent. The primary objective of the model implementation was to verify the temperature distribution in the cell. The model generation was accompanied by direct comparison with experimental data from the literature. The model was validated using a 1C discharge cycle, which evidenced its high accuracy, except of the last 60 s of discharge (a hardly predictable field of action in a real operating regime). The CFD analysis showed hot spots on the lateral sides of the cell. It is observable that the generation of heat is increased in conjunction with the reduction of the ambient temperature (case study with T_0 equal to 0 °C) due to the increase of the internal resistances of the cell. Moreover, it also increases with increasing C-rates (current 2C discharge) because of the internal ohmic losses. The obtained results show how an undesired peak temperature, above 50 °C (which is the maximum recommended temperature by the manufacturers), could arise in hot spots when the cell is exposed to high external temperature (above 45 °C). That just described leads to a conclusion: cooling by natural convection is not enough to keep the temperature of the cell below the set limits. A proper cooling strategy needs to be implemented. Four different cooling methods including air, fin, pure PCM and composite cooling for single LIB cell were investigated. First, an analysis was carried out on the effects that these cooling systems have on the behaviour of the single cell. The purpose of this study is to assess the maximum temperature value and the maximum temperature difference of the cell. Later, to obtain a more complete study, it was decided to analyze a battery pack consisting of three cells arranged in series. The cooling systems adopted are the same described for the case of the single cell. To optimize the BTMS, sensitivity analysis of parameters such as PCM thickness, thickness and spacing of cooling fins was conducted. The purpose of this analysis is to obtain the best configuration of the cooling system concerning the maximum temperature and maximum temperature difference of the module. The concluding remarks could be made as follow:

- Decreasing fin thickness could reduce the maximum temperature and temperature difference of the battery module by increasing the heat exchange area with PCM.
- The fin spacing is also an important factor, which should be carefully considered when designing the PCM-fin structure. Using too small wing spacing, in this case,

led to the best result in terms of reduction of the maximum temperature of the module. The reason lies in the fact that the larger exchange area has a better effect than the reduction in the volume of phase change material. On the other hand, such behaviour produces a greater maximum temperature difference in the module. The convenience of using a more or less large spacing is to be found in the specific request of the user.

- Increasing appropriately the PCM thickness could improve the thermal performance and is more efficient than other factors. After the PCM thickness exceeded the critical value of 11 mm, the enhancement of the heat dissipation efficiency was insignificant in the thermal management system investigated in this work.

This confirms the importance of LIBs modelling to monitor temperature distribution, avoid thermal runaway and guarantee safety.

References

- [1] Ezio Spessa, “Controllo delle Emissioni di Inquinanti”, Politecnico di Torino, 2020.
- [2] S. Panchal, I. Dincer, M. Agelin-Chaab, R. Fraser, M. Fowler, Experimental and simulated temperature variations in a LiFePO₄–20 Ah battery during discharge process, *Appl. Energy* 180 (2016) 504–515.
- [3] Z. Rao, S. Wang, A review of power battery thermal energy management, *Renew. Sustain. Energy Rev.* 15 (2011) 4554–4571.
- [4] M. Malik, I. Dincer, M.A. Rosen, Review on use of phase change materials in battery thermal management for electric and hybrid electric vehicles, *Int. J. Energy Res.* 40 (2016) 1011–1031.
- [5] Ruiz, V.; Pfrang, A.; Kriston, A.; Omar, N.; Van den Bossche, P.; Boon-Brett, L. A review of international abuse testing standards and regulations for lithium ion batteries in electric and hybrid electric vehicles. *Renew. Sustain. Energy Rev.* 2018, 81, 1427–1452.
- [6] G. Zubi, R. Dufo-López, M. Carvalho, G. Pasaoglu, The lithium-ion battery: State of the art and future perspectives, *Renew. Sustain. Energy Reviews* 89 (April) (2018) 292–308.
- [7] Goodenough JB, Park K-S. The Li-ion rechargeable battery: a perspective. *J Am Chem Soc* 2013;135:1167–76.
- [8] K. Yeow, H. Teng, M. Thelliez, E. Tan, 3D Thermal Analysis of Li-ion Battery Cells with Various Geometries and Cooling Conditions Using Abaqus, 2012 SIMULIA Community Conference, no. Figure 1 (2012) 1–17.
- [9] P. Peng, F. Jiang, Thermal safety of lithium-ion batteries with various cathode materials: A numerical study, *Int. J. Heat Mass Transfer* 103 (2016) 1008–1016.
- [10] A123 Systems, Battery Pack Design, Validation, and Assembly Guide using A123 Systems AMP20M1HD-A Nanophosphate Cells, (2014) tech. rep.

- [11] H. Maleki, H. Wang, W. Porter, J. Hallmark, Li-Ion polymer cells thermal property changes as a function of cycle-life, *Journal of Power Sources* 263 (2014) 223–230.
- [12] J. Cannarella, C.B. Arnold, Stress evolution and capacity fade in constrained lithium-ion pouch cells, *J. Power Sources* 245 (2014) 745–751.
- [13] Huaqiang Liua, Zhongbao Weib, Weidong Hec, Jiyun Zhaoa, Thermal issues about Li-ion batteries and recent progress in battery thermal management systems: A review.
- [14] Ning G, Haran B, Popov BN. Capacity fade study of lithium-ion batteries cycled at high discharge rates. *J Power Sources* 2003;117:160–9.
- [15] Belt JR, Ho CD, Motloch CG, Miller TJ, Duong TQ. A capacity and power fade study of Li-ion cells during life cycle testing. *J Power Sources* 2003;123:241–6.
- [16] Park C, Jaura AK. Dynamic thermal model of Li-ion battery for predictive behaviour in hybrid and fuel cell vehicles. *SAE Int* 2003.
- [17] Zhao R, Zhang S, Liu J, Gu J. A review of thermal performance improving methods of lithium ion battery: electrode modification and thermal management system. *J Power Sources* 2015;299:557–77.
- [18] Cosley MR, Garcia MP. Battery thermal management system. *INTELEC 2004 26th annu int telecommun energy conf 2004*; 2004. p. 38–45.
- [19] Lin H-P, Chua D, Salomon M, Shiao H-C, Hendrickson M, Plichta E, et al. Low temperature behavior of Li-ion cells. *Electrochem Solid-State Lett* 2.
- [20] Fan J. On the discharge capability and its limiting factors of commercial 18,650 Li-ion cell at low temperatures. *J Power Sources* 2003;117:170–8.
- [21] Jaguemont J, Boulon L, Dubé Y. A comprehensive review of lithium-ion batteries used in hybrid and electric vehicles at cold temperatures. *Appl Energy* 2016;164:99–114.
- [22] Waldmann T, Wilka M, Kasper M, Fleischhammer M, Wohlfahrt-Mehrens M. Temperature dependent ageing mechanisms in Lithium-ion batteries – a Post Mortem study. *J Power Sources* 2014;262:129–35.

- [23] Pesaran A, Vlahinos A, Stuart T. Cooling and preheating of batteries in hybrid electric vehicles. 6th ASME-JSME therm eng jt conf. 2003; 2003.
- [24] J. Lamb, C.J. Orendorff, L.A.M. Steele, S.W. Spangler, Failure propagation in multi-cell lithium ion batteries, *J. Power Sources* 283 (2015) 517–523.
- [25] D.H. Doughty, E.P. Roth, A general discussion of Li ion battery safety, *Electrochem. Soc. Interface* 21 (2012) 37.
- [26] L. Ianniciello, P.H. Biwolé, P. Achard, Electric vehicles batteries thermal management systems employing phase change materials, *J. Power Sources* 378 (2018) 383–403.
- [27] Chen Y, Evans JW. Thermal analysis of lithium-ion batteries. *J Electrochem Soc* 1996;143:2708–12.
- [28] Bandhauer TM, Garimella S. Passive, internal thermal management system for batteries using microscale liquid-vapor phase change. *Appl Therm Eng* 2013;61:756–69.
- [29] S. Landinia, J. Leworthyb, T.S. O’Donovana, A Review of Phase Change Materials for the Thermal Management and Isothermalisation of Lithium-Ion Cells.
- [30] Q. Wang, B. Jiang, B. Li, Y. Yan, A critical review of thermal management models and solutions of lithium-ion batteries for the development of pure electric vehicles, *Renewable and Sustainable Energy Reviews* 64 (2016) 106–128.
- [31] W. Li, M. Xiao, X. Peng, A. Garg, L. Gao, A surrogate thermal modeling and parametric optimization of battery pack with air cooling for EVs, *Applied Thermal Engineering* 147 (October 2018) (2019) 90–100.
- [32] X. Li, F. He, G. Zhang, Q. Huang, D. Zhou, Experiment and simulation for pouch battery with silica cooling plates and copper mesh based air cooling thermal management system, *Applied Thermal Engineering* 146 (October 2018) (2019) 866–880.
- [33] A.A. Pesaran, S. Burch, M. Keyser, An Approach for Designing Thermal Management Systems for Electric and Hybrid Vehicle Battery Packs Preprint, National Renewable Energy Laboratory report (January) (1999).

- [34] D. Chen, J. Jiang, G.H. Kim, C. Yang, A. Pesaran, Comparison of different cooling methods for lithium ion battery cells, *Appl. Thermal Eng.* 94 (2016) 846–854.
- [35] H. Liu, Z. Wei, W. He, J. Zhao, Thermal issues about Li-ion batteries and recent progress in battery thermal management systems: A review, *Energy Convers. Manag.* 150 (May) (2017) 304–330.
- [36] L.H. Saw, Y. Ye, M.C. Yew, W.T. Chong, M.K. Yew, T.C. Ng, Computational fluid dynamics simulation on open cell aluminium foams for Li-ion battery cooling system, *Applied Energy* 204 (2017) 1489–1499.
- [37] L.H. Saw, H.M. Poon, H.S. Thiam, Z. Cai, W.T. Chong, N.A. Pambudi, Y.J. King, Novel thermal management system using mist cooling for lithium-ion battery packs, *Appl. Energy* 223 (December 2017) (2018) 146–158.
- [38] K. Chen, W. Wu, F. Yuan, L. Chen, S. Wang, Cooling efficiency improvement of air-cooled battery thermal management system through designing the flow pattern, *Energy* 167 (2019) 781–790.
- [39] E. Jiaqiang, M. Yue, J. Chen, H. Zhu, Y. Deng, Y. Zhu, F. Zhang, M. Wen, B. Zhang, S. Kang, Effects of the different air cooling strategies on cooling performance of a lithium-ion battery module with baffle, *Applied Thermal Engineering* 144 (August) (2018) 231–241.
- [40] Joris Jaguemont, Joeri Van Mierlo, A comprehensive review of future thermal management systems for battery electrified vehicles.
- [41] J. Kim, J. Oh, H. Lee, Review on battery thermal management system for electric vehicles, *Applied Thermal Engineering* 149 (December 2018) (2019) 192–212.
- [42] I. Dincer, H.S. Hamut, J. Nader, *Thermal Management of Electric Vehicle Battery Systems*, Wiley, (2017).
- [43] G. Xia, L. Cao, G. Bi, A review on battery thermal management in electric vehicle application, *Journal of Power Sources* 367 (2017) 90–105.

- [44] S. Yang, C. Ling, Y. Fan, Y. Yang, X. Tan, H. Dong, A Review of Lithium-Ion Battery Thermal Management System Strategies and the Evaluate Criteria, *International Journal of Electrochemical Science* 14 (2019) 6077–6107.
- [45] A.A. Pesaran, *Battery Thermal Management in EVs and HEVs : Issues and Solutions*, Advanced Automotive Battery Conference (2001).
- [46] T. Han, B. Khalighi, Li-ion Battery Pack Thermal Management Liquid vs Air Cooling, *Journal of Thermal Science and Engineering (c)* (2018).
- [47] Z. Shang, H. Qi, X. Liu, C. Ouyang, Y. Wang, Structural optimization of lithium-ion battery for improving thermal performance based on a liquid cooling system, *International Journal of Heat and Mass Transfer* 130 (2019) 33–41.
- [48] S. Chen, X. Peng, N. Bao, A. Garg, A comprehensive analysis and optimization process for an integrated liquid cooling plate for a prismatic lithium-ion battery module, *Applied Thermal Engineering* 156 (January) (2019) 324–339.
- [49] Y. Huang, P. Mei, Y. Lu, R. Huang, X. Yu, Z. Chen, A. Paul, A novel approach for Lithium-ion battery thermal management with streamline shape mini channel cooling plates, *Applied Thermal Engineering* 157 (November 2018) (2019) 113623.
- [50] J. Yan, K. Li, H. Chen, Q. Wang, J. Sun, *Energy Convers. Manag.* 128 (2016) 12–19.
- [51] X. Duan, G.F. Naterer, *Int. J. Heat Mass Transf.* 53 (2010) 5176–5182.
- [52] T.M. Bandhauer, S. Garimella, *Appl. Therm. Eng.* 61 (2013) 756–769.
- [53] Y. Ren, Z. Yu, G. Song, *J. Power Sources* 360 (2017) 166–171.
- [54] R.W. van Gils, D. Danilov, P.H.L. Notten, M.F.M. Speetjens, H. Nijmeijer, *Energy Convers. Manag.* 79 (2014) 9–17.
- [55] M. Al-Zareer, I. Dincer, M.A. Rosen, *J. Power Sources* 363 (2017) 291–303.

- [56] A. Sharma, V.V. Tyagi, C.R. Chen, D. Buddhi, Review on thermal energy storage with phase change materials and applications, *Renew. Sustain. Energy Rev.* 13 (2) (2009) 318–345.
- [57] N.O. Moraga, J.P. Xaman, R.H. Araya, *Appl. Therm. Eng.* 108 (2016) 1041–1054.
- [58] J. Yan, Q. Wang, K. Li, J. Sun, *Appl. Therm. Eng.* 106 (2016) 131–140.
- [59] M. Malik, I. Dincer, M. Rosen, M. Fowler, *Electrochim. Acta* 257 (2017) 345–355.
- [60] R. Zhao, J. Gu, J. Liu, *Energy* 135 (2017) 811–822.
- [61] Jingwei Chen, Siyi Kang, Jiaqiang E, Effects of different phase change material thermal management strategies on the cooling performance of the power lithium ion batteries: A review.
- [62] Y. Tian, C.Y. Zhao, Thermal and exergetic analysis of Metal Foam-enhanced Cascaded Thermal Energy Storage (MF-CTES), *Int. J. Heat Mass Transfer* 58 (2013) 86–96.
- [63] A. Sciacovelli, F. Gagliardi, V. Verda, Maximization of performance of a PCM latent heat storage system with innovative fins, *Appl. Energy* 137 (2015) 707–715.
- [64] Huaqiang Liua, Zhongbao Weib, Weidong Hec, Jiyun Zhaoa, Thermal issues about Li-ion batteries and recent progress in battery thermal management systems: A review.
- [65] Holman JP. *Heat transfer*. 10th ed. McGraw-Hill Higher Education; 2010.
- [66] Xiao M, Choe S-Y. Theoretical and experimental analysis of heat generations of a pouch type LiMn₂O₄/carbon high power Li-polymer battery. *J Power Sources* 2013;241:46–55.
- [67] lithium ion batteries based on the electrochemical-thermal model at high discharge rates. *Int J Hydrogen Energy* 2015;40:13039–49.
- [68] Zhang X. Thermal analysis of a cylindrical lithium-ion battery. *Electrochim Acta* 2011;56:1246–55.

- [69] Nyman A, Zavalis TG, Elger R, Behm M, Lindbergh G. Analysis of the polarization in a Li-ion battery cell by numerical simulations. *J Electrochem Soc* 2010;157:A1236.
- [70] Bernardi D. A general energy balance for battery systems. *J Electrochem Soc* 1985;132:5.
- [71] C. Heubner, M. Schneider, C. Lämmel, A. Michaelis, Local heat generation in a single stack lithium ion battery cell, *Electrochim. Acta* 186 (2015) 404–412.
- [72] ANSYS Fluent Advanced Add-On Module, Release 17.0, January 2016.
- [73] Min Chen, Student Member, IEEE, and Gabriel A. Rincon-Mora, Accurate Electrical Battery Model Capable of Predicting Runtime and I–V Performance.
- [74] B. Schweighofer, K. M. Raab, and G. Brasseur, “Modeling of high power automotive batteries by the use of an automated test system,” *IEEE Trans. Instrum. Meas.*, vol. 52, no. 4, pp. 1087–1091, Aug. 2003.
- [75] Dutil Y, Rouse DR, Salah NB, Lassue S, Zalewski L. A review on phase-change materials: mathematical modeling and simulations. *Renewable and Sustainable Energy Reviews* 2011;15:112–30.
- [76] Abduljalil A. Al-abidi, Sohif Bin Mat, K. Sopian, M.Y. Sulaiman, Abdulrahman Th. Mohammed, CFD applications for latent heat thermal energy storage: a review.
- [77] Joulin A, Younsi Z, Zalewski L, Rouse DR, Lassue S. A numerical study of the melting of phase change material heated from a vertical wall of a rectangular enclosure. *International Journal of Computational Fluid Dynamics* 2009;23:553–66.
- [78] Voller VR, Prakash C. A fixed grid numerical modelling methodology for convection-diffusion mushy region phase-change problems. *International Journal of Heat and Mass Transfer* 1987;30:1709–19.
- [79] Manuel Antonio Perez Estevez, Sandro Calligaro, Omar Bottesi, Carlo Caligiuri, Massimiliano Renzi, An electro-thermal model and its electrical parameters estimation procedure in a lithium-ion battery cell.

- [80] Shuanglong Du, Ming Ji, Yun Cheng, Yiwei Tang, Hongliang Zhang, Lihua Ai, Kai Zhang, Yanqing Lai, Study on the thermal behaviors of power lithium iron phosphate (LFP) aluminum-laminated battery with different tab configurations.
- [81] Manuel Antonio Perez Estevez, Carlo Caligiuri¹ and Massimiliano Renzi, A CFD thermal analysis and validation of a Li-ion pouch cell under different temperatures conditions.
- [82] Ping Pinga, Rongqi Peng^b, Depeng Kong^b, Guoming Chen^b, Jennifer Wenc, Investigation on thermal management performance of PCM-fin structure for Li-ion battery module in high-temperature environment.
- [83] S.C. Chen, C.C. Wan, Y.Y. Wang, Thermal analysis of lithium-ion batteries.
- [84] Meng Xu, Zhuqian Zhang, Xia Wang, Li Jia, Lixin Yang, A pseudo three-dimensional electrochemicothermal model of a prismatic LiFePO₄ battery during discharge process.
- [85] N. Javani, I. Dincer, G.F. Naterer, G.L. Rohrauer, Modeling of passive thermal management for electric vehicle battery packs with PCM between cells.
- [86] Francis Agyenim, Neil Hewitt, Philip Eames, Mervyn Smyth, A review of materials, heat transfer and phase change problem formulation for latent heat thermal energy storage systems (LHTESS).
- [87] Anton Lidbeck, Kazim Raza Syed, Experimental Characterization of Li-ion Battery cells for Thermal Management in Heavy Duty Hybrid Applications.
- [88] Siddique A. Khateeb, Shabab Amiruddin, Mohammed Farid, J. Robert Selmana, Said Al-Hallaj, Thermal management of Li-ion battery with phase change material for electric scooters: experimental validation.
- [89] D. R. Caudwell, J. P. M. Trusler, V. Vesovic and W. A. Wakeham, The Viscosity and Density of n-Dodecane and n-Octadecane at Pressures up to 200 MPa and Temperatures up to 473 K.

[90] Jaeshin Yi, Ui Seong Kim, Chee Burm Shin, Taeyoung Han and Seongyong Park, Three-Dimensional Thermal Modeling of a Lithium-Ion Battery Considering the Combined Effects of the Electrical and Thermal Contact Resistances between Current Collecting Tab and Lead Wire.

[91] Bin Wu, Zhe Li, and Jianbo Zhang, Thermal Design for the Pouch-Type Large-Format Lithium-Ion Batteries.

[92] Lin C, Wang F, Fan B, Ren S, Zhang Y, Han L, et al. Comparative study on the heat generation behavior of lithium-ion batteries with different cathode materials using accelerating rate calorimetry. *Energy Procedia*, 2017.